U.S. DEPARTMENT OF ENERGY | Energy Efficiency & Renewable Energy

DOE/EE-1103

Propulsion Materials

2013

VEHICLE TECHNOLOGIES OFFICE

CONTENTS

INTRODUCTION..... 1

Project 18516 – Materials for H1ybrid and Electric Drive Systems 4
Agreement 19201 – Non-Rare Earth Magnetic Materials 4
Agreement 23278 – Low-Cost Direct-Bonded Aluminum Substrates 11
Agreement 23279 – Improved Organics for Power Electronics and Electric Motors..... 18
Agreement 23726 – Novel Manufacturing Technologies for High-Power Induction and Permanent Magnet Electric Motors (General Motors CRADA) 22
Agreement 26461 – Enabling Materials for High-Temperature Power Electronics..... 30

Project 18518 – Materials for High-Efficiency Engines 32
Agreement 8697 – NO_x Sensor Development 32
Agreement 13329 – Design Optimization of Piezoceramic Multilayer Actuators for Heavy-Duty Diesel Engine Fuel Injectors 42
Agreement 17058 – Compact Potentiometric NO_x Sensor..... 52
Agreement 17257 – Materials for Advanced Turbocharger Designs 57
Agreement 18571 – Materials Issues Associated with Exhaust Gas Recirculation Systems..... 62
Agreement 23284 – Friction Reduction Through Surface Modification: Integrated Surface Texturing and Coating..... 71
Agreement 23425 – Lightweight Heavy-Duty Engine 77
Agreement 23725 – Tailored Materials for Improved Internal Combustion Engine Efficiency 82
Agreement 24034 – High-Strength and High-Temperature Materials for Heavy-Duty Engines 94
Agreement 25736 – Computational Design and Development of a New, Lightweight Cast Alloy for Advanced Cylinder Heads in High-Efficiency, Light-Duty Engines..... 103
Agreement 25737 – ICME Guided Development of Advanced Cast Aluminum Alloys for Automotive Engine Applications 110
Agreement 26190 – High-Temperature Materials for High-Efficiency Engines..... 114

Project 18519 – Materials for Exhaust and Energy Recovery..... 118
Agreement 9130– Development of Materials Analysis Tools for Studying NO_x Adsorber Catalysts (CRADA with Cummins Inc.) 118
Agreement 10461 – Durability of Diesel Particulate Filters (CRADA with Cummins, Inc.) 127
Agreement 10635 – Catalysis by First Principles..... 134
Agreement 19214 – Biofuels Impact on Diesel Particulate Filters Durability 147
Agreement 26462 – International Characterization Methods..... 154
Agreement 26463 – Biofuel Impact on Aftertreatment Devices 156

Project 18865 – Application-Specific Materials Simulation, Characterization, and Synthesis 158
Agreement 9105 – Ultra-High Resolution Electron Microscopy for Characterization of Catalyst Microstructures and Reaction Mechanisms..... 158
Agreement 14957 – Modeling of Thermoelectrics..... 165
Agreement 15529 – Erosion of Materials by Nanofluids 171
Agreement 16308 – Thermoelectrics Theory and Structure..... 176
Agreement 26391 – Applied ICME for New Propulsion Materials 184
Agreement 26464 – Materials Characterization and Evaluation 188

INTRODUCTION

Propulsion Materials Research and Development: Enabling Materials Technologies to Meet Vehicle Technologies Office Goals

The U.S. Department of Energy's Vehicle Technologies Office (VTO) is pleased to introduce the *FY 2013 Annual Progress Report for the Propulsion Materials Research and Development Program.* Together with Department of Energy national laboratories and in partnership with universities and private industry across the United States, the Propulsion Materials Program continues to invest in research and development (R&D) that provide enabling materials technologies for fuel-efficient and environmentally friendly commercial and passenger vehicles.

This introduction summarizes the objectives and progress of the program in fiscal year 2013. The Propulsion Materials Program actively supports the energy security and reduction of greenhouse emissions goals of VTO by investigating and identifying the materials properties that are most essential for continued development of cost-effective, highly efficient, and environmentally friendly next-generation heavy and light-duty powertrains. The technical approaches available to enhance propulsion systems focus on improvements in both vehicle efficiency and fuel substitution, both of which must overcome the performance limitations of the materials currently in use. Propulsion Materials Program activities include work with national laboratories, industry experts, and VTO powertrain systems (e.g., Advanced Combustion Engines [ACE], Advanced Power Electronics and Electrical Machines [APEEM], and fuels) teams to develop strategies that overcome materials limitations in future powertrain performance. The technical maturity of the portfolio of funded projects ranges from basic science to subsystem prototype validation.

Propulsion Materials Program activities are structured to serve as an enabling partner and supporter of the following VTO R&D activities:

- Hybrid and vehicle systems
- Energy storage
- APEEM
- ACE
- Fuels and lubricants

Projects within a Propulsion Materials Program activity address materials concerns that directly impact critical technology barriers within each of the above programs, including barriers that impact fuel efficiency, thermal management, emissions reduction, improved reliability, waste-heat recovery, and reduced manufacturing costs. The program engages only the barriers that result from material property limitations and represent fundamental, high-risk materials issues.

Enabling Advanced Technologies

A Propulsion Materials Program activity focuses on key technical deficiencies in materials performance that limit the expanded capabilities of advanced combustion engines, electric-drive systems, and fuels and lubricants. It provides materials R&D expertise and advanced materials testing and development that support the goals of combustion, hybrid, and power electronics development. The program provides enabling materials support for combustion, hybrid, and power electronics development, including the following:

- Materials for high-efficiency combustion strategies such as homogenous-charge compression ignition
- Materials for 55% thermal efficiency for heavy-duty diesel engines
- Materials for waste-heat recovery using mechanical (such as turbo compounding) and solid-state approaches, with the potential for a 10% increase in fuel efficiency
- Materials technologies for effective reduction of tailpipe emissions, including diesel particulate filters, low-temperature catalyst development, characterization and testing, and exhaust gas recirculation coolers
- Materials technologies for electric and hybrid-electric vehicles, including thermal management of advanced power electronics materials and reducing dependence on rare earth elements in electric motors
- Materials for alternate-fuels, including engine and exhaust aftertreatment materials compatibility and corrosion in biofuels
- Support for the Materials Genome Initiative through identifying effective computational approaches and tools to accelerate the development and deployment of new materials with improved properties.

The program supports these core technology areas by providing materials expertise, testing capabilities, and technical solutions for materials problems. The component development, materials processing, and characterization that the program provides are enablers of the successful development of efficient, durable, and emissions-compliant engines.

Program Organization

The Propulsion Materials Program consists of the following four R&D projects, which support VTO propulsion technologies. Each project consists of several R&D agreements.

1. Materials for Electric and Hybrid Drive Systems
    - Develop materials appropriate for automotive power electronics, electric motors, and other electric and hybrid system applications.
2. Materials for High-Efficiency Engines
    - Develop materials for next-generation, high-efficiency engines and address anticipated issues with engine cylinder block, head, crankshafts, pistons, valves and valve train, fuel injectors, turbochargers, and exhaust gas recirculation systems.
3. Materials for Control of Exhaust Gases and Energy Recovery Systems
    - Develop materials for exhaust aftertreatment and waste heat recovery applications.
4. Materials by Design (Application-Specific Materials Simulation, Characterization, and Synthesis)
    - Adopt computational materials design, including an atomic-scale characterization protocol to develop advanced materials for NOx catalysts, cast engine components, and electric motors and providing a pathway to transition Basic Energy Science research to practical applications.

R&D projects are evaluated annually using strategic objectives. Activities are evaluated based on their relevance to VTO objectives, the supported team's (i.e., ACE, APEEM, and fuels) assessment of the work, and the strength of industrial support for the activity. In order to meet future efficiency improvement targets, new projects and areas of research will be identified by assessments of VTO stretch objectives and resultant demands for increased material performance.

Edwin Owens
Program Manager, Materials Technology
Vehicle Technologies Office
Energy Efficiency and Renewable Energy

Jerry L. Gibbs
Technology Manager
Vehicle Technologies Office
Energy Efficiency and Renewable Energy

Project 18516 – Materials for Hybrid and Electric Drive Systems

Agreement 19201 – Non-Rare Earth Magnetic Materials

M. A. McGuire
Materials Science and Technology Division
Oak Ridge National Laboratory
P.O. Box 2008, MS 6056, Bldg. 4100
Oak Ridge, TN 37831-6068
Phone (865) 574-5496; fax: (865) 576-5023; e-mail: mcguirema@ornl.gov

DOE Technology Manager: Jerry L. Gibbs
Phone (202) 586-1182; fax: (202) 586-1600; e-mail: jerry.gibbs@ee.doe.gov
ORNL Technical Advisor: J. Allen Haynes
Phone (865) 576-2894; fax: (865) 574-4913; e-mail: haynesa@ornl.gov

Contractor: Oak Ridge National Laboratory, Oak Ridge, Tennessee
Prime Contract No.: DE-AC05-00OR22725

Objectives

- Discover new permanent magnet (PM) materials that do not contain rare earth (RE) elements.
- Develop an understanding of the magnetic properties of discovered materials using properties measurements and first principles calculations to direct work toward improved PM properties.

Approach

- Investigate understudied known materials and search for new materials in RE-free chemical systems that hold promise for the discovery of new high-temperature ferromagnets, with the large magnetic moments and strong anisotropies required for technologically useful PM materials.
- Target materials that contain a high concentration of magnetic 3*d* elements (e.g., Cr, Mn, Fe, and Co), along with heavier 4*d* or 5*d* transition metals (e.g., Zr, Hf, Nb, Ta, Mo, and W), which have strong spin-orbit coupling.
- Focus on anisotropic crystal structures to allow strong magnetocrystalline anisotropy.

Accomplishments

- Published technical report highlighting promising PM properties of melt-spun $Hf_2Co_{11}B$ alloys.
- Submitted provisional patent application entitled, "Hf-Co-B alloys as permanent magnet materials."
- Demonstrated enhanced stability of the anisotropic ($L1_0$) ferromagnetic phase of FePd using high magnetic fields.
- Discovered new ferromagnetic compositions $Fe_{2.85}Mo_{0.15}P$ and $Fe_{2.85}W_{0.15}P$, which include heavy transition metals in an iron-rich phosphide.

Future Direction

- Funding for this project concluded in fiscal year (FY) 2013.

Introduction

The strategic importance of RE elements and the associated potential problems are receiving increased attention due to their use in PMs for electric motors. Currently, there are no alternative PM materials competitive with $Nd_2Fe_{14}B$ that do not contain RE elements. The development of such materials would allow progress in lowering the cost of electrical propulsion systems toward the performance goals of $12/kW by 2015 and $8/kW by 2020 for the Hybrid and Electric Propulsion subprogram set forth by the U.S. DRIVE and Vehicles Technologies Office. The Propulsion Materials Technology activity has identified a limited domestic supply of materials required for advanced vehicle technology, among them RE elements, as a key barrier to enabling expanded capabilities of electric drive systems.

An important figure-of-merit for PM materials is called the maximum energy product (BH_{max}). It measures a material's ability to maintain its magnetization, or magnetic induction (B), in the presence of a demagnetizing field (H). If a large magnetization can be maintained even for large demagnetizing fields, then a large BH_{max} results. Note that MGOe (mega-Gauss-Oersted) is a unit of energy density, and 1 MGOe = 7.96 kJ/m^3.Typical values of BH_{max} at room temperature for the best RE magnets are 40 to 50 MGOe. Achieving large values of BH_{max} requires a large magnetic moment to persist upon removal of the magnetizing field (i.e., remanent magnetization or remanence) and a large field required to reverse the direction of that moment (i.e., coercive field or coercivity). A material with high coercivity (i.e., generally greater than 1,000 Oe) is termed a "hard" ferromagnet. The Curie temperature is the temperature above which ferromagnetism vanishes. Typically, the coercivity drops rapidly upon approaching this temperature from below. Therefore, good PM materials must have high Curie temperatures, typically at least 200°C above the maximum operation temperature is desired.

The technical barrier that must be overcome in this research area is related to the role that RE plays in current state-of-the-art PMs. Realizing good PM behavior (i.e., large remanence and high coercivity) requires strong magnetic anisotropy. This anisotropy gives preference to a particular orientation of the magnetic moment and presents an energetic barrier to the reorientation of the net moment required to demagnetize the material. There are two sources of magnetic anisotropy: shape anisotropy (an extrinsic property) and magnetocrystalline anisotropy (an intrinsic property). Shape anisotropy results from the difference in demagnetization factors along different directions in non-spherical magnetic particles. Magnetocrystalline anisotropy arises from the interactions between the magnetic moments and the crystal lattice, giving a preferred direction for the magnetization. Spin-orbit interactions couple the magnetic moment (spin) to the atomic orbitals of the magnetic atoms. Strong covalent bonding can fix the orientation of these atomic orbitals with respect to the crystal structure. The combination of these two phenomena (covalent bonding and spin-orbit coupling) results in a preferred direction for the alignment of the magnetic moments, which is manifested as magnetocrystalline anisotropy. This is expected to be strongest in materials with anisotropic (non-cubic) crystallographic structures.

In RE magnets, the strong spin-orbit coupling and large magnetic moment of the RE is crucial to providing magnetic anisotropy. The primary technical barrier to development of better non-RE PMs is achieving strong magnetocrystalline anisotropy in the absence of these constituents. Strong spin-orbit coupling is not unique to REs. Its strength increases rapidly with increasing atomic number; therefore, it is high in all heavy elements. PtCo has strong magnetocrystalline anisotropy due to the large spin-orbit coupling of Pt and its interaction with the 3*d* Co moments. Despite the high cost of Pt, this material has seen commercial use in magnetic recording applications. This example demonstrates the potential of using heavy *d*-block transition metals like Pt to play the role of the RE.

Some of the most promising chemical systems for development of new PM materials are those that include the 3*d* transition metals Cr, Mn, Fe, and Co with heavy 4*d* or 5*d* metals

(e.g., Zr, Hf, Nb, Ta, Mo, and W). Analyzing known compounds containing these elements is one path toward new hard ferromagnets. However, the discovery of entirely new materials is likely to have the largest long-term impact on technology. This usually requires examining chemical systems containing at least three elements, because binary compositional phase diagrams are generally well characterized. Indeed, moving beyond binary compounds was the key to developing $Nd_2Fe_{14}B$-based materials as replacements for $SmCo_5$ magnets.

The objective of this project is to use the ideas outlined above to target new and known materials to identify RE-free chemical systems that contain PMs with potential for use in electric motors. Replacing $Nd_2Fe_{14}B$ is a serious and important materials challenge that will require long-term research efforts and must include advancements in performance and understanding of non-RE magnets and, perhaps most importantly, the discovery and development of new materials.

Results

Accomplishments from FY 2013 related to several ferromagnetic material systems are summarized in the following paragraphs. These include the hard ferromagnetic Hf-Co-B alloys, the ferromagnetic phosphide Fe_3P, and the order-disorder alloy FePd. We submitted a provisional patent application and published a technical report concerning $Hf_2Co_{11}B$ and applied synchrotron x-ray scattering to probe local atomic structure of the material. We discovered and characterized new Fe_3P-based materials, which include heavy transition metals and display evidence of increased magnetic anisotropy. Finally, we used neutron diffraction to study the structure and magnetic order in FePd, examined the effects of substituting Ni in place of the expensive Pd, and achieved enhanced stability of the magnetically anisotropic tetragonal phase using thermomagnetic processing techniques.

Hf-Co-B Melt-Spun Alloys

In early FY 2013, we submitted a provisional patent application related to our development of promising PM properties in melt-spun ribbons of composition $Hf_2Co_{11}B$; we subsequently published some of our findings in the form of a technical report in the open scientific literature (McGuire et al. 2012). The most important finding is that energy products as high as 6.7 MGOe are obtained from as-spun ribbons without the need for subsequent thermal processing. This is as high as most grades of AlNiCo (the best non-RE PM) and about half the value obtained in optimized melt-spun ribbons of $Nd_2Fe_{14}B$.

Recently, we have employed synchrotron x-ray scattering techniques to study the phase composition and atomic structure in these materials. Some results are shown in Figure 1. This figure shows results from pair distribution function analysis of x-ray data obtained in collaboration with Mikhail Feygensen of Oak Ridge National Laboratory using the Advanced Photon Source at Argonne National Laboratory. The figure also shows room temperature magnetization loops and scanning electron microscopy (SEM) micrographs of the materials used for the study.

The pair distribution function technique probes the local atomic structure of a material. The reduced pair distribution function G(r) plotted in Figure 1 is related to the likelihood of finding pairs of atoms separated by a distance r. Structures with high periodicity will have large G(r) persisting to large values of r, while amorphous materials, for which correlations between atomic positions are limited to a few near neighbors, will have small G(r).

Figure 1a shows G(r) for a ribbon melt-spun with a sufficiently high quench rate to produce very soft magnetic behavior (i.e., coercivity near zero). The SEM micrograph shows contrast modulations; however, the pair distribution function data show G(r) is small for all values of r, indicating the material to be amorphous. The contrast in the SEM image is then attributed to compositional modulations in the amorphous phase. Figure 1b shows data for a ribbon quenched at a rate that produces some small and/or poorly crystalline precipitates embedded in the amorphous matrix, as indicated by the oscillatory behavior of G(r) confined to low values of r.

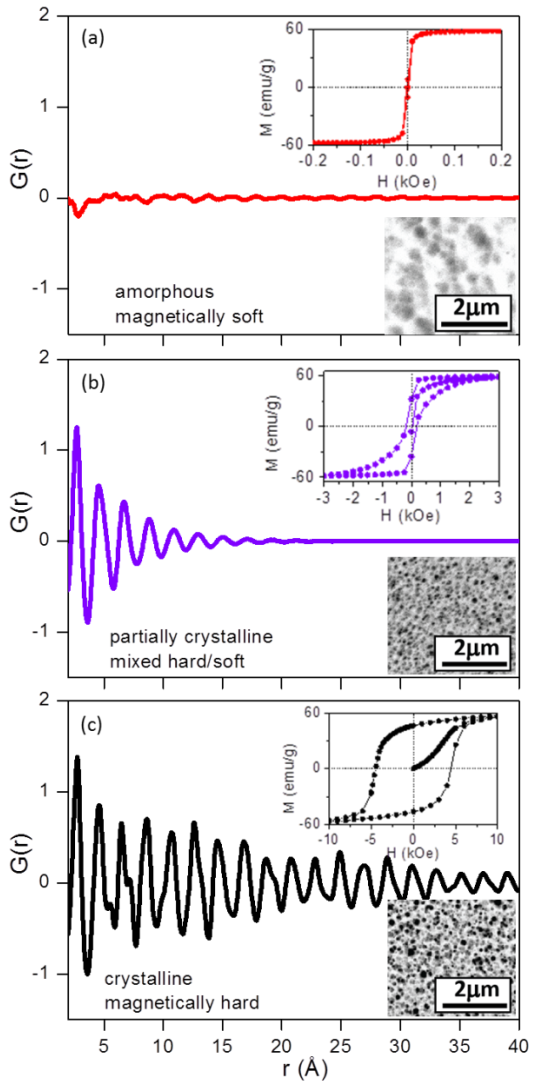

Figure 1. Reduced pair distribution function G(r) for $Hf_2Co_{11}B$ melt-spun ribbons. (a) No strong pair correlations at any length scale are indicative of amorphous material. (b) Oscillations for low values of r indicate short range order in nano-grains. (c) Long-range order is apparent from the oscillations persisting to large r. The insets show the corresponding room temperature magnetization loops and SEM micrographs.

This results in a magnetization curve that displays the components associated with both hard and soft behavior. Figure 1c shows data for the materials quenched at a lower rate still, which results in nearly complete crystallization of the sample. G(r) oscillations extend to large r and the magnetic properties are best in this material.

Synchrotron x-ray diffraction patterns also have been collected. Together with the pair distribution function data, these will be key in understanding the crystallographic and microstructural properties associated with the best permanent magnetic behavior in these complex materials.

New Fe_3P-Based Ferromagnets

Transition metal-rich phosphide compounds were targeted in the search for new hard ferromagnets. Synthesis techniques employed included arc-melting and crystal growth using molten metal fluxes. The later technique involves dissolving starting materials at high temperatures in a low melting point metal (called the flux; tin, antimony, and alloys of the two were employed here), cooling slowly to allow crystalline phases to precipitate and decanting the flux at a temperature above its melting point. These experiments produced a variety of ternary compounds, including crystals combining Mo, Fe, and P, which were identified as promising due to their high Fe content and pursued further. The composition of the crystals indicated the materials were likely best described as Mo-substituted Fe_3P. Fe_3P, are tetragonal, and are a ferromagnet with a Curie temperature of 700K and a large magnetic moment (1.9 μ_B/Fe). To our knowledge, this was the first example of substitution of a heavy transition metal into the crystal lattice of Fe_3P.

Subsequent experiments included arc-melting to target composition close to that observed in the single crystals. For this purpose, FeP, Fe_2P, and Fe_3P were synthesized by carefully reacting Fe powder with P in evacuated silica ampoules. These binary compounds were combined with heavy transition metal elements via arc melting. $Fe_{3-x}M_xP$ was examined with *M* = Nb, Ta, Mo, and W.

The results indicated that significant amounts of Mo and W were substituted into the structure, while little or no Nb and Ta could be incorporated. This was based on observation of lattice parameter changes when compared to Fe_3P determined by x-ray diffraction.

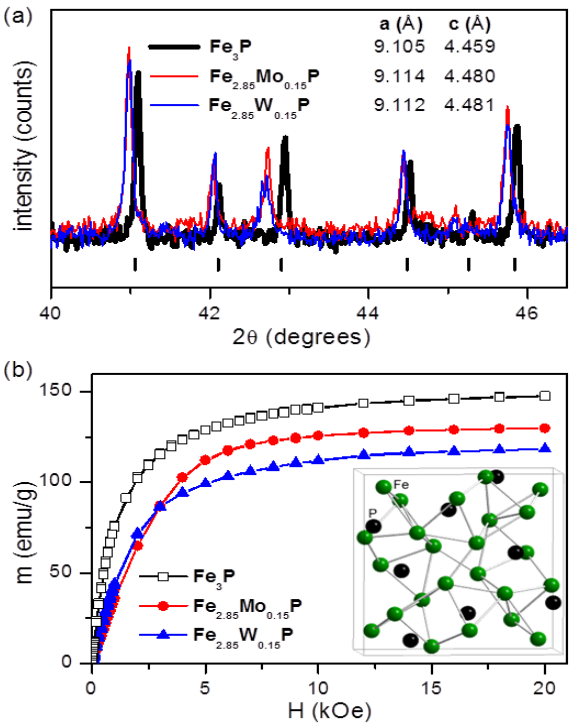

Figure 2. (a) X-ray diffraction patterns showing the lattice parameter shifts associated with replacement of Fe in tetragonal Fe_3P by the larger and heavier elements Mo and W. Lattice parameters are listed on the figure. (b) Magnetization isotherms at room temperature

Diffraction data are shown in Figure 2a. A clear shift of the Bragg peaks to lower angles is observed when the large Mo or W is substituted for Fe. Lattice parameters determined from fitting of the full diffraction patterns are indicated on the figure and show a significant expansion of the unit cell with substitution. The crystal structure is shown in the inset of Figure 2b. Compositional analysis was performed using energy dispersive x-ray analysis in a SEM, suggesting compositions with approximately 5 % of the Fe replaced by the heavier element. Samples were then synthesized at this stoichiometry ($Fe_{2.85}M_{0.15}P$) for further characterization.

Magnetization measurements were performed to determine the effect of heavy element substitution on the magnetic properties. The materials indeed remain ferromagnetic, as indicted by the magnetization curves measured at room temperature (Figure 2b). The saturation magnetization was decreased by substitution, primarily due to dilution of the strongly magnetic Fe sublattice with the weakly magnetic Mo or W. The magnetic moment per Fe was not significantly affected. Because the microstructure is not controlled in these samples, little or no coercivity is observed. However, some information regarding the magnetic anisotropy can be obtained from the approach to saturation in Figure 2b. In a polycrystalline material, a slow approach to saturation is indicative of the presence of some direction along which it is difficult to direct the magnetic moments (i.e., at least one hard direction). Comparison of the three curves in Figure 2b shows that the materials with the heavier transition metals included approach saturation more slowly than Fe_3P. This suggests that the magnetic anisotropy has been increased to some degree by incorporation of the heavy transition metal. The effect of the substitution on the crystallographic orientation of the easy and hard directions is not clear at this time. In Fe_3P, the easy axis is in the ab-plane of the tetragonal structure. For good PM performance, the easy axis would need to be rotated to the unique c-axis to eliminate the possibility of rotation of the moment in the ab-plane, which would significantly limit the coercivity. This may be achievable by chemical substitutions through a modification of the local environment of the Fe atoms and the tuning of the electronic structure that accompanies the compositional variation.

FePd-Based Materials

One important class of anisotropic ferromagnets is the family of $L1_0$ binary intermetallic compounds. The notation $L1_0$ refers to the tetragonal crystal structure adopted by the materials, which is shown in Figure 3a. Members of this family include MnAl, CoPt, CoPd, FePd, FePt, and FeNi, represented as *AB*. Excluding MnAl, all of these *AB* compounds undergo an order disorder transition upon heating, converting from an ordered intermetallic with specific site preferences for *A* and *B* to an alloy with equal probability of finding *A* or *B* on each site. The disordered structure is face-centered cubic and the ordered structure is primitive tetragonal (Figure 3a). The red lines in Figure 3a outline the primitive

tetragonal cell. In the tetragonal structure, the materials show strong magnetic anisotropy.

FeNi is particularly interesting because of the low cost of the constituents. Unfortunately, the driving force for atomic ordering is lowest in this compound and it has proved exceedingly difficult to prepare in the ordered tetragonal structure. It occurs naturally in meteorites as the mineral tetrataenite, which presumably equilibrates over very long time scales. In this work, we explored a possible means to improving the rate at which the conversion takes place in these materials.

One study investigated the effects of Ni substitution into FePd. FePd is relatively easy to form in either the cubic or tetragonal structure by arc-melting and annealing at appropriate temperatures, as shown in the powder x-ray diffraction patterns in Figure 3b for a slightly Pd-rich composition. A selected region of similar patterns from several samples is shown in Figure 3c. These include equiatomic FePd and Ni-containing samples $FePd_{1-x}Ni_x$ and $FePd_{1-y}Ni_y$. For comparison with the Ni-containing samples, both cubic and tetragonal samples of FePd are shown. For low Ni content, represented by x, the tetragonal structure was formed under conditions similar to those used to form tetragonal FePd. However, thermal treatment under the same conditions was not sufficient to induce atomic ordering in the sample with higher Ni content, represented by y. These results show that Ni-containing $L1_0$ phases can be stabilized relatively easily for low Ni content, but that moving to the more promising Ni-rich side of the phase diagram will require significantly longer thermal treatments or the application of more advanced material processing techniques. Importantly, it highlights a route to pursue stabilization of Ni-containing, Fe-based, $L1_0$ ferromagnets by working one's way across the phase diagram from easy to form tetragonal FePd to the desired Ni compounds.

We also studied the effects of strong magnetic fields on the order disorder transition, targeting a means to facilitate the transformation. FePd-based samples were prepared for thermomagnetic processing. Experiments were carried out by Orlando Rios in the Materials Science and Technology Division at Oak Ridge National Laboratory. Samples of varying composition were cycled through the order-disorder transition, which occurs near 700°C in FePd in equilibrium.

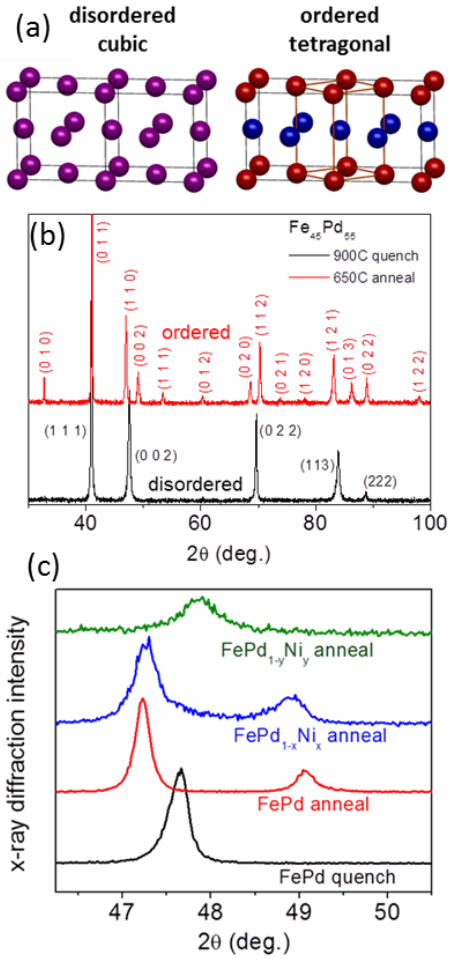

Figure 3. (a) Representation of the disordered, cubic structure and ordered, tetragonal structure of FePd. Purple spheres represent mixed Fe/Pd sites and red and blue spheres represent Fe and Pd sites, respectively. (b) Diffraction patterns from the two states of $Fe_{45}Pd_{55}$. (c) Diffraction patterns from $FePd_{1-x}Ni_x$ showing the tetragonal state for low Ni content and the cubic state for higher Ni content.

The transition can be monitored by *in situ* electrical resistance measurements. The black curve in Figure 4 shows the increase in resistance that occurs upon cooling FePd through the phase transition. Significant undercooling is observed here due to the

relatively high temperature sweep rate of 10°C/min. The same experiment was then performed in the presence of a 9 T magnetic field. The result of this measurement is also shown in Figure 4 (red curve). The magnetic field had two notable effects: the transition occurred at higher temperature and the increase in resistance was more abrupt. The former shows that the magnetic field stabilizes the ordered tetragonal crystal structure relative to the disordered cubic structure. The latter indicates increased kinetics of the transition in the presence of the magnetic field. Both observations suggest that high magnetic field processing is a promising technique for forming $L1_0$-type anisotropic ferromagnets.

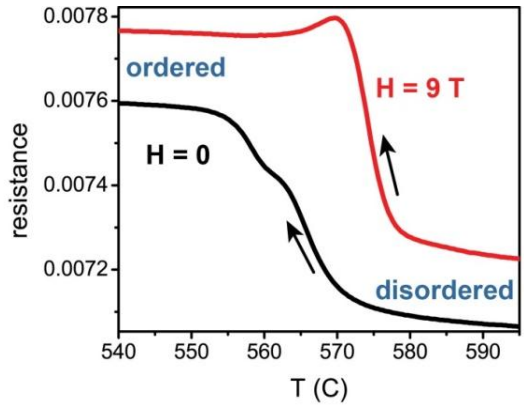

Figure 4. Electrical resistance vs. temperature (T) of FePd measured upon cooling through the transition from the cubic, disordered structure to the tetragonal, ordered structure. Effects of applying a magnetic field (H) during the measurement include increases in the transition temperature and the sharpness of the transition.

Other efforts in this direction and for which data analysis are ongoing include neutron diffraction studies of the structure, magnetism under applied pressure, and study of the full solid solution $FePd_{1-x}Ni_x$ using x-ray diffraction and magnetization measurements.

Conclusions

Accomplishments in FY 2013 included important contributions to our understanding of RE-free $Hf_2Co_{11}B$-based magnetic materials in the form of a published technical report, submitted provisional patent application, and new information from synchrotron diffraction studies regarding the structure of the materials. Effects of Zr substitution for Hf on the magnetic performance should be examined in an effort to maintain or improve magnetic properties while lowering material cost. In addition, new ferromagnetic materials were identified, which combine heavy transition metals in the ferromagnetic Fe_3P structure. These compounds may have increased magnetic anisotropy and first principles calculations should be pursued to examine the feasibility of achieving strong uniaxial anisotropy in this structure type. Finally, efforts to stabilize $L1_0$ structures identified alloying and thermomagnetic processing as means to achieve the desired magnetic properties while minimizing precious metal content.

References

McGuire, M. A., O. Rios, N. J. Ghimire, M. Koehler, 2012, “Hard ferromagnetism in melt-spun $Hf_2Co_{11}B$ alloys,” *Appl. Phys. Lett*. 101, 202401.

Project 18516 – Materials for Hybrid and Electric Drive Systems

Agreement 23278 – Low-Cost Direct-Bonded Aluminum Substrates

H.-T. Lin, S. B. Waters, and A. A. Wereszczak
Ceramic Science and Technology Group
Oak Ridge National Laboratory
P.O. Box 2008, MS 6068, Bldg. 4515
Oak Ridge, TN 37831-6068
Phone (865) 576-8857; fax: (865) 574-6098; e-mail: linh@ornl.gov

DOE Technology Manager: Jerry L. Gibbs
Phone (202) 586-1182; fax: (202) 586-1600; e-mail: jerry.gibbs@ee.doe.gov
ORNL Technical Advisor: J. Allen Haynes
Phone (865) 576-2894; fax: (865) 574-4913; e-mail: haynesa@ornl.gov

Contractor: Oak Ridge National Laboratory, Oak Ridge, Tennessee
Prime Contract No.: DE-AC05-00OR22725

Objectives

- Develop low-cost, high-quality, and thermomechanically robust direct-bonded aluminum (DBA) substrates.
- Develop low-cost DBA substrates that are at least 25% lighter than conventional direct-bonded copper (DBC) substrates.

Approach

- Develop innovative ways to fabricate the ceramic constituent (e.g., low-cast AlN substrate).
- Benchmark existing commercially available DBA and DBC substrates.
- Develop test method to measure interfacial shear strengths of Al-ceramic interface.

Accomplishments

- Completed Al-Si paste, Si powders, and Al-Si-Mg alloy films approaches to fabricate DBA and DBC substrates.
- Demonstrated that a compromise between the low-cost and performance of DBA and DBC substrates must be struck.
- Completed initial development and demonstration of a silicon nitride ceramic substrate with both a high mechanical and thermal conductivity property.
- Funding for this project concluded in fiscal year 2013.

Future Direction

- Develop and optimize silicon nitride ceramic substrates with both high mechanical performance and thermal conductivity property for the next generation of DBC and DBA substrates with GaN and SiC.

Introduction

Application of low-cost DBA substrates will enable the reduced cost of the inverter insulated gate bipolar transistor power modules, while concomitantly sustaining or improving thermal management and improving thermomechanical reliability. Compared to copper and DBC substrates, aluminum (Al) has a lower elastic modulus; therefore, it imparts a lower stress on the ceramic substrate it sandwiches. This contributes to the improved mechanical reliability of the entire substrate. Also, the wire and ribbon used for bonding in power electronic modules tends to be Al; therefore, the apparent coefficient of thermal expansion of DBAs is compatible, unlike DBCs. New sintering technologies also are more compatible with DBAs than DBCs. The use of a DBA substrate will lessen the weight up to 50% compared to the presently used DBC substrates. This would contribute to the substantial weight reduction goals of the inverter and converter in the Advanced Power Electronics and Electric Motors (APEEM) Program as well.

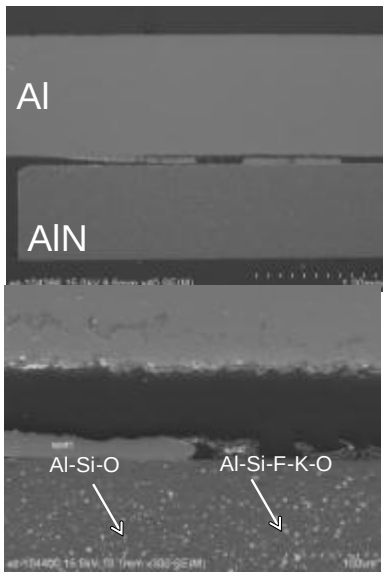

Figure 1. Scanning electronic microscopy of polished cross section of Al/AlN specimen after bonding process.

On the other hand, reducing cost, improving volumetric power, extending reliability, and improving thermal management are all barriers to the goals of the Vehicle Technology's APEEM Program. If DBAs could be fabricated cheaply, then their use would inherently address those other barriers. DBA substrates presently are very difficult to fabricate due to the inherent issues with Al to alumina. DBAs are now only available from a limited numbers of suppliers and are expensive. Although Toyota presently uses DBA substrates in the 2010 Prius, domestic automotive original equipment manufacturers would only consider using DBA substrates in their own inverters if they were cheaper and more readily available.

The objective of this subtask is to develop low-cost, high-quality, and thermomechanically robust DBA substrates, which are comparable to commercially available units. The ultimate goal is to facilitate the achievement of the 2015 APEEM goal of $12/kW for an electric traction system. Also, a secondary goal is to develop a silicon nitride (Si_3N_4) ceramic substrate with both excellent mechanical properties and high thermal conductivity for next generation DBC and DBA substrates with GaN and SiC.

Results

Processing of Low Cost Direct-Bonded Aluminum Substrates

Experiments were carried out to bond the Al metal plate to both Al_2O_3 and AlN ceramic substrates using a commercial $Al_{-12}Si$ brazing paste (designated as DayBraze 729) acquired from Johnson Manufacturing Company, Princeton, Iowa. The Al_2O_3/Al and AlN/Al specimens with $Al_{-12}Si$ brazing paste were hot pressed at 640°C and 15 MPa for 30 minutes in a flowing argon or argon + 4% hydrogen environment. The purpose of using the argon gas + 4% hydrogen was to further reduce the oxygen content in the hot pressing furnace to inhibit the oxidation of Al-Si paste and Al plate. Visual observations after hot pressing both Al_2O_3/Al and AlN/Al specimens looked sound. However, these samples were readily peeled off by hand, which is indicative of poor bonding. The detailed scanning electronic microscopy analysis of the AlN/Al specimen polished cross section showed the presence of Al-Si brazing paste, meaning that it was not completely reacted during the hot-pressing as evident by the presence of fluorine (F) and potassium (K)

(Figure 1). Also, composition analysis showed that the interfacial Al-Si reaction layer contained a high concentration of oxygen. The Al-Si brazing paste could be oxidized during the heating process, thus resulting in the formation of an Al-Si-O compound that prevents sound bonding between Al and the ceramic substrates.

A subsequent detailed chemical element mapping further confirmed the above stated results of the partially reacted paste, which is evident by the presence of fluorine, potassium, and oxygen (Figure 2).

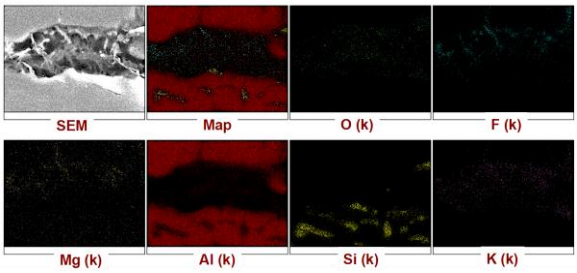

Figure 2. EDAX element map of polished cross section of an Al/AlN interface.

Alternatively, Al-Mg-Si and Al-Si-Cu alloys thin foils were used as a second approach to achieve a strong bond between Al and the ceramic substrates. The types of Al-Si alloy foils used were a 5250 alloy (Al-Mg-Mn-Si) and a 6061 alloy (Al-Si-Cu-Cr). The microstructure of the as-received 5250 and 6061 foil after metallographic polishing is shown in Figure 3. The light-contrast, second-phase that is present was identified as Al-Si-containing particles via EDAX analysis. Joining was carried out at 610°C in flowing N_2 gas via the applied load of 5 MPa. After hot pressing, the joined pieces also appeared sound. However, once again, these pieces were readily separated by hand, indicative of poor interfacial bonding strength. The poor interfacial strength was independent of the type of ceramic plate used.

Figure 4 shows the optical micrographs of the surface features after manual separation. Observations revealed that the Al-Si alloys did not evenly and completely spread out on the Al metal surface; also, there was no sign of wetting on ceramic surfaces. The scanning electronic microscopy examination showed formation of Al-Si droplets, indicating poor wetting, with high oxygen content confirmed by EDAX analysis. The presence of high oxygen is very likely part of the cause of poor wetting and bonding between Al and the ceramic plates.

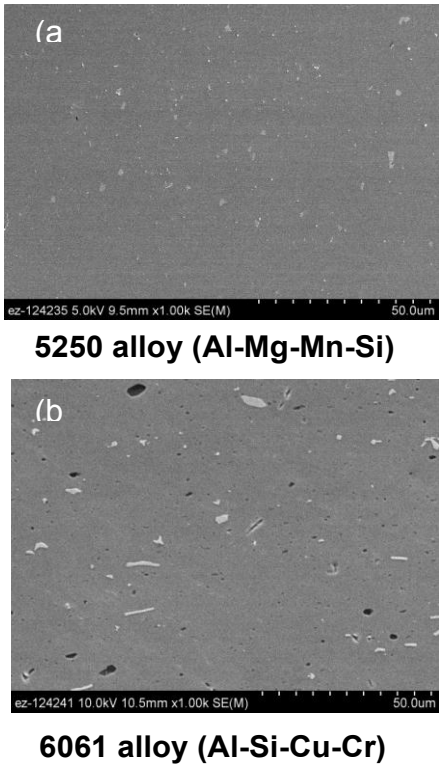

Figure 3. Polished cross section of commercial Al-Si foils of (a) 5250 and (b) 6061.

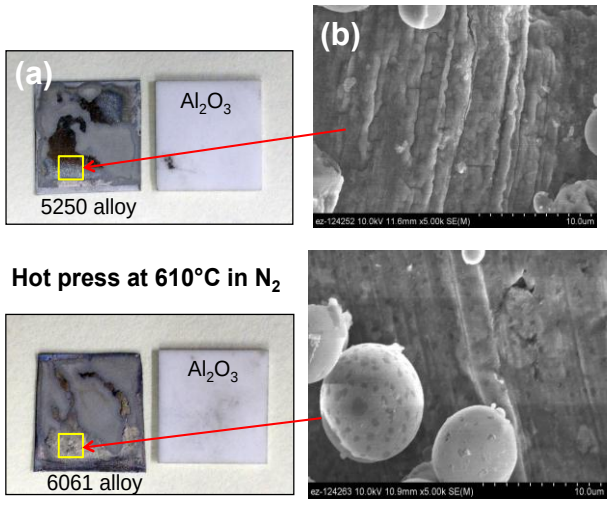

Figure 4. Photos showing (a) the surfaces of Al and Al_2O_3 ceramic after manual separation and (b) scanning electronic microscopy photomicrographs showing the Al surface at high magnification.

Metal powders were subsequently evaluated. Commercially available Al-Si-Mg (manufactured by READE Advanced Materials) and Si powders (manufactured by Vesta Si) were purchased to bond the Al and ceramics substrates. Figure 5 shows the particle morphology of both Al-Si-Mg (Figure 5a) and Si (Figure 5b) powders. Both the Al-Si-Mg and Si films were prepared via use of a polymer binder, which was hot pressed with Al_2O_3 ceramic at 610°C in a flowing N_2 environment. Again, poor bonding was observed after hot pressing due to the presence of a high oxygen content and poor wettability of the Al-Si-Mg alloy with the ceramic substrate. Results and lessons learned from Al-Si pastes, foils, and powders demonstrate that successful formation of a sound and adherent interface between Al and a ceramic substrate is a substantial technical challenge. As a result, DBA suppliers worldwide are limited and the products are very costly. These studies clearly demonstrated that a compromise between low-cost and reliable performance must be struck and that other materials must be considered

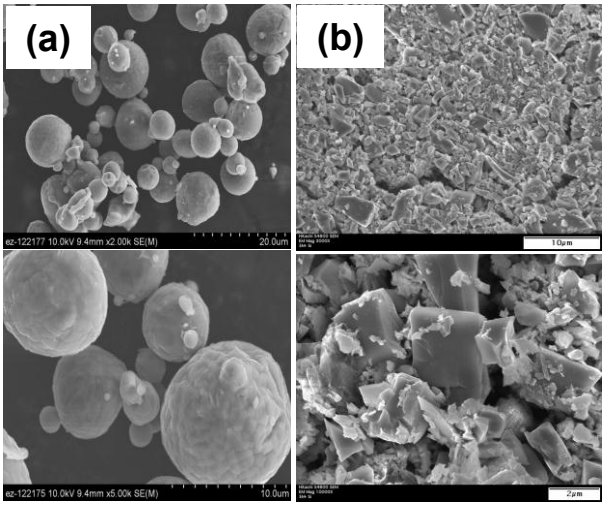

Figure 5. Scanning electronic microscopy photomicrograph of (a) as-received Al-Si powder and (b) Si powder.

Development of High-Performance Silicon Nitride Ceramic Substrate

It has been widely reported that the electronic substrates with silicon nitride (Si_3N_4)` ceramic substrates have been developed and commercialized for higher-temperature and higher-voltage application conditions due to its much better mechanical performance (e.g., fracture strength and toughness) compared to Al_2O_3 and AlN. Development of DBC substrates with Si_3N_4 ceramic is mostly conducted in foreign countries (mainly in Japan, including Kyocera and Toshiba). Therefore, these high-performance substrates with Si_3N_4 ceramics have to be imported from Japan. There is a critical need for the United States to develop its own electronic substrates with Si_3N_4 ceramic.

Therefore, a study to re-manufacture and characterize the thermal conductivity of silicon nitride ceramics developed at Oak Ridge National Laboratory (ORNL) with both high fracture toughness (up to 12 MPa•$m^{0.5}$) and strength (up to 1200 MPa) was initiated in this final year of the project (Becher et al. 2008, 2010). The patent application of ORNL silicon nitride ceramics was officially granted in June 2011. The microstructure and composition of these ORNL Si_3N_4 ceramics were tailored for the purpose of high-performance structural component applications at elevated temperatures (Figure 6). It is reasonable to anticipate that the thermal conductivity of the ORNL Si_3N_4 ceramics could be significantly improved via careful engineering of microstructure and compositions. It has been reported the presence of oxygen has a detrimental impact on the thermal conductivity of Si_3N_4 due to more phonon scattering (Figure 7; Hirao et al. 2001, Zhou et al. 2011). In addition, the presence of secondary phases and grain boundary glassy films with low thermal properties also could have a significant impact on the thermal property of the silicon nitride ceramic. Therefore, control of the sintering cycle and environment, plus additional post-thermal heat treatment, could be implemented to remove the oxygen from the beta silicon nitride grains and secondary phases(s), resulting in significant improvement of thermal conductivity.

The powder mixtures in this study consisted of UBE E-10 or ESP Si_3N_4 powder with an additive composition of 8 wt% Gd_2O_3 and Lu_2O_3 with 2 wt% MgO. Note the cost of ESP powder is relatively less expensive than E-10, but the chemical compositions are similar. In order to blend the powders well, isopropanol was added

to each powder mixture; this slurry was then attritor-milled for 2 hours using 2-mm silicon nitride balls. The alcohol–powder slurry was poured through a 90-mm sieve to separate the milling media from the powder–alcohol slurry, which was then captured in a stainless steel tray. The slurry was then air-dried in a hood for 24 hours; after drying, the powder was gently ground and poured through a 425-mm sieve to break up agglomerates. The desired amount of the powder mixture was then placed into a graphite die and a pressure of about 20 MPa was applied via the graphite rams.

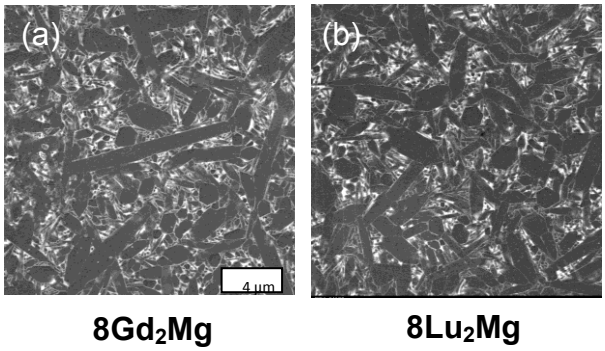

Figure 6. Scanning electronic microscopy photomicrographs of ORNL Si_3N_4 ceramics with (a) $8Gd_2O_3$-2MgO and (b) $8Lu_2O_3$-2MgO composition.

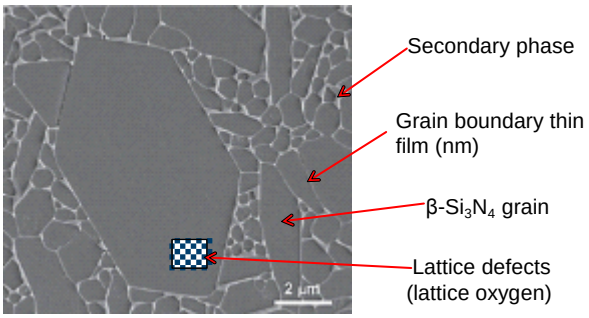

Figure 7. Scanning electronic microscopy photomicrograph used to depict the effect of defects, secondary phase, and grain boundary film on thermal conductivity.

The loaded die assembly was placed into a hot press, which was evacuated and backfilled with nitrogen three times to provide a nitrogen-rich gaseous environment. Billets of Si_3N_4, plus additive compositions, were densified at 1800°C for 1 hour under an applied uniaxial pressure of 22 MPa, with a continuous flow of nitrogen through the chamber. Mechanical properties at room temperature and 1200°C were determined using machined flexure bars (3 x 4 x 45 mm) from the hot-pressed billets via ASTM Standard C-1161. The thermal properties at room temperature were measured via the laser flash approach.

Figure 8 shows the fracture strength of ORNL Si_3N_4 ceramics measured at room temperature and 1200°C. The $8Gd_2MgO$ samples exhibited fracture strength of 900 to 950 MPa and were insensitive to the silicon nitride powders used (E10 vs. ESP powder). The $8Lu_2MgO$ had the strength of 1025 MPa, consistent with those reported by ORNL in the published reference (Becher at al. 2008, 2010). Results of high-temperature mechanical property testing at 1200°C in air shows that there is a minor decrease in fracture strength, indicative of excellent high-temperature mechanical properties and again consistent with those previously reported.

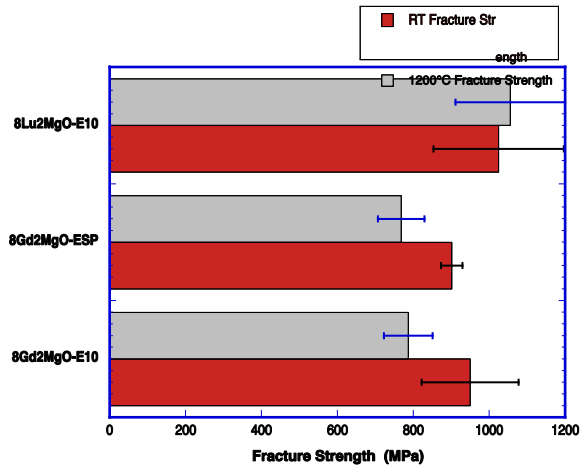

Figure 8. Fracture strength of ORNL Si_3N_4 ceramics with $8Gd_2O_3$-2MgO and $8Lu_2O_3$-2MgO composition and manufactured with E10 and ESP Si_3N_4 powder.

The thermal conductivity of Si_3N_4 discs with 12.7-mm diameter and 2-mm thickness was measured using a laser flash technique. The thermal conductivity of Si_3N_4 ceramics processed with E-10 or ESP powders and with $8Lu_2MgO$ and $8Gd_2MgO$ additives is provided in Figure 9. The measurements were repeated

five times for each disk and two disks were measured from each hot-processed billet to obtain statistical results. Note that the heat capacity value experimentally obtained (i.e., 0.7) is used to calculate the thermal conductivity (Figure 10). The obtained heat capacity of 0.7 is consistent with the reported value (Yu et al 2012). Results showed that the ORNL Si_3N_4 with $8Gd_2MgO$-E10 and $8Lu_2MgO$-ESP exhibited high thermal conductivity values between 99 and 120 W/m•K. However, silicon nitrides with $8Gd_2MgO$-ESP and $8Lu_2MgO$-E-10 exhibited thermal conductivity values of 52 to 80 W/m•K. The difference in measured thermal conductivity as a function of composition might be related to the secondary phases present after sintering.

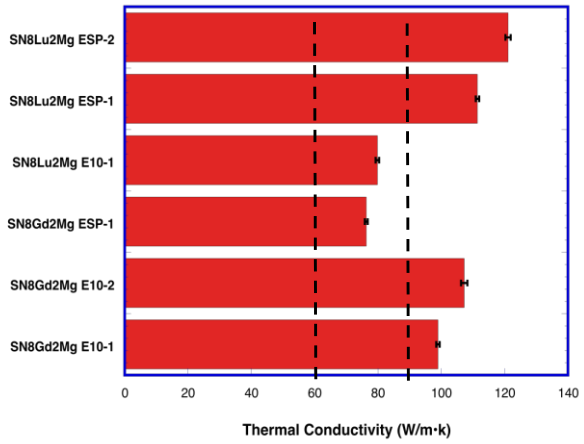

Figure 9. Thermal conductivity of ORNL Si_3N_4 ceramics with $8Gd_2O_3$-2MgO and $8Lu_2O_3$-2MgO composition and manufactured with E10 and ESP Si_3N_4 powder.

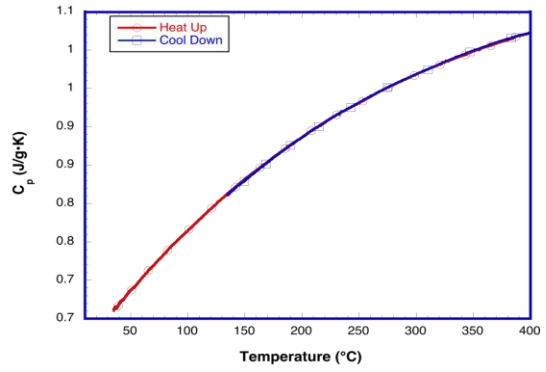

Figure 10. Heat capacity of ORNL Si_3N_4 with $8Gd_2O_3$-2MgO composition.

The variation in alpha/beta silicon nitride ratio and content of crystalline or amorphous phase also could have an influence on the thermal conductivity. Note that the thermal conductivity reported for silicon nitride ceramic used in Kyocera and Toshiba DBC substrate is 60 and 90 W/m•K, respectively. The Toshiba Si_3N_4 (SN90) and Kyocera Si_3N_4 (SN46) exhibited fracture strengths of 650 MPa and 850 MPa, respectively. Thus, by comparing the mechanical strength and thermal conductivity, the ORNL silicon nitride ceramic appears to have comparable or superior properties to those manufactured by Toshiba and Kyocera for electronic device applications.

Conclusions

This activity was brought to a conclusion in 2013. Results of DBA substrates made with commercial Al-Si paste showed very weak bonding, accompanied with cracks and delamination. The application of Al-Si alloy foils also showed no bonding between Al-Si alloys used and ceramic substrate due to the very poor wettability. Alternatively, Al-Si and Si powders also were used to bond the Al and ceramic substrates. Again, poor bonding was observed after hot pressing due to the presence of high-oxygen content and poor wettability of the Al-Si-Mg alloy with the ceramic substrate. Results demonstrated that formation of a DBA substrate with excellent interfacial bonding is a significant technical challenge. These studies clearly demonstrated that a compromise between low-cost and reliable performance must be struck.

The Si_3N_4 ceramics developed and patented at ORNL for high-temperature hot section components were re-fabricated for potential application as power electronic substrates. The test results confirmed the excellent mechanical performance at temperatures up to 1200°C in air consistent with those reported previously. The fracture strength at 1200°C is by far the highest value obtained when compared with those reported in data found in the literature. In addition, the ORNL Si_3N_4 ceramics exhibited comparable and/or higher thermal conductivity than those developed for commercial companies. Thus, by comparing the combined mechanical

strength and thermal conductivity, the ORNL Si_3N_4 ceramic have potential to provide better performance than those that are currently used by industry. As a result, the ORNL Si_3N_4 ceramics exhibit significant potential to be used in the next generation WBG insulated gate bipolar transistor with GaN and SiC devices.

References

ASTM Standard C1161, "Standard Test Method for Flexural Strength of Advanced Ceramics at Ambient Temperature."

Becher, P. F., G. S. Painter, N. Shibata, S. B. Waters, and H. T. Lin, 2008, "Effects of Rare Earth (RE) Intergranular Adsorption on the Phase Transformation and Microstructure Evolution in Silicon Nitride with RE2O3 + MgO Additives: Fracture Behavior," *J. Am. Cera. Soc.*, 91 [7], 2328-2336.

Becher, P. F., N. Shibata, G. S. Painter, F. Averill, K. Benthem, H. T. Lin, and S. B. Waters, 2010, "Observations on the Influence of Secondary Me Oxide Additives (Me = Si, Al, Mg) on the Microstructural Evolution and Mechanical Behavior of Silicon Nitride Ceramics Containing RE2O3 (RE = La, Gd, Lu)," *J. Am. Cera. Soc.*, 93[2], 570-580.

Hirao, K., K. Watari, H. Hayashi, and M. Kitayama, 2001, "High Thermal Conductivity Silicon Nitride Ceramic," *MRS Bulletin*, 26, 06, 451–455.

Yu, B., D. Chen, Y. Li, and Y. Jia, 2012, "Predictions of High-Pressure Structural, Electronic and Thermodynamic Properties for alpha- Si3N4," *Acta Metall. Sin*, 25, 2, 31–140.

Zhou, Y., H. Hyuga, D. Kusano, Y. Yoshizawa, and K. Hirao, 2011, "A Tough Silicon Nitride Ceramic with High Thermal Conductivity," *Adv. Mater*., 23, 4563–4567.

Publications/Presentations

Poster on this project was presented at the Department of Energy Advanced Power Electronics and Electric Motors Research and Development Fiscal Year 2013 Kickoff Meeting, November 14 and 15, 2012.

Oral presentation on this project was presented at Department of Energy Annual Merit Review, Arlington, Virginia, May 13 through 16, 2013.

Project 18516 – Materials for Hybrid and Electric Drive Systems

Agreement 23279 – Improved Organics for Power Electronics and Electric Motors

A. A. Wereszczak and H. Wang
Oak Ridge National Laboratory
P.O. Box 2008, MS 6068, Bldg. 4515
Oak Ridge, TN 37831-6068
Phone (865) 576-1169; fax: (865) 574-6098; e-mail: wereszczakaa@ornl.gov

DOE Technology Manager: Jerry L. Gibbs
Phone (202) 586-1182; fax: (202) 586-1600; e-mail: jerry.gibbs@ee.doe.gov
ORNL Technical Advisor: J. Allen Haynes
Phone (865) 576-2894; fax: (865) 574-4913; e-mail: haynesa@ornl.gov

Contractor: Oak Ridge National Laboratory, Oak Ridge, Tennessee
Prime Contract No.: DE-AC05-00OR22725

Objectives

- Develop thermally conductive and low-cost epoxy molding compounds (EMCs) with sustained electrical insulation, magnetic insusceptibility, thermal expansion control, and mechanical resilience for power electronic and electric motor application.
- Enable new or improved thermal management strategies in power electronics and electric motors that decrease the maximum temperature of their operation.

Approach

- A thermal conductivity of 3 W/mK in an inexpensive magnesium oxide (MgO)-filled EMC in FY 2013; in FY 2013, an attempt to achieve 5 W/mK, recognizing that more expensive (and more thermally conductive) fillers will need to be used.
- Blend inexpensive MgO with boron nitride (BN) with the intent keep total filler cost low, while maximizing thermal conductivity.

Accomplishments

- Developed hybrid MgO/BN-filled EMCs.
- Achieved a thermal conductivity of 5 W/mK, which is approximately a 5x improvement over currently used silica-containing EMCs.
- Filed an invention disclosure on development of hybrid-filled EMCs.
- Filed an invention disclosure on a hydrostatically compressed power electronic device package using MgO filler.

Future Direction

- Project ended on September 30, 2013.
- Promote development of 200°C-capable, thermally conductive (MgO-filled) EMCs in other Vehicles Technology Office programs.

Introduction

The Vehicle Technology Program's Advanced Power Electronics and Electric Motors Program has expressed emphasis on cost-reducing research targets, challenges, and areas. These include high-temperature components, packaging, and reliability for long-term transformation technologies and thermal management technologies to reduce volume and enhance thermal reliability. The technical goals of this project strike directly at that emphasis.

The goals of this project are to develop, characterize, and test candidate organic or EMCs that are thermally conductive and that have the potential to be low-cost, volume-reducing, and better-performing alternatives to presently used compounds for at least the following applications:

- Dielectrics in power electronic devices
- Potting compounds used with capacitors
- Potting compounds used in motors
- Potting compounds for future wireless charging stations.

For all of these applications, any candidate EMC must, first and foremost, possess electrical insulative behavior. However, it needs to be insusceptible to magnetic fields so that autogeneous heating does not occur. The EMC also needs to provide a barrier to moisture penetration to the constituents it mechanically protects. Lastly, the thermal expansion response of the EMC must sufficiently match that of the constituents it projects.

Our focus last year (fiscal year 2012) was on use of MgO-filled EMCs. MgO is an attractive, low-cost filler. Its use sustains electrically insulative behavior. Our work showed that a thermal conductivity of 3 W/mK can be achieved with a (low-cost) MgO-filled EMC for a volume content of 56% MgO. This thermal conductivity is approximately 3 to 4 times higher than the state-of-the-art silica-filled EMCs.

But thermal analysis of a wide variety of power electronic and electric motor components showed that a thermal conductivity of 5 W/mK of an EMC could offer significantly better thermal management options. It was recognized that expensive alternative fillers (with higher thermal conductivity than MgO) would be required; however, the satisfaction of it would at least provide a cost boundary of such a thermally conductive EMC.

The considerations of aluminum nitride (AlN) and BN fillers, hybrid blended with MgO to try to keep cost minimized, occurred in fiscal year 2013. Processing difficulties with AlN resulted in our focus being turned to the use of BN. We were able to achieve a thermal conductivity of 5 W/mK and an EMC that had a blend of MgO and BN.

Results

A blend of AlN spheres (FAN-f50, Tokuyama Americas, Arlington Heights, Illinois) with MgO powder, used in fiscal year 2012's work (10C, Ube, Japan), were used. SolEpoxy (Olean, New York) performed the processing work. The AlN was not coated with an organic; therefore, there were difficulties getting it to bond to the epoxy matrix because of AlN's affinity to react with atmospheric moisture. This poor bonding resulted in poor thermal transfer to and through the AlN.

The consequence of this was that the EMCs with AlN in them actually had lower thermal conductivities than those with just MgO as filler. It was recognized that to exploit AlN's high thermal conductivity, a coating needed to be applied and likely optimized for these EMCs. However, because of time and funding limitations, it was deemed prudent to turn our attention to BN instead, because it is not degraded by environmental moisture like AlN.

BN spheres (CarboTherm CTS2M, Saint-Gobain Advanced Ceramics, Amherst, New York) were blended with 10C MgO powders, and then used to fill EMCs. The particle side distributions are shown in Figure 1.

The EMC composites were fabricated by SolEpoxy. A range of blended ratios were examined with the intention to produce a thermal conductivity of 5 W/mK or greater in an EMC, but without compromise to processibility. A thermally conductive EMC that cannot be

processed into needed shapes for power electronic or electronic motor components is not useful; therefore, easy processibility is important.

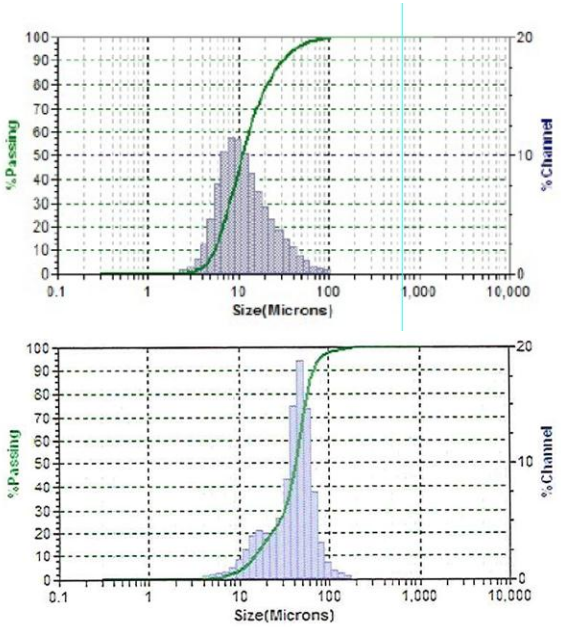

Figure 1. Particle size distributions of (top) MgO and (bottom) BN filler.

Fifteen different blends were examined and are listed in Table 1. Numerous electrical properties were measured and the primary dependent parameter, thermal conductivity, was also measured.

Table 1. List of evaluated hybrid MgO-BN sets.

Sample ID 2907-	% filled wt	% filled vol	MgO:BN ratio wt
44B	75.0	51.35	90--10
44C	70.0	45.10	90--10
44D	65.0	39.56	90--10
45A	65.0	41.83	75--25
45B	65.0	45.25	50--50
49A	60.0	40.00	50--50
49B	60.0	42.96	25--75
49C	50.0	33.42	25--75
49D	50.0	35.88	0--100
59A	56.8	40.56	17--83
59B	59.0	40.81	34--66
59C	60.0	42.03	33--67
64A	62.0	44.02	34--66
64B	62.0	44.22	32--68
64C	61.0	43.60	28--72

The thermal conductivities of all MgO-BN EMC blends are compared in Figure 2. The thermal conductivity of three of the compositions (59C, 64C, and 49B) was 5 W/mK. All three had excellent electrical characteristics (e.g., electrically insulative and low dissipation factors). Additionally, they all were processible, with 59C having the most attractive flow characteristics (as indicated by the large-valued spiral flow dimension shown in Table 2). Therefore, among the three, the 59C MgO-BN EMC is recommended. It had 42 volume % total solids content and an MgO:BN ratio of 1:2.

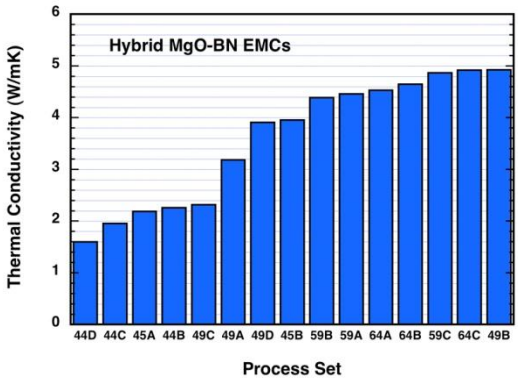

Figure 2. Comparison of thermal conductivities of the compositions listed in Table 1.

Table 2. Properties of the three hybrid MgO-BN EMC sets having the highest thermal conductivities.

Property	59C	64C	49B
MgO:BN wt. ratio	33:67	28:72	25:75
Vol % epoxy	58.0	56.4	57.0
Vol % MgO	8.9	7.6	6.6
Vol % BN	33.1	36.0	36.4
Density (g/cc)	1.736	1.731	1.29
Thermal conductivity at 110°C (W/mK)	4.87	4.92	4.93
Spiral flow distance (cm)	76	36	20
Tg (°C)	164	160	158
Dielectric strength, 900 µm film, (kV/mm)	35	55	24
Volume resistivity, 500 V, (Ω•cm)	4.0E+16	7.3E+16	2.0E+16
Dielectric constant, at 10 kHz	4.59	4.45	4.60
Dissipation factor, at 10 kHz	0.007	0.006	0.007

Although a thermal conductivity of 5 W/mK was achieved, it needed the relatively expensive BN for its filler. MgO is inexpensive (about $3/kg) and can be used to produce 3 W/mK. The BN spheres were $90/kg (AlN spheres were $128/kg for comparison); therefore, the cost of getting that additional 2 W/mK is high.

Conclusions

A thermal conductivity of 5 W/mK was achieved with a hybrid blend of MgO and BN used as filler in an EMC. It had a total filler volume fraction of 42% and a 1:2 weight ratio of MgO/BN. These hybrid MgO-BN EMCs had excellent electrical characteristics.

A thermal conductivity of 3 W/mK can be achieved inexpensively with MgO-filled EMCs. However, the high cost of materials (i.e., BN) for increasing that to 5 W/mK results in the hybrid MgO-BN EMCs being relegated to niche applications, where thermal performance characteristics are more important than cost savings.

Publications

Wereszczak, A. A., 2012, "Hybrid-Filled Epoxy Molding Compositions," DOE S-Number S-124,532, Invention Disclosure Number 201202955, File date October 11, 2012.

Wereszczak, A. A., C. W. Ayers, and M. S. Chinthavali, 2013, "Hydrostatically Compressed Power Electronic Device Package," DOE S-Number S-124,704, Invention Disclosure Number 201303116, File date July 17, 2013.

Wereszczak, A. A., T. G. Morrissey, C. N. Volante, P. J. Farris, Jr., R. J. Groele, R. H. Wiles, and H. Wang, 2013, "Thermally Conductive MgO-Filled Epoxy Molding Compounds," *IEEE Transactions on Components, Packaging and Manufacturing Technology*, DOI 10.1109/ TCPMT.2013.2281212.

Project 18516 – Materials for Hybrid and Electric Drive Systems

Agreement 23726 – Novel Manufacturing Technologies for High-Power Induction and Permanent Magnet Electric Motors (General Motors CRADA)

Glenn J. Grant
Transportation and Industrial Materials
Pacific Northwest National Laboratory
902 Battelle Blvd., K2-03
Richland, Washington 99356
Phone (865) (509) 375-6890; fax: (509) 375-4448; e-mail: glenn.grant@pnnl.gov

Blair E. Carlson
Manager, Lightweight Materials Processing
General Motors Research and Development
30500 Mound Rd
Warren, Michigan 48090
E-mail: blair.carlson@gm.com

DOE Technology Manager: Jerry L. Gibbs
Phone (202) 586-1182; fax: (202) 586-1600; e-mail: jerry.gibbs@ee.doe.gov
Field Technical Manager: Dean Paxton
Phone (509) 375-2620; fax (509) 375-2186; e-mail: dean.paxton@pnnl.gov

Contractor: Pacific Northwest National Laboratory
Prime Contract No.: DE-AC05-76RL01830

Objectives

- Develop and deploy high-power induction and permanent magnet rotors and stators that are lighter weight, have better cooling, and are a lower cost to manufacture through the application of novel solid-state joining and fabrication technologies.
- Apply solid-state processing techniques to improve performance of a low-cost soft magnetic material used in the rotors of high-power induction motors.

Approach

- Develop solid-state joining techniques and manufacturing processes that will increase the efficiency of electric motors through lightweighting; improvements in electric and magnetic properties; and improvements in assembly space efficiency, packaging, and cost.
- Develop the friction-stir welding (FSW) process parameters and evaluate proper tool materials and techniques to produce defect-free FSWs in copper (Cu) alloys specified by project partners.
- Develop a fundamental understanding of solid-state joints between Cu materials and between dissimilar Cu/aluminum (Al) materials. This fundamental knowledge is expected to lead to strategies and techniques that will be used to produce a joining process with low thermal input and low distortion of adjacent parts and to produce joints with a high degree of structural integrity and with high thermal and electrical continuity.

- Using fundamental information gained, develop techniques to manufacture Cu and Al rotor and stator assemblies for high-power induction and permanent magnet motor systems. Joined or processed components will be evaluated and tested by industry collaborators to demonstrate efficiency benefits and commercial applications.
- Transfer performance data and manufacturing technology to industry through a cooperative research and development agreement (CRADA) with General Motors (GM), ensuring a clear path to commercialization.

Accomplishments

- **Milestone**: Completed characterization of the microstructure and mechanical properties of Cu/Cu joints. Gate is established on the minimum mechanical performance threshold established by the project team.
- First go/no go gate has been achieved with the mechanical testing of a FSW rotor at GM. Test was completed on a FSW rotor using a 10,000–revolutions-per-minute run-up test.
- **Milestone**: Completed development, fabrication, and testing of an actively cooled welding fixture to allow for FSW of Cu and Al rotor parts.
- **Milestone**: Demonstration of a robust weld process on Cu/Al dissimilar material welds and verification that mechanical properties pass the metrics established by the project team are on schedule.

Future Direction

-

Introduction

The purpose of this project is to develop and deploy high-power induction and permanent magnet rotors and stators that are lighter weight, have better cooling, and are a lower cost to manufacture through the application of novel solid-state joining and fabrication technologies. Barriers to achieving these objectives that focus on the manufacturability of novel rotor designs have been identified. The project team will apply friction-stir welding (FSW) to join Cu subassemblies and Cu/Al joints to eventually produce prototype lightweight, high-efficiency rotor assemblies. Fundamental work tasks will first focus on Cu/Cu FSW and dissimilar Cu/Al FSW joints. Later tasks will involve full rotor assembly and testing by GM.

In addition, the project will apply solid-state processing techniques to improve the performance of a low-cost soft magnetic material used in the rotors of high-power induction motors. GM will provide the motor design and Pacific Northwest National Laboratory (PNNL) will employ a novel method to fabricate the ferrous-based laminates specific to the GM motor design. The PNNL-developed method is based on nanoscale powder synthesis and friction extrusion/consolidation. This new fabrication process may allow for fewer energy-intensive processing steps to reach the microstructure and laminate thicknesses required for a high-performance soft magnetic material at a lower manufacturing cost. The project is a cost-shared CRADA between PNNL and GM.

Background

New manufacturing techniques can cause step changes in the overall cost of manufactured assemblies if the new technique can create a fundamental shift in the way a subsystem is constructed. For example, an electric motor has numerous components that are sensitive to high temperature. Fusion welding, which requires very high temperature to melt the materials being joined, cannot be accomplished directly adjacent to heat-sensitive parts (e.g., sensitive electronics, wiring, and insulation) or where coated laminates or substrates are located nearby. This restriction might require the part to be assembled through a much more complicated multistep process. If another joining technology were available that did not heat the part, then the multistep assembly could be avoided, saving cost.

One example of a joining technology that could satisfy the need for lower adjacent part temperatures is FSW. Previous work by PNNL and others has shown that FSW can be made in Cu alloys that have excellent mechanical, electrical, and thermomechanical performance. FSW has a particular advantage in welding Cu due to the wide range of weld-specific energy levels that can be applied by the process. Conventional fusion welding must deliver a high level of energy to melt the Cu on each side of the joint line. In many applications, the high part temperatures during fusion welding can lead to distortion or overheated adjacent parts. Often, Cu joining is required in assemblies where heat-sensitive electronics, wiring, or coated laminates or substrates are located nearby. FSW may provide a lower heat input joining technique in these special applications where adjacent parts in the assembly can be damaged.

In addition, the next generation of rotor designs may be Cu/Al hybrids or have Al components to reduce the rotating mass. It is anticipated that joints will be needed between Cu and Al. Solid-state joining techniques such as FSW are logical to develop for specialized dissimilar joints like these that cannot be fusion welded due to the radically different melt temperatures of the components.

Approach

The project will develop the FSW process parameters and evaluate proper tool materials and techniques to produce defect-free FSWs in Cu alloys specified by project partners. In addition, the project team will develop statistical confidence around the manufacturing process used to fabricate high-power induction motor rotor assemblies by applying a set of mechanical test methods and procedures to evaluate process robustness. The project team also will investigate the application of FSW to other joining issues around electric drive systems, including dissimilar joining between Al/Cu and

potentially Al/Al joints in specific configurations.

Finally, to address the overarching goal of an improved energy efficiency of the induction motor design, the project team will apply solid-state processing techniques to fabricate a low-cost soft magnetic material with unique properties that has the potential to display high magnetic flux density (B) and low iron loss (W). Amorphous iron-based metal and alloys offer excellent soft magnetic properties. Literature reports that the material could reduce the core losses of motors by more than 70% and that the efficiency of an induction motor with amorphous iron core could easily reach 80%. However, the production cost of an amorphous iron core is high. Specifically, the thickness of an amorphous iron sheet cannot exceed 25 μm because of the requirement of ultra-fast quenching. In this task, we will focus on developing a cost-effective method to produce soft iron alloy sheet with magnetic properties comparable to those of the amorphous iron alloy and with thickness greater than 100 μm. This method is based on a modified friction consolidation and extrusion method, where the material is subjected to high strain under a hydrostatic state of stress. This solid-state process has shown the ability to produce ultra-fine grain size in bulk solids.

This project will be divided into three primary task areas. Task 1 will focus on solid-state joining of Cu materials used in the rotor assemblies of high-power induction motors. Task 2 will focus on dissimilar material joining, primarily Cu to Al, with an emphasis on components and assembly performance improvement. Task 3 will develop a unique solid-state process to create appropriate microstructures and magnetic performance in bulk soft magnetic materials that may be able to improve on the efficiency of stack laminates in the rotor assembly.

Results

Work completed during fiscal year (FY) 2013 focused primarily on FSW trials on Cu bar materials and Cu rotor end caps (Task 1). The induction motor rotor represents an excellent example of a multi-material assembly that may be manufactured more efficiently and at a lower cost if new manufacturing techniques could be developed (Figure 1). This project is investigating using solid-state welding (FSW) to assemble this component.

Figure 1. Rotor concepts fabricated with FSW.

The primary scope of Task 1 is to develop a weld process to join the Cu end cap to the shorting bars that traverse the soft magnetic core of the rotor. These bars carry current up and down the rotor between the end caps to produce the magnetic moment that drives the rotor. The joint has several important characteristics. It needs strength because it will be subjected to high tensional and cantilever loads when the rotor is moving at high revolutions per minute, it needs to have optimum electrical conductivity for high efficiency, and during the joining operation it cannot get hot enough for the underlying electric steel laminates to melt their polymeric insulating coatings. Figure 2 shows a schematic of a rotor and a photo of a rotor end cap in place on the shorting bars just prior to joining.

Maximum electrical continuity is one of the key factors in rotor efficiency and lightweighting. The joint must be designed for the highest electrical cross section at the minimum weight penalty. The thickness of the heavy Cu end cap is a key variable to optimize. It is desired to have the minimum end cap thickness for weight savings, yet the highest electrical cross section for current flow. This requires the joined region to have the largest possible area between the end cap and the shorting bar. Figure 3 shows, schematically, the challenge. The joined area intersecting the end cap and shorting bar must have maximum width and appropriate depth. The better the electrical continuity and current flow in this area, the

thinner the end cap, and the greater the weight savings. Much of the work during FY 2013 was directed at creating an FSW joint that satisfies these demands. The joined area is a function of tool design, tool materials, process parameters, and boundary conditions during welding.

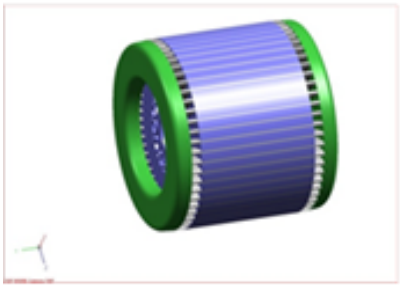
(a)


(b)


(c)

Figure 2. (a) Rotor schematic, (b) Cu end cap positioned on shorting bar ends prior to joining, and (c) FSW tool and rotor in fixture prior to welding.

Figure 3. Schematic of end cap/shorting bar joined area.

During FY 2013, the project team investigated a wide range of tool materials, tool designs, and process parameters to aid in establishing a robust process. Figure 4 shows a process window established for C101 Cu using a FerroTic® tool with a 0.25-in.-deep penetration. The circular dots indicate conditions in which either the tool failed or the weld had significant defects. Square symbols are successful welds (based on surface condition only). Welds, with optimum mechanical properties will exist within the region of the square symbols. The process of parameter development narrows the weld conditions to those with the appropriate defect-free quality and appropriate mechanical performance.


(a)

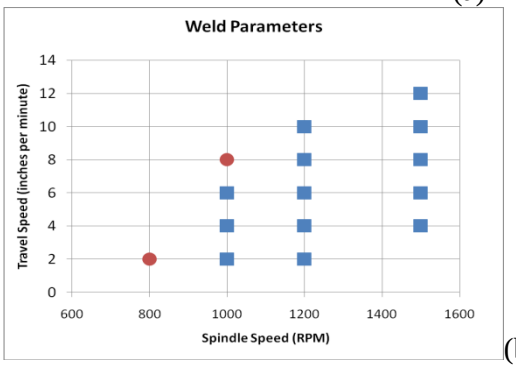

(b)

Figure 4. (a) Typical FSW weld in C101 Cu and (b) Cu FSW parameter map using a FerroTic stepped spiral tool. Circle symbols indicate failed welds and square symbols indicate conditions where the visual observation of the weld surface passed a set of criteria.

The weld process parameter development also focused on several tool designs. Figure 5 shows two of the primary tool concepts being tested: the stepped spiral tool and the triflat tool. The designs and variations of these tools are well known in commercial applications of FSW,

especially in Al welding, but their performance in Cu welds is yet to be determined.

FSW trials have been completed on both linear welds on the Cu plate and on two-dimensional circular configurations. Welds have been developed for both monolithic materials and for plates that have cutouts for Cu bars running the length of the rotors. Short bar segments are inserted into the larger plates and welded in one assembly (Figure 6).

Figure 5. Two tool designs that will be investigated in this project include the stepped spiral tool (on the left) and the three flat tool (on the right). (Pictures are for illustration only; actual designs will vary.)

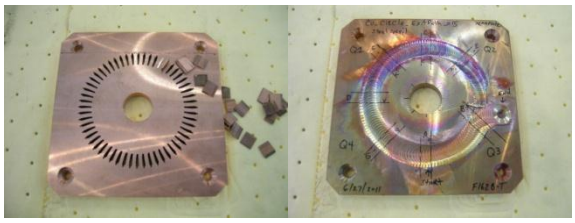

Figure 6. Cu plates with small Cu bar segments welded to simulate the rotor end cap configuration.

Several challenges have emerged involving control of the process and weld quality. A circular weld involves returning to the beginning of the weld start area and, in some cases, over-running an area previously welded. This creates an ever changing set of boundary conditions, including a temperature field that changes throughout the weld.

Figure 7 show a plot of tool temperature vs. time taken during the course of a circular weld. This plot shows a continuously increasing temperature during welding. The lack of stability of the tool (and thus weld) temperature can create a wide range of defects, including excess flash and loss of material (Figure 8).

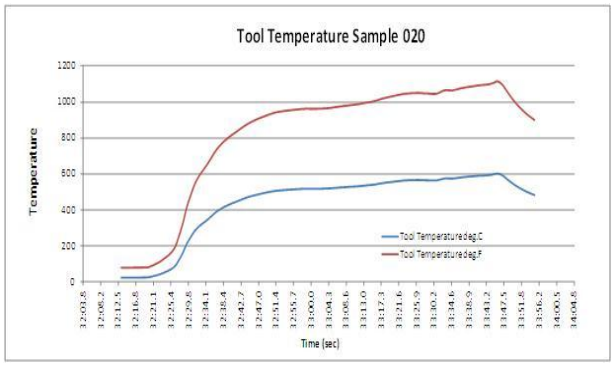

Figure 7. Tool temperature vs. time during a circular weld.

(a)

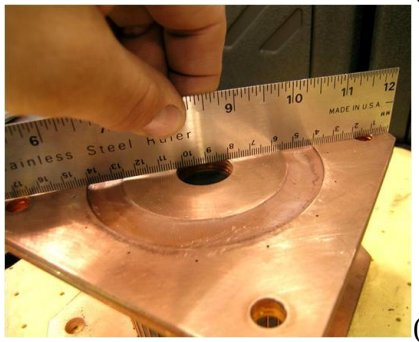

(b)

Figure 8. Circular weld run too hot showing (a) excessive flash and loss of material and (b) excessive distortion.

Loss of weld material leads to internal defects and loss of electrical continuity in the joint, a particularly important property that must be maintained in an end cap weld. To compensate for a weld that is too hot, the process parameters can be set to generate less heat in the process. However, if the parameters are set too low, this can lead to defects that are

usually manifested by voids developed in the weld direction (Figure 9).

Figure 9. Surface breaching void defect due to weld parameters that did not deliver enough weld energy for a consolidated joint.

One strategy developed in FY 2013 to control weld temperature and distortion has been to control the temperature boundary conditions in the fixtures. During FY 2013, an actively cooled fixture has been implemented that uses an internally water-cooled clamp ring to constrain the end cap during welding and extract heat from the process. This ring has been successful in helping to stabilize the rate of heat generation in the part and has virtually eliminated distortion of the end cap. Figure 10 illustrates features of the cooled fixture design.

While the cooled fixtures help control cooling rate and distortion, the weld peak temperature primarily is controlled by process parameters. During FY 2013, the project also started implementation of an adaptive power control system. To adapt to changing temperature conditions, the weld parameters are allowed to change through a torque and power-based feedback system. This system controls power and tool temperature through a feedback nested loop controller and can make high-speed adjustments to power to keep tool temperatures within a set range. The system, once fully developed, is expected to solve several of the current challenges to maintaining welds of consistent quality.

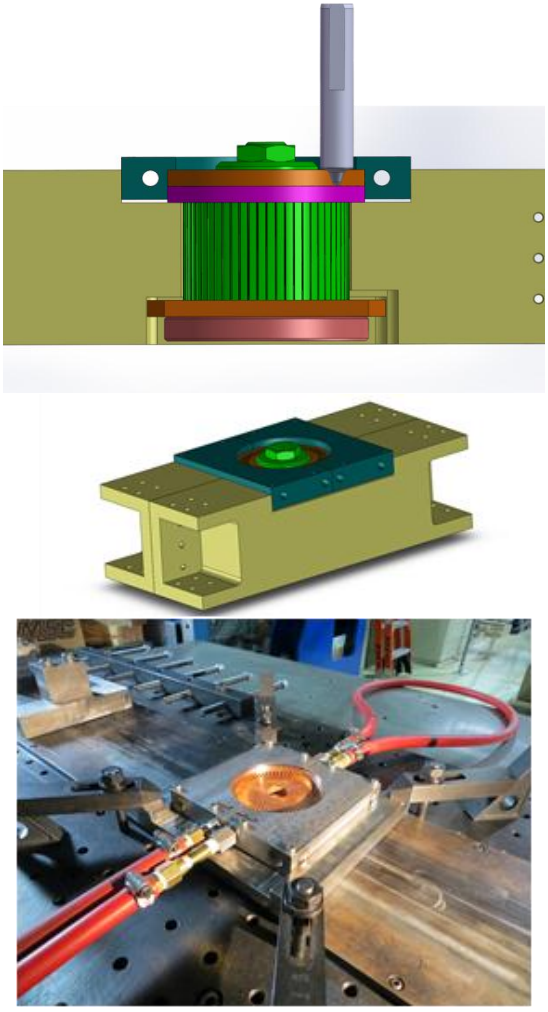

Figure 10. Cooled fixture can control temperature boundary conditions and reduce distortion.

Conclusions

Motor designs, like all complex assemblies, are a compromise between performance and cost (i.e., cost of materials and of manufacturing). New manufacturing processes can be critical in this balance because they can enable lower cost materials and introduce a lower cost manufacturing process. In many cases, the new manufacturing process may even directly increase the efficiency of the part by producing an assembly that displays better thermal, mechanical, or electric/magnetic properties. This project will use new solid-state joining and processing technologies to achieve increased performance and a lower manufacturing cost. Figure 11 is an illustration of how this project

maps to the goals of the U.S. Department of Energy's program on Advanced Power Electronics and Electrical Motors.

Specifically, the project will develop the fundamental understanding of solid-state joints between Cu materials and between Cu/Al dissimilar joints so that they can be achieved with low thermal input, low distortion of adjacent parts, a high degree of structural integrity, and a high degree of thermal and electrical continuity. The fundamental information gained will be used to develop techniques to manufacture Cu and Al rotor and stator assemblies for high-power induction and permanent magnet motor systems. Joined or processed components will be evaluated and tested by industry collaborators to demonstrate efficiency benefits and commercial applications

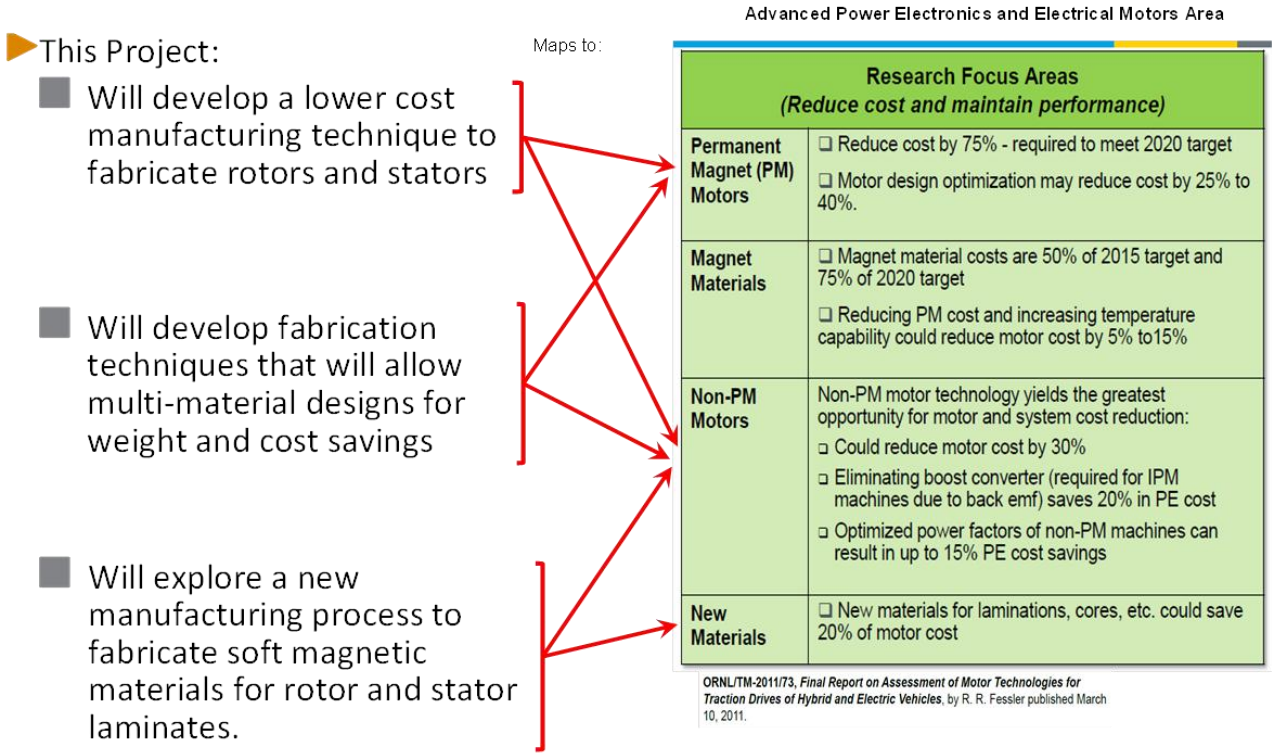

Figure 11. Project objectives and how they map to the U.S. Department of Energy's goals and targets for the Advanced Power Electronics and Electrical Motors area.

.

Project 18516 – Materials for Hybrid and Electric Drive Systems

Agreement 26461 – Enabling Materials for High-Temperature Power Electronics

Andrew A. Wereszczak and Zhenxian Liang†*
Oak Ridge National Laboratory
P.O. Box 2008, MS 6068, Bldg. 4515
Oak Ridge, TN 37831-6068
Phone (865) 576-1169; fax: (865) 574-6098; e-mail: wereszczakaa@ornl.gov
** Materials Science and Technology Division † Energy and Transportation Science Division*

DOE Technology Manager: Jerry L. Gibbs
Phone (202) 586-1182; fax: (202) 586-1600; e-mail: jerry.gibbs@ee.doe.gov
ORNL Technical Advisor: J. Allen Haynes
Phone (865) 576-2894; fax: (865) 574-4913; e-mail: haynesa@ornl.gov

Contractor: Oak Ridge National Laboratory, Oak Ridge, Tennessee
Prime Contract No.: DE-AC05-00OR22725

Objectives

- Develop material technologies that enable a 200°C-capable, low-cost, and reliable electronic package with at least a 15-year-life that can exploit wide bandgap (WBG) semiconductor technology.
- Initially focus on the research and development and demonstration of 200°C-capable (1) interconnection material technologies, and (2) thermally-conductive, high-temperature-capable dielectric composite materials.

Approach

- Demonstrate efficacy of bonding silicon carbide WBG die to metal-clad ceramic substrates using silver (Ag) sintering. Evaluate the effect of plating material on the shear-strength limitation of Ag-sintered joints.
- Collaborate with the National Renewable Energy Laboratory on evaluating and predicting delamination onset with 200°C-capable interconnect materials.
- Process fluoropolymer-matrix dielectric composites, measure thermal properties, and confirm 200°C serviceability.
- Collaborate with U.S. manufacturers of potentially new 200°C-capable interconnect materials and organic dielectrics.

Accomplishments (new start in fourth quarter of fiscal year 2013)

- Defined a test matrix to compare the shear strength of Ag and gold-plated substrates that are bonded using sintered Ag joints. Procured plated test coupons and silver paste for processing.
- Identified a new 200°C-capable polymer as a candidate matrix for fabricating a thermally conductive dielectric composite. Procured the polymer and filler material to be used for composite processing/compounding.

Expected Benefits

- Increase the temperature tolerance of state-of-the-art electronic packaging by at least 50°C and further the efforts of the Advanced Power Electronics and Advanced Motors Program to reach the 2020 power electronic targets of $3.30/kW, 14.1 kW/kg, and 13.4 kW/l.
- This work will benefit industry and, ultimately, the consumer because it will help hasten sought-after WBG semiconductor use and exploitation. This project's results also will assist in the cost, size, and weight reduction of inverters and their sustained operation in harsher conditions.

Project 18518 – Materials for High-Efficiency Engines

Agreement 8697 – NO_x Sensor Development

Leta Y. Woo and Robert S. Glass
Lawrence Livermore National Laboratory
P.O. Box 808, L-103
Livermore, CA 94551-9900
Phone (925) 423-7140; fax: (925) (422-5844); e-mail: glass3@llnl.gov

DOE Technology Manager: Jerry L. Gibbs
(202) 586-1182; fax: (202) 586-1600; e-mail: jerry.gibbs@ee.doe.gov

Contractor: Lawrence Livermore National Laboratory, Livermore, California
Prime Contract No.: W-7405-Eng-48; LLNL-TR-510234

Objectives

- Develop an inexpensive, rapid-response, high-sensitivity, and selective electrochemical sensor for oxides of nitrogen (NO_x) for compression-ignition, direct-injection (CIDI) OBD II systems.
- Explore and characterize novel, effective sensing methodologies based on impedance measurements and designs and manufacturing methods that are compatible with mass fabrication.
- Transfer the technology to industry for commercialization.

Approach

- Use an ionic (O^{2-}) conducting ceramic as a solid electrolyte and metal or metal-oxide electrodes.
- Correlate NO_x concentration with changes in cell impedance.
- Evaluate sensing mechanisms and aging effects on long-term performance using electrochemical techniques.
- Collaborate with Ford Research Center and EmiSense Technologies, LLC to optimize sensor performance and perform dynamometer and on-vehicle testing.

Accomplishments

- Successful technology transfer activities as part of a Cooperative Research and Development Agreement (CRADA) with EmiSense Technologies, LLC, a Salt Lake City, Utah company, which has licensed the Lawrence Livermore National Laboratory (LLNL) NO_x sensor technology. This has resulted in more advanced sensor designs amenable to mass manufacturing. The commercialization goal is for 2016 car models.
- Completed advanced vehicle dynamometer testing at Ford Motor Company of fiscal year 2013 sensor prototypes using newly developed prototype electronics for data acquisition. Good performance was obtained in these tests.
- Publications/presentations/patents:

- Du Frane, W. L., L. Y. Woo, R. S. Glass, R. F. Novak, and J. H. Visser, 2013, "Substrate Effects on Electrochemical NO_x Sensor Based on Porous Y_2O_3-Stabilized ZrO_2 (YSZ) and Sr-doped $LaMnO_3$ (LSM)," *ECS Transactions*, 45 (14), 3–11.
- Woo, L. Y., R. S. Glass, R. F. Novak, and J. H. Visser, "Zirconia-electrolyte-based impedancemetric sensors using Sr-doped $LaMnO_3$ (LSM) electrodes for measuring NO_x in combustion exhaust streams," *The 10th Pacific Rim Conference on Ceramic and Glass Technology*, in San Diego, California, June 2–7, 2013.
- New patent application (No. 14055562) entitled, "Electrochemical Sensing Using Voltage-Current Time Differential," filed on October 16, 2013.

Future Direction

- Working through the CRADA with EmiSense Technologies, LLC and in collaboration with Ford Motor Company, complete the technology transfer and bring the NO_x sensor technology to the commercialization stage.

Introduction

NO_x compounds, specifically NO and NO_2, are pollutants and potent greenhouse gases. Compact and inexpensive NO_x sensors are necessary in the next generation of diesel (i.e., CIDI) automobiles to meet government emission requirements and enable the more rapid introduction of more efficient, higher fuel economy CIDI vehicles (Yamazoe 2005, Moos 2005, and Akbar et al. 2006).

Because the need for a NO_x sensor is recent and the performance requirements are extremely challenging, most are still in the development phase (Menil et al. 2000, Zhuiykov and Miara 2007, and Fergus 2007). Currently, there is only one type of NO_x sensor that is sold commercially and it seems unlikely to be able to meet the more stringent future emission requirements.

Automotive exhaust sensor development has focused on solid-state electrochemical technology, which has proven to be robust for in situ operation in harsh, high-temperature environments (e.g., the oxygen stoichiometric sensor). Solid-state sensors typically rely on yttria-stabilized zirconia (YSZ) as the oxygen-ion conducting electrolyte (which has been extensively explored) and then target different types of metal or metal-oxide electrodes to optimize the response (Moos 2005, Akbar et al. 2006, Menil et al. 2000, Zhuiykov and Miara 2007, and Fergus 2007).

Electrochemical sensors can be operated in different modes, including amperometric (current based) and potentiometric (potential based), both of which are direct current (DC) measurements. Amperometric operation is costly due to the electronics necessary to measure the small sensor signal (nanoampere current at ppm NO_x levels) and cannot be easily improved to meet future technical performance requirements. Potentiometric operation has not demonstrated enough promise in meeting long-term stability requirements, where the voltage signal drift is thought to be due to aging effects associated with electrically driven changes (both morphological and compositional) in the sensor (Song et al. 2006).

Our approach involves impedancemetric operation, which uses alternating current (AC) measurements at a specified frequency. The approach is described in detail in previous reports and several publications (Martin et al. 2007 and Woo et al. 2007, 2008, 2010, 2011). Impedancemetric operation has shown the potential to overcome the drawbacks of other approaches, including higher sensitivity toward NO_x, better long-term stability, potential for subtracting out background interferences, total NO_x measurement, and lower cost materials and operation (Martin et al. 2007, Woo et al. 2007, 2008, 2010, and 2011).

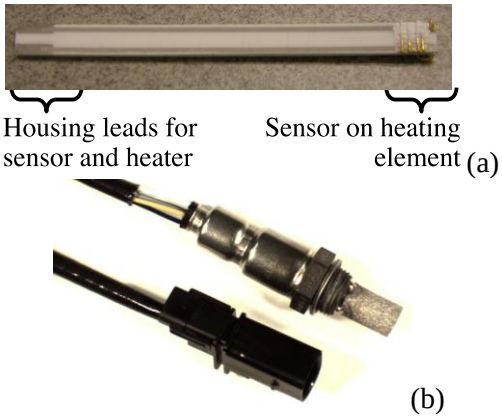

Figure 1. Picture of (a) alumina substrate with imbedded heater, provided by Ford Motor Company, suitable for packaging into (b) protective sensor housing.

Past LLNL research and development efforts have focused on characterizing different sensor materials and understanding complex sensing mechanisms (Martin et al. 2007 and Woo et al. 2007, 2008, 2010, 2011). Continued effort has led to improved prototypes with better performance, including increased sensitivity (to less than 5 ppm) and long-term stability, with more appropriate designs for mass fabrication, including incorporation of an alumina substrate with an imbedded heater and a protective sensor housing (see Figure 1). Using multiple frequency measurements, an algorithm has been developed to subtract out that portion of the response due to interfering species.

Efforts in FY 2013 have focused on working with Ford Motor Company and CRADA partners EmiSense to modify prototypes for

improved performance. Three major accomplishments this year include (1) completing evaluation of strontium-doped lanthanum manganite (LSM) metal oxide electrodes to enable a material down-select to focus on Au-based electrodes; (2) development of new portable electronics for experimental control and data acquisition using low-cost components; (3) further development of a voltage-current time differential measurement strategy that has shown improved results in vehicle dynamometer testing at Ford; and (4) evaluation of processing methods more suitable for mass manufacturing. We have had great success in technology transfer to EmiSense, which licensed the LLNL NO_x sensor technology, and made great progress in commercialization efforts, which are directed toward a 2016 model year goal.

Background

For a two-electrode electrochemical cell, impedancemetric sensing requires that at least one of the electrodes act as the "sensing" electrode with selective response to NO_x over other gas phase components. This contrasts to the case in potentiometric sensing, which relies on differential measurements between the two electrodes. The impedancemetric sensor design is quite flexible and can either contain one sensing electrode and one counter (i.e., non-sensing) electrode or two sensing electrodes. It opens up the opportunity to use a wide variety of materials, both metal and metal oxides.

Both electrode composition and microstructure influence sensitivity, which relies on limiting the oxygen reaction on the electrode so that the NO_x reaction can be resolved (Woo et al. 2007, 2008, 2010, and 2011). In general, for the "sensing" electrode, a dense microstructure is required with appropriate composition to limit the catalytic activity toward oxygen (Woo et al. 2008, 2010, and 2011).

Measured sensor impedance is a complex quantity with both magnitude and phase angle information. The phase angle has been found to provide a more stable response at higher operating frequencies and we prefer it for the sensor signal (Martin et al. 2007 and Woo et al. 2007, 2008, 2010, 2011).

In previous work, impedancemetric sensing using either Au or strontium-doped LSM electrodes (the latter being an electronically conducting metal oxide) was investigated in laboratory and engine testing. Preliminary results indicated that Au electrodes have good stability and the potential for low water cross-sensitivity, but also have a higher thermal expansion coefficient and lower melting temperature than the YSZ electrolyte, which limits processing flexibility. LSM electrodes have high melting temperatures and better thermal expansion match with YSZ, but have shown higher water cross-sensitivity than gold.

Results and Discussion

Metal Oxide Electrodes

To further understand impedancemetric sensing mechanisms and to aid in down selection for either metal-oxide or Au-based electrodes, multiple configurations of the strontium-doped LSM metal oxide electrode prototype sensor were investigated. To conserve space, experimental details of sensor preparation and measurement protocol are omitted, but the interested reader can find these in the fiscal year 2012 Annual Report for this project and elsewhere (Woo et al. 2008, 2010, and 2011).

Figure 2a shows a schematic of the previously studied symmetric (i.e., electrode materials the same) in-plane LSM prototype (Du Frane 2013). This design resulted in poor sample-to-sample reproducibility and variability in performance attributable to the formation and growth of random microcracks due to the thermal expansion mismatch between the sensor components (YSZ and LSM) and the substrate (alumina) (Du Frane 2013).

In an attempt to reduce microcracking, an asymmetric (LSM/YSZ/Pt) through-plane geometry (Figure 2b) was evaluated next. Figure 3 shows a comparison of the sensing behavior of the symmetric side-by-side (LSM/YSZ/LSM) and asymmetric through-plane (LSM/YSZ/Pt) configurations (see Figure 2a and 2b) in 10.5% O_2 when 100 ppm NO is added. The asymmetric (LSM/YSZ/Pt) showed lower sensitivity than the symmetric configuration.

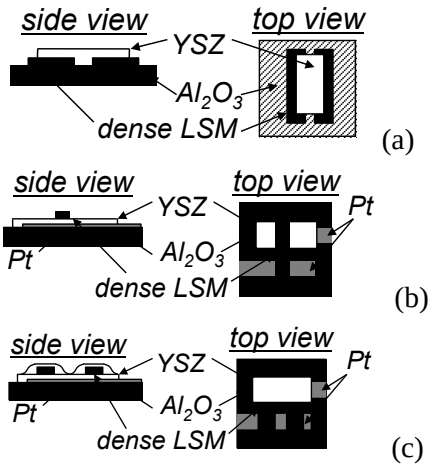

Figure 2. Schematic of NOx prototype with LSM metal oxide electrode in (a) symmetric side-by-side configuration and (b) alternative asymmetric through-plane configurations with both LSM and Pt electrodes (LSM/YSZ/Pt), and (c) additional LSM electrode.

Figure 2c shows the schematic of a third configuration, which was used to investigate the role of increasing the electrode surface area by adding an additional electrode of dense LSM. Figure 3c shows that this increase in surface area, only the sensitivity further reduced to NO.

In the final design investigated, the bottom platinum electrode was replaced with a piece of LSM, resulting in a symmetric through-plane configuration with two LSM electrodes. Figure 3d shows an increase in NO sensitivity, similar to the sensitivity of the side-by-side configuration. Based on previous studies, it is anticipated that the through-plane geometry would have better tolerance to microcracks than the side-by-side geometry.

The study of LSM configurations demonstrated that reasonable sensor behavior could be achieved by controlling configuration and materials. This evaluation of alternative LSM configurations allowed for a more complete comparison with the sensing performance of previously studied Au-based designs. Both LSM configurations and Au-based designs had comparable sensitivity to NO_x. Therefore, the down select between the two electrode materials was determined by the potential for more straight-forward mass manufacturing methods using metal-based pastes and inks, which is an area of expertise for our industrial partner EmiSense.

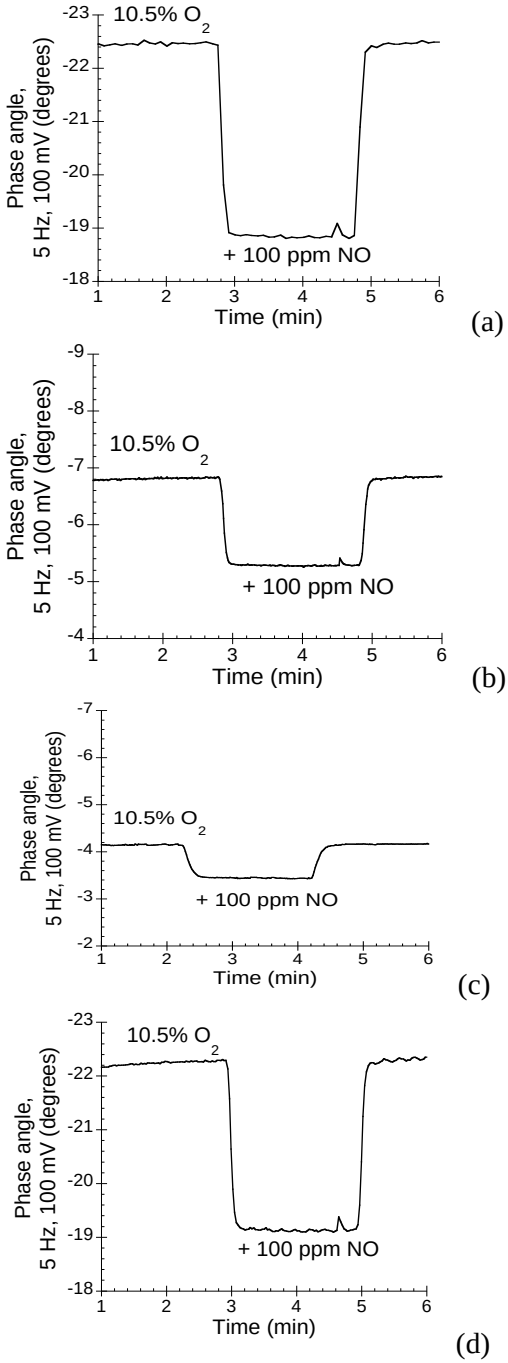

Figure 3. Sensing behavior of (a) symmetric side-by-side, (b) asymmetric through-plane (LSM/YSZ/Pt) with single LSM and (c) additional top LSM electrode, and (d) symmetric through-plane with LSM electrodes (LSM/YSZ/LSM).

Dynamometer Testing with EmiSense Electronics

To aid in development of new electronics for dynamometer testing, the prior studied Au wire-based designs were used. Figure 4 shows a schematic of the sensor using Au wire as the sensing electrode and alumina with an imbedded Pt resistive heater as the substrate (70 × 4 × 1 mm; see Figure 1a). The substrate has a total of four leads: two leads for the Pt resistive heater located on one side and two leads for the sensor located on the opposite side.

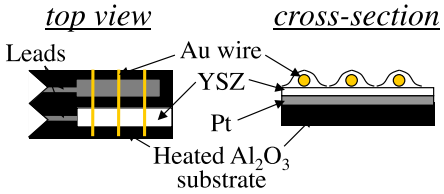

Figure 4. Schematic of Au wire NOx prototype sensor.

One of the substrate leads contacted the Pt counter electrode. YSZ slurry was then applied on top of the Pt. Au wires were added and additional YSZ slurry was applied on top of the wires with the entire assembly fired at 1000°C to produce the porous YSZ electrolyte. The second substrate lead for the sensor housing contacted the Au wire.

Dynamometer testing of real diesel exhaust was performed at the Ford Research Center using a test vehicle mounted on a chassis. The vehicle exhaust system had a urea-based selective catalytic reduction system for reducing NO_x emissions. The exhaust gas composition was evaluated using both Fourier transform infrared spectroscopy (FTIR) and bench analyzers, including a chemiluminescent NO_x analyzer and a paramagnetic oxygen analyzer. Prototype sensors were packaged by a U.S. supplier into appropriate housings (see Figure 1b) and placed directly into the exhaust manifold at the tailpipe for exposure to real-world diesel exhaust.

In preparation for fiscal year 2013 testing in real diesel exhaust, new electronics were developed with LLNL's CRADA partner EmiSense. In our previous work, we focused on frequency-domain impedancemetric modes of operation using the phase angle as the sensor signal. A surprising discovery occurred during development of inexpensive digital electronics to monitor the voltage-current differential in the time domain, the source and response waves exhibited similar peak-to-peak values, indicating that no phase angle shift or phase angle difference occurred. In contrast, previous impedancemetric modes of operation in the frequency domain using expensive electrochemical equipment indicated phase angle changes. The result was an entirely new mode of time-domain operation, as opposed to frequency-domain operation, using low-cost portable digital electronics to measure the voltage-current time differential as the sensor signal. We have filed a patent application to protect this new intellectual property.

Figure 5 shows measured dynamic data from a portion of the vehicle dynamometer testing using EPA Federal Test Procedure (FTP-75), which was designed to simulate a city driving cycle and was used to measure tailpipe emissions and fuel economy. In Figure 5a, the dynamic NO_x concentration changes are shown as measured by the chemiluminescent NO_x analyzer (blue), the FTIR (red), and the commercial sensor (green), showing some variation between the methods. In Figure 5b, the left y-axis corresponds to the oxygen concentration as measured by the paramagnetic analyzer (blue) and the right y-axis corresponds to the temperature measurement. The oxygen concentration is changing dynamically, along with the NO_x concentration, whereas the overall temperature remained constant during this portion of testing. In Figure 5c, the sensor signal, as measured by the new digital EmiSense electronics, is shown for three different Au-wire-based prototypes. As expected, the Au-wire prototypes responded to changes in both oxygen and NO_x. The rising background observed between 60 and 110s for the sensor prototype is related to other interferences but is not completely understood.

Commercial sensor packages (sensor plus electronics) provide for additional data processing of the raw data, whereas the data shown above for the Au prototype sensor represents the raw sensor signal. Further

development of the LLNL/EmiSense sensor will allow for additional signal processing to remove the obvious oxygen interference. Previously, we have demonstrated algorithms suitable for compensating for interferences, in particular, oxygen (Woo et al. 2011).New algorithms for the digital EmiSense electronics package are being developed.

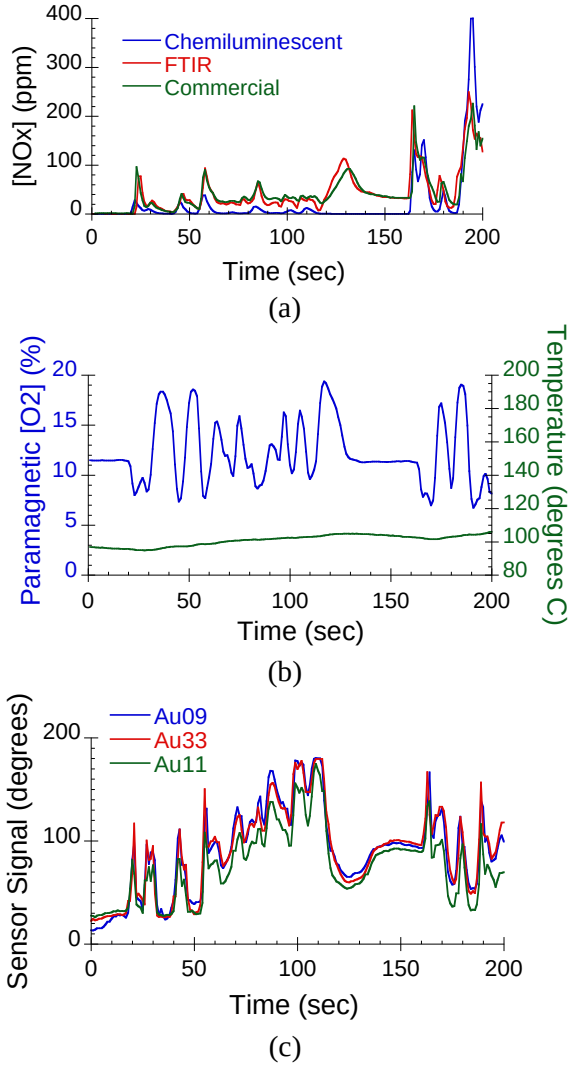

Figure 5. Portion of vehicle dynamometer test: (a) NOx concentration in ppm as measured by bench chemiluminescent NOx analyzer (blue), FTIR (red), and commercial NOx sensor (green); (b) oxygen concentration as measured by bench paramagnetic analyzer (blue, left y-axis) and temperature variation (green, right y-axis); and (c) sensor signal measured using new digital EmiSense electronics for three different Au-wire-based prototype sensors.

Additional fiscal year 2013 testing at the Ford Research Center included dynamometer vehicle evaluation in steady-state (non-dynamic) modes for various vehicle speeds. Evaluation also was conducted on an advanced high-flow (40 L/min) test stand with controlled mass flow controllers to alter a range of gas concentrations (O_2, CO_2, H_2O, and NO_x). The test stand also included output from a commercial sensor located near the prototype sensor under evaluation. These data are now being used to further refine strategies for reducing interferences.

Processing Methods for Mass Manufacturing

As a result of extensive testing over several years, a down select was made to focus on Au-based electrodes. In part, this decision was made based on trades offs in sensitivity, selectivity, and, more importantly, on processing ease and capability. A factor in this was the expertise resident at EmiSense for screen printing metal pastes and inks and previous success in development of Au-based pastes suitable for mass manufacturing processes. In contrast, much additional research would have been necessary in order to use metal oxides as electrode materials. In addition to the use of Au-based pastes to replace the Au wire electrode, another processing concern for mass manufacturing was the number of firing steps required. A single high-temperature (greater than 1500°C) co-firing process is desired for sintering with a green (unfired) alumina substrate. As discussed above, previous prototypes with Au-wire electrodes used low-fired (1000°C) porous YSZ electrolyte materials. Therefore, work in fiscal year 2013 concentrated on the use of Au paste electrodes and a single sintering step compatible with a green alumina substrate.

Figure 6a shows a schematic of a symmetric side-by-side prototype design used to evaluate two different Au-based pastes, with either a 100% Au composition (ESL 8880-G) or a mixture of Pt and 4% Au (ESL 5801). For a comparison of the effect of firing temperature, the pastes were applied to the substrate, YSZ slurry was then added on top, and the entire

assembly fired at 1000°C. To investigate the influence of high-fired porous YSZ, another symmetric configuration was used that incorporated a slab of porous YSZ (2 × 2 × 5 mm), formed by firing with graphite pore formers at 1550°C (see Figure 6b). In this second sensor, Au-based paste was applied to the fully sintered porous YSZ and the entire assembly was fired at 1000°C. The resulting porous microstructures for the low-fired and high-fired YSZ are shown in Figure 7.

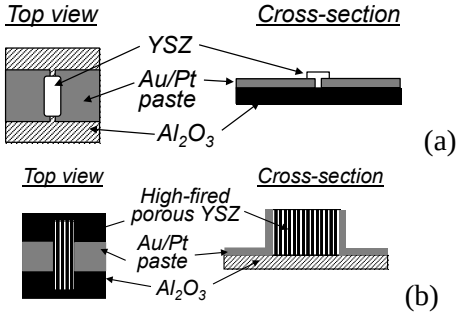

Figure 6. Schematic of NOx sensor prototypes used to evaluate Au-based pastes with (a) porous YSZ low-fired at 1000°C and (b) porous YSZ high-fired at 1550°C.

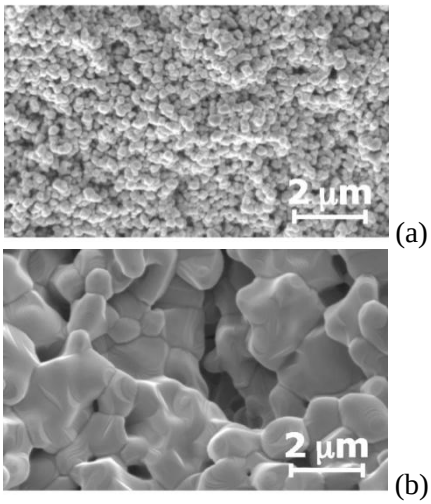

Figure 7. Schematic of NOx sensor prototypes used to evaluate Au-based pastes with (a) porous YSZ low-fired at 1000°C and (b) porous YSZ high-fired at 1550°C.

Figure 8a shows the sensor behavior of the earlier design using an Au-wire electrode in 10.5% O_2 and following the addition of 90 ppm and 10 ppm NO. In Figure 8b, the results for the low-T fired sensor design shown in Figure 6a are shown using 100% Au paste electrodes, where reduced sensitivity and signal-to-noise are noted. However, when Pt/4% Au paste electrodes are used (Figure 8c), sensor performance improves.

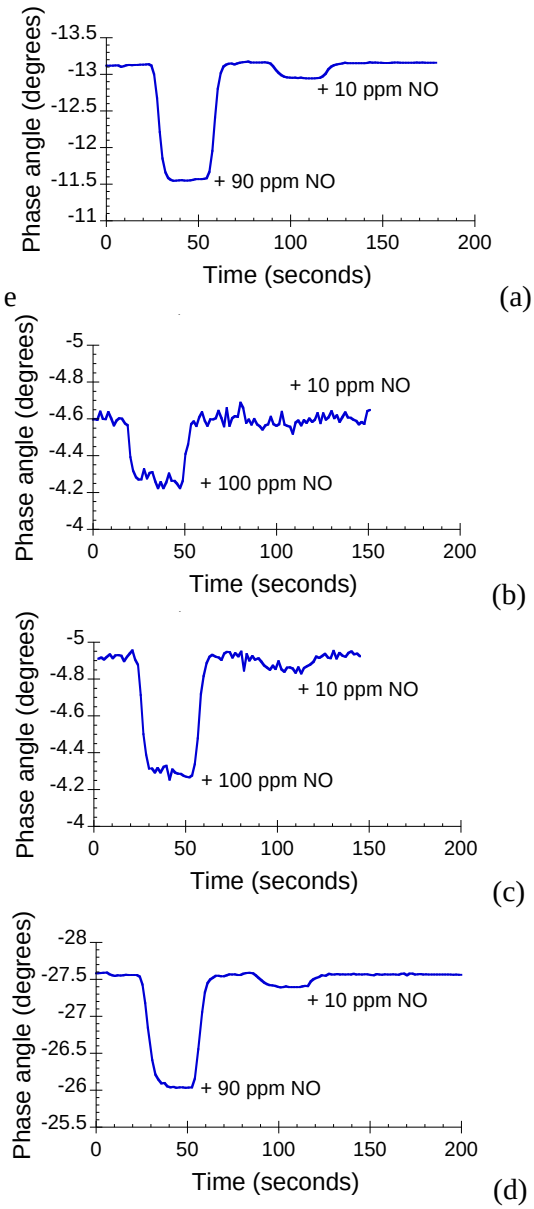

Figure 8. Sensing behavior of (a) Au-wire based design, (b) 100% Au paste with low-fired porous YSZ, (c) Pt/4% Au paste with low-fired porous YSZ, and (d) Pt/4% Au paste with high-fired porous YSZ.

Finally, when Pt/4% Au paste electrodes were used with a fully sintered porous YSZ

electrolyte (design shown in Figure 6b), the sensor performance was found to be very similar in magnitude and signal-to-noise compared with the Au-wire based design (shown in Figure 8a). The results indicated the feasibility for using a traditional screen-printing process for electrode deposition, followed by a single step co-firing manufacturing process.

Conclusions

Work in fiscal year 2013 focused on continuing to work with the Ford Motor Company and CRADA partner EmiSense to improve sensor performance and to initiate completion of the technology transfer to industry for commercialization. The three accomplishments this year included (1) down select of materials to focus on Au and Pt-Au electrodes; (2) development of a new portable electronics package for data acquisition fabricated using low-cost components; (3) development of a voltage-current time differential measurement strategy that has shown improved results in vehicle dynamometer testing; and (4) evaluation of processing methods more suitable for mass manufacturing.

To address micro-crack growth and poor sample-to-sample reproducibility for the in-plane geometry, a through-plane geometry was demonstrated. These results for LSM oxide electrodes showed that improved sensor behavior could be achieved by controlling geometry and materials. The completed evaluation of LSM configurations allowed for a better comparison with the sensing performance of Au-based designs and a subsequent electrode materials down select. Because both materials had comparable sensitivity to NO_x, the Au-based materials were chosen based on the potential for more convenient mass manufacturing methods using metal-based pastes and inks, which is an area of particular expertise for EmiSense (the LLNL technology licensee).

A new electronics package for data acquisition was developed by EmiSense. A serendipitous discovery showed that an entirely new measurement strategy in time-domain gave better results than frequency-domain operation, which had been used in all previous studies. As an added bonus, time-domain operation enabled the use of lower cost electronic components.

Attention has been given to replacing early prototype Au-wire electrode sensors with materials more suitable for mass manufacturing. To this end, Au-based and Pt-Au-based pastes were explored. In addition, a final, single-step sensor firing process was sought that used a high-T fired porous YSZ pellet electrolyte. Prior work focused on use of low-fired porous YSZ. The processing steps are intended to be compatible with firing temperatures of the (green body) alumina substrates. From this work, a Pt/4% Au paste composition was found to have better performance than an Au-only paste, and a design incorporating high-fired porous YSZ with the Pt/4% Au paste electrodes was found to have similar performance as earlier Au-wire prototypes with low-fired YSZ. The results indicated the feasibility for using a traditional screen-printing process and single-step co-firing routine for sensor fabrication using either Au or Pt/Au paste electrodes.

A major milestone for this past year was filing of a patent to protect jointly developed (LLNL and CRADA partner EmiSense) intellectual property. The intellectual property development and technology transfer activities this past year are accelerating efforts to bring the LLNL NO_x sensor technology to commercialization. We continue our long-standing collaboration with Ford Motor Company in this effort to test prototype sensors in dynamometers.

References

Akbar, S., P. Dutta, and C. Lee, 2006, "High-temperature ceramic gas sensors: a review," *Int. J. Appl. Ceram. Technol.*, 3, 302.

Du Frane, W. L., L. Y. Woo, R. S. Glass, R. F. Novak, and J. H. Visser, 2013, "Substrate Effects on an Electrochemical NO_x Sensor Based on Porous Y_2O_3- Stabilized ZrO_2 (YSZ) and Sr-doped LaMnO3 (LSM)," *ECS Transactions*, 45, 3.

Fergus, J. W., 2007, "Materials for high temperature electrochemical NO_x gas sensors," c*Sens. Actuators, B*, 121, 652.

Martin, L. P., L. Y. Woo, and R. S. Glass, 2007, "Materials for high temperature electrochemical NO_x gas sensors," *J. Electrochem. Soc.*, 154, J97.

Menil, F., V. Coillard, and C. Lucat, 2000, "Critical review of nitrogen monoxide sensors for exhaust gases of lean burn engines," *Sensors and Actuators B*, 67, 1.

Moos, R., 2005, "A brief overview on automotive exhaust gas sensors based on electroceramics," *Int. J. Appl. Ceram. Technol.*, 2, 401.

Song, S.-W., L. P. Martin, R. S. Glass, E. P. Murray, J. H. Visser, R. E. Soltis, R. F. Novak, and D. J. Kubinski, 2006, "Aging Studies of Sr-Doped $LaCrO_3$/YSZ/Pt Cells for an Electrochemical NOx Sensor," *J. Electrochem. Soc.*, 153, H171.

Woo, L. Y., L. P. Martin, R. S. Glass, and R. J. Gorte, 2007, "Impedance characterization of a model Au/yttria-stabilized zirconia/Au electrochemical cell in varying oxygen and NO_x concentrations," *J. Electrochem. Soc.*, 154, J129.

Woo, L. Y., L. P. Martin, R. S. Glass, W. Wang, S. Jung, R. J. Gorte, E. P. Murray, R. F. Novak, and J. H. Visser, 2008, "Effect of electrode composition and microstructure on impedancemetric nitric oxide sensors based on YSZ electrolyte," *J. Electrochem. Soc.*, 155, J32.

Woo, L. Y., R. S. Glass, R. F. Novak, and J. H. Visser, 2010, "Effect of electrode material and design on sensitivity and selectivity for high temperature impedancemetric NO_x sensors," *J. Electrochem. Soc.*, 157, J81.

Woo, L. Y., R. S. Glass, R. F. Novak, and J. H. Visser, 2011, "Diesel engine dynamometer testing of impedancemetric NO_x sensors," *Sensor Actuat. B-Chem.*, 157, 115.

Yamazoe, N., 2005, "Toward innovations of gas sensor technology," *Sens. Actuators*, B, 108, 2.

Zhuiykov, S. and N. Miura, 2007, "Development of zirconia-based potentiometric NO_x sensors for automotive and energy industries in the early 21st century: What are the prospects for sensors?" *Sens. Actuators, B*, 121, 639.

Publications/Presentations/Patents

Du Frane, W. L., L. Y. Woo, R. S. Glass, R. F. Novak, and J. H. Visser, 2013, "Substrate Effects on Electrochemical NO_x Sensor Based on Porous Y_2O_3-Stabilized ZrO_2 (YSZ) and Sr-doped $LaMnO_3$ (LSM)," *ECS Transactions*, 45 (14), 3–11.

Woo, L. Y., R. S. Glass, R. F. Novak, and J. H. Visser, 2013, "Zirconia-electrolyte-based impedancemetric sensors using Sr-doped $LaMnO_3$ (LSM) electrodes for measuring NOx in combustion exhaust streams," *The 10th Pacific Rim Conference on Ceramic and Glass Technology*, in San Diego, California, June 2–7, 2013.

New patent application (No. 14055562) entitled, "Electrochemical Sensing Using Voltage-Current Time Differential," filed on October 16, 2013.

Project 18518 – Materials for High-Efficiency Engines

Agreement 13329 – Design Optimization of Piezoceramic Multilayer Actuators for Heavy-Duty Diesel Engine Fuel Injectors

Hua-Tay Lin, Hong Wang, and Andrew A. Wereszczak
Ceramic Science and Technology Group
Oak Ridge National Laboratory
P.O. Box 2008, MS 6068
Oak Ridge, TN 37831-6068
Phone (865) 576-1169; fax: (865) 574-6098; e-mail: linh@ornl.gov

DOE Technology Manager: Jerry L. Gibbs
Phone (202) 586-1182; fax: (202) 586-1600; e-mail: jerry.gibbs@ee.doe.gov
ORNL Technical Advisor: J. Allen Haynes
Phone (865) 576-2894; fax: (865) 574-4913; e-mail: haynesa@ornl.gov

Contractor: Oak Ridge National Laboratory, Oak Ridge, Tennessee
Prime Contract No.: DE-AC05-00OR22725

Objectives

- Apply established structural ceramic probabilistic design and reliability analysis to piezoelectric multilayer actuators (PMLAs).
- Generate required micromechanical property data on lead zirconate titanate (PZT) piezoceramics and macromechanical property data on PMLAs for input into the design and reliability analysis of the latter.
- Identify minimum mechanical performance requirements for fuel injector PMLAs.
- Adapt these strategies to improve the reliability of PMLAs that are candidates for use in diesel engine fuel injectors.

Approach

- Evaluate PMLA reliability under representative service conditions.
- Link constituent piezoceramic micromechanical and PMLA macromechanical responses.

Accomplishments

- Experimental study on the down-selected piezo stacks for heavy-duty diesel engine fuel injector has been completed successfully by using low-profile stacks, namely 20/10-layer plate specimens extracted from the prototype stacks.
- The 20-layer specimens, with a range of resistances, were tested and characterized. The lifetime of the specimens under the accelerated electric fatigue depends on the pre-existing condition.
- The specimens that finished 10^8 cycles demonstrated a defined degradation trend during the cycle tests. Some fluctuation was observed in the individual cycle test, and discrepancy of fatigue responses also was observed between specimens.

Future Direction

- Complete study of the effects of humidity and temperature (80% RH, 85°C) on the mechanical properties of down-selected PZT ceramics.
- Complete study of cyclic fatigue of short PZT stacks in higher-temperature plus humidity environment.

Introduction

The use of PMLAs as diesel fuel injectors has the potential to reduce injector response time, provide greater precision and control of the fuel injection event, and reduce energy consumption. Compared with conventional solenoid operation of an injector, the alternative use of a PMLA can enable precise rate shaping of the entire injection cycle that accurately controls injection timing and fuel quantity. PMLA (or piezo-stack) fuel injectors contain a solid-state ceramic actuator that converts electric energy into linear motion, precisely controlling the needle's opening and closing. This capability results in an engine with outstanding performance, improved fuel economy, low noise, and low emissions. However, even though their use is very attractive for the reasons mentioned, uncertainty continues about how reliable piezo-actuated fuel injectors will be in the challenging environment of a heavy-duty vehicle diesel engine. Piezoelectric function is the obvious primary function of PZT ceramic PMLAs for fuel injectors; however, their reliability may be a performance and life limiter because the PZT ceramic within them is brittle, lacks high strength, and may exhibit fatigue susceptibility. This brittleness and relatively low strength can be overcome with a proper probabilistic component design methodology.

This project undertakes the reliability characterization of candidate PMLAs used in these fuel injectors and the piezoceramics used in the PMLAs. Testing and characterization of the piezo-stacks and piezoceramics have continued based on recommendations from Cummins, Inc.

Approaches

Characterization of PMLA

The objective of this work is to develop an experimental approach for conducting accelerated electric fatigue testing and, at the same time, characterize the fatigue responses and lifetime of candidate or down-selected piezo-stacks. The database and understandings generated in this study are to be applied by the end users for optimizations of the design and deployment of piezo-stacks for heavy-duty fuel injection systems.

The down-selected piezo-stack (manufactured by EPCOS) for heavy-duty engine fuel injectors has dimensions of 12 × 12 × 54 mm (Figure 1). The rated capacitance is 16.15 mF. Testing stacks of this size presents substantial challenges to the electronic systems used to drive and control stacks. In addition, the stacks are provided without encapsulation; partial discharge near the surface of the stacks can be easily induced during cycling.

The testing of the piezo-stacks was conducted by using a piezodilatometer system designed by Oak Ridge National Laboratory (ORNL). The piezodilatometer system is equipped with an electronic liquid, FC-40, to control the partial discharge near the surface of the stack specimens. Furthermore, testing of EPCOS stacks has to use low profile stacks with 10 and 20-layer plates for the high-voltage power supply to accommodate the electric current requirement. The 10 and 20-layer plates are structurally independent and compose elements of the whole stack. Therefore, they can be decomposed or structurally separated for this study.

These 10 and 20-layer plates were provided by Cummins, Inc. At first, the stacks were sorted according to the soundness of the surface condition. These specimens were then wired as shown in Figure 1b and examined using a voltmeter for electric resistance, then further measured with an impedance analyzer (model Solartron 1260) prior to the electric fatigue tests. The impedance data were collected using a 50-mV amplitude over a frequency range of 10 mHz to 100 KHz and analyzed using an equivalent electric circuit through curve fitting. An RC element consisting of a parallel connection of a capacitor C and a resistor R is usually employed for analysis. Variations of R and C values were observed from specimen to specimen during this process. The specimens with good electrode condition were selected for the subsequent electric cycle tests.

The ORNL piezodilatometer was used in the cycle test. Figure 2 shows the setup with a specimen connected to the high-voltage power

cables. The cycle test for 10 and 20-layer specimens followed the procedures described previously in (Zeng et al. 2013). Particularly, both large signal and small signal measurements were used for testing. The large signal measurement for piezoelectric response involved a 0.1-Hz triangle wave with amplitudes of 1.5/0 and 3.0/0 kV/mm, while those for dielectric response consists of a 50-Hz sine wave with the same amplitudes of 1.5/0 and 3.0/0 kV/mm. The small signal measurement was accomplished by using an impedance analyzer. The impedance data were collected over a frequency range of 10 mHz to 100 KHz and analyzed using the RC element through curve fitting as mentioned above.

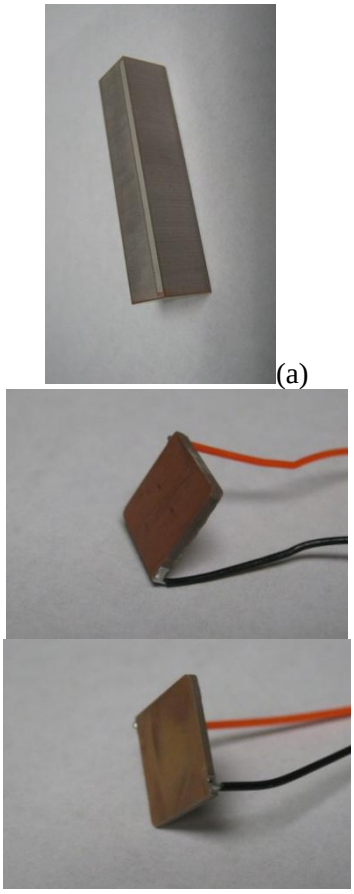

(a)

(b)

Figure 1. (a) 54-mm piezo multilayer stack that can be decomposed into 10 and 20-layer specimens to be used in electric and mechanical testing of this project; (b) A 20-layer specimen in upper view and 10-layer specimen in lower view are wired after the extraction process from the whole stack.

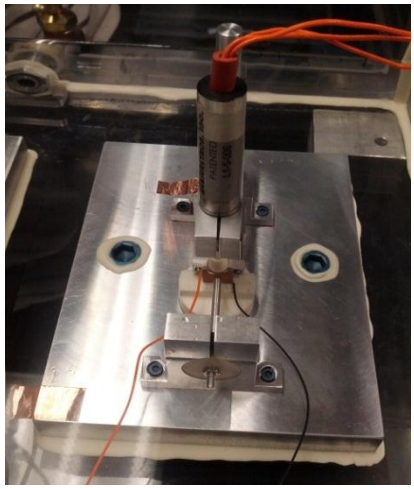

Figure 2. Setup of electric cycle test for 20-layer specimen.

A number of 20-layer specimens were used in a series of preliminary cycle tests to determine the electric field level and frequency for the long-term cycle test. With the field level increased from 0.2 to 3 kV/mm, these specimens displayed a defined electric current waveform at 50 and 100 Hz. In the associated measurements with 0.1-Hz triangular waves, tests showed that specimens failed when the field level was increased to 4.5 or 6 kV/mm. Therefore, an electric field of 3 kV/mm at 100 Hz has been selected to be used in the cycle test for 10 and 20-layer specimens.

Characterization of Pieozceramics

The objective of this work is to develop an effective approach to testing PZT ceramics and to establish a database for the down-selected PZT ceramics for the fuel injection system in heavy-duty diesel engines. The testing of PZTs for the EPCOS stacks has been shown to be quite challenging because the single-layer PZT, as required for such a task, cannot be readily obtained. Therefore, the work has been directed to test the sub units (e.g., 10-layer plates) that are extracted from the prototype PZT stacks. Testing of the 10-layer plates also provides an opportunity to examine the interaction between individual PZT layers, which cannot be achieved via use of a single-layer plate.

Results

Characterization of PMLA

The cycle tests of four 20-layer specimens were successfully completed. The estimated R (resistance) and C (capacitance) values of the four specimens according to the impedance analysis are given in Table 1. For these four specimens, R values of tested specimens range from 37 to 970 $\times 10^6$ ohms, while C values are between 242 and 294 nF.

Table 1. 20-layer specimens used in the cycle test.*

Specimen	Capacitance, nF	Error, %	Resistance, x10^6 ohm	Error, %
P2005	277	0.49	572	6
P2007	242	0.39	873	27.8
P2010	294	1.1	37.4	5.5
P2011	285	0.39	970	36.7

*Fitting frequency range, 0.01 Hz to 100 KHz.

Large Signal Measurement

Among the tested specimens, all were finished up to 10^8 cycles as designed, except specimen P2010. The specimen P2010 failed after 10^5 cycles. The fatigue responses in terms of mechanical strain and hysteresis of all the four tested specimens are given in Figure 3. The curves of P2005 display an abnormal drop attributed to loose specimen contact. The fatigue curves of P2007 and P2011 exhibit a defined decreasing trend in both mechanical strains and hysteresis, although the local fluctuations exist.

In addition, the charge density and hysteresis responses of the tested specimens are shown in Figure 4. It can be seen that specimen P2005 did show a fatigue curve consistent with those of other specimens, even though it did not display a consistent mechanical strain response due to the loose electrical contact. Apparently, the response increased with the increasing measurement field level. Moreover, a large variety of fatigue responses also were observed among the tested specimens. The difference of fatigue curves is especially large between specimen P2005 and P2007.

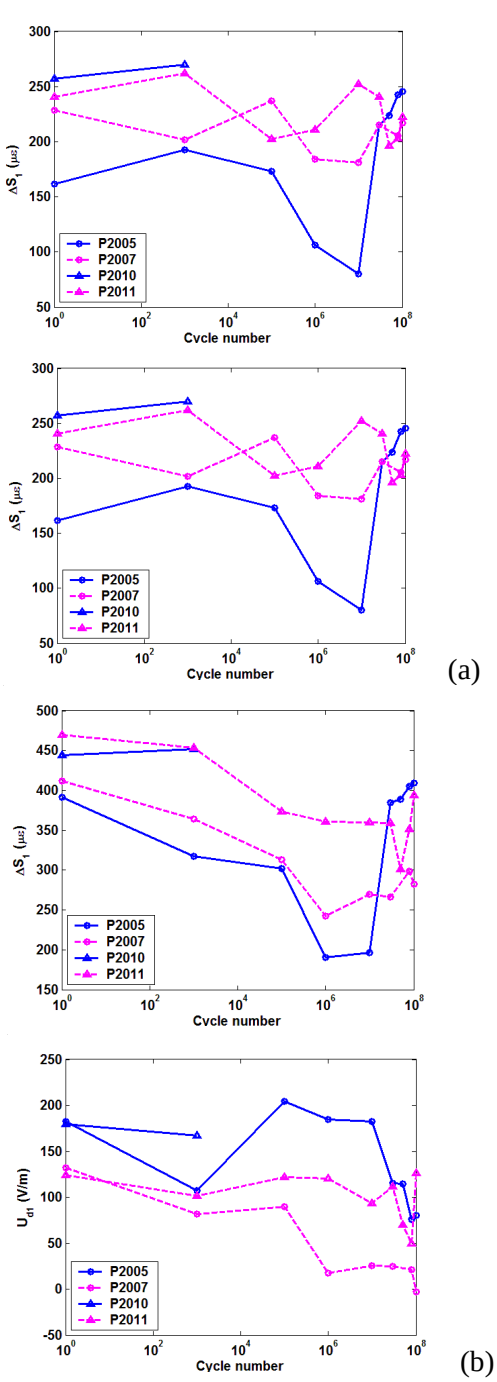

Figure 3. Variation of mechanical strains ΔS_1 and piezoelectric hysteresis U_{d1} as a function of cycle number measured at (a) 1.5 kV/mm and (b) 3.0 kV/mm.

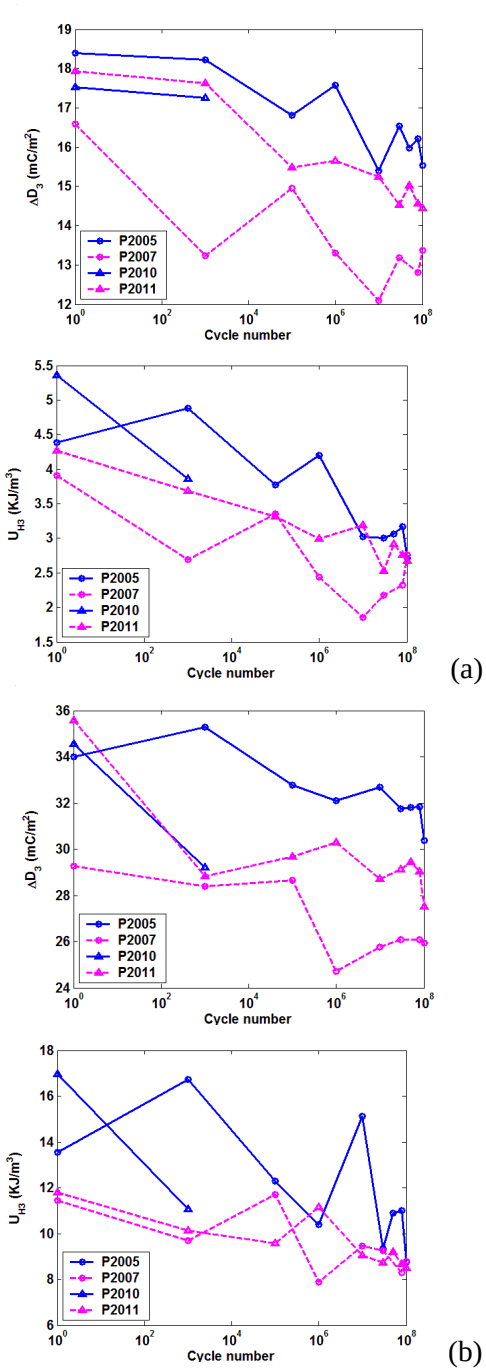

Figure 4. Variation of charge density ΔD_3 and electric hysteresis U_{H3} as a function of cycle number measured at (a) 1.5 kV/mm and (b) 3.0 kV/mm.

The fatigue responses in terms of piezoelectric, dielectric coefficients, and loss angles of these tested specimens are given in Figure 5 and Figure 6. It can be seen that the measurement at 1.5/0 and 3.0/0 kV/mm delivered a reasonably consistent fatigue response. Both the absolute value of piezoelectric coefficient and loss angle exhibited decreasing trend, along with the cycle number. The same observation also applied to the dielectric coefficient and loss angle. It is worthwhile noting that the piezoelectric and dielectric coefficients measured prior to fatigue tests at both electric fields were all comparable with the published data of equivalent PZT materials (Wang et al. 2010, Noliac Group 2013). These results demonstrated that the integrity of specimens as a piezo-stack has been largely maintained, even though the specimens were extracted from as-manufactured whole stacks and were not delivered as a standard product.

Small Signal Measurement

The R (resistance) and C (capacitance) values based on the impedance analysis largely exhibited a defined decreasing trend in the cycling fatigue test (Table 2). However, the exception existed for specimen P2007, in which the R value appeared to increase after the cycle test. It also is seen that the fitting of R values involved a high error percentage in several measurements because of the limited frequency range of the equipment, especially near the low end of the frequency range.

The Z-plots of specimen P2005 and specimen P2010 are presented in Figure 7. The impedance curve of specimen P2005 (Figure 7a) exhibited a trend of first decreasing and then increasing R value. On the other hand, specimen P2010 exhibited a certain amount of electric resistance at the beginning of the cycle test (Figure 7b). However, the curve changes dramatically into a well-defined semi-circle after the breakdown of the specimen (as shown in the insert).

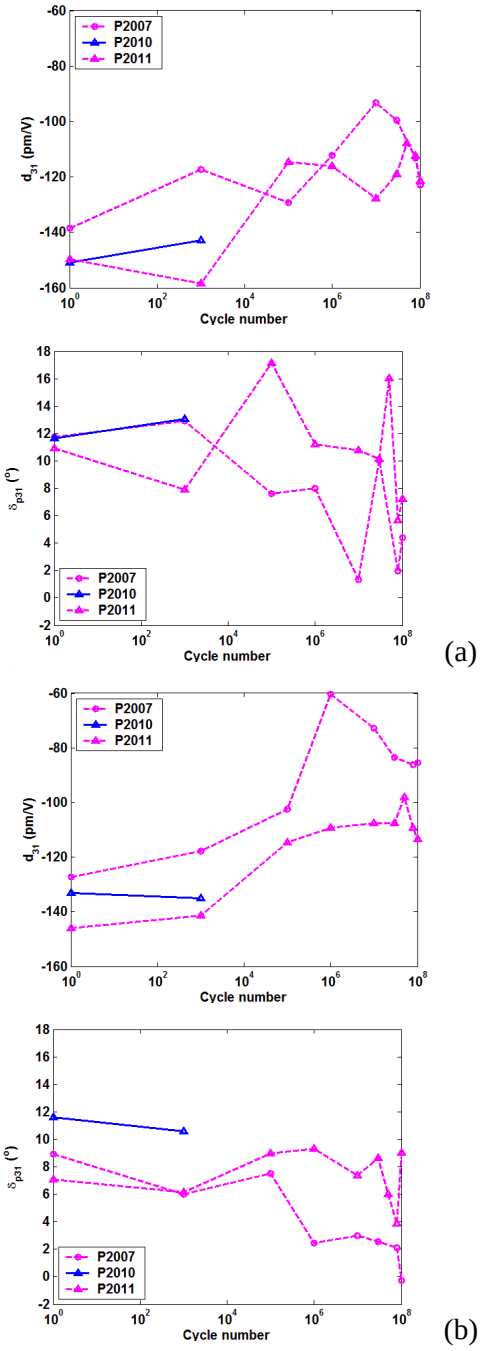

Figure 5. Variation of piezoelectric coefficients d_{31} and piezoelectric loss angle δ_{p31} as a function of cycle number measured at (a) 1.5 kV/mm and (b) 3.0 kV/mm.

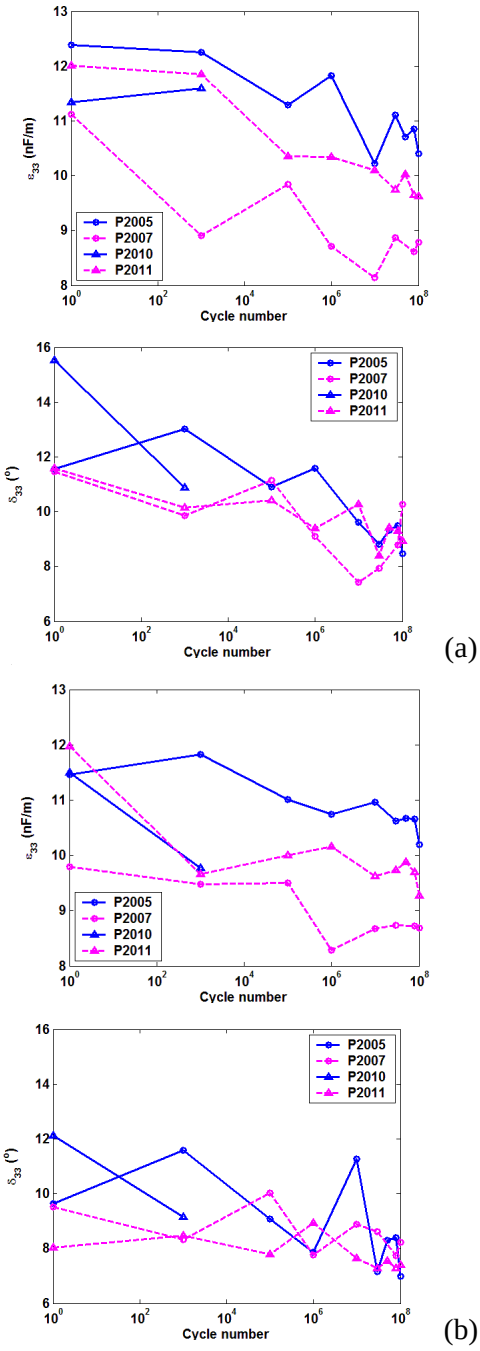

Figure 6. Variation of dielectric coefficients ε_{33} and piezoelectric loss angle δ_{33} as a function of cycle number measured at (a) 1.5 kV/mm and (b) 3.0 kV/mm.

Table 2. Variation of R and C values in cycle tests.*

Specimen	Cycles	Capacitance, nF	Error, %	Resistance, ohm	Error, %	Note
P2005	1.00E+00	296.3	0.56	9.42E+08	52.8	
	3.00E+07	280	0.51	5.00E+08	24.2	
	1.00E+08	269.4	0.4	6.05E+08	27.9	
P2007	1.00E+00	255.4	0.4	9.44E+07	36.7	
	1.00E+08	227.3	0.4	1.60E+08	50	
P2010	1.00E+00	285.4	0.65	1.82E+08	11.6	
	1.00E+05	245.1	0.47	3.72E+05	0.54	Breakdown
P2011	1.00E+00	293.8	0.73	8.45E+08	58.1	
	1.00E+08	262.7	0.36	5.05E+08	16.3	

*Fitting frequency range, 0.01 Hz to 100 KHz.

Characterization of Piezoceramics

The mechanical response of the EPCOS 10-layer PZT has been studied under various temperatures via the use of a self-aligning ball-on-ring technique. Two different specimen sizes were tested (6.8 × 6.8 × 0.76 mm and 11.5 × 11.5 × 0.74 mm), while the PZT and internal electrode materials were similar in these specimens.

Mechanical results showed that the temperature effects are quite consistent independent of specimen size. For the large size, the mechanical strength reduction was found to be about 12%, with temperature increase from 22 to 200°C. A significant mechanical strength reduction also was observed with the increase of specimen size (Figure 8). This size scaling effect, typically observed for brittle ceramics, diminished at high temperatures greater than or equal to 100°C.

In a preliminary study, the effect of humidity was investigated by pre-treating commercial PZT (PSI 5A4E) specimens in a humidity chamber at room temperature for a specified period of time. The mechanical strength of the PZT was tested against various time periods using a ball-on-ring setup. Results showed that the measured mechanical strength under the applied electric field effect was consistent with those previously reported. Also, the effect of humidity and time of treatment on the mechanical strength was very minimal (Figure 9). Therefore, the results demonstrated that PZT ceramic is very stable within the tested periods of treatment. However, the response of PZT in an extreme environment remains to be explored.

Testing on the EPCOS PZT for further database development and environmental effect studies is required; this will be the focus of fiscal year 2014. The planned tests would be on 10-layer specimens supplied by Cummins, Inc.

Conclusions

Experimental study on the down-selected piezo-stacks for heavy-duty diesel engine fuel injectors has been conducted using low-profile stacks, namely 10- and 20-layer plate specimens extracted from the prototype stacks.

The technical approach to test and characterize the 10 and 20-layer plate specimens has been developed using electrical cycle tests. This involves a modified ORNL piezodilatometer with an upgraded power supply.

The 20-layer specimens, with a range of resistances, were tested and characterized under the electrical cycle condition. The lifetime of the specimens depends on the pre-existing conditions of surface defect and soundness of electrode connection. The following conclusions can be drawn from these tests:

- The specimen with lowest resistance exhibited a short lifetime, while those with higher resistance finished 10^8 cycles as designed by the manufacturer.

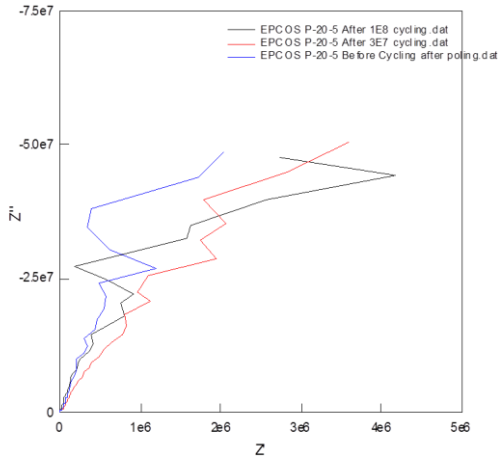

(a)

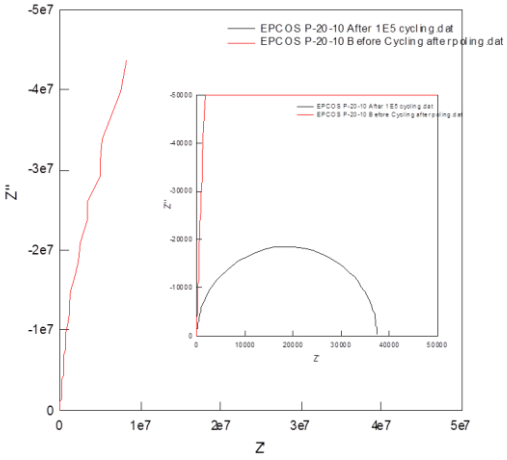

(b)

Figure 7. Z-plots at difference number of cycles during the cycle test for (a) P2005, and (b) P2010. The insert in (b) (Z' and Z'' have a maximum of 5,000) shows the enlarged region of the Z-plot near a low frequency range with a whole semi-circle revealed because of the dielectric breakdown occurring in P2010.

- The specimens showed pre-fatigue piezoelectric and dielectric coefficients comparable to the published data of equivalent piezoelectric materials, including specimen with a short lifetime.
- The breakdown of the specimen was observed to be spontaneous, while the decreases in piezoelectric and dielectric coefficients were not clearly defined based on the trend observed.
- The specimens that finished 10^8 cycles exhibited a defined degradation trend during the cycle tests. However, some fluctuation was observed over the individual cycle test, and discrepancy of fatigue responses also was observed between specimens.

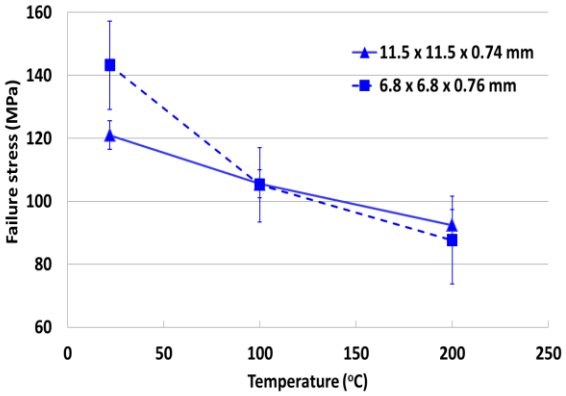

Figure 8. Temperature dependence of flexural strength of 10-layer specimens. The results are based on the ball-on-ring testing consisting of double (for small specimens) and triple (for large specimens) alumina tube support and alumina loading ball. A configuration of ϕ12.7-mm ball and ϕ5-mm ring was used for small specimens; the ϕ19.05-mm ball and ϕ9.5-mm ring was used for large specimens. Each data set consists of 22 to 24 test points.

Future Work

Future work consists of the following:

- Complete preparation of setup for mechanical testing and finish treatment of PZT specimens in controlled humidity and temperature (80% RH, 85°C).
- Complete study of the effects of humidity and temperature on the mechanical properties of supplied down-selected PZT ceramics provided by Cummins and equivalent commercially available PZT ceramics.

- Complete preparation of the set up and adaptation of testing facility for the electric cycle fatigue test of PZT stacks at a controlled temperature environment.
- Complete study of cyclic fatigue of down-selected PZT stacks in a temperature environment equivalent to that of a fuel injection system in a heavy-duty diesel engine (100 to 200°C).

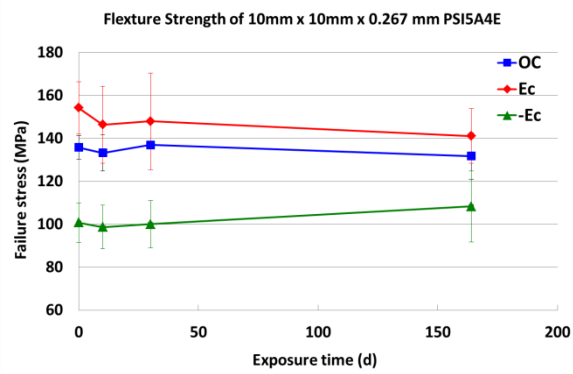

Figure 9. Variation of flexural strength of single layer PZT-5A along with exposure time under various electrical conditions; OC – open circuit, Ec – coercive electrical field. The specimens were pre-treated in an 85% R.H. chamber at room temperature.

References

[1] Zeng, F. W., H. Wang, and H.-T. Lin, 2013, "Fatigue and failure responses of lead zirconate titanate multilayer actuator under unipolar high-field electric cycling," *J. of Appl. Phys.*, 114, 024101.

[2] Wang, H., T. A. Cooper, H.-T. Lin, and A. A. Wereszczak, 2010, "Fatigue responses of lead zirconate titanate stacks under semi-bipolar electric cycling with mechanical preload," *J. Appl. Phys.*, 108, 084107.

[3] Noliac Group, "Piezo Ceramics," http://www.noliac.com, accessed October 12, 2013.

Presentations and Publications

1. Zeng, F. W., H. Wang, and H.-T. Lin, 2013, "Fatigue and failure responses of lead zirconate titanate multilayer actuator under unipolar high-field electric cycling," *J. of Appl. Phys.*, 114, 024101.
2. Zhang, K., F. W. Zeng, H. Wang, and H.-T. Lin, 2013, "Biaxial flexural strength of poled lead zirconate titanate in high electric field with extended field range," *Ceramic International*, 39, 2023–2030.
3. Zhang, K., F. W. Zeng, H. Wang, and H.-T. Lin, 2012, "Strength properties of aged poled lead zirconate titanate subjected to electromechanical loadings," *Smart Mater. Struct.*, 21, 117001 (7 pp).

Project 18518 – Materials for High-Efficiency Engines

Agreement 17058 – Compact Potentiometric NO_x Sensor

Dileep Singh
Argonne National Laboratory
9700 S. Cass Avenue
Argonne, IL 60439
Phone (630) 252-5009; fax: (630) 252-2785; e-mail: dsingh@anl.gov

DOE Technology Manager: Jerry L. Gibbs
Phone (202) 586-1182; fax: (202) 586-1600; e-mail: jerry.gibbs@ee.doe.gov

Contractor: UChicago Argonne LLC
Prime Contract No.: DE AC03 06CH11357

Objectives

- Use plastic joining technique to produce compact nitrous oxide (NO_x) and bifunctional (NO_x and O_2) potentiometric sensors with internal reference
- Develop electronic conducting ceramic to replace the platinum (Pt) electrodes in the sensor
- Develop technique to directly join the conducting ceramic to the yittria-stabilized zirconia body of the sensor
- Conduct tests to determine the range of NO_x concentrations that can be sensed accurately.

Approach

- Modification/optimization of the Pt/zeolite filter to increase the sensing concentration for NO_x.

Accomplishments

- Strong, pore-free joints have been made with various ceramics, cermets, intermetallics, composites, and biomaterials, with and without various interlayers; the fracture occurs away from interface at the region of maximum residual stress
- Demonstrated that grains in $SrTiO_3$ rotate during deformation
- Research and Development 100 Award for oxygen sensor
- Developed NO_x sensor
- Published 27 journal papers, three patents issued for plastic joining process, two patents issued for the NOx and O_2 sensors, and one patent issued on LSAM interconnect, with several companies having expressed interest in the sensors.

Future Direction

- The project was concluded in fiscal year 2011. However, additional effort was initiated to establish the range of NO_x concentrations that can be measured accurately when using the sensor. In the future, optimization of filter material will be carried out to increase the upper limit for NOx concentration sensing, which is required by heavy-duty engine manufacturers.

Introduction

Monitoring gas composition (e.g., O_2, NO_x, CO, and CO_2) in the combustion environment with good accuracy has been of great importance for the advancement of combustion heat engines. Monitoring oxygen and NO_x concentrations in combustion gases is crucial to optimizing combustion efficiency in engine and power plant applications; therefore, it is important to improving energy efficiency and minimizing environmental pollution. NO_x ($NO + NO_2$) sensing also has been considered one of the key elements of the next generation internal combustion engines. A reliable and accurate NO_x sensor is needed to monitor NO_x and trigger the regeneration of NO_x adsorption catalysts or control the injection of reductants for continuous NO_x reduction.

Previously, we have demonstrated that it is possible to form pore-free, high-strength joints in YTZP by applying a small stress at elevated temperatures ($T/T_m \approx 0.5$, where T_m is the melting temperature in K) (Gutierrez-Mora et al. 1999, 2002). This technique has been used to produce oxygen sensors by encapsulating a metal/metal oxide powder in a container consisting of a lower YTZP disk joined to an YTZP cylinder (Spirig et al. 2007). A metal/metal oxide powder is placed in the cavity that is then sealed by plastic joining to another YTZP disk with a thin Pt electrode attached to the top and bottom side (Figure 1). When placed in a combustion environment, the metal/metal oxide powder decomposes to produce oxygen. The difference between the internal oxygen activity and the activity of the gas to be measured, is that it produces an emf that is proportional to $\ln(a_O/a_{Oref})$, where a_o is the oxygen activity of the gas to be measured and a_{oref} is the activity of the reference gas.

This technique has been applied further to produce NO_x sensors (Yang et al. 2008) that could enable simultaneous measurements of NO_x and O_2 in a combustion environment. The Pd/PdO-containing reference chamber was sealed within the stabilized zirconia superstructure by a high-pressure/temperature bonding method that initiated grain boundary sliding between the ceramic components. NO_x sensing was conducted in both amperometric and potentiometric modes. Pt-loaded zeolite Y was used to obtain total NO_x capacity and to cover Pt electrodes for detecting oxygen in the presence of NO_x. Both amperometric and potentiometric-type sensors demonstrated excellent signal stability, total NO_x response, and minimal NO_x-O_2 cross interference. As reported earlier, total NOx concentrations as high as 600 ppm were detected.

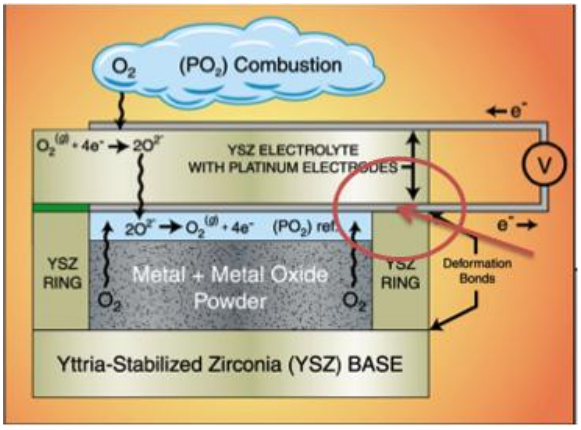

Figure 1. Schematic of the internal reference oxygen sensor.

In the present work, the focus was to determine the highest limit of NO_x that can be sensed accurately using the sensor developed. In this regard, basic sensor packages were fabricated and tested. The key hurdle was to develop the optimum Pt(Y) filter compositions to equilibrate the NO_x in the combustion environment. Currently, no commercial sensors are available that can operate in NO_x concentrations in the order of several thousand ppms.

Experimental Details

Pt(Y) Filter Synthesis

The platinum-loaded zeolite y (PtY) was made by first adding water to 334 mg of $Pt(NH_3)_4Cl_2H_2O$, resulting in a 0.1-M $Pt(NH_3)_4Cl_2$ stock solution. Then 5 mL of the stock solution was diluted to 50 mL, using distilled water, and 1.0008 g of zeolite Y (Si/Al =2.55) were added. The zeolite was ion exchanged for 1 day using a stir plate. The resulting solution was vacuum filtrated and allowed to dry in an oven overnight. In order to

reduce the platinum, the zeolite was first slowly heated to 300°C for 2 hours under a constant flow of 20% O_2 and 80% N_2. Lastly, the zeolite was slowly heated to 450°C for 6 hours under a flowing atmosphere of 5% hydrogen. The resulting powder (Figure 2) was a dark brown color. For the sensing experiments, about 100 mg of this PtY powder were loaded into a quartz u-tube and testing gas was flowed through the tube before reaching the sensor. This filter was kept at 400°C.

Figure 2. Synthesized Pt(Y) powder for the filter for the NO_x sensor.

Sensor Fabrication

YSZ rods (Ortech, 8 mol %), 10 mm in diameter, were cut into 2-mm thick discs. Two 1-cm, Pt-wire electrodes were attached to each sensor using Pt ink. The sensors were then heated to 900°C, ramping at 2°C/min and dwelling for 2 hours. After the electrodes were secure, WO_3 (Alfa Aesar, 99.8%) was painted on and heated to 900°C for 2 hours. PtY was painted on next and heated to 600°C for 2 hours, ramping by 3°C/min. A picture of the sensors is shown in Figure 3.

Gas Sensing

For gas sensing, sensors were tested at 600°C in a tube furnace. Sensors were conditioned at 600°C for at least 3 hours but, often, conditioned overnight. NO concentrations up to 3,000 ppm were tested in 3% oxygen environments using nitrogen as the balance gas at a flow rate of 100 sccm.

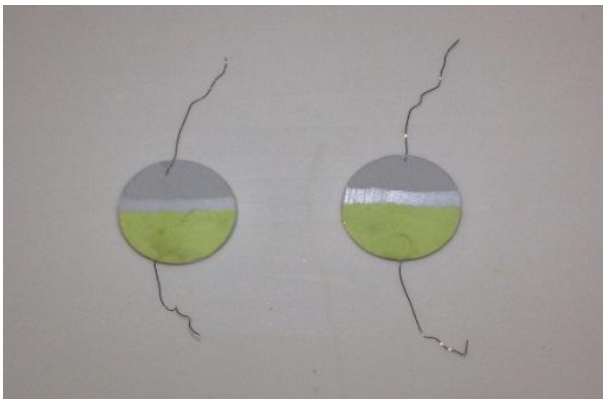

Figure 3. Fabricated NO_x sensors.

Results

Figures 4 through 6 show the sensor response as a function of NO concentrations and time. The voltage output for the sensors is stable and reproducible, as indicated by switching ON and OFF. However, as shown in Figures 4 through 6, the voltage signal gets saturated quite rapidly with increasing NO concentrations.

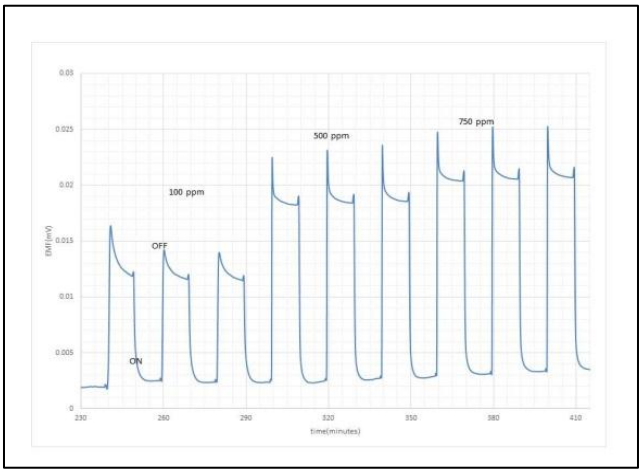

Figure 4. Sensor response for 100, 500, 750 ppm NO concentrations in 3% oxygen (flow rate 100 sccm).

Figure 7 shows the measured voltage signal as a function of the NO concentration in the test gas. Clearly, there is an increasing voltage as the NO concentration goes from 100 to 1,000 ppm. However, between 1,000 and 3000 ppm, the signal does not increase significantly. It is believed that the reason for this is the incomplete equilibration of NO/NO_2 in the Pt(Y) filter. It is envisioned that further optimizing the

Pt-loaded zeolite powder can lead to rapid equilibration and increased signal strengths at high NO concentrations. One of the approaches being considered is to increase the surface area of the powders by going to submicron-scale size powders, providing increased surface area for catalytic activity.

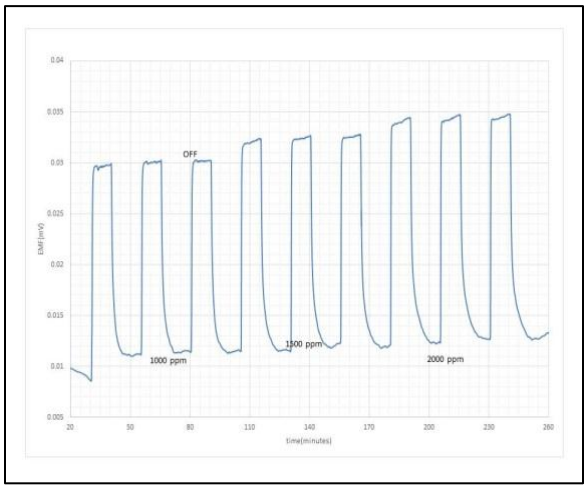

Figure 5. Sensor response for 1,000; 1,500; and 2,000 ppm NO in 3% oxygen (flow rate 100 sccm).

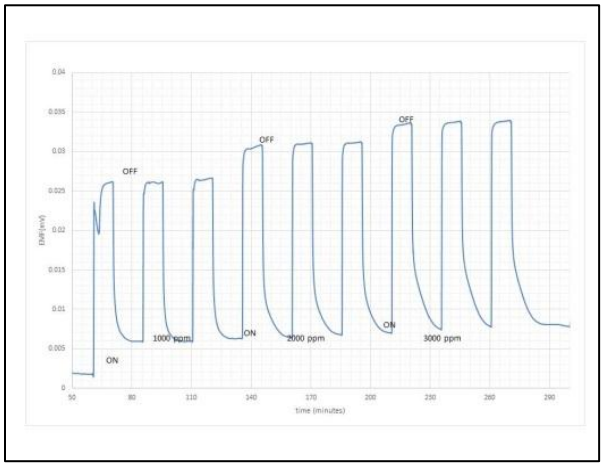

Figure 6. Sensor response for 1,000; 1,200; and 3,000 ppm NO in 3% oxygen (flow rate 100 sccm).

Conclusions

One of the major challenges with NOx sensors is their limited use in terms of the NOx concentrations they can accurately sense. As part of this effort, sensors were fabricated and tested with NO concentrations up to 3,000 ppm. The sensors were found to function quite well up to 1,000 to 1,500 ppm. However, signal saturations occur beyond 1,500 ppm NO. As part of future work, the morphology and composition of the platinum-loaded zeolite filter will be optimized to improve sensor performance to 3,000 ppm NO sensing.

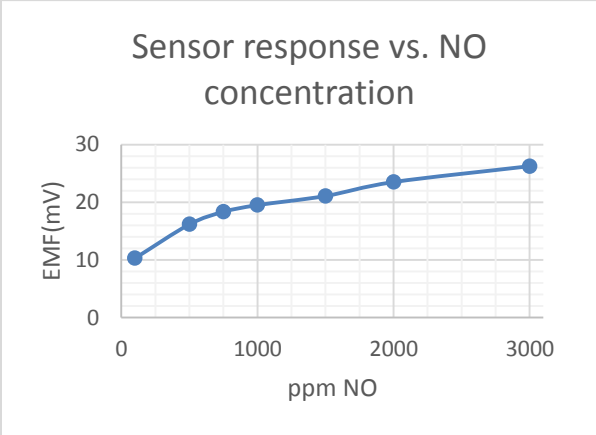

Figure 7.Sensor response versus NO concentration (100 to 3,000 ppm).

Acknowledgements

Collaboration with Professor Prabir Dutta and his group at Ohio State University is much appreciated.

References

Gutierrez-Mora, F., A. Dominguez-Rodriguez, J. L. Routbort, R. Chaim, and F. Guiberteau, 1999, "Joining of Yttria-tetragonal Stabilized Zirconia Polycrystals using Nanocrystals," *Scripta Mater*, 41, 455–60.

Gutierrez-Mora, F., K. C. Goretta, S. Majumdar, J. L. Routbort, M. Grimdisch, and A. Domínguez-Rodriguez, 2002, "Influence of Internal Residual Stresses in Superplastic Joining of Zirconia Toughened Alumina," *Acta Mater*, 50, 3475–3486.

Spirig, J. V., R. Ramamoorthy, S. Akbar, J. L. Routbort, D. Singh, and P. K. Dutta, 2007, "High-temperature Zirconia Oxygen Sensor with Sealed Metal/Metal Oxide Internal Reference," *Sensors and Actuators*, B 124, 192–201.

Yang, J.-C., J. V. Spirig, D. Karweik, J. L. Routbort, D. Singh, and P. K. Dutta, 2008, "Compact electrochemical bifunctional NO_x/O_2 sensors with metal/metal oxide internal reference for high-temperature applications," *Sensors and Actuators*, B 131(2), 448–454, Patent issued.

Project 18518 – Materials for High-Efficiency Engines

Agreement 17257 – Materials for Advanced Turbocharger Designs

P. J. Maziasz
Materials Science and Technology Division
Oak Ridge National Laboratory
P.O. Box 2008, MS-6115
Oak Ridge, TN 37831-6068
Phone (865) 574-5082; fax: (865) 576-6298; e-mail: maziaszpj@ornl.gov

K. Pattabiraman
Global Materials Engineering Manager
Honeywell – Turbo Technologies
3201 W. Lomita Blvd.
Torrance, CA 90505
Phone (310) 571-1616; fax: (310) 539-7061; e-mail: kalathur.pattabiraman@honeywell.com

DOE Technology Manager: Jerry L. Gibbs
Phone (202) 586-1182; fax: (202) 586-1600; e-mail: jerry.gibbs@ee.doe.gov
ORNL Technical Advisor: J. Allen Haynes
Phone (865) 576-2894; fax: (865) 574-4913; e-mail: haynesa@ornl.gov

Contractor: Oak Ridge National Laboratory, Oak Ridge, Tennessee
Prime Contract No.: DE-AC05-00OR22725

Objectives

- Cooperative Research and Development Agreement (CRADA) NFE-08-01671 – Provide critical test data for new, improved high-temperature structural materials, which, in turn, will enable the design of advanced turbocharger systems with upgraded performance, durability, and reliability relative to conventional systems.

Approach

- CRADA NFE-08-01671 – This project received a 2-year extension and is designed to consider both materials for the turbine and compression sections and to consider turbochargers for both passenger/gasoline and commercial/diesel engines. Honeywell assesses and prioritizes the components that benefit the most from materials upgrades or alloy development. Oak Ridge National Laboratory (ORNL) works with Honeywell materials/component suppliers to obtain new materials for testing and evaluation.

Accomplishments

- Long-term creep testing of cast CF8C-Plus continued at 600°C and was completed at 750 to 850°C. Oxidation evaluation of CF8C-Plus cast stainless steel in a diesel exhaust environment at 800°C began this year.
- Honeywell began a review of the data and discussions to evaluate CF8C-Plus as the turbo-housing material for prototype opportunities on turbocharged gasoline engine models that include General Motors, Ford, and Volkswagen.

Future Direction

- CRADA – Testing of CF8C-Plus for automotive turbocharger applications will continue and discussions of prototyping opportunities will continue. Supporting the Honeywell commercialization of CF8C-Plus for light-duty truck and automotive turbine housing applications is a priority.

Introduction

This ORNL CRADA project with Honeywell (NFE-08-01671) addresses the limitations of lifetime or use-temperature for the various components (i.e., casing, wheel, shaft, and bearings) of both the turbine and compressor parts of the turbocharger system. Turbochargers are an attractive way to boost engine power to increase fuel efficiency. Requests for more detailed information on this CRADA project should be directed to Honeywell, Inc.

Approach

The CRADA project, which began several years ago, extends over a 5-year period and covers several different tasks. The first task assesses and prioritizes the various components that need or would most benefit from materials upgrades to increase temperature capability and performance, as well as durability and reliability. The next tasks examine current performance and degradation modes of wheel/shaft assemblies for turbines, compressors, and turbine housings, particularly for automotive applications. Cast CF8C-Plus stainless steel is being considered as the new material upgrade to cast-irons used as the turbocharger housing for diesel and automotive applications.

Technical Progress

This CRADA project began several years ago and is comprised of six tasks. ORNL and Honeywell discussed the priority of the various tasks and turbocharger components for materials upgrades at a kick-off meeting held in Torrance, California.

The turbine wheel-shaft assembly was chosen as the first component for analysis of residual stresses near the weld-joint of the Ni-based superalloy wheel to the steel shaft, using neutron-scattering at the High-Flux Isotope Reactor at ORNL.

These wheel-shaft assemblies can develop vibrations if there is any asymmetry in the weld-joint. Several sets of experiments were completed last year and show that there is an asymmetry in the residual hoop stress circumferentially in the as-welded condition. Last year, additional measurements were done on larger wheel-shaft assembly components with stainless steel shafts. The asymmetric residual hoop stresses present after welding are shown in Figure 1. Stress relief of the welded regions was done with fast induction-coil heating and two conventional furnace heat-treatment conditions at 593 and 649°C. Figure 1 shows that the induction coil stress relief does not reduce the tensile residual stresses or remove their asymmetry. By contrast, the conventional furnace heat-treatment at 593°C is relatively effective at removing both the residual stresses and their asymmetry. These results are being applied by Honeywell in optimizing manufacturing processes to maximize wheel-shaft assembly component performance and lifetime.

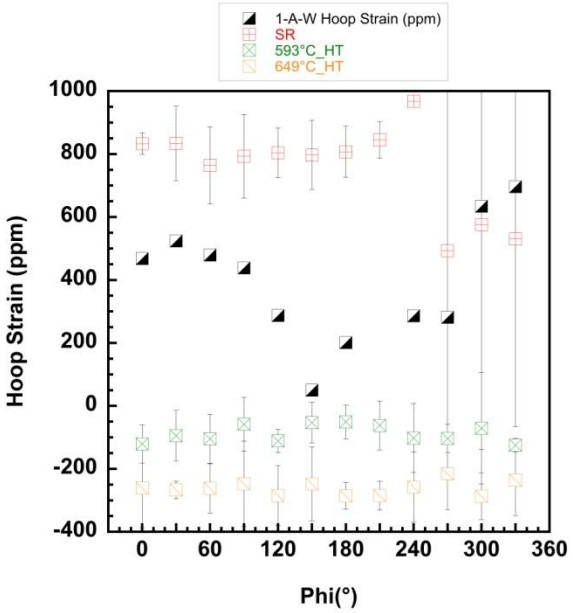

Figure 1. Neutron hoop strain maps versus circumferential angle of wheel/shaft assemblies in four different conditions: as-welded, stress relieved via fast induction coil heating, and conventional furnace stress relief heat treatments at 593 and 649°C. Error bars represent multiple measurements. Furnace stress relief at 593°C reduces the residual stresses and their asymmetry.

Materials testing was done in support of advanced materials for turbocharger housings. A typical diesel turbocharger housing is shown in Figure 2. Additional testing was done to extend

previous work by ORNL and Honeywell, comparing the new CF8C-Plus steel to HK30-Nb (a standard commercially available upgrade material for turbochargers for heavy-duty truck diesel engines) when temperatures exceed the limitations of SiMo cast iron. Previous work clearly showed that CF8C-Plus had better yield strength at 800 and 900°C than HK30Nb. Previous shorter-term creep testing at several different conditions at 700 to 900°C also clearly showed that CF8C-Plus steel had better creep resistance than the HK30-Nb alloy.

Figure 2. A typical diesel turbocharger housing made of SiMo cast iron.

Additional, longer-term creep testing was done this year on the CF8C-Plus steel at 600°C and at 750 to 850°C. At 600°C, one creep test at 275 MPa failed after 7,300 hours, while another one at 180 MPa has exceeded 20,000 hours without rupture. A creep test at 750°C and 100 MPa lasted for 1,784 hours.

By comparison, HK30-Nb steel creep tested at the same conditions lasted less than 100 hours, clearly demonstrating the superior creep resistance of CF8C-Plus steel. A creep test at 800°C and 75 MPa failed after 1,850 hours, while another test at 850°C and 50 MPa ruptured after 2,250 hours. All of these tests exceeded expectations and failed with greater than 25% rupture ductility. Materials comparisons and additional testing will be included to enable CF8C-Plus steel to be evaluated for turbine housings for passenger vehicle gasoline engines.

This year, a diesel genset at the National Transportation Research Center was modified to conduct oxidation coupon testing in the exhaust gas at temperatures of up to 800°C. The initial tests ran for 100 hours at 800°C and suggested much less oxidation of SiMo cast iron and CF8C-Plus steel than found in similar testing in air plus 10% water vapor. Additional and more thorough oxidation testing is planned for next year, but an upgrade of the diesel Genset facility is required.

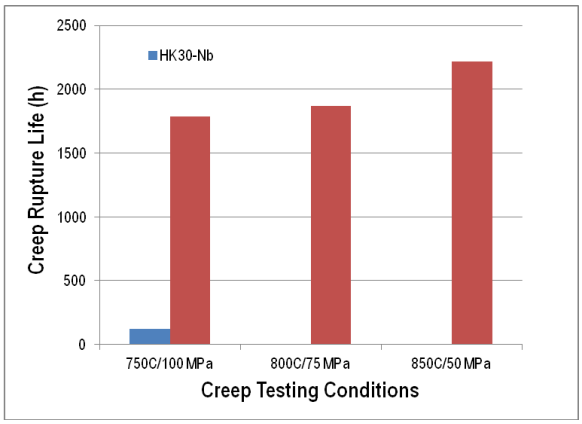

Figure 3. Comparison of creep-rupture lifetimes for CF8C-Plus and HK-30Nb cast stainless steels tested at 750 to 850°C.

Finally, new dialogue and discussions began with Honeywell on opportunities to implement CF8C-Plus stainless steel as an upgrade to several cast-irons used by Honeywell for automotive turbocharger applications. Discussions included a comprehensive review of the physical and mechanical properties of CF8C-Plus and commercial upgrade materials (e.g., HK30-Nb alloy, which is several times more expensive than CF8C-Plus steel). The large advantage in creep-rupture strength and use temperature of CF8C-Plus steel over current automotive turbocharger cast irons, including Ni-resist (which is slightly more expensive than CF8C-Plus steel), is shown in Figure 4. CF8C-Plus steel also could be considered for the turbocharger material for Ford, GM, and Volkswagen automotive engine applications. This focused discussion and effort will continue into fiscal year 2014.

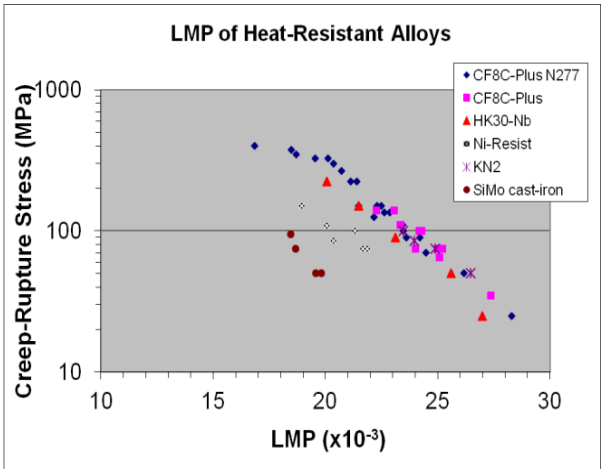

Figure 4. A plot of creep-rupture stress as a function of Larson-Miller parameter for various creep-rupture temperatures and rupture lives for a variety of alloys, including several heats of CF8C-Plus stainless steel, HK30-Nb alloy, and SiMo and Ni-resist cast-irons.

Conclusions

The benefits of CF8C-Plus steel relative to HK-30Nb steel at 700 to 900°C were defined for diesel turbocharger housing applications. Additional long-term creep testing of CF8C-Plus at 600°C and 750 to 850°C continued. CF8C-Plus steel possesses a dramatic increase in creep-rupture strength, maximum use temperature, and oxidation resistance relative to cast-irons, including Ni-resist.

Honeywell has opened up new discussions on the detailed properties advantages of CF8C-Plus steel for automotive turbocharger applications, which should lead to new opportunities for prototyping and commercialization.

Special Recognitions and Awards/Patents Issued

Phil Maziasz received the 2012 William Hunt Eisenman award from the American Society for Metals International in October 2012. The award was given for outstanding success in alloy development of heat-resistant stainless steels and alloys with commercial potential, including CF8C-Plus cast stainless steel.

Project 18518 – Materials for High-Efficiency Engines

Agreement 18571 – Materials Issues Associated with Exhaust Gas Recirculation Systems

M. J. Lance, C. S. Sluder, J. M. E. Storey*, Samuel A. Lewis Sr.*, and H. Z. Bilheux[#]*
Ceramic Science and Technology Group
Oak Ridge National Laboratory
P.O. Box 2008, MS 6068, Bldg. 4515
Oak Ridge, TN 37831-6068
Phone (865) 241-4536; fax: (865) 574-6098; e-mail: lancem@ornl.gov
**Fuels, Engines, and Emissions Research Center #Neutron Sciences Directorate*

DOE Technology Manager: Jerry L. Gibbs
Phone (202) 586-1182; fax: (202) 586-1600; e-mail: jerry.gibbs@ee.doe.gov
ORNL Technical Advisor: J. Allen Haynes
Phone (865) 576-2894; fax: (865) 574-4913; e-mail: haynesa@ornl.gov

Contractor: Oak Ridge National Laboratory, Oak Ridge, Tennessee
Prime Contract No.: DE-AC05-00OR22725

Objectives

- Provide information to industry specialists about fouling deposit properties to enable improved models and potential design improvements to reduce fouling and its impact on the performance of exhaust gas recirculation (EGR) coolers.

Approach

- Assemble EGR engineers from member companies of the Diesel Crosscut Team to serve as an advisory board for this project.
- Obtain and evaluate EGR coolers from industry members that exemplify plugging failure.
- Investigate the influence that cooler geometry has on deposit formation and removal.

Accomplishments

- Completed chemical analysis of industry-provided deposits that exhibited the plugging failure mode and submitted the results in a paper to the Society of Automotive Engineers (SAE).
- Completed paper summarizing neutron tomography investigations on EGR cooler fouling and submitted it to SAE.
- Compared flat to spiral tube geometries and showed a large geometry effect on the deposit microstructure.

Future Direction

- Deposit densification: Establish digital image correlation methodology and measure deposit density changes caused by temperature and water condensation under controlled conditions.
- Deposit permeability: Manufacture porous aluminum tubes and foul them using our tube sampling system and Ford 6.4L engine at NTRC and measure the permeability of the deposit using at least two different gases (air and cetane).

Introduction

High-pressure exhaust gas recirculation (EGR) is the primary NO_x reduction technology used by the diesel industry. Exhaust gas is directed through a heat exchanger (or EGR cooler), where the EGR stream is cooled before being directed back into the engine intake. Inclusion of EGR in the incoming charge reduces the combustion temperature and oxygen content, thereby reducing the oxidation of N_2. The EGR stream also is laden with particulate matter (PM) and hydrocarbons (HC), which, when directed through the EGR cooler, cause deposits to form through thermophoresis and condensation, respectively. Under some combustion and EGR cooler conditions, high concentrations of HCs in the exhaust gas may accelerate the rate of deposition, causing plugging of the EGR cooler channels. Such conditions may occur, for example, during regeneration of diesel particulate filters. As EGR utilization continues to be expanded to new operating regimes, EGR fractions are likely to increase and the coolant used to cool the EGR stream will likely decrease in temperature. These trends may exacerbate the EGR cooler plugging.

In February 2009, a team consisting of engineers responsible for EGR systems was assembled from nine diesel engine manufacturers, Caterpillar, Cummins, Detroit Diesel, Ford, GM, John Deere, Navistar, DAF Trucks, Volvo/Mack, and one heat exchanger supplier, Modine. They were asked what the biggest problem is facing EGR cooling systems and the clear winner was fouling. Over the course of this project, the EGR team has been notified of results generated, has contributed coolers for forensic analysis, and has provided real-world coolers for analysis. To-date studies of EGR fouling have focused mainly on the cause and mitigation of stabilized effectiveness loss, whereby low-HC deposits form but rapidly reach a plateau in thickness (Lepperhoff and Houben 1993, Lance et al. 2013, Sluder et al. 2013, Abarham et al. 2013, Warey et al. 2012, Warey et al. 2013, Bika et al. 2013). Only recently have researchers begun to focus on the origin of EGR plugging (Furukawa et al. 2012). In order to better understand EGR plugging, coolers from applications likely to show the plugging failure mode were requested from the EGR team. These applications tended to require long idling times (e.g., school buses, delivery trucks, etc.). This paper reports on the analysis of deposits contained within these EGR coolers. This study compliments an earlier study where coolers run for "half-useful-life" were requested from industry (Lance et al. 2010). Additionally, preliminary investigations of the role of cooler geometry on EGR fouling were conducted.

Results

Analysis of Industry-Provided Plugging Deposits

Seven fouled EGR coolers that had been run using engine protocols known to produce plugging were provided by industry EGR engineers. Of these coolers, four (coolers #1 through #4) were plugged as evidenced by either the inlet or outlet being completely or partially occluded with deposit. Coolers #5 through #7 were not plugged and contained deposits commonly observed in coolers exhibiting a stabilized effectiveness loss due to fouling, but where exhaust gas may still flow through the cooler. With the exception of coolers #3 and #6, all of the coolers had two passes, with the second pass usually operating at a lower coolant temperature than the first pass.

Figure 1 shows the deposit mass per substrate surface area measured on all seven coolers. Individual measurements were taken from three locations (i.e., inlet, middle, and outlet) along the length of each pass. Deposit mass was measured by cutting a single tube into segments 19 mm in length. Each segment was weighed both before and after being heated to 600°C and final cleaning. The deposit mass was established by difference using these measurements. The four plugged coolers exhibited deposits with higher mass than the three unplugged coolers. Cooler #5 was an exception, because it contained a higher-mass deposit than cooler #4. This trend compares well to our previous study on field-aged EGR coolers (Lance et al. 2010) where the two coolers (out of 10) that were plugged also tended to be exhibit higher mass deposits than the unplugged coolers. In that study, unplugged coolers that contained

anomalously high mass deposits also had oil, hydrated metal sulfates, or silicate debris, which accounted for most of the mass of the deposit. It is possible that similar substances may be present in cooler #5. The plugged coolers contained a deposit mass averaged at over 10 mg/cm^2, with the outlet of cooler #1 reaching nearly 50 mg/cm^2.

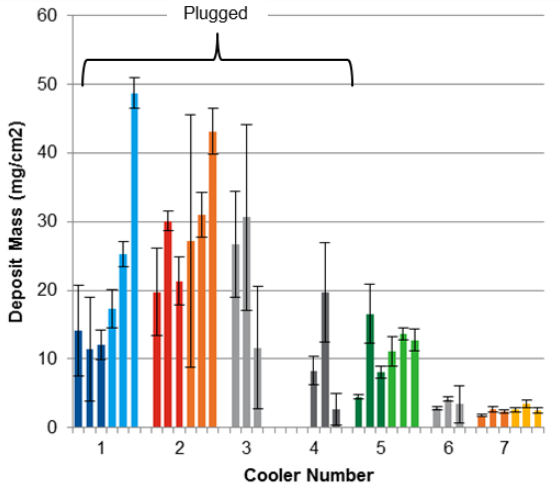

Figure 1. Deposit mass per unit area for each cooler measured from left to right at the inlet, middle, and outlet. The second pass is designated by a lighter color than the first pass. Error bars are one standard deviation of three measurements.

Deposits in the second pass tended to have higher masses than the deposits in the first pass. This tendency is expected, because the lower coolant temperature in the second pass would increase both the rate of thermophoretic deposition of PM and HC condensation. This effect was particularly evident with cooler #4, which contained only a dusting of PM in the first pass (i.e., less than 0.05 mg/cm^2), which suggests that this cooler was operated with a relatively high wall temperature in the first pass.

Deposits collected from the four plugged coolers were further studied using thermogravimetric analysis. Analyses were conducted by heating samples in pure N_2 and subsequently in air up to 700°C at 5°C/min using a Q5000IR thermogravimetric analysis (TA Instruments). The volatile content of each deposit was estimated by measuring the weight loss of the deposit following heating in pure N_2. The ash content was estimated by measuring the remaining weight after complete combustion in air. These measurements are shown in Table 1. The deposit from cooler #1 contained the highest volatile fraction and almost no ash. This deposit was shiny and brittle and left no sooty residue on surfaces. Thus, this deposit was similar in nature to a lacquer coating. The EGR engineer who provided this sample described it as the result of a 65-hour test of an EGR valve sticking where the EGR valve and throttle were forced open and the engine run at low idle with retarded injection timing.

Cooler #2 contained a deposit that was oily and sticky and smelled like oil. The high ash content indicates the presence of oil in the deposit, possibly from an oil seal leak upstream of the EGR cooler.

The deposit from cooler #3 was similar to cooler #1 because it also contained shiny lacquer-like shards interspersed with soot. The deposits in this cooler had little ash content. This deposit tended to stick to surfaces similar to the deposit from cooler #2.

The deposit from cooler #4 was different from the first three in that it was dry and powdery, which is similar to EGR deposits collected under controlled laboratory conditions with low HC (Lance et al. 2009). These deposits had the lowest volatile content.

Table 1. Compositions and descriptions of the deposit collected from the four plugged coolers.

Cooler #	Volatile %	Ash %	Visual Description
1	78	0	Shiny, brittle, lacquer-like
2	59	13	Oily, tacky
3	55	1	Tacky, lacquer-like shards
4	26	8	Dry, powdery

The deposits from the plugged coolers also were optically examined to provide insight into their physical structure at elevated temperatures. The deposits were individually heated in air using a microscope heating stage (Linkam TS1500) and observed with an optical microscope. The deposit from cooler #1 appeared to melt at approximately 50°C and started bubbling around 150°C, indicating that

the deposit was experiencing out-gassing of semi-volatile species. Similarly, the lacquer-like shards in the deposit from cooler #3 started melting at about 100°C, slightly higher than that from cooler #1. These observations confirm that these deposits are likely to be viscous fluids at typical EGR cooler wall temperatures.

The derivative weight loss curves of the four deposits measured in air up to 700°C are shown in Figure 2. Deposits from coolers #1 and #3 behaved similarly, with volatilization of HC centered around 200°C and oxidation of the remaining deposit at 525°C. The deposit from cooler #2 lost volatiles centered at 250°C and oxidized over a broad range starting from about 400°C to above 600°C. Deposits from cooler #4 exhibited significantly different behavior, showing little volatile loss and oxidation at much lower temperatures, starting at about 350°C and completing by 520°C. More significantly, this deposit also exhibited sudden rapid weight losses, which correspond to the large spikes in Figure 2. These rapid weight losses persisted even after the volatiles were removed by heating to 700°C in N_2 prior to heating in air.

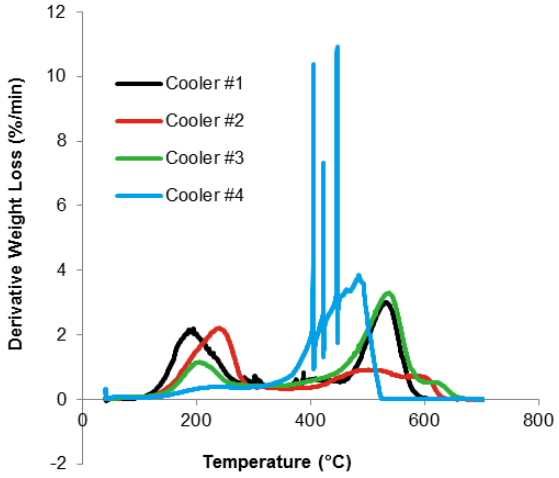

Figure 2. The first derivative of the weight loss versus temperature of the four cooler deposits.

In order to better understand the origin of the rapid weight losses of deposits from cooler #4, some deposit was heated in air using the microscope heating stage. During this process, a video of the oxidation was collected using an infrared camera (Radiance, Amber Engineering) from which the snapshot shown in Figure 3 was extracted. The bright spot in the image is from heat given off during rapid local oxidation of the deposit. The deposit near the hot spot rapidly shrinks in size, which produces the rapid weight losses shown in Figure 2. Therefore, this deposit is self-combusting to a degree and must contain relatively large amounts of oxygenated species that are not readily volatilized.

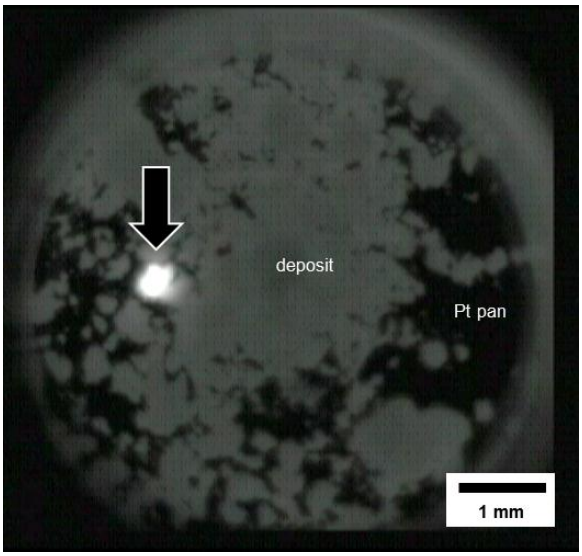

Figure 3. A snapshot extracted from a video of the infrared light emitted during oxidation of the deposit from cooler #4. The arrow points to a local temperature elevation.

Thermal desorption-pyrolysis gas chromatography-mass spectrometry was performed on the four deposits. Figure 4 shows the GC trace from the deposit from cooler #1, which was pure lacquer. The peaks corresponded to variants of 2 to 4-ring polycyclic aromatic hydrocarbons (PAHs) and oxygenated PAHs with a narrow range of melting/boiling points. No paraffinic or oil peaks were present. This deposit chemistry is representative of species collected from low-temperature combustion regimes that have not lost all of the hydrogen necessary to form PM.

In contrast to the lacquer deposit, the oily deposit from cooler #2 was mostly composed of high molecular weight paraffins, which indicates that this sample was mostly oil. In addition,

there were some aromatic species commonly found in the EGR PM deposits.

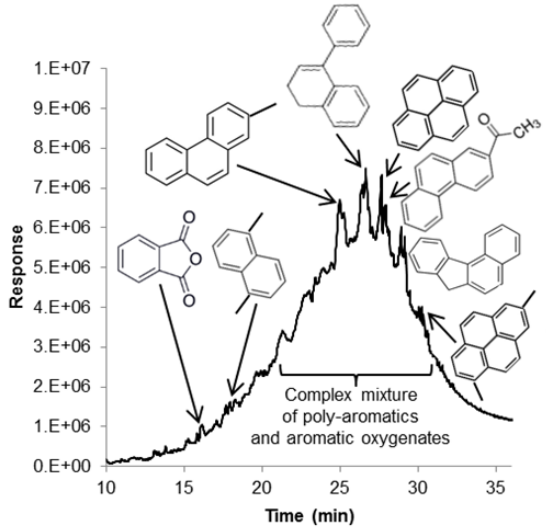

Figure 4. GC trace from the deposit collected from cooler #1. Selected molecular species measured by MS are shown.

The deposit from cooler #3 contained a chemical species that was a mixture of those detected in cooler deposits #1 and #2. The PAHs detected in this deposit were, on average, a higher molecular weight than those in the deposit from cooler #1, which may explain the higher melting temperature of the lacquer-like shards described above.

Finally, cooler #4 contained similar HC species to deposits from coolers #1 and #3, but at far lower concentrations and more dispersed within the soot. The local heterogeneous oxidation observed in Figure 3 was likely caused by these oxygenated PAHs feeding the combustion.

Physical Properties of Lacquer-Like Deposits

As described above, cooler #1 was substantially plugged with a lacquer-like deposit with almost no PM. As shown in a picture taken of the outlet diffuser in Figure 5, much of the deposit appeared to have melted and flowed down the cooler, collecting at the outlet where the deposit reached a thickness of 1 cm. This cooler provided a unique opportunity to measure physical properties of this type of deposit because samples with controlled dimensions necessary for various property measurements could be readily made.

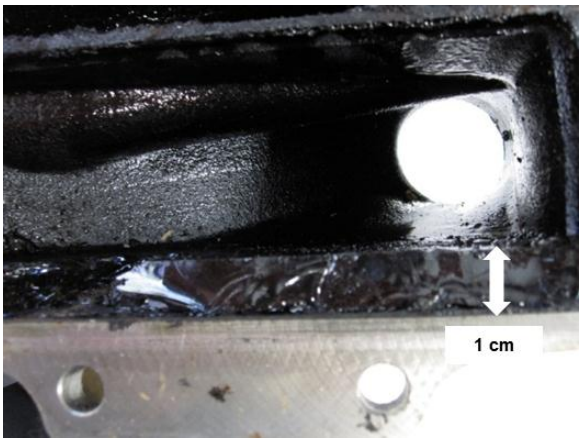

Figure 5. The outlet diffuser of cooler #1, which contained a centimeter-thick, lacquer-like deposit.

Disks with a diameter of 1 and 2-mm thick were machined from the deposit in cooler #1 (shown in Figure 5). The softening point of the deposit was measured using a Q400 thermomechanical analyzer (TA Instruments) by applying a 20-mN load using a flat punch onto the sample disk and measuring the displacement of the punch as a function of temperature. The lacquer-like deposit was found to soften at 27°C, just slightly above room temperature. This compares well to the visual observation of the melting point described above. This low temperature will be easily reached during engine operation, potentially allowing the deposit to flow through the cooler forming thick deposits (Figure 5).

In order to better understand the effect the lacquer-like deposits have on the thermal effectiveness of EGR coolers, the thermal conductivity was measured. Thermal conductivity (K) can be calculated using the equation:

$$K = \alpha \rho C_p, \qquad (1)$$

where α is the thermal diffusivity, ρ is the density, and C_p is the heat capacity. Thermal diffusivity was measured on the extracted 2-mm thick disks using the xenon flash lamp method as described in Lance et al. (2009). Density was

measured using Archimedes' principle (Watanabe and Kato 2004) and the heat capacity was measured as a function of temperature using a Q20 differential scanning calorimeter (TA Instruments) by first cooling the sample to -95°C and heating to 35°C below the onset of lacquer volatilization. Table 2 compares the thermal properties of the lacquer-like deposit to a laboratory-generated deposit composed of low-HC PM from Lance et al. (2009). The thermal conductivity of the lacquer-like deposit was nearly five times that of the low-HC deposit. The biggest cause of this difference was the density, which was about 34 times higher with the lacquer deposit than the porous low-HC deposit. Moreover, the thermal conductivity and density of the lacquer is higher than that of typical hydrocarbons (Sluder et al. 2008). This relatively high thermal conductivity suggests that there is elemental carbon (PM) dispersed in the lacquer, which enhances the heat transfer.

Table 2. Thermal properties at room temperature of the lacquer-like deposit from cooler #1 and a low-HC PM deposit from Lance et al. (2009).

Deposit	Thermal Diffusivity (cm^2/s)	Density (g/cm^3)	Heat Capacity (J/gK)	Thermal Conductivity (W/mK)
Lacquer	0.0011	1.176± 0.004	1.589	0.202
PM	0.014± 0.006	0.035± 0.003	0.851± 0.030	0.041± 0.014

Discussion of EGR Cooler Plugging

The four plugged coolers studied here contained deposits that were all unique, which shows that there are multiple processes that can result in plugging in an EGR cooler. The driving force for formation of EGR deposits is the temperature difference between the hot exhaust gas and the cold metal wall, which causes PM to deposit on the metal through thermophoresis and HC to condense. The deposition rate usually reaches a plateau in the first few hours of operation, causing the loss of thermal effectiveness of the cooler to stabilize (Lepperhoff and Houben 1993). The main cause of this stabilization is the low thermal conductivity of the deposit, which is just slightly higher than stagnant air. As the deposit increases in thickness, the surface temperature increases due to the inability of the heat in the gas to be transferred through the low-K deposit to the metal. This reduces the temperature gradient between the gas and the deposit surface, thereby reducing the rate of thermophoretic deposition and leading to stabilization. In this way, deposit growth in EGR coolers is self-limiting.

The critical difference between a stabilized deposit and a plugging deposit is the thermal conductivity, which, for the lacquer-like deposit measured here, was 5 times higher than the low-HC, low-density PM deposit (see Table 2). The higher deposit thermal conductivity results in a greater deposit thickness for a given surface temperature rise. If this greater thickness exceeds the available space within the cooler gas channels, a plug results.

For cooler #1, the conditions appear to have favored the condensation of PAHs at a high enough rate than any PM was quickly immersed in HC, preventing the formation of a high-porosity, low-thermal conductivity deposit. The dew point of these species is well above the coolant temperature typically used in EGR coolers (40 to 90°C) and condensation would have continued as the deposit thickened, given the higher thermal conductivity. The composition of the deposit was similar to that described by Furukawa et al. (2012), who formed lacquer deposits using phenolic or polyaromatic ingredients, along with formaldehyde as a reactive HC and nitric acid as a catalyst. It was found that all three of these components were necessary to promote a polymerization reaction, which formed a lacquer deposit. The oil discovered in cooler #2 must have come from a leak, possibly in the turbocharger assembly, that flowed into the EGR cooler, mixing with PM from the exhaust gas. This mixture formed a slurry that eventually plugged the cooler. The higher thermal conductivity of the oil would have increased the rate of thermophoretic deposition over a typical low-HC, PM-based deposit. In this process, the soot likely acted to increase the viscosity of the slurry. Oil also was discovered in one cooler during our previous study of industry-provided coolers (Lance et al. 2010); therefore, this failure mode may be fairly common in the field.

The deposit in cooler #3 apparently underwent the same chemical reactions as that in cooler #1, because the lacquer-like deposit was present. However, oil also was found, which complicates the explanation of the origin of this deposit. Furukawa et al. (2012) were unable to produce lacquer deposits using diesel fuel as a precursor; therefore, oil also should not lead to lacquer formation. It can only be speculated that both of the plugging mechanisms that occurred in coolers #1 and #2 were happening in cooler #3, possibly at different times.

Finally, cooler #4 contained similar PAH species to coolers #1 and #3, but at far lower concentrations and more dispersed by PM. This deposit also exhibited more oxygenation of the PAHs, which resulted in the heterogeneous oxidation shown in Figure 3. It is speculated that the engine was mostly run under conditions producing PM with low amounts of HC and only sporadically under conditions conducive to the formation of large amounts of PAHs. The high concentration of PM in the deposit may be hindering the gas-liquid phase reaction (Furukawa et al. 2012) that produced lacquer-like deposits in coolers #1 and #3.

Based on these observations, the following recommendations can be made for reducing the likelihood of plugging in EGR coolers:

5. The hydrocarbon content in the exhaust can be reduced by using a catalyst upstream of the EGR cooler, which was shown by Sluder et al. (2008) to significantly reduce HC levels in the EGR deposit.
6. The EGR coolant temperature must be maintained at temperatures that exceed the dew points of the hydrocarbons leading to lacquer formation. This could be accomplished by increasing coolant temperature during long periods of engine idling, thereby reducing the condensation rate of lacquer precursors.
7. The inlet gas temperature could be significantly increased for a period of time in order to partially volatilize the deposit, which may lead to deposit spallation (Lance et al. 2013).

Effect of Cooler Geometry on Fouling

In order to test the effect of turbulation on deposit formation and removal, an individual tube with a spiral groove harvested from an Ensa cooler was fouled, using our tube sampling system, and compared to a flat tube (see Figure 6), using the same engine operating conditions. The tube with the spiral groove had a deposit that was substantially rougher, with clear evidence of deposit removal. Some removal occurred at the peak of the spiral groove, which compares well to previous observations on industry-provided deposits {Lance, 2010 #1791}. Additionally, far away from the groove, a deposit appears to have been removed. This suggests a large effect of tube turbulation on deposit formation and removal. Future work will focus on introducing dimples onto square tubes and modeling the flow and shear forces with computational fluid dynamics.

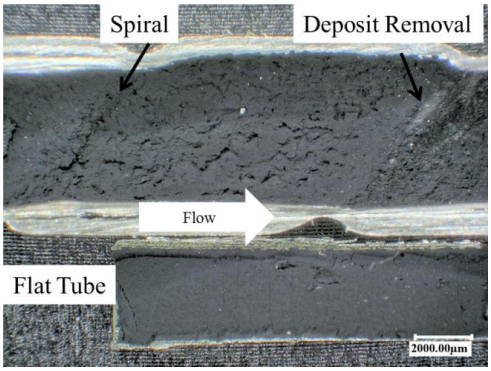

Figure 6. Deposit surface formed on a spiral tube (top) and a flat tube (bottom).

References

Abarham, M. et al., 2013, "CFD analysis of particle transport in axi-symmetric tube flows under the influence of thermophoretic force," *International Journal of Heat and Mass Transfer*, 61, 94–105.

Bika, A. S. et al., 2013, "An Investigation of Diesel EGR Cooler Fouling and Effectiveness Recovery," SAE International.

Furukawa, N., S. Goto, and M. Sunaoka, 2012, "On the mechanism of exhaust gas recirculation valve sticking in diesel engines," *International Journal of Engine Research*.

International, A., 2013, "Standard Test Methods for Density of Compacted or Sintered Powder Metallurgy (PM) Products Using Archimedes' Principle," ASTM International: West Conshohocken, PA.

Lance, M. J. et al., 2009, "Direct Measurement of EGR Cooler Deposit Thermal Properties for Improved Understanding of Cooler Fouling," SAE International.

Lance, M. J. et al., 2010, "Characterization of Field-Aged EGR Cooler Deposits," *SAE Int. J. Engines*, 3, (2), 126–136.

Lance, M. J. et al., 2013, "Microstructural Analysis of Deposits on Heavy-Duty EGR Coolers," SAE International.

Lepperhoff, G. and M. Houben, 1993, "Mechanisms of Deposit Formation in Internal Combustion Engines and Heat Exchangers," SAE (931032).

Sluder, C. S. et al., 2008, "Hydrocarbons and Particulate Matter in EGR Cooler Deposits: Effects of Gas Flow Rate, Coolant Temperature, and Oxidation Catalyst," *SAE Int. J. Engines*, 1, (1), 1196–1204.

Sluder, C. S. et al., 2013, "Removal of EGR Cooler Deposit Material by Flow-Induced Shear," *SAE Int. J. Engines*, 6, (2), 999-1008.

Warey, A. et al., 2012, "A One-Dimensional Model for Particulate Deposition and Hydrocarbon Condensation in Exhaust Gas Recirculation Coolers," *Aerosol Science and Technology*, 46, (2), 198–213.

Warey, A. et al., 2013, "Influence of water vapor condensation on exhaust gas recirculation cooler fouling," *International Journal of Heat and Mass Transfer*, 65, 807–816.

Watanabe, H. and H. Kato, 2004, "Thermal conductivity and thermal diffusivity of twenty-nine liquids: Alkenes, cyclic (alkanes, alkenes, alkadienes, aromatics), and deuterated hydrocarbons," *Journal of Chemical and Engineering Data*, 49, (4), 809–825.

Publications and Presentations

Published

Abarham, Mehdi, Parsa Zamankhan, John W. Hoard, Dan Styles, C. Scott Sluder, John M. E. Storey, Michael J. Lance, and Dennis Assanis, 2013, "CFD analysis of particle transport in axi-symmetric tube flows under the influence of thermophoretic force," *International Journal of Heat and Mass Transfer*, 61, 94–105.

Bilheux, H., K. Crawford, L. Walker, S. Voisin, M. Kang, M. Harvey, B. Bailey, M. Phillips, J. C. Bilheux, K. Berry, J. Anknera, J. Warren, J. Nanda, S. Pannala, and M. Lance, 2013, "Neutron imaging at the Oak Ridge National Laboratory: present and future capabilities," *7th International Topical Meeting on Neutron Radiography, Physics Procedia*.

Lance, Michael J., John Storey, C. Scott Sluder, Harry Meyer III, Brad Watkins, Michele Kaiser, and Ponnaiyan Ayyappan, 2013, "Microstructural Analysis of Deposits on Heavy-Duty EGR Coolers," SAE Technical Paper 2013-01-1288.

Sluder, C. Scott, John Storey, Michael J. Lance, and Teresa Barone, 2013,"Removal of EGR Cooler Deposit Material by Flow-Induced Shear," SAE Technical Paper 2013-01-1292.

Storey, John M. E., C. Scott Sluder, Michael J. Lance, Daniel J. Styles, Steven J. Simko, 2013, "Exhaust Gas Recirculation Cooler Fouling in Diesel Applications: Fundamental Studies of Deposit Properties and Microstructure," *Heat Transfer Engineering*, 34, (8-9), 655–664.

Submitted

Lance, Michael J., John M. E. Storey, Samuel A. Lewis, and C. Scott Sluder, 2013, "Analysis of Lacquer Deposits and Plugging Found in Field-Tested EGR Coolers," SAE Paper 14HX-0057.

Lance, Michael J., Hassina Z. Bilheux, Jean-Christophe Bilheux, Sophie Voisin, Joe Stevenson, and C. Scott Sluder, 2013, "Neutron Tomography of Exhaust Gas

Recirculation Cooler Deposits," SAE Paper 14HX-0056.

Sluder, C. Scott, John M. E. Storey, and Michael J. Lance, 2013, "Effectiveness 'Stabilization' and Plugging in EGR Cooler Fouling" submitted to *SAE International Journal of Engines*.

Sluder, C.S., J. M. E. Storey, and M. J. Lance, 2013, "Temperature and Thermal Conductivity of Soot Deposits in EGR Coolers: Measurements and Challenges," submitted to *Heat Transfer Engineering*.

Project 18518 – Materials for High-Efficiency Engines

Agreement 23284 – Friction Reduction Through Surface Modification: Integrated Surface Texturing and Coating

Peter J. Blau
Oak Ridge National Laboratory
P.O. Box 2008, MS 6063
Oak Ridge, TN 37831-6068
Phone (865) 574-5377; fax: (865) 574-4913; e-mail: blaupj@ornl.gov

Stephen M. Hsu
George Washington University, Exploration Hall
20101 Academic Way
Ashburn, VA 20147
Phone (703) 726-8365; e-mail: stevehsu@gwu.edu

DOE Technology Manager: Jerry L. Gibbs
Phone (202) 586-1182; fax: (202) 586-1600; e-mail: jerry.gibbs@ee.doe.gov
ORNL Technical Advisor: J. Allen Haynes
Phone (865) 576-2894; fax: (865) 574-4913; e-mail: haynesa@ornl.gov

Contractor: Oak Ridge National Laboratory, Oak Ridge, Tennessee
Prime Contract No.: DE-AC05-00OR22725

Objectives

- To develop and compare surface engineering methods for applying friction-reducing, micro-scale patterns (textures) to the sliding surfaces of diesel engine components.
- To demonstrate the frictional benefits of applying surface texturing to curved surfaces like those on piston rings, cam lobes, and connecting rod bearings.
- To provide guidelines to engine makers on the application of engineered surfaces.

Approach

- Fabricate and optimize integrated surface texture designs on diesel engine piston rings and curved surfaces that simulate cam lobes and connecting rod bearing inserts.
- Investigate surface texturing using micro-lithography and compression texturing.
- Test for efficacy in friction reduction using laboratory tests, including ASTM standards.
- Explore methods of preserving textures by using wear-resistant coatings.

Accomplishments

- Published a literature review on the production and use of patterned surfaces to control friction and wear behavior of a variety of lubricated interfaces and applications.
- Demonstrated the ability to pattern curved piston ring surfaces and discovered an optimal shape factor for achieving lowest friction with combined circular and elliptical dimples.
- Developed a one-step method that forms curved bearing surfaces and textures them.

Future Direction

- Apply coatings to protect textures from wear and maintain longer-term functionality.
- Explore the feasibility of micromachining technology to create effective textures.

Introduction

The U.S. Department of Energy has focused research and development efforts on achieving a 50% increase in freight efficiency (measured in ton miles per gallon) for heavy vehicles. This multi-pronged approach includes a reduction in parasitic engine and drivetrain losses, novel waste heat recovery systems, and the use of lightweight materials. The current project is aimed at reducing friction losses and wear in the moving parts of diesel engines by applying micro-scale features (textures) and coatings.

Friction between the piston ring and cylinder bore is responsible for as much as 40 to 50% of the total engine friction losses, the proportion depending on engine speed and design. Engine bearings and valve train friction contributes about 15% each to these losses. Options for reducing friction include advanced lubricant formulations, reduction in churning losses (low viscosity oils), tighter manufacturing tolerances on bearing components, and application of surface engineering. Here, surface engineering refers to the design of chemical, physical, metallurgical, and/or geometrical features of solid surfaces in order to improve desired functional characteristics such as low friction and low wear.

The application of patterns (sometimes called surface textures) is among the most promising advances in surface engineering (Figure 1). Friction-controlling features work by altering the flow of lubricants through the confined interface and by trapping harmful debris particles. Textures can be produced in numerous ways, including micro-machining, laser ablation, roll-forming, and photo-lithography (Blau 2012). Two different methods of texturing are being investigated in the current project. In addition, it is possible to combine texturing with coatings or other surface treatments to realize greater benefits.

Approach

This joint effort teams the micro-texturing expertise of a subcontractor (Professor S. M. Hsu, George Washington University [GWU]) with Oak Ridge National Laboratory's (ORNL's) experience in tribology and unique friction testing capabilities. In addition, ORNL is exploring a second approach to texturing.

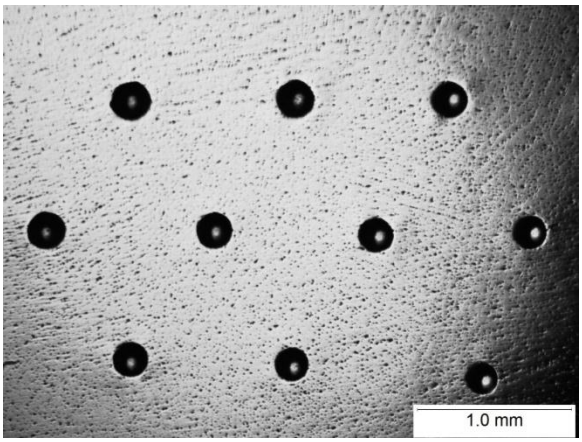

Figure 1. Array of spherical impressions on a CDA 932 bronze-bearing surface formed by pressing an array of high-precision steel spheres.

Surface engineering in this project uses two main methods: photo-lithography (GWU) and mechanical compression (ORNL). Frictional effects on lubricated surfaces are being investigated using four kinds of bench-scale tests: reciprocating sliding friction with a piston ring segment on cast iron, reciprocating ball-on-flat, block-on-ring, and a turning cylinder against either a flat or curved surface. This suite of tests simulates engine component geometries such as the piston-ring-on-cylinder liner, a cam lifter, and a connecting rod large end bearing insert. Spectrum loading procedures mimic the changes in the lubrication regime that occurs during typical engine operation.

During fiscal year (FY) 2014, friction-reducing patterns will be coated to prolong texture retention. A limited study of the use of commercial micro-machining technology to produce textures is planned for FY 2014. The project's final report will contain a summary of the friction data and a set of bearing surface design guidelines for engine makers.

Progress during FY 2013

A primary finding, based on a review of past work in this area (Blau 2012), was that patterns and processes must be matched to the application. Otherwise, there may be no benefit, or even negative effects on friction and wear.

GWU research on micro-lithographically textured coupons indicated that, in general, a mixture of shapes can produce greater frictional benefits than circles or ellipses used alone (Figure 2). Experiments were conducted to optimize aspect ratios of features to produce the lowest friction. Additional GWU results and recommendations are given later in this report.

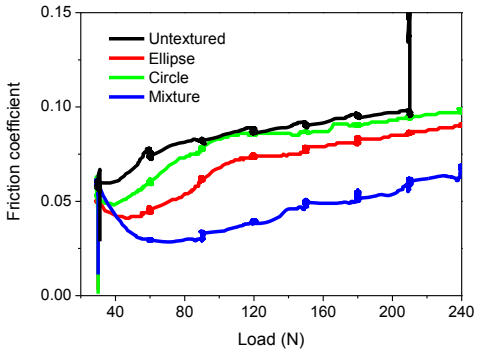

Figure 2. Mixtures of circles and ellipses resulted in a lower friction than either shape alone (GWU data).

During FY 2013, ORNL continued to develop a wire compression-texturing (CTx) process that can produce curved and textured surfaces in one step. CTx using high-strength wire meshes could produce a complex pattern of grooves and dimples (see Figure 3). Grooves serve as feeder channels and alternating oval cross-over features serve as elliptical dimples. Vertical scanning interferometry was used to measure the texture features such as those in Figure 3. A sample vertical scanning interferometry image is shown in Figure 4.

Using servo-hydraulic loading and a custom curved die, the feasibility of simultaneously forming and texturing a curved bearing insert was demonstrated (see Figure 5). These contoured test strips were designed to fit against rotating alloy steel shafts that are used in lubricated friction tests, which are described later.

Applied load and displacement data for CTx strip forming trials were correlated with pattern depths to determine how forming conditions affected feature micro-geometry and areal coverage of grooves and dimples. Specimens with CTx surfaces then were friction-tested using a variable-load bearing tester to simulate the changing loads on engine components such as a connecting rod bearing or cam lobe.

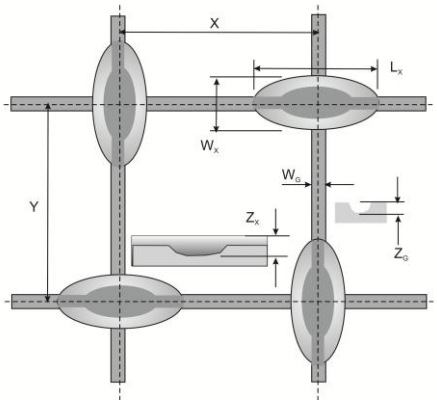

Figure 3. Characteristics of a CTx surface that affect lubricant flow and film thickness.

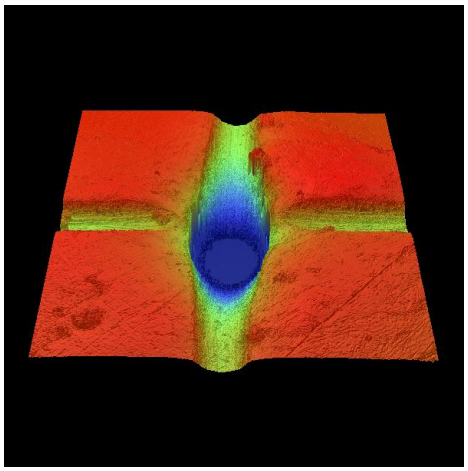

Figure 4. Vertical scanning interferometry image of a crossover point showing the intersection of lubricant channels and a deeper elliptical depression.

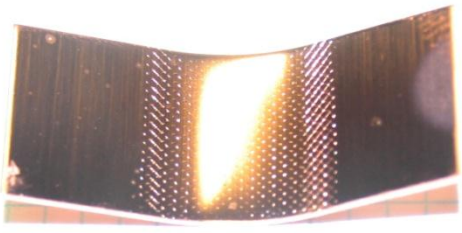

Figure 5. Curved strip of CDA 260 brass formed with a textured pattern on the load bearing surface.

In the FY 2012 annual report, it was shown that the coarseness of the CTx pattern determined whether lubricated friction was higher or lower than non-textured, smooth surfaces. Results from a set of variable load tests (load range: 32 to 100 N) of rotating alloy steel shafts against CTx curved strips are shown in Figure 6. The labels at the bottom of the chart show the number of grooves in a 25 × 25-mm square area. The finer pattern (50 × 50) produced much lower and consistent friction coefficients.

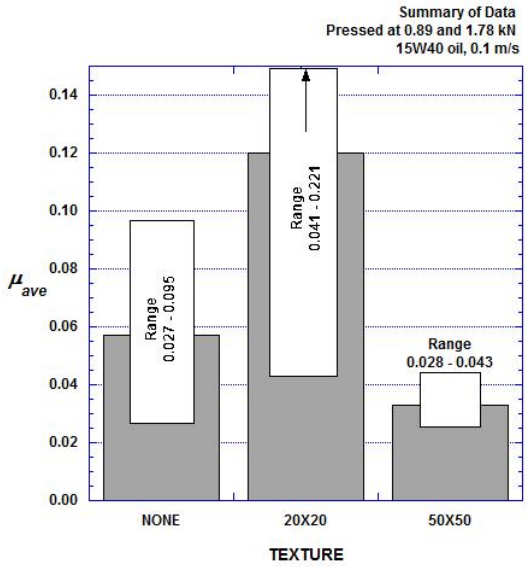

Figure 6. Average (gray bar) and range (white bar) of friction coefficients in spectrum-load tests of CTx curved surfaces against AISI 8620 steel in 15W40 oil. Specimens were shaped as shown in Figure 5.

When lubricant films fail, frictional heating can cause localized surface degradation and subsequent wear. During the summer of 2013, an undergraduate mechanical engineering student (N. Davies) from the University of Alabama conducted a study of four popular frictional heating models using a set of sliding loads and speeds. Various material combinations, including those in this project, were considered. The study concluded that even when using the same material properties and sliding conditions, frictional heating (flash temperature) predictions vary widely. An ORNL report was prepared and is under review at the time of this writing.

Progress at George Washington University

FY 2013 marks completion of the GWU subcontract and a final report is in preparation at the time of this writing. The report will describe successful production of curved textured surfaces using micro-lithography, provide data on the effects of texture feature shapes and combinations of shapes on friction reduction, and give general guidelines for reducing friction through surface modification by texturing certain engine components.

During FY 2013, GWU conducted friction experiments on combinations of circular and elliptical features to determine the value of the optimal parameter (D) for friction reduction. Here, D is defined as the ratio of the diameter of the circular dimples in the pattern to the short axis of the ellipses (at constant aspect ratio for the ellipses). Using a commercial reciprocating wear testing machine, piston ring segments with various D values were tested in a stabilized mineral oil against cross-hatched bore segments cut from a production diesel engine liner.

A step-loading test procedure was used to measure the friction coefficient versus load under a 24-Hz oscillating frequency. Results are shown in Figure 7. The data indicate that the optimal D parameter value was 4.2 ± 0.02 for these sliding conditions. The top curve, which ends with a seizure event at 210 N load, is the non-textured baseline case. Friction coefficient reductions as high as 75% could be achieved under some of the test conditions

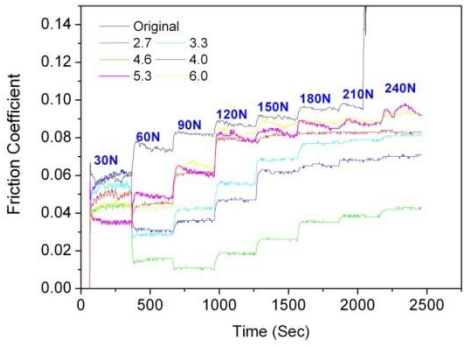

Figure 7. Effects of pattern geometry on reciprocating friction coefficient at various applied loads.

Based on results from friction tests, including a four-ball tester, a ball-on-three flats rig, a pin-on-disk device, and a ring-on-block tester, a basic design guideline was established for using textured surfaces in engine components that experience three primary lubrication regimes (see Table 1).

The guidelines summarized in relative terms in Table 1 serve as a starting point for integrated surface design, but must be tailored to specific duty cycles of the engine components of interest and to the initial surface roughness. Because a relatively small percentage of the bearing surface is textured, the bearing area roughness will dictate both the baseline friction level and the potential for friction reduction by texturing.

Table 1. Guidelines for Selecting Dimple Shapes and Sizes to Reduce Friction.*

Lubrication Regime	Dimple Shape	Area Density/ Depth/Size	Pitch (parallel to S. D./ perpend. to S.D.)
HD	C	H/S/L	M/M
EHL	C+E	M/M/M	L/L
BL	E	L/D/M	L/M

*Key: *HD* = hydrodynamic, *EHL* = elastohydrodynamic, *BL* = boundary lubrication; Shapes: C = circle, E = ellipse, Area Density: H = high, M = medium, L = low; Depth: S = shallow, M = medium, D = deep; Size: L = large, M = medium; S. D. = sliding direction, M = medium, L=large

Work Plans for FY 2014

The following tasks are planned for ORNL in FY 2014:

- Lubricated sliding friction experiments will continue using a typical diesel oil (15W40) and a lower viscosity oil (0W30) to determine whether textures can offset the effects of using lower viscosity oils in engines.
- Exploration of commercial micro-machining techniques as an alternative texturing method to micro-lithography and CTx.
- Application of thin films or coatings to protect patterns and extend their operating life.

Conclusions

- The feasibility of microlithography to texture piston rings has been demonstrated under a subcontract to GWU.
- Combinations of circles and ellipses can be optimized for friction reduction by as much as 75%, but achieving these benefits requires optimization of shapes, sizes, orientation, and feature surface roughness for each application.
- Compression texturing by fine mesh imprints can reduce friction relative to polished surfaces under variable load, lubricated tests, but coarser mesh patterns increased friction, confirming the need to optimize design. Results from both ORNL and GWU tests suggest the need to optimize texture designs to fit the specific engine components of interest.
- In FY 2014, research will investigate coatings to protect textures from wear and the possible use of micro-machining as an alternative to micro-lithography and CTx.
- Findings and data from this work will be summarized in a final report and communicated to engine makers.

References

Blau, P. J., 2012, *Use of Textured Surfaces to Mitigate Sliding Friction and Wear of Lubricated and Non-Lubricated Contacts*, ORNL Tech Report ORNL/TM-2012/20, 19 pp.

Blau, P. J., K. M. Cooley, and D. L. Erdman, 2014, "Effects of Indentation and Compression Texturing on the Lubricated Friction of Non-Ferrous Surfaces under Spectrum Loading," presentation accepted for the *2014 Annual Meeting, Society of Tribologists and Lubrication Engineers (STLE)*, May 18–22, 2014.

Davies, N. R. and P. J. Blau, 2013, *Comparison of Frictional Heating Models*, ORNL Tech Report ORNL/TM-2013/398, 14 pp.

Project 18518 – Materials for High-Efficiency Engines

Agreement 23425 – Lightweight Heavy-Duty Engine

G. Muralidharan, A. Shyam, M. P. Brady, R. R. DeHoff, and T. R. Watkins
Materials Science and Technology Division
Oak Ridge National Laboratory
P.O. Box 2008
Oak Ridge, TN 37831-6068
Phone (865) 574-4281; fax: (865) 574-4357; e-mail: muralidhargn@ornl.gov

Roger England
Cummins Technical Center
1900 McKinley Ave.,
Columbus, IN 47201
Phone (812) 377-3135; e-mail: roger.d.england@cummins.com

DOE Technology Manager: Jerry L. Gibbs
Phone (202) 586-1182; fax: (202) 586-1600; e-mail: jerry.gibbs@ee.doe.gov
ORNL Technical Advisor: J. Allen Haynes
Phone (865) 576-2894; fax: (865) 574-4913; e-mail: haynesa@ornl.gov

Contractor: Oak Ridge National Laboratory, Oak Ridge, Tennessee
Prime Contract No.: DE-AC05-00OR22725

Objectives

- The primary focus of this project is to develop/identify alternate materials for heavy–duty diesel engine exhaust manifolds and pistons that would enable improvements in high-temperature capabilities of these components and facilitate improvements in brake thermal efficiency (BTE) and power density.

Approach

- Evaluation of component design, materials, and manufacturing process for selected components with an impact on engine BTE.
- Evaluation of alternate materials, materials testing, and component design modification.
- Prototype component fabrication and testing.

Accomplishments

- Constrained thermal fatigue tests have been completed on several candidate alloys for exhaust manifolds.
- Oxidation testing has been completed up to a period of 5,000 hours on several candidate alloys for exhaust manifolds.
- Coatings with lower thermal conductivity have been processed on 4,140 steel pistons.

Future Direction

- Identify most promising alloy for exhaust manifold and cast trial component.
- Identify candidate substrate-coating material combinations.

Introduction

This project with Cummins supports development of next generation, heavy-duty diesel engines that can achieve a 50% or better BTE. The fuel efficiency roadmap for the 50% BTE engine considers six main areas for efficiency improvement in the baseline engine, several of which involve making more efficient use of thermal energy (i.e., heat) in the engine. Increased operating temperatures and improved thermal management are expected to enable significant increases in power density, resulting in greater power output for the same sized engine or engine downsizing (or light weighting) for the same power output. However, it is becoming apparent that several key components will be exposed to temperatures beyond the capabilities of current engine and exhaust materials, requiring the availability of the next generation of high-temperature materials to allow the engine to reach the efficiency, commercially viable durability, and emission targets. Because of different combinations of property requirements, new materials technologies specific to the targeted engine components are needed to enable operation in the higher-temperature environment.

A detailed analysis of the development of the high-efficiency engine being envisioned by Cummins showed that a higher-temperature capability in the exhaust system has significant impact on technologies that improve BTE by waste heat recovery from exhaust gases. In addition, an increase in the temperature capability of piston materials also had a positive influence on the efficiency of the next generation diesel engines. Because the current materials (high SiMo cast irons in exhaust manifolds and 4140 steel in pistons) are already operating near their limits of their temperature and strength capabilities, it has been determined that new materials with the right combination of properties are required for these components. Replacement of current materials with new materials that have a higher strength and oxidation resistance at higher temperature also allows redesign of components to have thinner walls for the same stress levels, thus facilitating light weighting and increased power density. It is anticipated that critical technologies (such as waste heat recovery) will not only demand the availability of improved materials to achieve the efficiency targets for the SuperTruck Program in short-term engine efficiency measurements, but will continue to drive development of advanced materials that would enable the manufacture of a durable, commercially viable, high thermal efficiency engine. Table 1 shows the key properties initially identified by the team to be of interest for the two components. These properties will be used for initial screening of new materials for this application and to define the initial test matrix.

Table 1. Components down selected and the critical materials properties of interest.

Component	Critical Material Properties of Interest
Exhaust Manifold	Constrained thermal fatigue strength, elevated temperature strength, high-temperature fatigue strength, creep strength, oxidation resistance, thermal expansion coefficient, specific heat, density, elastic modulus, thermal conductivity, microstructural stability at high temperatures, and the ability to be cast into complex shapes.
Piston	Constrained thermal fatigue strength, high-temperature strength, high-temperature fatigue strength, thermal conductivity, density, specific heat, and oxidation resistance.

Results

Exhaust Manifolds

Several new classes of materials have been identified as alternatives to the high SiMo cast irons currently used in exhaust manifolds. Three major classes of materials are as follows:

1. D5S-austenitic nodular cast iron
2. Cast austenitic stainless steels (chromia-forming)
3. Alumina-forming, cast austenitic stainless steels.

Table 2 shows some example candidates of cast austenitic stainless steels being considered for this application. The ORNL in parenthesis shows that a particular class of alloy was developed at Oak Ridge National Laboratory (ORNL).

Table 2. Compositions of cast austenitic stainless steels being evaluated for application in exhaust manifolds.

Alloy	Type of Alloy	Fe	Cr	Ni	Mn	Mo	Nb	W	Si	C	Remarks
High SiMo Cast Iron	Nodular ferritic cast iron	Bal.			0.3	0.6			4.0	3.45	Baseline alloys
D5S	Nodular austenitic cast iron	Bal.	2	35	0.5				5	1.9	High-performance cast iron
Cast CF8C+	Cast Austenitic	Bal.	19	12.5	4.0	0.3	0.8	0	0.5	0.1	0.25 N
TMA®4705 (ORNL) Typical	Cast austenitic	Bal.	26	23.5	0.6	0.47	0.35	0.28	1.33	0.6	Centrifugal casting data only
TMA®6301 (ORNL) Typical	Cast austenitic	Bal.	24	34.2	1.0	0.02	0.41	0.35	1.22	0.43	Centrifugal casting data only
Cast AFA (ORNL) Typical	Alumina-forming Cast austenitic	Bal.	14	25	2	2	1	1	1	0.45	Vacuum casting data only, Al 3.5 C:0.2-0.5

Two major properties were considered as key for prolonged exhaust manifold life: resistance to constrained thermal fatigue and oxidation resistance. As an initial evaluation of their potential to perform adequately in an exhaust manifold application, constrained thermal fatigue tests and oxidation resistance were evaluated for the baseline high SiMo cast iron and other candidate alloys, including D5S, Cast CF8C+, TMA®4705, and TMA®6301. These results will be highlighted in this report.

Constrained Thermal Fatigue Testing

The test specimens were rigidly constrained in this testing methodology, in a servohydraulic test machine in displacement control. Cyclic stresses were generated by temperature cycling in the gage section of the specimen between specified temperatures and at a specified heating rate. Heating of specimens was achieved by combining several resistance heaters. In addition, a hold time at the maximum temperature in the cycle was introduced to generate a trapezoidal temperature versus time control signal. All reported tests in the present investigation had a maximum temperature of 800°C and a hold time of 60 seconds at the maximum temperature. Heating/ cooling rates of 1°C/second were employed in the reported tests with a feedback loop temperature controller (with proportional, integrative, derivative, and PID control). Precise temperature control (i.e., less than 5°C variation) in the gage section of the specimen was achieved by a Labview® software code. A high-temperature extensometer was placed in the gage section of the specimen and evolution of the stress and strain signals with thermal cycling was continuously recorded. The specimens were cycled to failure. Figure 1 shows results from CTF tests of the six examined cast ferrous alloys. The maximum temperature for the reported tests was 800°C, with heating cooling rates of 1°C/second and a hold time of 60 seconds at the maximum temperature. Arrows in Figure 1 indicate runout specimens, where the tests were terminated prior to failure.

It can be observed in Figure 1 that, as the temperature range (ΔT) increases, the time to failure decreases. This is due to the fact that under constraints, an increase in ΔT directly corresponds to an increase in the stress range during temperature cycling.

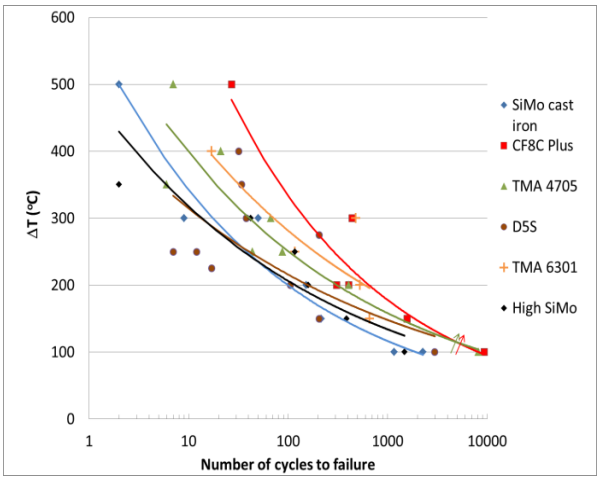

Figure 1. Results from constrained thermal fatigue of cast irons and cast austenitic stainless steels.

The temperature in Figure 1 can be considered to be analogous to stress in S-N curves generated by isothermal load controlled tests. The results in Figure 1 indicate that at high values of ΔT, failure can occur in less than 10 cycles, whereas thousands of cycles are required at a ΔT value of 100°C. Power law fits to the data for the six alloys are also included in Figure 1. Other than D5S, the fits are reasonably good for the other five alloys. The Ni-resistant alloy D5S displayed unusually short CTF lifetimes at intermediate ΔT values of 225 to 250°C. In general, it can be concluded from Figure 1 that alloys that have curves with a longer lifetime at the same ΔT have higher CTF resistance. Accordingly, the higher CTF-resistant alloys have longer CTF lifetimes at the same value of ΔT and/or an increased tolerance for a higher ΔT at a given CTF lifetime. As observed in the figure, cast austenitic steels display better CTF performance than the cast irons (SiMo and D5S) under these testing conditions.

Oxidation Testing

Oxidation tests were conducted by exposing specimens to an environment consisting of air +10 vol. % H_2O. Mass changes were measured by removing the specimens after exposure to 100-hour cycles at 650, 700, 750, and 800°C. Figure 2 shows an example for the specific mass changes as a function of exposure time at 800°C.

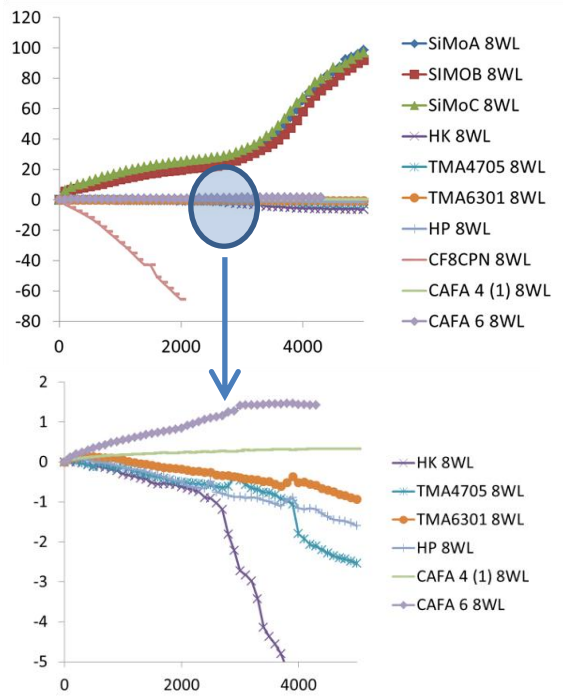

Figure 2. Higher-Ni austenitics show much lower oxidation rates than SiMo cast Fe at 800°C.

Differences can be observed in the behavior of various materials that were tested at this temperature. SiMo cast iron shows a significant growth of thick oxide scales, but minimal spallation was observed. Cast austenitic alloys show slow oxidation rates, moderate Cr_2O_3 volatility driven by linear mass loss for higher-Ni austenitics. The HK (^{25}Cr-^{20}Ni) alloys at 800°C show increasing mass loss beyond 2,500 to 3000 h. CF8C Plus (^{19}Cr-^{12}Ni) shows substantial spallation of oxide at 800°C. The cast alumina-forming alloys show small, positive mass gains consistent with protective behavior and perform the best under these conditions.

The overall oxidation performance of the various alloys can be summarized as follows and is in the order of decreasing oxidation resistance:

- Cast alumina-forming austenitic alloys form a thin adherent Al_2O_3-base oxide, show no spallation or volatility, and provide the best oxidation resistance
- Cast austenitic alloys such as TMA 6301 (^{25}Cr-^{35}Ni), HP (^{25}Cr-^{35}Ni) have good oxidation resistance, but show mass loss due to Cr_2O_3 volatility-driven mass loss
- The HK (^{25}Cr-^{20}Ni) and TMA 4705 have good performance at temperatures up to 800°C, but transition to Fe-oxide formation at 800°C
- CF8C+ shows Fe-oxide formation and spallation at 700 to 800°C
- SiMo cast irons form a thick but adherent oxide. D5S shows comparable rates from 650 to 800°C due to the semi-protective SiO_2 underlayer formation at 750 to 800°C
- D5S shows a moderately slower oxidation than SiMo cast irons at 650°C, but also shows spallation/mass loss at 700 and 750°C.

In summary, constrained thermal fatigue tests and oxidation tests have been completed on several candidate alloys for exhaust manifolds. Thermal-physical properties are being obtained for the most promising alloys to enable component modeling and down select the most suitable alloy for component casting.

Piston Materials

One method for increasing the temperature capability of pistons is to coat the pistons with a low thermal conductivity metallic alloy. Figure 3 shows a cross-section optical image of a 4140 steel substrate coated with a low thermal conductivity coating.

It is important to note that the interface between the coating and the 4140 substrate looks relatively free of defects. Thermal conductivity measurements will be performed on the composite to understand the effect of the lower thermal conductivity coating on the thermal conductivity of the composite.

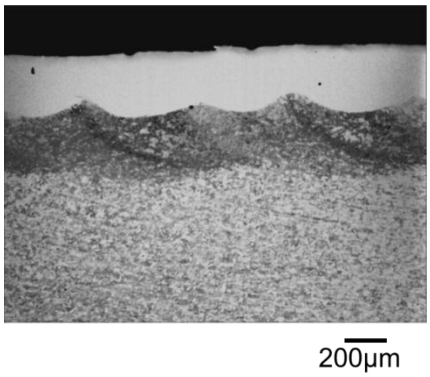

Figure 3. Cross-section of a 4140 steel coated with a low thermal conductivity material.

Conclusions

Constrained thermal fatigue tests show that cast austenitic steels perform better than SiMo cast iron and D5S cycled from 800°C to lower temperatures.

Oxidation testing shows that the cast austenitic steels have improved oxidation resistance when compared to SiMo cast iron and D5S at temperatures up to 800°C.

Feasibility of coating 4140 steel with a low thermal conductivity material has been demonstrated.

Project 18518 – Materials for High-Efficiency Engines

Agreement 23725 – Tailored Materials for Improved Internal Combustion Engine Efficiency

Glenn J. Grant
Energy Materials and Manufacturing
Pacific Northwest National Laboratory
902 Battelle Blvd., K2-03
Richland, Washington 99356
Phone (509) 375-6890; fax: (509) 375-4448; e-mail: glenn.grant@pnnl.gov

Blair E. Carlson
Manager, Lightweight Materials Processing
General Motors R&D
30500 Mound Rd
Warren, MI USA 48090
e-mail: blair.carlson@gm.com

Rajiv S. Mishra
University of North Texas
Professor, Department of Materials Science and Engineering
Site Director, NSF IUCRC for Friction-Stir Processing
1155 Union Circle #305310
Denton, Texas 76203-5017
Phone (940) 565-2316; fax (940) 565-4824

DOE Technology Manager: Jerry L. Gibbs
Phone (202) 586-1182; fax: (202) 586-1600; e-mail: jerry.gibbs@ee.doe.gov
Field Technical Manager: Dean Paxton
Phone (509) 375-2620; fax (509) 375-2186; e-mail: dean.paxton@pnnl.gov

Contractor: Pacific Northwest National Laboratory
Prime Contract No.: DE-AC05-76RL01830

Objectives

- To develop friction-stir processing (FSP) to tailor the properties of conventional, low-cost engine materials (i.e., cast iron, alloy steels, and aluminum alloys) with the goal of increasing their high-temperature performance, durability, and thermal properties.
- To deploy FSP components that can enable energy-efficient combustion strategies, especially those that will require higher peak combustion pressure or higher-temperature operation, where component durability is the primary barrier to using the energy-efficient combustion strategy.

Approach (Including Partner/Collaborator and Path to Technology Transfer and Commercialization)

- Develop surface-modification techniques, modified materials, and components. The project is a collaboration with General Motors, with General Motors providing in-kind and materials (i.e., aluminum castings, cylinder heads, engine components, and testing).

- The project primarily is investigating FSP, a new technology that can produce functionally graded surfaces with unique and tailored properties that will allow propulsion materials to withstand higher temperatures and pressures without appreciably losing strength, hot hardness, or wear resistance, and exhibit improved resistance to thermal fatigue.
- FSP-treated components will be evaluated and tested by industry collaborators to demonstrate efficiency benefits and potential commercial applications.

Accomplishments

- **Milestone**: Demonstrate property improvements from FSP that can reach the following metrics established by the project team: minimum two-fold improvement in fatigue life and 20% improvement in average failure stress level at N cycles. This was completed and exceeded (an order-of-magnitude improvement in fatigue life).
- **Milestone**: Demonstrate consolidated FSP regions in aluminum and ferrous materials typical of cylinder head, cylinder liner, block, crankshaft, rod, piston, and bearing materials on a subscale, two-dimensional shape relevant to real part geometry (TRL 3 to 4 transition). This is on schedule.

Future Direction

- **Milestone:** Demonstrate prototype part that can show durability advantage from FSP that allows high peak combustion pressures (PCPs) and document energy savings potential. This is a future milestone.

Introduction

The purpose of this project is to improve the durability and thermal properties of conventional, low-cost materials so they can withstand the increased level of mechanical performance required in new combustion strategies (such as homogenous charge compression ignition [HCCI], low-temperature combustion, and other conditions where higher PCPs are anticipated). HCCI, premixed charge compression ignition, low-temperature combustion, and other strategies can produce higher specific power levels that can allow engine downsizing and decreased fuel consumption, but increases in PCP are often a result. A barrier to fully realizing these energy-efficient strategies can be the engine component materials themselves. Increasing the durability of engine components can increase the operational envelopes of the engine, allowing designers of the combustion process to access areas of engine control where increased specific power and low emission levels are found, but where high PCPs can create reliability problems.

The proposed project aims to achieve the U.S. Department of Energy goals for increased fuel and thermal efficiency in both light and heavy-duty engines by developing and deploying FSP, a new surface-modification technology that has been shown to significantly improve the strength and durability of current engine materials. This project proposes to experimentally develop the FSP required to engineer the surface of propulsion materials for improved properties, then fabricate prototype parts that will be tested in-engine by project partners. The microstructural modification created by FSP is expected to lead to a set of materials with enhanced surface properties that can handle increased combustion pressures, resulting in improved engine efficiency.

Background

Almost since the inception of internal combustion engines, there has been a steady rise in specific power (SP) output. SP is correlated with efficiency and is the combined effect of better optimization of combustion, fuels, engine materials and design, reduction in parasitic losses, and improved heat management. Figure 1 shows a steady increase in SP from 1970 to 2001. After 2001, SP levels dropped due to emission and aftertreatment devices and controls mandated by federal legislation (primarily increased exhaust gas recirculation rates and particulate filters). The drop in SP from 2001 to about 2003 would have been even greater were it not for significant advances (e.g., in-engine management, computer control, and higher injection pressures) made during this period to compensate for the power losses. However, around 2003, a different restriction on the optimization of the combustion process was beginning to force diminishing returns. The restriction is illustrated in Figure 1 as the PCP plot.

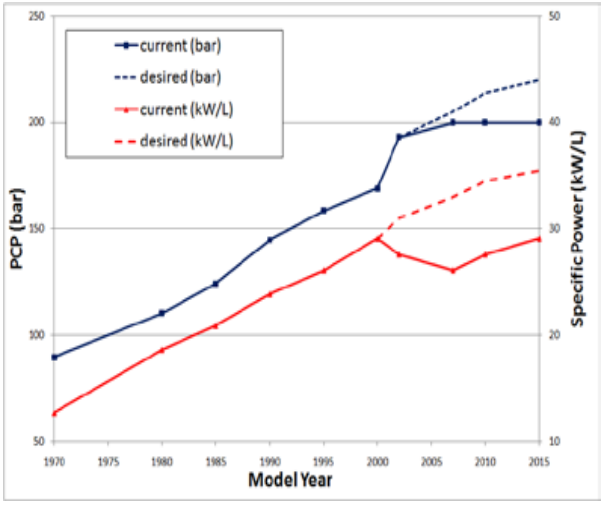

Figure 1. Plot showing the increase in SP and PCP for typical heavy-duty diesel engines from 1970 to 2003 (projected until 2015) (figure from the Southwest Research Institute http://www.swri.org/3pubs/brochure/d03/DieselCylHeadDev/DieselCylHeadDev.pdf).

Since 2003, PCP has leveled at around 190 to 200 bar. Above this level, conventional engine materials will be beyond strength and fatigue limits.[a] To increase efficiency further, either unconventional, expensive materials (i.e., Ni alloys, Ti, CGI, or micro-alloyed steels) must

[a] Figure 1 represents data primarily from medium-duty to heavy-duty diesel engines. Production automotive diesel engines (i.e., light duty, high speed) achieve SP levels above 75 kW/L in turbocharged and intercooled configurations.

be used or conventional materials must be modified in a way that increases their durability. New energy-efficient combustion strategies, especially HCCI, will increase PCP potentially above 220 bar. Accordingly, materials must be improved to enable this process.

One of the major challenges for conventional materials under increasing peak pressure environments is resistance to thermal-fatigue failure. Figure 2 shows typical examples of thermal-fatigue problem along the bowl rim of a piston. Pistons and cylinder heads are particularly vulnerable to this failure mode because of the cyclic nature of the loading and temperature changes in the combustion chamber.

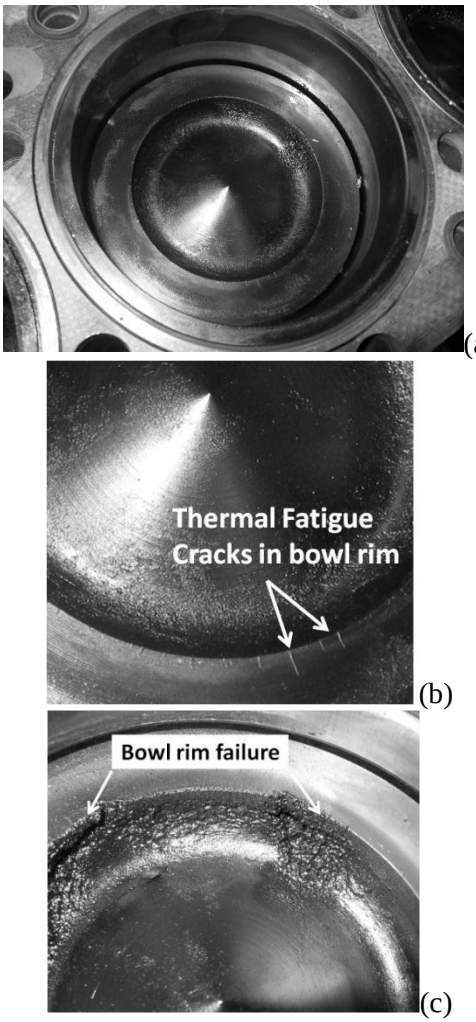

(a) (b) (c)

Figure 2. (a) Piston in bore; (b) cracks on inside edges of bowl rim; and (c) bowl rim failure.

Rather than substitute a potentially high-cost, high-temperature, monolithic material, one low-cost strategy to enable higher PCP involves using techniques to improve the thermal-fatigue performance of current materials. In the case of thermal fatigue in the bowl rim area, the technique need only be applied to the narrow area around the bowl rim itself because failures of this area drive the overall material selection.

FSP is a new technology that can be used to create engineered regions on selective areas of a part. In recent years, Pacific Northwest National Laboratory has developed techniques and tools that allow FSP to be accomplished in steel, cast iron, and aluminum. The process can be selectively applied to the surface of a material, and it alters the microstructure by severe plastic deformation that occurs in the processed zone.

FSP produces a surface-modified region that is different from a coating. Commonly, surface treatments designed to enhance wear or thermal performance include various coating methods or fusion-welded hard facings. Most of these processes are liquid state and often involve detrimental temperature effects on the base material. Heat-affected zones in the base metal and various deleterious high-temperature reactions can create a coated part with less-than-desirable properties.

Further, traditional thin coatings can suffer from issues involving the nature of the interface between the coating and the base material (e.g., spalling, debonding, and cracking on the interface), especially under high-stress, gouging wear conditions or under cyclic-thermal conditions where coefficient of thermal-expansion mismatch is an issue. Also, failure of a coating under high-loading conditions can occur when the substrate below a thin, hard coating fails by plastic deformation.

Regions treated with FSP can be significantly more robust than traditional coatings for two reasons: (1) FSP produces a modified region that transitions to the base material without a sharp interface and (2) the modified region is generally thicker and the transition region wider than traditional coating because the plasticized region depth is related to

the tool geometry, specifically the depth and size of the pin.

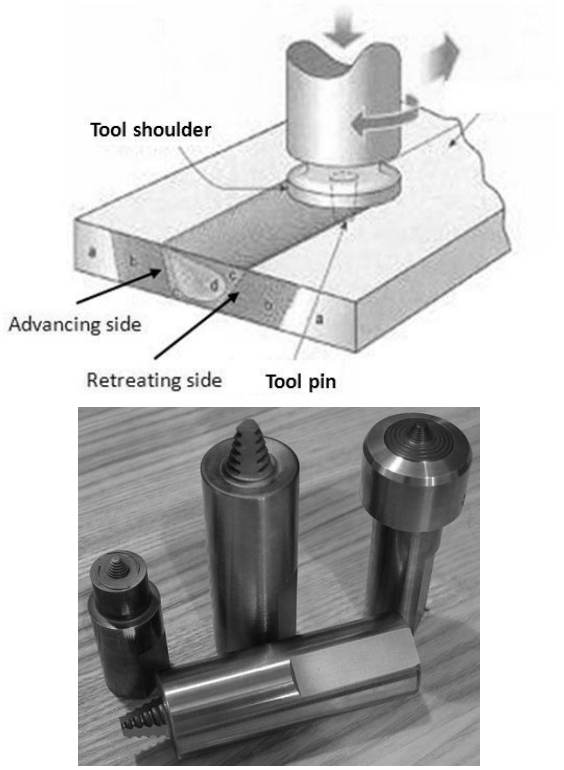

Figure 3. FSP illustration (top) and typical friction-stir tools (bottom).

Approach

The current project will prototype and test up to four separate internal engine components that are expected to have limited durability at very high peak cylinder pressures or high load-rise times during engine operation. These components will have FSP selectively applied to the regions of the part where durability issues are either found or anticipated. Example components will be cylinder heads, blocks, and potential components in the rotating assembly, including, but not limited to, crankshafts and camshafts.

A number of different localized material durability issues that limit highly efficient engine design have been identified and include resistance to thermal fatigue, improved hot strength, improved resistance to erosive or adhesive wear in piston ring grooves, and improved performance and strength in aluminum blocks and cylinder heads of small displacement turbo-gas and turbo-diesel engine materials. These durability issues have been identified as potential opportunities where FSP may be able to produce property improvements.

The project will develop and use FSP to produce surface-modified regions on parts composed of conventional engine materials to address barriers related to durability at high PCP without the increased raw material costs associated with the introduction of exotic or expensive materials.

- The project will develop the FSP manufacturing parameters and select and evaluate proper tool materials and techniques to produce defect-free FSP regions.
- Coupon-level testing and evaluation of the thermal and mechanical properties will be conducted, focusing on specific performance targets identified by project partners. If performance metrics are met for sample materials enhanced by FSP, additional research will include developing and demonstrating the appropriate method to apply this process to the two-dimensional and three-dimensional (3D) geometry of the selected parts.
- Once process schedules are established, prototype parts will be fabricated to specifications provided by project partners and relevant part testing will be completed (i.e., in-engine or other tests specified by partners).
- Project tasks will be divided by part or application. The physical parts to be tested are expected to define several primary tasks surrounding development of the FSP for that part and the actual test runs in realistic environments.

Task 1: Cylinder head thermal-fatigue life improvement:

- Subtask 1a – Chill casting of A356 plate stock for experimental trials
- Subtask 1b – FSP trials for thermal-aging studies

- Subtask 1c – FSP trials for stable microstructure (resistance to abnormal grain growth [AGG])
- Subtask 1d – Room temperature (RT) fatigue studies on FSP coupons (miniature fatigue testing)
- Subtask 1e – Elevated temperature fatigue testing on FSP coupons
- Subtask 1f – Translating the process to a 3D part and producing a processed region on an actual head or head analog
- Subtask 1g – Operating-temperature, cylinder head thermal-shock testing (General Motors).

Task 2: Block and head-casting FSP to close near-surface porosity for improved strength and durability:

- Subtask 2a – FSP trials on block materials in plate form for thermal-aging studies
- Subtask 2b – FSP trials for stable microstructure (resistance to AGG)
- Subtask 2c – RT fatigue studies on FSP coupons (miniature fatigue testing)
- Subtask 2d – Translating the process to a 3D part and producing a processed region for microstructural examination and testing.

Task 3: Fillet, oil hole, or flange fatigue performance improvement on rotating shafts:

- Subtask 3a – FSP trials on steel alloy plate for process parameter development
- Subtask 3b – Mechanical and toughness testing of FSP coupons
- Subtask 3c – RT fatigue studies on FSP coupons (e.g., rotating beam fatigue or ultrasonic testing on subscale specimens) (General Motors)
- Subtask 3d – Translating the process to a 3D part and producing a processed region on an actual rotating shaft assembly
- Subtask 3e – In-engine, or other appropriate, testing.

Technology transfer both during and at the end of this project will be directly through the project participant General Motors (and potentially a Tier 1 supplier), who will implement the technology.

Results

During fiscal year 2013, work focused primarily on Tasks 1 and 2. Specifically, the following areas have been studied in detail:

- The role of FSP parameters on AGG behavior
- Mechanical testing of the processed region.

The Role of Process Parameters on AGG

FSP leads to significant microstructural refinement (e.g., eutectic Si particle and grain size), removal of casting porosity, and breakdown of dendritic structure. However, some FSP microstructures can undergo excessive grain coarsening (i.e., AGG) when exposed to elevated temperatures. It is not yet known if AGG will produce a microstructure with lower thermal-fatigue performance, but it is known to restrict ductility at RT. Because the processed part will be exposed to elevated temperature, it is imperative to learn what controls AGG during FSP of A356 alloy. Table 1 shows the test matrix that was created to learn the possible effects of process parameters on AGG. A friction-stir welding tool with concave shoulder and stepped spiral pin was used to carry out the first round of welds.

Following FSP, metallographic cross sections were obtained at a location 1 in. behind the exit hole for each weld condition. This was done to check for AGG characteristics when subjected to post-weld heat treatment (PWHT), which includes soaking at 535°C for 2.5 hours and water quenching.

Weld temperature was recorded continuously for all process conditions by placing a thermocouple behind the friction-stir welding tool shoulder. Figure 4 plots the tool temperature as s function of tool revolutions per minute (RPM). Tool temperature increases with an increase in tool RPM. Most process conditions resulted in a tool temperature above

400°C, with the exception of the lowest RPM conditions.

Table 1. Process parameters used in current study.

Tool RPM	Feed Rate (in./min)	Plunge Depth (in.)	Machine Control
1,500	4	0.215	Z position
300	4	0.215	Z position
300	4	0.218	Z position
700	4	0.215	Z position
700	4	0.220	Z position
300	4	0.220	Z position
1,200	4	0.220	Z position
1,500	4	0.220	Z position
450	4	0.220	Z position

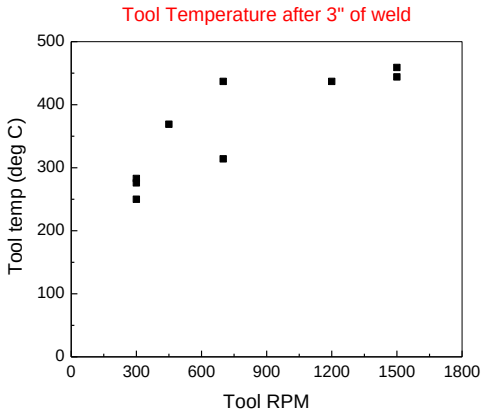

Figure 4. Tool temperature as a function of tool RPM.

The microstructure of each weld after PWHT showed significant differences. All the welds, where tool temperature was higher than 400°C, showed AGG. One such representative macrograph of a weld done at 1,500 RPM is shown in Figure 5. Formation of very large-sized grains inside the weld nugget after PWHT is evident in this image.

However, Figure 6 shows, in the 700-RPM weld where tool temperature was about 300°C, fine-grained microstructure present at a few locations. Similarly, existence of fine-grained microstructure also was confirmed for 300-RPM welds. Weld temperature for 300 RPM was below 300°C. Figure 7 shows images of 300-RPM welds. No large-sized grains could be identified in these images. Therefore, it is likely that there may be a relation between weld temperature and AGG characteristics. It is possible that there is a critical temperature around 300°C, below which AGG will not occur.

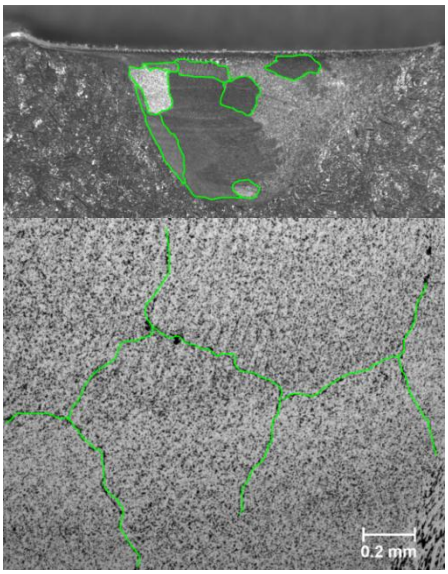

Figure 5. Weld nugget macrograph after PWHT, 1,500-RPM weld (top) and higher mag image (bottom).

In summary, the above study revealed that AGG characteristics after PWHT can be affected by weld parameters. Temperature or another feature dictated by RPM can produce a microstructure that shows or suppresses AGG. AGG is expected to affect the mechanical response of the weld to creep and creep fatigue. In an effort to quantify the effects, both AGG and non-AGG heat-treated welds will both be tested. The results of this work will help determine if AGG has a positive or negative effect on the properties of interest.

Mechanical Testing of Processed Region

Microstructural examination of the processed plate showed the absence of dendritic structure and a homogeneous distribution of Si particles throughout the Al matrix inside the weld nugget. Because the as-received alloy was an Sr-modified alloy, the extent of particle refinement was minimal. Figure 8 shows a comparison of the microstructures between the as-cast and the FSP condition. A notable

difference is the change in shape of Si particles, with most of the particles becoming equiaxed after FSP.

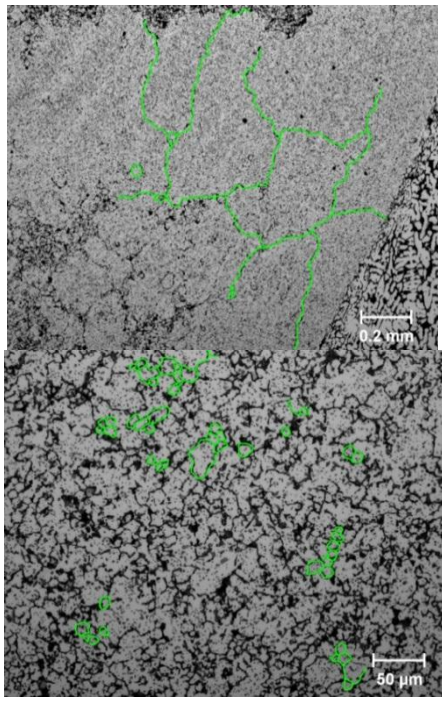

Figure 6. Grain structure in a 700-RPM weld (weld temperature about 300°C), showing regions of fine-grained and coarse-grained microstructures.

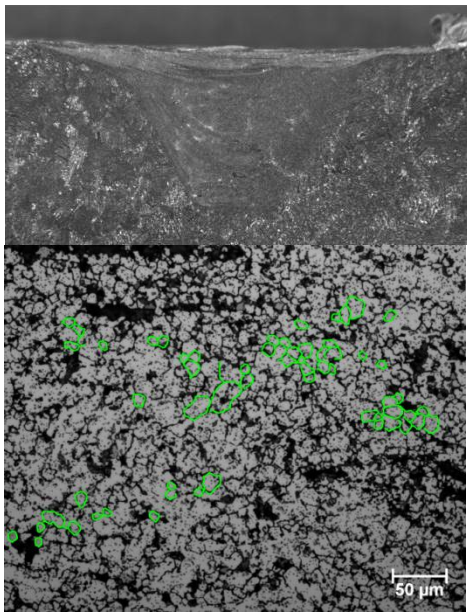

Figure 7. Images of weld carried at 300 RPM. Weld temperature is below 300°C. No evidence of large-grain structures was present.

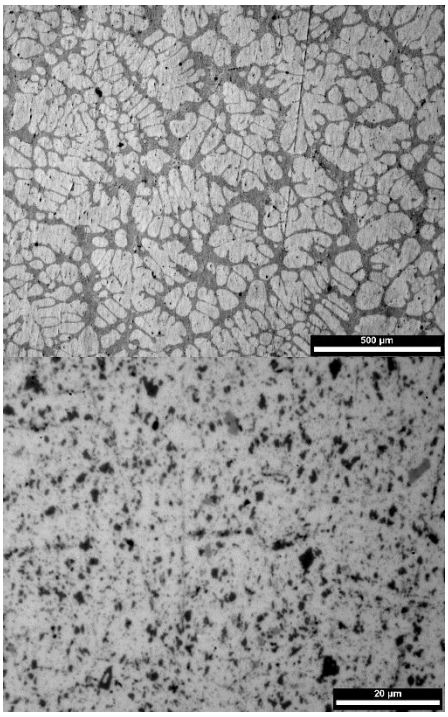

Figure 8. Microstructures of A356; as-cast, 50x, (top) and FSP, with 1,000x (bottom).

Mechanical properties were evaluated for three microstructural conditions (e.g., [i] as-cast + T6, [ii] FSP + aged, and [iii] FSP + AGG + aged).

As-Cast + T6

The most common heat-treatment procedure to improve the strength of the as-cast A356 is the T6 treatment. The treatment consists of solutionizing the alloy at 535°C for 5 hours, quenching in water at 90 ±5°C, followed by aging treatment at 160°C for 5 hours. Solutionizing the alloy achieves multiple objectives, including homogenizing the microstructure, spheroidizing the Si particles, reducing micro-segregation of alloying elements, dissolving Mg and Si, and forming a supersaturated solution. During the subsequent aging, Mg_2Si precipitates into the Al matrix (dendrites). Mg_2Si precipitates form very fine, coherent, and shearable particles and are the main strength-providers in the alloy.

FSP + Aged

After FSP of the cast A356 plates, some processed material was subjected to aging

treatment at 160°C for 5 hours to increase the strength by precipitating any Mg_2Si that might have gone into solution during processing. Because FSP results in severe plastic deformation and subsequent dynamic recrystallization, the grain size of the Al matrix inside the weld nugget is significantly refined. Therefore, determination of mechanical properties in FSP + aged condition would provide valuable insight about the performance of fine-grained microstructure.

FSP + AGG + Aged

After FSP, some of the processed material was solutionized at 535°C for 2.5 hours. This resulted in AGG in the stir zone. The Si particle distribution and sizes remain the same as in the as-FSPed material. Migration and elimination of grain boundaries result in the enlarged grains. This AGG material is subsequently water-quenched and aged at 160°C for 5 hours for strength enhancement.

Figure 9 shows electron back scattered diffraction images of the three microstructures: (i) as-cast + T6, (ii) FSP + aged, and (iii) FSP + AGG aged condition. For the as-cast + T6 condition, the entire picture consists of a single grain, which contains several dendrites and an interdendritic network of eutectic Si particles. A different grain is partially visible at the bottom right. The secondary dendritic arm spacing in this material is 20 to 30 µm. The microstructure of the FSP + aged sample indicates refinement of grain size. The average grain size is 8 µm. The microstructure of the FSP + AGG + aged material shows presence of very large grains due to exposure at 535°C for 2.5 hours. The average grain size is 18 µm; however, some abnormally grown grains are in the range of 80 to 100 µm.

Mini-tensile testing of nugget material was used to evaluate mechanical properties because this approach can evaluate local mechanical properties. Figure 10 shows the dimensions of the gage section of one such mini-tensile sample. The gage length is 2-mm, width and thickness are 1 mm each. The orientation of the tensile sample is along the longitudinal direction, along the FSP run.

Tensile tests have been performed for the abovementioned microstructural conditions at RT, 150°C, 200°C, and 250°C, and at two strain rates (e.g., 10^{-3} s^{-1} and 10^{-4} s^{-1}). Figure 11 shows the typical stress-strain response. Strength drops as the test temperature increases for both as-cast and FSP condition. However, elongation to failure increases as a function of temperature. Additionally, FSP samples show much higher ductility than the as-cast counterpart. Such high ductility observed in FSP samples is related to the elimination of the dendritic structure, homogeneous distribution of Si particles, and the closure of casting porosity.

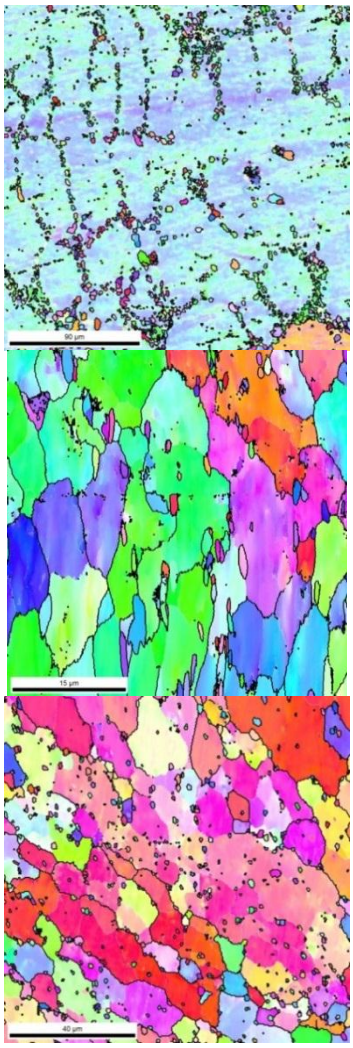

Figure 9. EBSD images of (i) as-cast + T6 microstructure (scale bar = 90 µm) (top); (ii) FSP + aged microstructure (scale bar = 15 µm) (middle); (iii) FSP + AGG + aged microstructure (scale bar = 40 µm) (bottom).

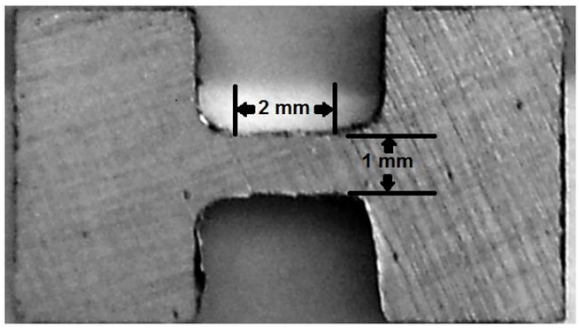

Figure 10. Mini-tensile sample used to evaluate tensile properties.

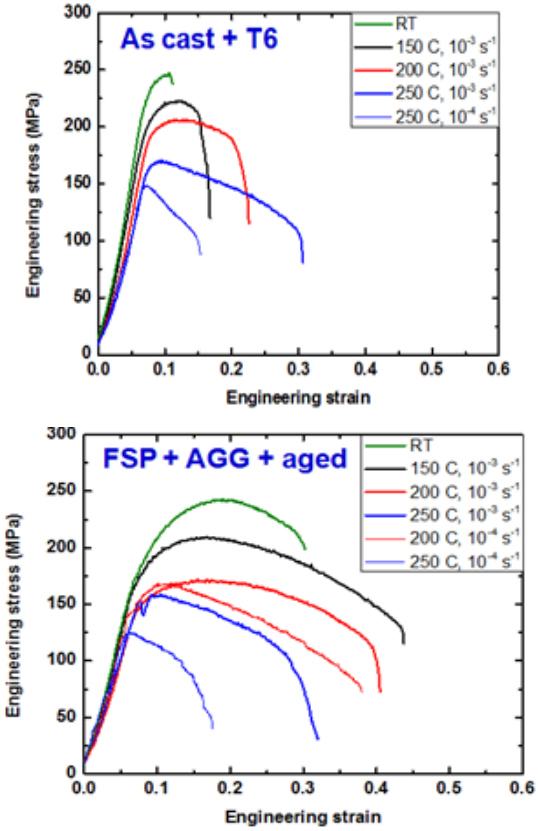

Figure 11. Engineering stress-strain plots comparing as-cast versus FSP conditions.

Yield strength and elongation to failure data for four different microstructural conditions (FSP, FSP+ age, FSP +AGG + age, and as-cast + T6) as a function of test temperature are shown in Figure 12. As expected, the as-cast + T6 condition results in highest strength for this class of alloy. Samples in as-FSP condition show the lowest strength. This is because of the absence of strengthening precipitates in the Al matrix. An aging treatment leads to significant strength recovery at RT.

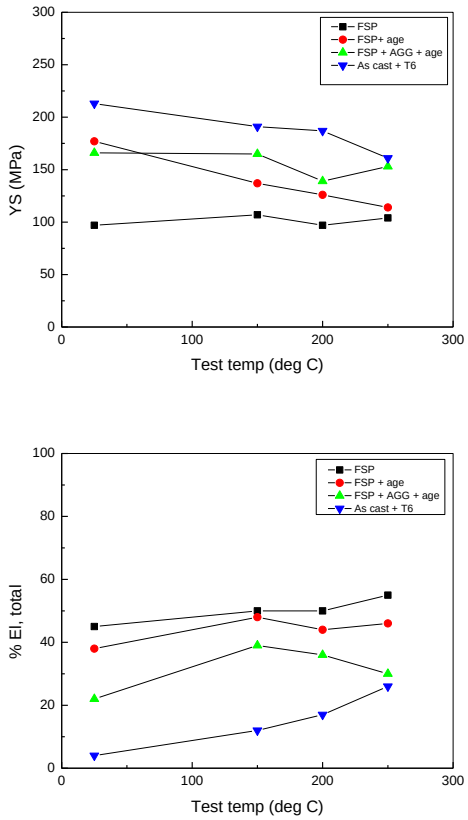

Figure 12. Yield strength (top) and % elongation to failure (bottom) data as a function of test temperature, strain rate is 1E-3 s-1

In addition, samples with AGG microstructure have high strength at elevated temperatures. Elongation to failure is the lowest for the as-cast + T6 condition. As-FSP condition showed the highest ductility. Samples with AGG microstructure show moderate level of ductility at all temperatures. However, it should be noted that only AGG microstructure shows a trend of reduced ductility with increased test temperature. The microstructure must be more thoroughly examined to find the cause. In summary, samples with AGG microstructure offer the best combination of strength and ductility at elevated temperatures.

To evaluate fatigue properties, a bending fatigue test was performed for three microstructural conditions: as-cast + T6, FSP +

aged, FSP + AGG + aged. Miniature fatigue testing was employed in this study, because of the small size of the processed region. Figure 13 shows the specimen geometry and the specimen orientation with respect to the FSP region. The gage length is 3.6 mm. There are holes on the grips (wide regions at either end) that help in aligning the sample at a fixed position in the machine during fatigue testing. Point A represents the loading point. The broad end of the sample is fixed. The maximum bending stress is experienced by the gage section and is given by

$$\sigma = \frac{6PL}{t^2 w}$$

where P is the force measured at point A using a load cell, t is the thickness of the sample, and w is the width of the sample at a distance L from the point of load application.

Miniature fatigue samples were machined in a computer numerical controlled milling machine from the top of the processed region. The orientation was such that the gage length was parallel to the FSP run along the longitudinal/processing direction. After milling, samples were mechanically polished to mirror finish before testing

S-N curves from the RT fatigue test are shown in Figure 14. Cycles to failure are almost one order of magnitude higher for the FSP condition compared to as-cast condition. In general, higher fatigue life was seen in the FSP + AGG + aged condition compared to the FSP + aged condition. Yield strength was similar between the FSP + aged and the FSP + AGG + aged condition at RT; however, the FSP + aged condition showed higher ductility. The FSP + AGG + aged condition was not expected outperform the FSP + aged condition in fatigue life. More work is needed to discover what drives the higher fatigue life in the FSP + AGG + aged condition.

Figure 15 compares the fracture surface appearance of broken fatigue specimens in three different microstructural conditions. As-cast samples show a large proportion of rough areas on the fracture surface, indicating rapid crack propagation. Fracture surfaces of FSP + aged and FSP + AGG + aged samples show smooth areas with very few rough regions, implying slower crack growth before final failure.

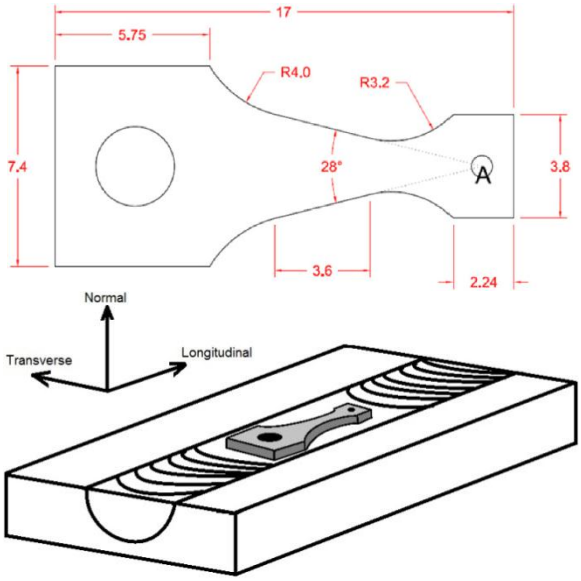

Figure 13. Geometry of miniature bending fatigue sample (dimensions in mm) (top) and specimen orientation (bottom).

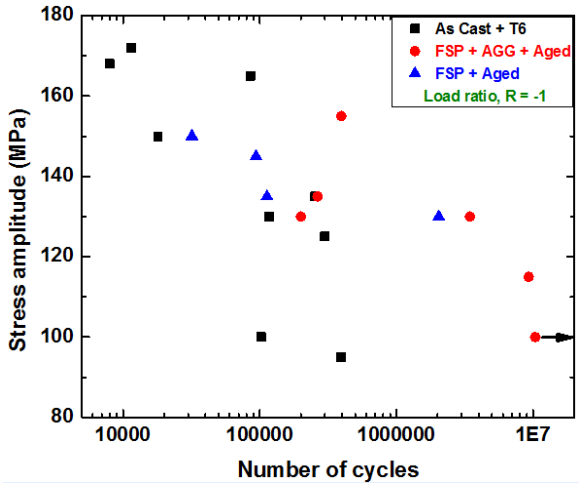

Figure 14. S-N curves generated from fatigue testing of samples of as-cast + T6, FSP + aged, and FSP + AGG + aged samples.

Characteristic fatigue striations were identified in the FSP samples. The striation spacing was about 0.5 μm (Figure 17), further establishing that crack propagation in the FSP microstructures occurs at a very slow rate. No such striations were observed in as-cast + T6 samples.

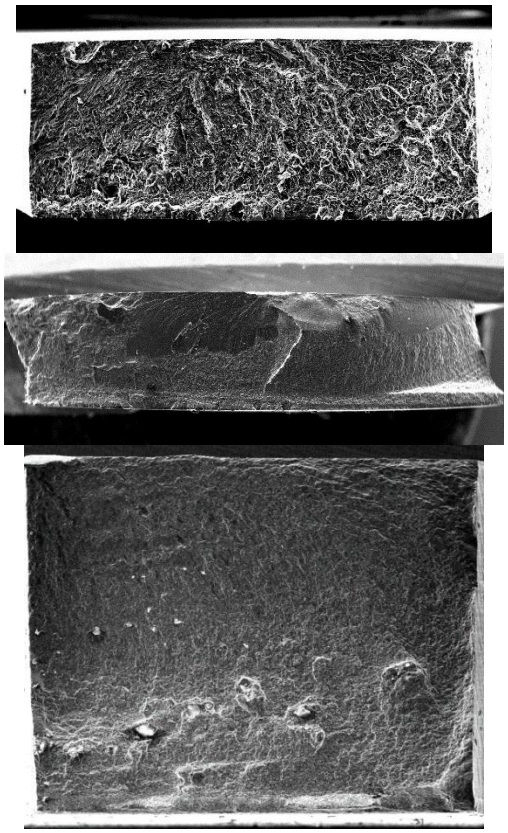

Figure 15. Fracture surfaces of failed fatigue samples of three different microstructures: (top) as-cast + T6, S = 135 MPa, N = 2.55 x 105 cycles; (middle) FSP + AGG + aged, S = 130 MPa, N = 3.54 x 106 cycles; (bottom) FSP + aged, S = 130 MPa, N = 2.04 x 106 cycles.

Conclusions

The goal of this project is to use FSP to develop components that enable energy-efficient combustion strategies, especially strategies that require higher PCP or higher temperature operation. FSP produces selected, graded structures that have shown increased strength and durability in fatigue. Surface modification through FSP may address some emerging material problems seen in very high combustion pressure systems (e.g., HCCI engines).

FY 2013 accomplishments show that FSP conditions can produce a wide range of microstructures. Processed regions of these microstructures show different mechanical performance. FSP material, especially if processed to produce an AGG microstructure, has shown an order-of-magnitude improvement in RT fatigue life, far exceeding the project milestone of a two-fold improvement. This property improvement is a significant result for the potential to increase the performance of certain areas in the cylinder head and block. However, these results were obtained at RT, where classic fatigue mechanisms are in play. Many areas of the block are at sufficiently low temperature for this data to be relevant; however, other areas (e.g., the valve bridge area or near the combustion chamber) are at significantly higher temperatures. At high temperature, the failure mechanisms are a mix of classical fatigue and creep. FY 2014 work will focus on elevated temperature creep and fatigue testing to see how FSP microstructures will affect elevated temperature applications.

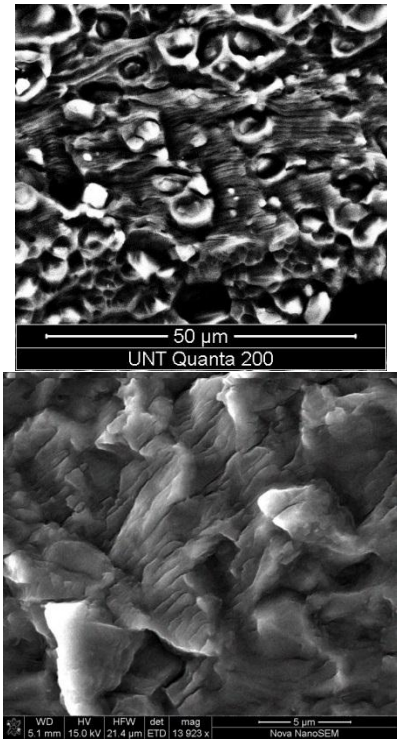

Figure 16. Very fine fatigue striations: (top) FSP + AGG + aged sample, striation spacing = 0.66 µm; (bottom) FSP + aged samples, striation spacing = 0.50 µm.

Project 18518 – Materials for High-Efficiency Engines

Agreement 24034 – High-Strength and High-Temperature Materials for Heavy-Duty Engines

Stan G. Pitman, PNNL
Energy Materials Group
Pacific Northwest National Laboratory
P.O. Box 999, MS K2-03
Richland, WA 99352
Phone (509) 371-6746; fax: (509) 375-4448; e-mail: stan.pitman@pnnl.gov

Howard Savage
Cummins, Inc.
CTC Metallurgical Engineering
1900 McKinley Avenue
Columbus, IN 47201
Phone (812) 377-5998; e-mail: howard.savage@cummins.com

DOE Technology Manager: Jerry L. Gibbs
Phone (202) 586-1182; fax: (202) 586-1600; e-mail: jerry.gibbs@ee.doe.gov
Field Technical Manager: Dean Paxton
Phone (509) 375-2620; fax: (509) 375-2186; e-mail: dean.paxton@pnnl.gov

Contractor: Pacific Northwest National Laboratory
Prime Contract No.: DE-AC05-76RL01830

Objectives

- To develop aluminum alloys in laboratory-scale processing, which have high-strength at elevated temperatures (300 MPa tensile strength at 300°C). This objective is being approached using melt-spinning processes to produce flake and consolidating the flake by extrusion.
- To produce high-strength aluminum alloys in commercial-scale processes using industrial suppliers for the melt-spinning and consolidation processes.
- To produce forgings that will be evaluated for a commercial application requiring high-temperature strength.

Approach

- Select three rapid solidification (RS) alloy compositions, based on literature review and laboratory experience, for evaluation using RS flake preparation and laboratory-scale extrusion.
- Measure elevated-temperature mechanical properties and compare to the mechanical properties of the baseline materials.
- Produce larger quantities of RS flake via Transmet, a Pacific Northwest National Laboratory (PNNL) subcontractor.
- Consolidate the flake by extrusion and subsequent forging.
- Evaluate mechanical properties of the extrusion and forgings and test full-scale components using the appropriate test system at Cummins, Inc.
- If the initial evaluation of full-scale components is successful, perform engine testing at Cummins, Inc. to establish performance and mass-reduction benefits.

Accomplishments

- Available RS alloys and an additional PNNL-developed alloy have been evaluated in laboratory-scale extrusions followed by tensile testing. Results are favorable, but commercialization of the extrusion and forging processes must be demonstrated.
- RS flake was produced in commercial-scale quantities (about 600 lb) via Transmet and the flake material has been canned and prepared for extrusion by a consolidation contractor.

Future Direction

- Complete consolidation of the RS flake material by extrusion and subsequent forging. Characterize the consolidated material using mechanical testing and metallographic methods and submit forgings to Cummins, Inc. for evaluation. If the results of this evaluation are successful, perform engine testing at Cummins, Inc.

Introduction

Aluminum alloys that possess strengths approaching 300 MPa at 300°C have been produced in small quantities by numerous mechanical attrition (MA) methods. Although MA can produce unique combinations of properties, MA processing approaches have not been able to meet the requirements for low-cost, high-volume production. The purpose of this project is to demonstrate that MA-type alloys can be produced with adequate high-temperature mechanical properties through development of a low-cost, high-volume, rapid solidification (RS) production process.

MA aluminum alloys with strengths approaching 300 MPa at 300°C have been produced by adding alloying elements with very low solubility and that form intermetallic dispersions (e.g., Fe, Ti, Cr, Mn, and Zr) in the aluminum matrix. Milling cycles can require hundreds of hours to adequately homogenize these alloys, resulting in diminished ductility. In the past, the Pacific Northwest National Laboratory (PNNL) has worked with melt spinning methods to produce RS alloys by using a process that produces a low surface area particulate (i.e., flake).

The RS flake can be consolidated by elevated temperature extrusion. This project intends to use the RS flake/extrusion process to produce an aluminum alloy with increased elevated temperature strength that can be used in diesel engine service environments up to 300°C.

Approach

High-Strength and High-Temperature Aluminum Alloy Development

Evaluate the feasibility of producing Al-Fe high-temperature alloys by two different RS methods: RS flake and rotating cup processing of powder particles (RS powder). The two methods are known to have solidification rates that differ by several orders of magnitude, with the cooling rate for RS flake estimated at 10^6 degrees/second and the RS powder estimated at 10^2 degrees/second. The RS powder method was being evaluated in spite of the lower solidification rate, because it is an established high-volume RS process and because the coarser shot particulate has some advantages in handling and consolidation.

This evaluation has been completed and will be discussed in a subsequent section of this report. The melt spinning method was chosen for use in the following steps:

1. Produce the RS alloy compositions using the PNNL pilot flake system. The PNNL flake melt spinning machine can produce limited quantities of experimental alloys in the form of rapidly solidified flake. The following subtasks were initiated after producing aluminum flake feedstock by melt spinning:
    a. Conduct a comprehensive technology review of prior high-temperature and high-strength aluminum alloy development, including alloys developed by Allied Signal and academic institutions.
    b. Select three alloy compositions, two similar to the early Allied Signal Al-Fe-X compositions the third the $Al_3Fe_2Cr_2Ti$ previously developed by MA.
2. Consolidate flake materials at PNNL via extrusion using laboratory-scale extrusion tooling. Rapidly solidified flake will be consolidated using the canning and indirect extrusion process previously developed by PNNL.
3. Measure elevated temperature mechanical properties and compare them to the mechanical properties of the baseline materials. Conduct elevated temperature tensile tests of sample materials to establish temperature-strength behavior for the materials.
4. Produce larger quantities of flake via Transmet (a PNNL subcontractor) using the production melt spinning system. The down-selected alloy composition(s) will be made into master alloy feedstock and provided to Transmet for melt spinning into rapidly solidified feedstock. Depending on the alloy systems selected, quantities of several hundred pounds are anticipated.

5. Consolidate the production flake by degassing, canning, and hot isostatic pressing, followed by extrusion. Larger-billet diameters will be used, and processing will simulate anticipated full-scale production.
6. Test full-scale components using the appropriate test system at Cummins, Inc. Cummins, Inc. will select components that will benefit from the high-temperature aluminum properties and process the materials supplied by PNNL into full-scale test components.
7. If component testing is successful, perform engine testing at Cummins, Inc. Use established rig testing to establish performance and mass-reduction benefits.

The primary deliverables for this project are as follows:

- Development and production of high-temperature aluminum alloys by rapid solidification
- Characterization of the RS alloys and baseline materials for elevated temperature fatigue strength
- Cost analysis of the process to produce full-scale extrusions
- Full-scale component testing to validate RS alloy performance.

Results and Discussion

Work on this project began in May 2011, conducted under a cooperative research and development agreement (CRADA) between Cummins, Inc. and PNNL. The first phase of the effort has focused on identification of candidate aluminum alloy systems that can provide higher strengths (300 MPa) at elevated temperatures of approximately 300°C and on evaluation of two methods for producing RS feedstock: melt spinning of flake and rotating cup processing of powder particles. The work with melt spinning is described next and a discussion of melt spinning relative to rotating cup processing follows.

A series of five alloy compositions were evaluated using two different consolidation and extrusion processes. All alloys contain Fe as a key alloy addition, along with smaller additions of silicon, Ti-Cr-V, and Mn. With the exception of silicon, alloy additions were chosen for their low solubility in aluminum and ability to form stable second-phase particles. Evaluated alloy compositions are listed in Table 1. The first two alloys contain Si and V, while the aluminum-iron-chrome/titanium (AFCT) alloy contains a lower level of Fe, combined with higher weight percentages of Cr and Ti. The aluminum-iron-manganese (AFM) alloy was developed at PNNL in earlier work.

The first three alloys (i.e., $Al^{-12}Fe$, $Al^{-8.5}Fe$, and AFCT) have been previously produced in small quantities and tensile tested at a range of temperatures. Tensile strengths for these alloys at 300°C have been reported in the 250 to 300 MPa range, close to or meeting the property goals.

The processing steps that were selected for this project include induction melting to produce suitable feedstock alloys that approximate the compositions of the alloys listed in Table 1, analysis of actual compositions and the alloy melting characteristics, induction re-melting of the alloys, and melt spinning to rapidly produce RS flake materials for subsequent processing. Figure 1 shows the RS flake material and the melt spinning equipment used to produce it.

The second focus of the project was development of laboratory-scale extrusion tooling to be used in the consolidation and extrusion of the RS flake materials to produce a wrought extruded rod. The extruded rod material provides sufficient material for machining of tensile specimens for room temperature and elevated (300°C) tensile. Two processing approaches were developed for preparing the RS flake material for extrusion into the wrought rod product. The first approach involved cold (room temperature) pressing of the RS flake into an aluminum can, followed by weld-sealing the can under vacuum conditions. The sealed can was heated and extruded to the rod product using a 19:1 extrusion ratio. In the second approach, the canned flake was placed in a vacuum hot press at 450°C and pressed to pre-consolidate the RS flake to approximately 90% theoretical density.

The canned and consolidated billet was then extruded into the rod using the same 19:1 extrusion ratio. Figure 2 shows an example of the canned billet (50-mm diameter) and the resulting extruded rod (11.4-mm diameter).

(a) (b)

Figure 1. (a) PNNL melt spinning machine with the front chamber removed and (b) typical RS flake product produced with the melt spinning equipment.

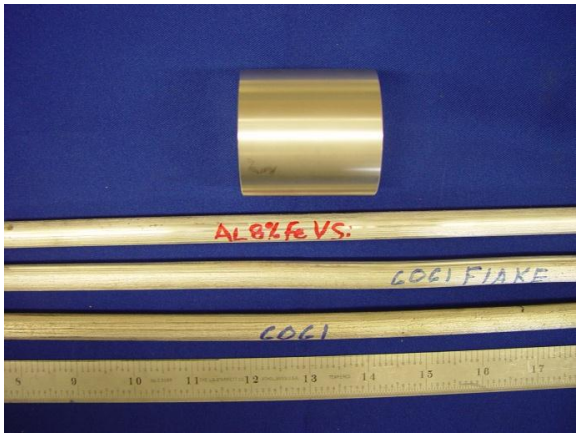

Figure 2. Photograph of the canned RS flake billet (top) and the extruded rod.

Following extrusion of the RS flake materials, the extruded rods were cut into lengths and machined into round sub-sized tensile specimens with a gage length and diameter of 25 and 6.4 mm, respectively. Approximately 150 mm of the nose and tail of the extrusion were discarded to minimize non-uniform material. Machined tensile specimens were then tested at room temperature and at an elevated temperature of 300°C. A minimum of three tests were conducted at each temperature. Results of the tensile tests for the various aluminum alloys are shown in Table 2 (room temperature) and Table 3 (300°C). The goal of this project is to approach a tensile strength of 300 MPa at 300°C test temperature. As shown in Table 3, the AFM-11 alloy comes the closest to meeting that goal. Based on the initial results for the candidate alloys, further processing of the AFCT and AFM-11 alloys has been initiated and a new version of the AFM-series of alloys (i.e., AFM-13 [with a higher Fe content]) has been included in the next phase of material processing. In addition to the elevated temperature strength goal, elevated temperature (300°C) fatigue strength is an important material performance property for heavy-duty engine applications. A key goal for FY 2013 was to scale-up the RS flake and extrusion processing steps so that a larger diameter and longer extrusion could be produced. This would provide sufficient material to conduct the room temperature and elevated temperature fatigue test series.

Metallographic examination of the extruded materials was conducted along with x-ray diffraction and scanning electron microscopy analysis. All three alloys are characterized by having sub-micron grain size and an extensive distribution of sub-micron secondary phase particles. Both the AL-8.5Fe and the AFM alloys have areas of larger, less dense secondary particles, indicating some phase growth during processing. Figure 3 shows low magnification micrographs of the three extruded aluminum alloys. As indicated in Tables 2 and 3, all three alloy compositions show an increase in the measured elastic modulus of the materials; however, this increase is most pronounced in the AFCT and AFM-11 alloys.

Table 1. Initial high-temperature high-strength aluminum alloys.

Alloy Designation	Fe	Si	V	Cr	Ti	Mn
Al-12Fe	12.4	2.3	1.2			
Al-8.5Fe	8.5	1.7	1.3			
AFCT	6.0			3.4	3.2	
AFM-11	11.4	1.8	1.6			0.9
AFM-13	13.2	2.6	.50			0.9

Table 2. Room temperature tensile test results for candidate high-temperature extruded aluminum alloys.

Alloy Designation	Extrusion Temperature(°C)	Elastic Modulus (GPa)	Tensile Yield Strength(MPa)	Tensile Strength (MPa)	Failure Strain (%)
Al-8.5Fe - EB	450	83.5	345.0	390.4	19.1
Al-8.5Fe - EB	500	84.2	331.2	389.4	18.0
Al-8.5Fe - HP	500	86.9	338.1	384.9	18.3
AFCT - HP	500	95.9	400.2	448.6	12.2
AFM-11-HP	500	96.0	427.8	493.6	7.2

EB= vacuum electron beam welded can without hot press
HP= vacuum hot pressed billet.
Failure strains measured using an extensometer.

Table 3. Elevated temperature (300°C) tensile test results for candidate high-temperature extruded aluminum alloys. Note yield strength and ultimate strength are the same at the 300°C test temperature. Extension at failure calculated from gage section measurements.

Alloy Designation	Extrusion Temperature(°C)	Elastic Modulus (GPa)	Tensile Yield/Ultimate Strength(MPa)	Failure Strain (%)
Al-8.5Fe - EB	450	74.5	210.9	25.1
Al-8.5Fe - EB	500	76.6	208.2	21.7
Al-8.5Fe - HP	500	71.8	204.2	18.4
AFCT - HP	500	80.7	226.7	18.8
AFM-11-HP	500	91.1	256.8	17.0

Table 4. Tensile test results for extruded RS flake and rotating cup shot material, alloys AFCT and AFM-11.

Alloy Designation	Test Temperature (°C)	Yield Strength (MPa)	Ultimate Tensile Strength (MPa)	Failure Strain (%)
AFCT flake	room	400.2	448.6	12.2
AFCT shot	room	169.0	215.3	4.9
AFM-11flake	room	427.8	493.6	7.2
AFM-11 shot	room	287.0	411.2	1.8
AFCT flake	300°C	(1)	226.7	18.8
AFCT shot	300°C	(1)	91.8	2.9
AFM-11flake	300°C	(1)	256.8	17.0
AFM-11 shot	300°C	(1)	185.6	5.8

(1) Yield and tensile strength were equal at 300°C test temperature.

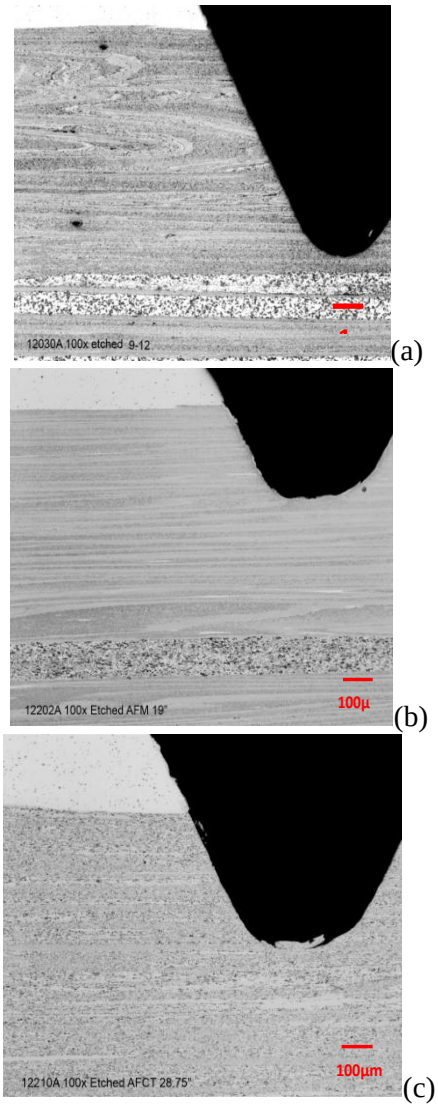

Figure 3. Low magnification micrographs of extruded aluminum alloys (a) AL-8.5Fe, (b) AFM-11, and (c) AFCT. Specimens are from the thread ends of actual tensile specimens as indicated by the black thread contour. The white upper material is the 6061 aluminum can used for extrusion.

Discussion of Melt Spinning Relative to Rotating Cup Processing for Processing of Al-Fe High-Temperature Alloys

Processing of Al-Fe series high-temperature alloys was conducted by two different RS methods: melt spinning of flake and rotating cup processing of powder particles. The two methods are known to have solidification rates that differ by several orders of magnitude, with the cooling rate of RS flake estimated at 10^6 degrees/second and the rotating cup particle process at 10^2 degrees/second. Two high-temperature aluminum alloys (AFCT and AFM-11) were processed by melt spinning and subsequently consolidated into extrusion billets and extruded to make a round rod product, as described above.

The same two alloys were then processed by Transmet Corporation (Columbus, Ohio) using their rotating cup RS powder process. NNL supplied induction-melted ingots of the two alloy compositions to Transmet, who then processed them into RS shot samples. After receiving the shot samples and performing optical metallography of the materials, the shot-processed alloys were canned, cold compacted, and consolidated using the same vacuum hot press parameters. Several consolidated billets were then extruded using the same temperatures and extrusion parameters used for the RS flake materials. As with the RS flake extrusions, a minimum of three tensile specimens were tested at room temperature and 300°C to measure the tensile properties of the RS shot materials.

3-1 Rapid Solidified Flake and Shot

In the RS flake process, the spinning copper wheel has a special knurled pattern of lines running in the direction of rotation and perpendicular to the rotation direction. This surface pattern produces discontinuous flakes that are approximately 1 × 1 mm, with a thickness of 35 to 55 µm, depending on the operating parameters and materials. This ensures very high through thickness cooling rates for the flake while the comparatively large length and width of the solidified flake reduces the surface area and oxygen content. A micrograph of the Al-Fe RS flake is shown in Figure 4. The RS flake shows nanocrystalline or amorphous structure near the wheel side. However, approximately 10 to 14 µm from the chilled wheel surface, the second or third dispersed phase appears from Al matrix. The size of these phases increases as the distance from the wheel is increased, corresponding to the lower cooling rate. The flake thickness of AFCT and AFM-11 are 55 and 42, respectively. Thicker flakes are

produced in alloys with higher melting points. The picture of shot made from Transmet's rotating cup process is shown in Figure 5. The shape of shot is similar to a water droplet with elongation in the direction of the centrifugal force. The average size of these shot materials is about 500 µm for AFCT and 400 µm for AFM-11. The second and third phases display a dendritic and needle-like structure. This indicates that the cooling rate for the shot is significantly lower than that of the RS flake, and based on the Hall-Petch equation, as the grain size is increased the tensile strength is decreased. The chemical composition of AFCT and AFM-11 for flake and shot analyzed and found to be close to the nominal alloy composition. The vol% of Al is about 94 and 92 percent for AFCT and AFM-11, respectively.

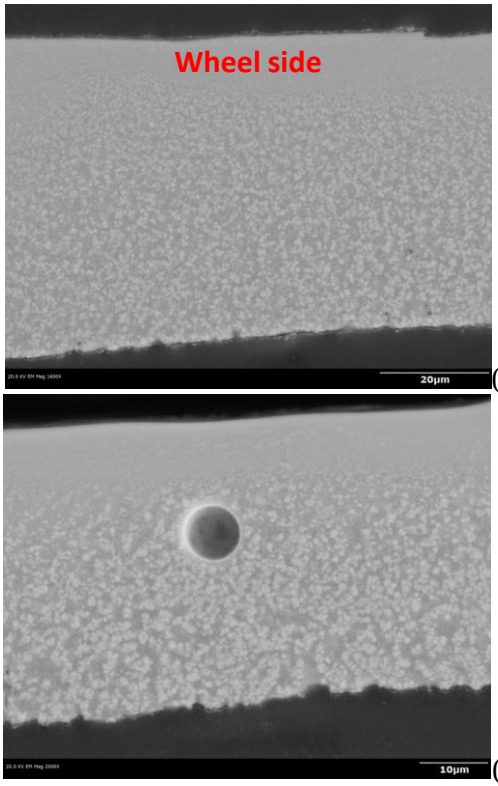

(a) (b)

Figure 4. Micrograph of typical Al-Fe-X RS flake: (a) AFCT and (b) AFM-11.

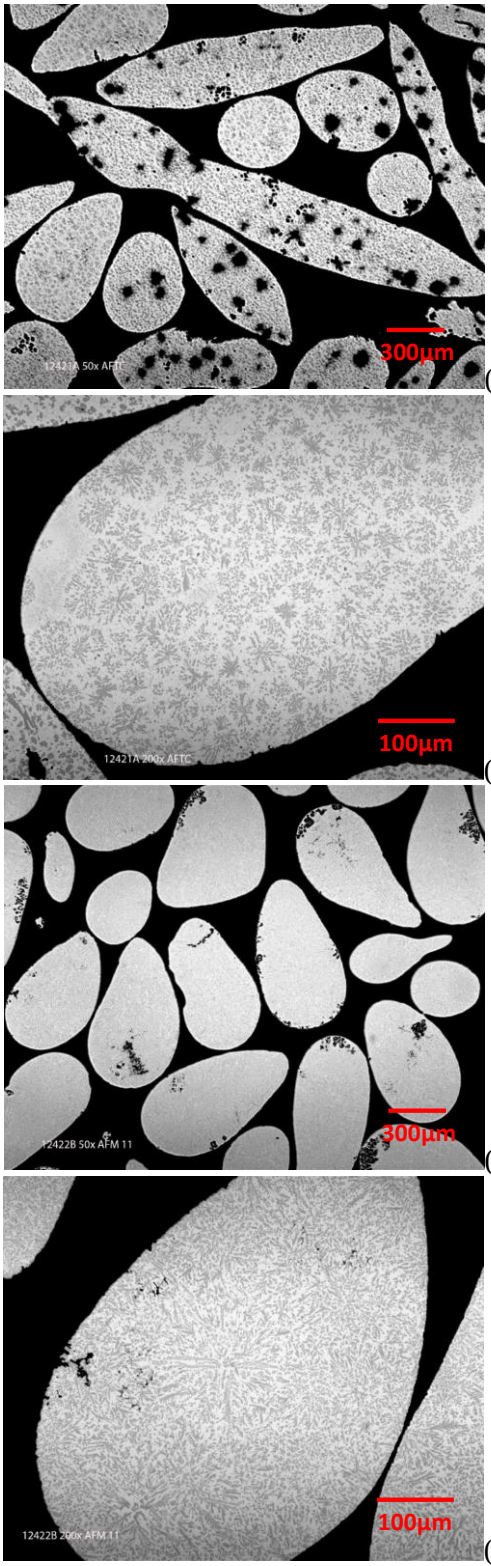

(a) (b) (c) (d)

Figure 5. Micrographs of as-received shot particles for AFCT (a and b) and AFM-11 (c and d).

Tensile tests were conducted of extruded flake material and extruded shot material at room temperature and at 300°C. The results of these tests are summarized in Table 4. Tensile test results show that the flake extrusion has significantly higher tensile strengths when compared to the extruded shot material. The extruded flake materials also display relatively high elongations to failure, which would indicate good consolidation during extrusion and a stable, refined microstructure. Based on previous microstructural characterization, RS flake materials were observed to have a much finer size and distribution of the secondary intermetallic particles combined with occasional bands of coarser particles. The slower cooling rate and cast-like structure of the rotating cup shot material appears to translate into fewer, coarser intermetallic particles in the final extruded product and, as a result, significantly lower room temperature and elevated temperature tensile strengths. It should be noted that the AFM-11 shot extrusion shows significantly better strengths than the AFCT shot extrusion, particularly at the 300°C test temperature. However, the tensile elongation of extruded shot AFM-11 is quite low, particularly compared to the AFM-11 flake extrusion.

Technology Transfer

By participating in this CRADA, Cummins, Inc. will benefit by applying new technology to improve the high-temperature performance and life of engine combustion components, air-handling systems, and emission-control components. In addition, Cummins, Inc. benefits by coupling its own engineering production experience and know-how with the scientific expertise and technical capabilities of PNNL staff and U.S. Department of Energy national laboratories to solve relevant problems that benefit the industry and achieve DOE fuel economy goals.

Conclusions

The High-Strength and High-Temperature Aluminum Alloys for Heavy-Duty Engine Applications Project started under a CRADA (agreement) in May 2011. The early phase of this project has evaluated potential high-temperature, high-strength aluminum alloy systems that can be produced by RS processing and subsequent processing into extruded or forged product forms. A group of candidate alloys were selected for processing and characterization, and feedstock melting methods were developed. RS processing using the PNNL/Transmet melt spinning equipment has been completed. Laboratory-scale extrusion tooling was designed and fabricated and the tooling was used to consolidate flake materials into extruded wrought aluminum alloy rods. Extruded materials of the three alloy compositions were machined into tensile test specimens and tested at room temperature and at an elevated temperature of 300°C. Test results show that the AFCT and AFM-11 alloys have higher tensile strengths at the 300°C test temperature when compared with the Al-8.5Fe alloy. Test results also show that the AFM-11 alloy has a tensile strength exceeding 250 MPa. The FY 2014 project work will focus on the AFCT and AFM alloys and on processing methods to produce sufficient materials for fatigue testing and engine-component fabrication.

Project 18518 – Materials for High-Efficiency Engines

Agreement 25736 – Computational Design and Development of a New, Lightweight Cast Alloy for Advanced Cylinder Heads in High-Efficiency, Light-Duty Engines

Mike J. Walker
General Motors Research and Development Center
30500 Mound Road
Warren, MI 48090-9055
Phone (586) 651-3757; fax: (586) 986-9204; e-mail: mike.j.walker@gm.com

Qigui Wang
General Motors Powertrain Division
823 Joslyn Ave
Pontiac MI 48340-2925
Phone (248) 762-6332; fax: (248) 857-4441; e-mail: qigui.wang@gm.com

DOE Technology Manager: Jerry L. Gibbs
Phone (202) 586-1182; fax: (202) 586-1600; e-mail: jerry.gibbs@ee.doe.gov
Field Technical Manager: Aaron Yocum
Phone (304) 285-4852; e-mail: Aaron.Yocum@netl.doe.gov

Contractor: General Motors, LLC
Prime Contract No.: DE-EE0006082

Objectives

- Develop a high-performance, lightweight, cast alloy that will provide significant improvement (i.e., at least 25%) in both high-temperature strength and fatigue performance relative to the existing state-of-the-art aluminum alloys used in engine applications (such as B319 or A356), with a similar material density (less than 3 g/cm^3).
- Utilize Integrated Computational Materials Engineering (ICME) tools to design a new, lightweight cast alloy with ideal multi-scale structures and minimal propensity to form casting defects (such as porosity, oxides, and hot tearing).
- Make a direct comparison of the measured microstructures, physical, and mechanical properties to the predictions to validate and assess the current state-of-the-art and identification of gaps that exist for these materials and ICME tools.
- Develop comprehensive cost models to include materials production, component casting, heat treatment, and machining costs for annual production runs up to 500,000 units of cylinder heads using the new alloy.
- The team's goal is for the cost to be less than 105% of the cost of the same components made from the current alloys.

Approach

- Apply QuesTek's *iCMD*™ approach and General Motor's Virtual Cast Component Development (VCCD) methodologies to accelerate development of cylinder head castings made from the new alloy by a state-of-the-art semi-permanent mold sand casting process.

- Cast heats at multiple project stages to produce test samples and castings.
- Use traditional and the most advanced analytical characterization tools (such as Atom-Probe Microscopy) to quantify the microstructure and material properties of these castings for comparison with the predicted values and as a required input for both the design and the structural and durability analyses of an engine component.
- Conduct a casting trial on the production cylinder head castings to fully evaluate the capability of the alloy and process to achieve the project's stated goals.

Accomplishments

- Defined a material requirement matrix based on Department of Energy FOA targets and engine performance requirements to direct the alloy design.
- Identified five alloy concepts. The alloy concepts are being studied and evaluated for their potential to meet project targets in terms of room and high-temperature mechanical properties, fluidity, and hot tearing resistance.
- Produced multiple plate castings and evaluated the tensile properties from one of the alloy concepts.
- Cast plates and button coupons to evaluate the properties of another alloy concept.

Future Direction

- Identify a few more alloy concepts using DFT methods
- Identify elements that can reduce coarsening of aging hardening precipitates in the existing concept alloys using ICME methods.
- Continue process simulation of plate castings with concept alloys and predicting casting defects and mechanical properties, including fatigue.
- Continue casting test samples and plates and conducting tests of fluidity, hot tearing, and shrinkage to evaluate castability of concept alloys.
- Validate simulation predictions with the most advanced experimental and analytical tools available.
- Refine alloy concepts to more practical casting alloys.
- Optimize alloy and process conditions and determine optimal alloy chemical tolerance limits.
- Proceed to a full casting trial on the production engine head and evaluate tensile and fatigue properties.
- Develop cost models for alloy and head casting for a production level of up to 500,000/year.

Introduction

The U.S. Department of Energy: Energy Efficiency and Renewable Energy Program is targeting a 25% lighter powertrain by 2025 and a 40% lighter powertrain by 2050. As a result, the engine power density will be increased significantly. This will result in higher exhaust temperatures and a doubling of the cylinder peak pressures by 2050. To meet these requirements and achieve the stated goals, the properties of the state-of-the-art materials (such as cast aluminum alloys) must increase substantially. Historically, it has taken about 10 years to develop and implement a new alloy and it has taken about 100 years to improve the performance of a material such as cast aluminum by 50%. Thus, traditional methods of experimental trial and error are no longer sufficient. Fortunately, both computational and analytical methods have been vastly improved in the last few decades. ICME and advanced analytical tools (such as focused ion beam microscope, high-resolution scanning transmission electron microscope, and local electron atom probe) instruments are now available to accelerate the timeframe to develop new alloys.

Approach

State-of-the-art ICME tools (such as first principle calculations, computational thermodynamic and kinetic models, computational materials design, virtual casting modules, and commercially available casting process simulation, and structural and durability analysis software) will be used to design a new, lightweight cast alloy with ideal multi-scale microstructures and a minimum tendency for casting defects to achieve the desired high-temperature strength and fatigue performance requirements in complex castings. The *iCMD*™ method for developing concepts, modeling, validating, and progressing to a more refined state has been selected as the approach for this project. QuesTek's proprietary *iCMD*™ platform is a core modeling software system that integrates proprietary and commercial mechanistic modeling tools to facilitate rapid design and development of new materials (see Figure 1).

General Motor's VCCD Program uses integrated state-of-the-art modeling and simulation methodologies for cast aluminum components, starting from computational alloy and casting design, through casting and heat treatment process modeling and multi-scale defect and microstructure simulation, and culminating in casting property and durability prediction (see Figure 2).

Progress

At the first stage of the project, a material requirement matrix was developed to guide alloy development. The first generation of the matrix was based on property requirements in the original Department of Energy FOA, as well as the best achievable properties of current alloys. Improvements to the matrix were based on a design for six sigma (DFSS) optimization. Input variables for the finite element analysis included coefficient of thermal expansion (CTE), thermal conductivity, heat capacity, Young's modulus, and density. The analysis looked at the temperature in the valve bridge area, deck face flatness (distortion), mean and alternating stresses on the flame, and water jacket sides of the combustion chamber. The simulation analysis looked at both the dual overhead cam and overhead valve architectures.

In this first year of the project, five alloy concepts have been identified. Phase diagram simulations, diffusion calculations, heat treatment studies, and porosity simulations have been carried out on various alloys. Differential scanning calorimetry, optical microscopy, scanning electron microscopy, and local electron atom probe have been utilized in characterization of microstructure and solidification sequences. Along with baseline A356 and B319 alloys, "chill plate castings" have been made of two of the concepts. These chill plate castings are used to produce test samples for tensile and fatigue testing and microstructural analysis (Figure 3). The unique chill plate castings have various values of secondary dendrite arm spacing that cover the cooling rates that the production cylinder heads usually experience in casting. Cast buttons were also produced.

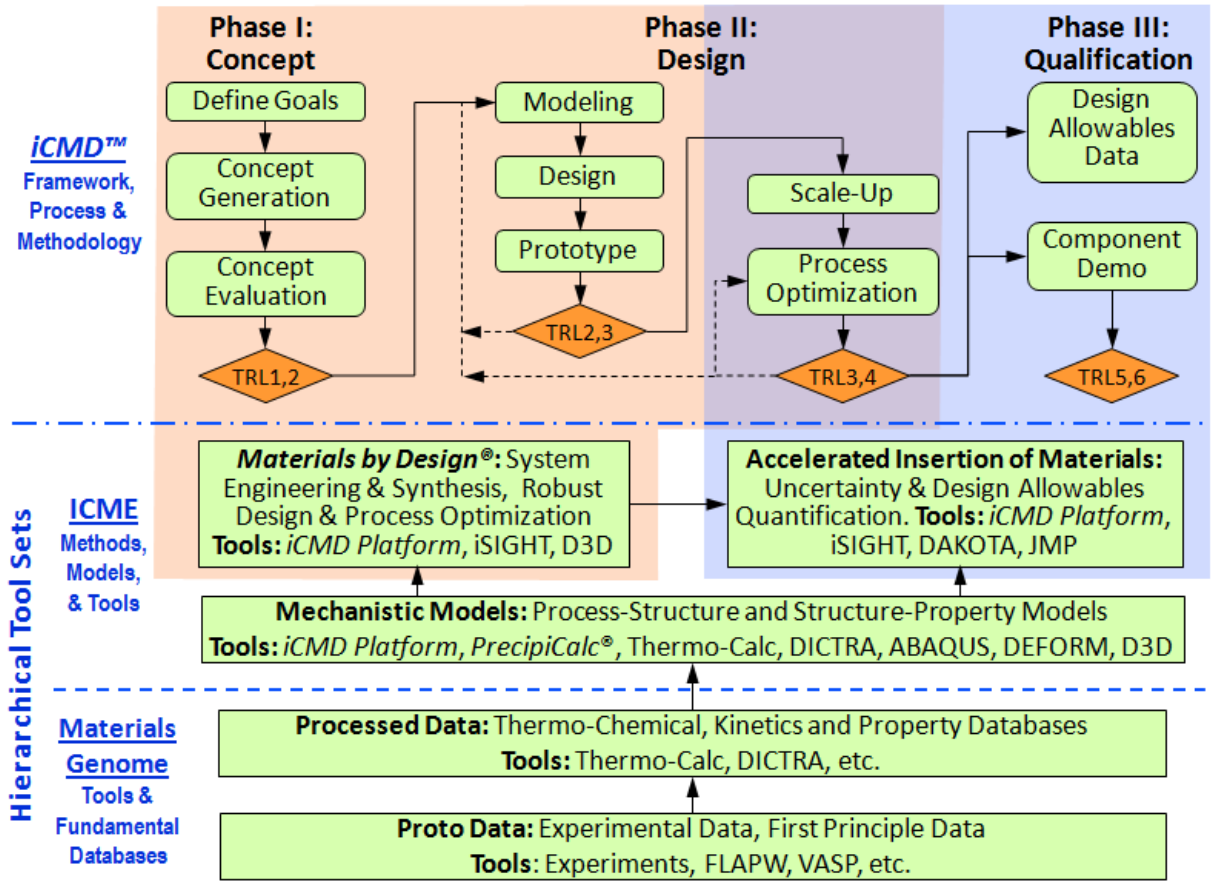

Figure 1. QuesTek's *iCMD*™ and ICME technology.

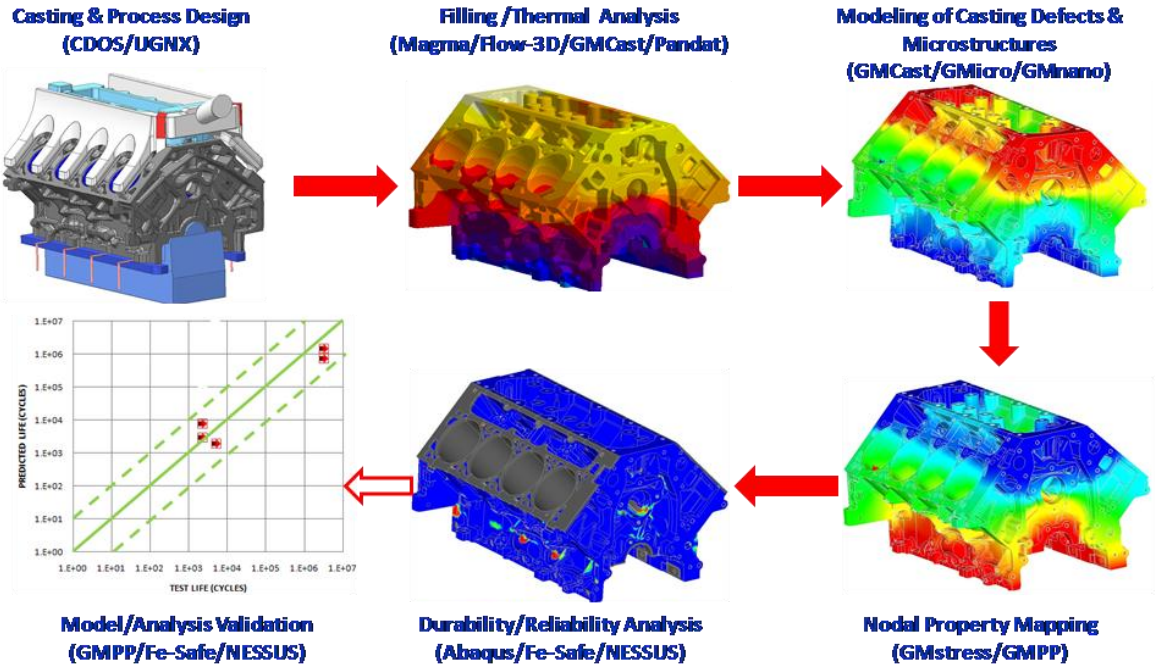

Figure 2. General Motor's VCCD modeling and simulation method for cast product property and life prediction.

Alloy buttons for four of the concepts have been produced. Those cast buttons are used to quickly evaluate the concepts and to generate data for the simulation models. Because castability of an alloy (such as fluidity, hot tearing resistance, and shrinkage) is also very critical to its success in making quality semi-permanent mold engine heads, N-Tek MetalHealth® Bench with fluidity, hot tear, and shrinkage molds, as well as General Motor's single slice engine casting, are being used to evaluate the castability of the alloys (Figures 4 and 5). To date, 38 chill plates, 12 fluidity castings, three single slice engine castings, and seven sets of alloy buttons have been produced. Tensile testing has been carried out on one of the alloy concepts and the two baseline alloys B319 and A356.

Figure 3. General Motors end-chill plate castings are used to make mechanical test samples at cooling rates similar to production head castings.

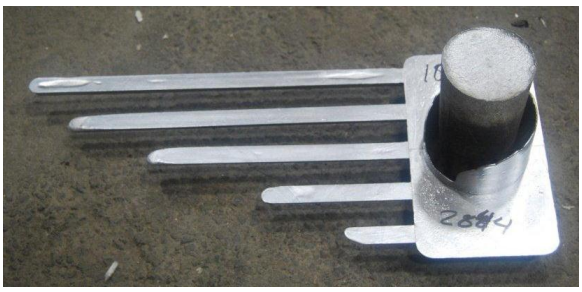

Figure 4. N-Tek MetalHealth® fluidity casting is used to evaluate the castability of the alloy.

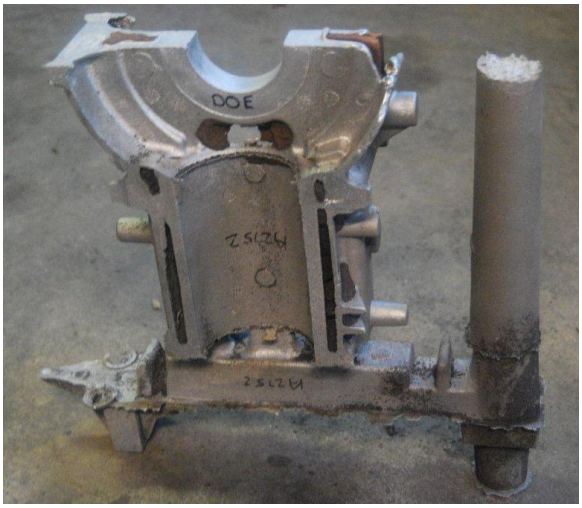

Figure 5. General Motors single slice block slice casting is used to evaluate castability in a complex geometry.

Results

The DFSS simulations identified thermal conductivity as the most important factor in determining the temperature in the valve bridges of the combustion chamber. Thus, thermal conductivity will be an important parameter in alloy design. Deck flatness is mostly affected by the coefficient of thermal expansion and to a lesser degree by thermal conductivity. Mean and alternating stresses are mostly impacted by Young's modulus and coefficient of thermal expansion. Based on this DFSS study, the materials requirement matrix has been revisited and is shown in Table 1. A second DFSS study, looking at nine input variables (including the thermal conductivity, ultimate tensile strength, strength coefficient, the hardening coefficient, and the low-cycle and high-cycle fatigue strengths at room and elevated temperatures), is being carried out to establish and identify the importance of room and high-temperature tensile and fatigue properties on engine performance.

Figure 6 compares the predicted microporosity of concept alloy #1 with the baseline alloys of A356 and B319. Looking at the bottom half of the plate (the material is used in mechanical property evaluation), the concept alloy #1 produces smaller micro pores than the B319 alloy and slightly larger pores compared with the A356 alloy.

Table 1. Revisited material requirement matrix.

Property	Temperature	Baseline	Targets		
		DOE Cast Aluminum *	DOE Cast Lightweight Alloy	GM Counter Proposal	Proposal Ranked Importance
Tensile Strength (MPa)	Room Temperature	227.5	275.8	349	8
	250 C	51.7	N/A	100	5
	300 C	N/A	65.5	65.5	19
Yield Strength (MPa)	Room Temperature	165.5	206.8	250	15
	250 C	34.5	N/A	82	16
	300 C	N/A	44.8	44.8	24
Plastic Elongation (%)	Room Temperature	3.5	3.5	> 2	9
	250 C	20	N/A	> 5	12
	300 C	N/A	< 20	> 5	25
Fatigue Strength at 10^7 cycles (MPa)	Room Temperature	58.6	75.8	86	13
	250 C	N/A	N/A	40	6
	300 C	N/A	N/A	29	20
Fatigue Strength at 10^4 cycles (MPa)	Room Temperature	N/A	N/A	200	14
	250 C	N/A	N/A	86	7
	300 C	N/A	N/A	60	21
Density (g/cm^3)	Room Temperature	2.7	< 6.4	< 3.0	4
Shear Strength	Room Temperature	179.3	206.8	206.8	26
Thermal Conductivity (mw / mm-C)	250 C	N/A	N/A	190	10
	300 C	N/A	N/A	210	22
Coefficient of Thermal Expansion (mm / mm-C)	250 C	N/A	N/A	2.25E-05	11
	300 C	N/A	N/A	2.31E-05	23
Fluidity (Die Filling Capacity / Spiral Test)		Excellent	Excellent	Same as 319	2
Hot Tearing Resistance		Excellent	Excellent	Same as 319	3
Manufacturing cost including alloy and processing			< 110% Baseline	< 105% Baseline	18
Corrosion resistance				GMW15272 for Underhood Vehicle Requirements (Neutral Salt Spray Testing) Compatibility with alternative fuels	17
Recyclability				Must comply with GMW3059 (GADSL: Global Automotive Declarable Substance List) GMW3116 Recyclability / Recoverability must be considered	1

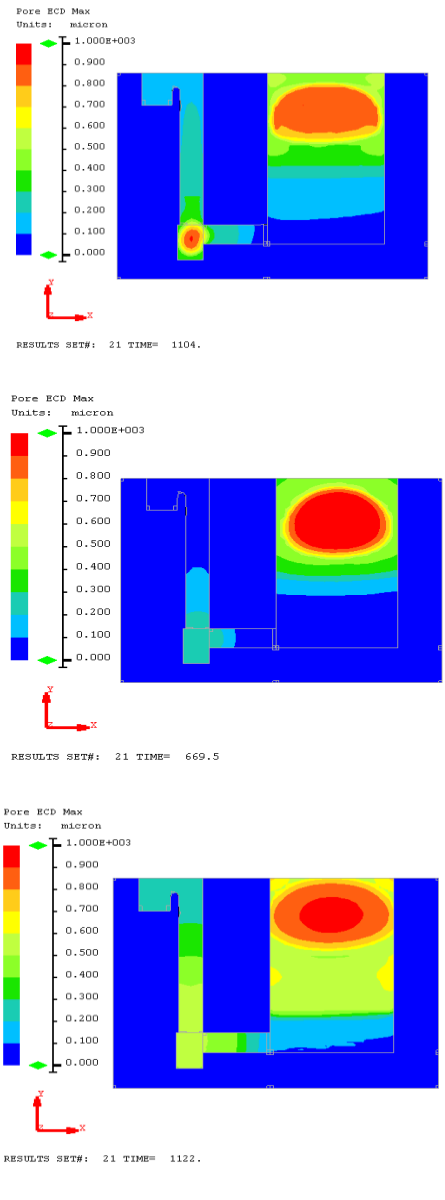

Figure 6. General Motor's VCCD tool simulated equivalent circle diameter of microporosity in the end-chill sand casting plate: (a) alloy concept #1, (b) A356, and (c) B319.

Mechanical testing of the concept #1 alloy shows excellent tensile strengths at room and elevated temperatures; however, elongation values are insufficient. Results are shown in Table 2. Microstructural analysis is now being carried out to establish the failure mechanisms. Efforts to reduce casting defects (such as porosity and oxides) will be explored using ICME tools and process optimization.

Table 2. Mechanical properties of concept alloy 1 measured from chill plate castings.

Test Temperature Celcius	UTS (MPa)	YS (MPa)	Plastic Elongation (%)
Room Temp	384	352	0.8
150 C	317	309	0.7
250 C	121	108	13.5
300 C	56	49	33

Conclusions

A material requirement matrix has been created to lead design of the new alloy. DFSS simulations have identified that thermal conductivity is the most important contributor to flame face temperatures in the combustion chamber.

To optimize material properties, a second DFSS trial will need to be conducted to determine the relative importance of room versus elevated temperature mechanical properties on engine performance.

Five alloy concepts have been identified to date and additional simulations are being performed to identify other potential concept alloys.

One alloy concept has progressed well into the casting and testing phase and, although the tensile strengths at room and high temperatures are excellent, ductility is insufficient to meet engine requirements. Further optimization of the casting and heat treatment process is needed to improve the ductility of the alloy concept.

Project 18518 – Materials for High-Efficiency Engines

Agreement 25737 – ICME Guided Development of Advanced Cast Aluminum Alloys for Automotive Engine Applications

Melissa Hendra
Research and Innovation Center
Ford Motor Company
2101 Village Road
Dearborn, MI 48121
Phone (313) 594-4714; fax: (313) 845-7307; e-mail: mhendra@ford.com

DOE Technology Manager: Jerry L. Gibbs
Phone (202) 586-1182; fax: (202) 586-1600; e-mail: jerry.gibbs@ee.doe.gov
Field Technical Manager: Mei Li
Phone (313) 206-4219; fax: (313) 390-0514; e-mail: mli9@ford.com

Contractor: Ford Motor Company, Dearborn, Michigan
Prime Contract No.: DE-EE0006020

Objectives

- To develop a new class of advanced, cost-competitive aluminum casting alloys, providing a 25% improvement in component strength relative to components made with A319 or A356 alloys using sand and semi-permanent casting processes for high-performance engine applications.
- To demonstrate the power of the Integrated Computational Materials Engineering (ICME) tools for accelerating development of new materials and processing techniques, as well as to identify the gaps in ICME capabilities.
- To develop comprehensive cost models to ensure that components manufactured with these new alloys do not exceed 110% of the cost using incumbent alloys A319 or A356.

Approach

- Comprehensive literature review on the mechanical properties and strengthening mechanisms of existing traditional state-of-the-art cast aluminum alloys in line with A319 and A356 alloys.
- Propose candidate alloys compositions that are likely to maximize the strengthening effect of precipitates, based on the existing qualitative knowledge in published literature and quantitative trends generated by ICME tools.
- Incorporate novel elements, at finely tuned levels, that could potentially enhance the high-temperature mechanical properties based on existing results in literature.
- Confirm the hypothesis by casting the materials and characterizing the mechanical properties.
- Optimize the final composition, based on the mechanical properties and other property criteria (castability).

Accomplishments

- Cast eight candidate alloys with commercially relevant compositions and different levels of novel elemental additions.

- Characterize the room temperature and high-temperature (300°C) strength and ductility of candidate alloys, which are close or better than the Department of Energy target.

Future Direction

- Detailed characterization of the type, morphology, size, volume fraction, and growth kinetics of precipitates observed in the candidate alloys via TEM.
- Adjust the composition of the initially proposed alloy composition, based on the attained mechanical testing results.

Introduction

Recent regulation on fuel economy of commercial vehicles has stimulated huge interests in incorporating new materials into automobiles. In this program, we aim to develop a new class of cast aluminum alloys that could possess both low-density and high-temperature capability (300°C), which are the two key factors for improving fuel efficiency. In this report, we provide results on the tensile property of several candidate alloys that we initially proposed.

Results

Alloy Fabrication

Six alloys (heat 2 through 7) with similar baseline composition, but different levels of novel elemental additions, were proposed and cast into torpedoes (Figure 1).

Figure 1. Casting of torpedo-shape ingots.

Heat Treatment

The 540°C/8-hour solution and 200°C/2-hour aging treatment (T6) were chosen for all alloys to give the peak hardness at an industry-relevant time scale. AS7GU alloys undergoing the same heat treatment also were included in this report to compare with our proposed alloys.

Tensile Property

The room temperature tensile property of heat 2 through 7 alloys is shown in Figure 2. The slightly decreased yield strength from heat 2 to heat 6 alloys and the much higher yield strength of AS7GU was confirmed to be caused by the difference in (Cu+Mg) levels in these alloys.

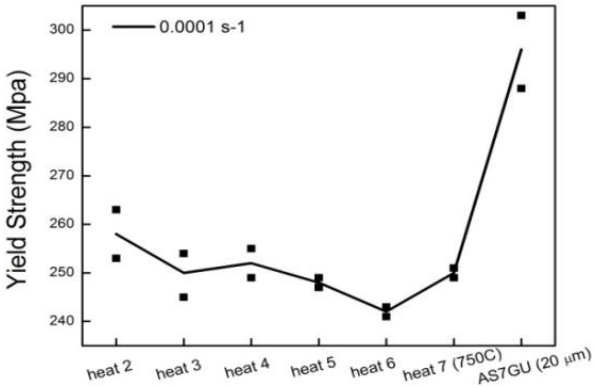

Figure 2. Room temperature yield strength of heat 2 through 7 alloys and AS7GU (T6).

The difference between heat 2 through 7 alloys and AS7GU was less pronounced when tested at 300°C (blue and black lines) (Figure 3). This difference is reversed when a 100-hours hold time at 300°C was applied prior to the tensile testing, with heat 4 and heat 7 alloys being stronger than AS7GU (red dots). This is believed to be related with the novel alloying additions in heat 2 through 7 alloys.

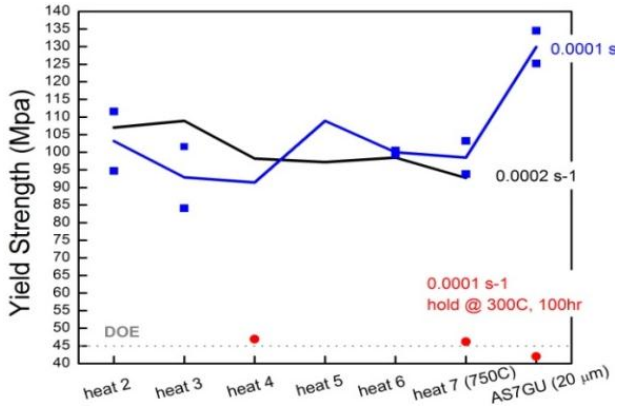

Figure 3. The 300°C yield strength of the heat 2 through 7 alloys and AS7GU (T6).

Microstructure Characterization

New precipitates were found in the tensile sample with the 100-hour hold time at 300°C (Figure 4).

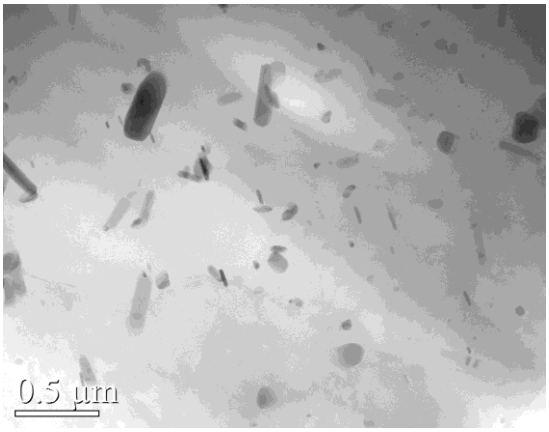

Figure 4. BF TEM image of precipitates formed during the 100-hour hold time at 300°C.

Conclusions

Optimal (Cu+Mg) levels are crucial for room-temperature strength, while novel elements are critical for high-temperature strength.

Project 18518 – Materials for High-Efficiency Engines

Agreement 26190 – High-Temperature Materials for High-Efficiency Engines

G. Muralidharan and B. Pint
Materials Science and Technology Division
Oak Ridge National Laboratory
P.O. Box 2008,
Oak Ridge, TN 37831-6068
Phone (865) 574-4281; fax: (865) 574-4357; e-mail: muralidhargn@ornl.gov

DOE Technology Manager: Jerry L. Gibbs
Phone (202) 586-1182; fax: (202) 586-1600; e-mail: jerry.gibbs@ee.doe.gov
ORNL Technical Advisor: J. Allen Haynes
Phone (865) 576-2894; fax: (865) 574-4913; e-mail: haynesa@ornl.gov

Contractor: Oak Ridge National Laboratory, Oak Ridge, Tennessee
Prime Contract No.: DE-AC05-00OR22725

Objectives

- Identify and catalog the materials property requirements for exhaust valves in next-generation, high-efficiency engines.
- Evaluate mechanical properties and oxidation resistance of leading, existing, nickel (Ni)-based alloys candidates and alternate materials with the capability to operate at temperature up to 950°C.
- Adopt integrated computational materials engineering-based techniques to develop alternate lower cost Ni-based alloys for exhaust valve applications at temperatures up to 950°C.

Approach

- Mechanical property requirements required for operation at 950°C will be defined and the microstructure required to achieve these properties will be identified.
- Oxidation tests will be performed to understand the composition effects on oxidation behavior and establish limits of critical elements.
- A synergistic computational modeling and experimental evaluation approach, followed in the design of new alloys for exhaust valve applications up to 870°C, will be refined and used to identify promising compositions for service at 950°C.
- Trial heats of new compositions will be prepared, properties measured, and compositions refined in an iterative manner.

Accomplishments

- An initial assessment of the tensile properties of several Ni-based alloys at 950°C has been completed.
- Oxidation behavior of several Ni-based alloys has been characterized at 800°C in air with 10% water vapor for times up to 250 hours.

Future Direction

- Understand the longer-term oxidation resistance behavior of candidate alloys and effect of alloying elements.
- Understand the effect of microstructure and tensile properties at 950°C.

Introduction

Improving the engine efficiencies of passenger and commercial vehicles is a major goal of the Vehicle Technologies Office and propulsion materials play a significant role in achieving this objective. One of the important strategies for improving engine thermal efficiency is by advancing technologies that increase engine combustion efficiency, which include lean-burn operation (High-Efficiency Clean Combustion), high levels of exhaust gas recirculation, turbocharging, variable valve actuation, and/or variable compression ratios. A barrier to achieving increased efficiency is the need to simultaneously reduce pollutant formation, achievable through high-efficiency combustion technologies. One potential method for achieving improved engine efficiency while reducing emissions is to retain more heat in the exhaust gas.

Strategies for retaining more heat in the exhaust naturally result in increased exhaust gas temperatures, thus increasing the operational temperature requirements of components in the exhaust gas path, including exhaust valves. It has been projected that exhaust gas temperatures would increase from a current value of 760°C to values of at least 870°C and very likely reaching near 1,000°C in the long-term. The availability of materials with adequate, high-temperature mechanical properties and oxidation resistance to enable the projected engine operating parameters without exceeding the cost constraints is a barrier to adoption of new high-efficiency technologies. The objective of this project is to address the needs of cost-effective materials for exhaust valves for operation up to 950°C.

A recently concluded project successfully addressed development of new lower cost alloys for use in exhaust valves at temperatures up to 870°C through a "materials-by-design" approach. "Materials-by-design" is a concept that encompasses a collection of materials-related techniques, including modeling, correlation, and materials modification. The premise behind materials-by-design is that mechanical properties are correlated to microstructure and phase chemistry. The phase composition and microstructure can be achieved through thermodynamic equilibrium or through non-equilibrium techniques such as quenching, rapid casting solidification, or mechanical working. These characteristics can be correlated to desired mechanical properties through computational equilibrium thermodynamics or through a variety of correlation techniques. The correlations allow untested compositions or treatments to be computationally modeled so that desired trends can be rapidly established. Small heats of targeted materials can be processed to confirm the modeled properties and to broaden the correlation database. Figure 1 captures the concepts in this approach.

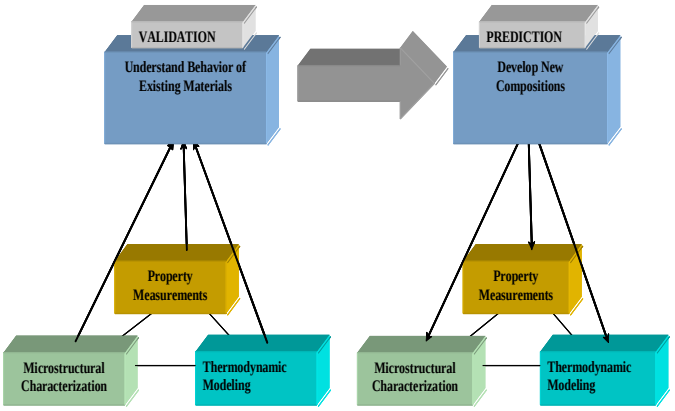

Figure 1. Overall approach for materials-by-design.

Exhaust valves, which are currently used at temperatures up to about 760ºC, are fabricated using Ni-based alloys such as alloy 751. Other high-performance, Ni-based alloys (primarily developed for aerospace applications) have the potential to operate at temperatures of 950ºC, with the desired strength and oxidation resistance; however, they may be too expensive for automotive applications. Therefore, new alloys with appropriate strength and oxidation resistance will have to be specifically developed for the operating characteristics and lifetime expectations of automotive valves.

In an earlier study on automotive valves for performance at 870ºC, a "materials-by-design" approach consisting of synergistic computational and experimental aspects was used to develop cost-effective, Ni-based alloys for use at this

temperature. High-temperature fatigue strength was identified as a critical factor in determining the performance of these alloys in valve application. An understanding of the strengthening mechanisms in existing commercial alloys was required to use the computational modeling approach to develop materials with improved properties and lower cost. A range of Ni-based alloys with potentially varying weight fractions (or volume fractions) of γ' were identified in efforts to correlate fatigue properties with the microstructure of the alloys. The selection of nine commercial Ni-based alloys included alloy 751, Waspaloy, Udimet 520, and Udimet 720 with Ni+Co contents ranging from 66 to 76 wt. %.

To obtain initial information on the microstructures of these alloys at equilibrium, thermodynamic calculations have been carried out. Comparison of the calculation results showed that all alloys have a matrix of γ, with the major strengthening phase as γ'. One or more carbide phases (such as $M_{23}C_6$, MC, and M_7C_3) may also be present in different alloys. The primary difference between the microstructures of the various alloys was the weight percent of the γ' phase at a given temperature and the highest temperature at which the γ' phase is stable in the different alloys. Because the size of the strengthening precipitates is also critical, it was anticipated that the kinetics of coarsening for this phase would be influential in the long-term performance of the alloys in this application.

Using the microstructures of these alloys as a guide, computational thermodynamics were used to design new alloys with a microstructure similar to the commercial alloys in an effort to obtain materials with desirable properties. In contrast to the commercially available alloys with Ni+Co contents greater than 66 wt%, the Ni+Co content in these newly identified candidate alloys was lower than 50 wt. % (Ni being replaced with other elements such as iron), with the potential to achieve comparable properties. The lower Ni content implies that the alloys would be of lower cost with the potential to achieve targeted fatigue life.

Based on the results of this computational alloy design process, small batches of the new lower-Ni candidate alloys were cast. The alloys were then homogenized and rolled at high temperatures. Small tensile specimens were machined from these alloys and tensile tests were conducted *in situ* at 870°C. Based on the results of the tensile tests, several of the candidate alloys from the newly developed suite of promising compositions with Ni+Co contents lower than 50 wt. % were down selected for the preparation of larger-sized heats. These were cast under inert gas cover and mechanically processed into plates for further machining. High-temperature fatigue tests were performed on the down-selected alloys. New alloys with fatigue lives of 100 million cycles at stresses of 25 to 30 Ksi at 870°C were identified and two invention disclosures have been filed.

The purpose of this newly initiated project is to extend this successful approach to the identification/development of materials for exhaust valves that could operate at temperatures up to 950°C. In addition to high-temperature mechanical properties (e.g., creep and fatigue), oxidation resistance is expected to play a role in determining the lifetime of exhaust valves at higher temperatures and will be considered in the identification/ development of new materials for exhaust valves. As part of this project, the required materials properties will be identified, baseline material properties will be evaluated, and the development of new materials will be targeted to achieve required properties at low cost. Initial work will be focused on Ni-based alloys. However, if properties and cost targets cannot be met, intermetallics will be considered as an alternate option.

Results

In an effort to understand the mechanical properties and oxidation resistance of candidate Ni-based alloys, high-temperature tensile testing and oxidation testing were initiated on selected commercial and newly developed Ni-based alloys. Figure 2 shows the effect of temperature on the tensile properties of baseline alloy and several developmental alloys. It can be observed that the yield strengths of the development

alloys at 870°C is about 41 to 51% of the yield strengths at room temperature, while the baseline alloy shows a more significant drop (about 38%) over the same temperature range. The yield strengths of the development alloys at 950°C are about 19 to 30% of the yield strengths at room temperature. These measurements will help identify alloys that show the least strength reduction, as well as the effect of alloying elements and microstructure in developing alloys with adequate strength at 950°C.

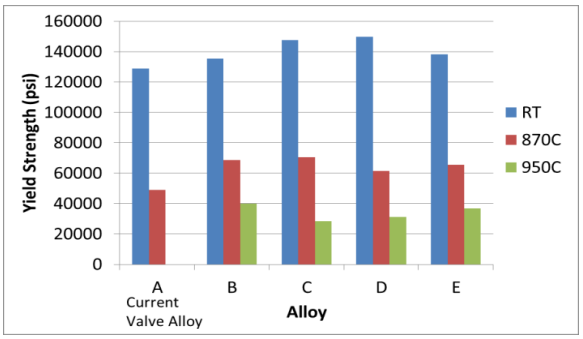

Figure 2. Tensile tests show a significant decrease in high-temperature strength when operating temperatures increase from 870 to 950°C.

Figure 3 shows the specific mass change in several development alloys and the higher Ni-baseline alloy 751 (which is currently used in exhaust valves) for oxidation exposure times of up to 250 hours. Note that the specific mass changes in all alloys studied were relatively small. However, small differences were observed in the specific mass changes in the various alloys over the exposure times. Longer time data will be obtained for these alloys and the effect of alloying element additions on the oxidation rates will be evaluated. Compositions of alloys will be modified based on the observed trends in the oxidation resistance of the alloys. It should be noted that all the development alloys have a higher yield and tensile strength at 870°C when compared to alloy 751. Furthermore, rotating beam fatigue tests at 870°C show that alloys 3 and 4 have significantly better fatigue life at 35 Ksi and lower stresses conducted in air than the baseline alloy 751. The impact of fatigue life and specific mass changes observed in laboratory tests in air with 10% water vapor must be correlated with exhaust valve performance.

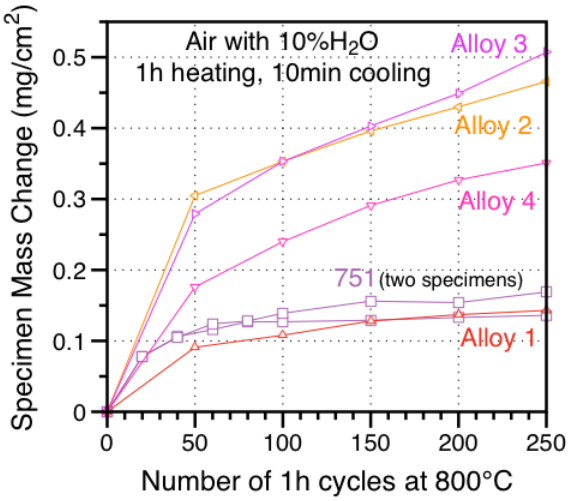

Figure 3. Specific mass change (mass change/ unit area) measured in several developmental alloys and baseline alloy 751.

Conclusions

A new project for developing exhaust valve materials for use at temperatures up to 950°C has been initiated. This project will adopt a synergistic approach that uses an experimental and computational methodology to develop cost-effective exhaust valve alloys for use at 950°C. High-temperature tensile tests have shown that the temperature dependence of yield strengths and the oxidation resistances of the development alloys as measured by specific mass changes are dependent on the compositions of the alloys. Further work will use computational methodologies to identify alloys with the required combination of oxidation resistance, high-temperature tensile, and fatigue properties.

Project 18519 – Materials for Exhaust and Energy Recovery

Agreement 9130– Development of Materials Analysis Tools for Studying NO_x Adsorber Catalysts (CRADA with Cummins Inc.)

Thomas R. Watkins, , Larry Allard, and Michael Lance
Oak Ridge National Laboratory
P.O. Box 2008, MS 6064
Oak Ridge, TN 37831-6068
Phone (865) 387-6472; fax: (865) 574-4913; e-mail: watkinstr@ornl.gov

Krishna Kamasamudram and Aleksey Yezerets
Cummins Inc.
1900 McKinley Av., MC 50183
Columbus, IN 47201
Phone (812) 377-4935; fax: (812) 377-7226; e-mail: Krishna.Kamasamudram@Cummins.com

DOE Technology Manager: Jerry L. Gibbs
Phone (202) 586-1182; fax: (202) 586-1600; e-mail: jerry.gibbs@ee.doe.gov
ORNL Technical Advisor: J. Allen Haynes
Phone (865) 576-2894; fax: (865) 574-4913; e-mail: haynesa@ornl.gov

Contractor: Oak Ridge National Laboratory, Oak Ridge, Tennessee
Prime Contract No.: DE-AC05-00OR22725

Objectives

- The objective of this effort is to produce a quantitative understanding of the process/product interdependence leading to catalyst systems with improved final product quality, resulting in diesel emission levels that meet the prevailing emission requirements.

Approach

- Characterize lab-engine tested samples with x-ray diffraction, spectroscopy, and microscopy. Correlate findings with Cummins, Inc. data and experience.

Accomplishments

- Clusters of Pt atoms in pre-particle state were observed to form nanoparticles during hydrotreatment.
- In-situ hydrothermal aging with HTXRD stage with gas-manifold system revealed catalyst is structurally stable under modest temperatures and 2 to 4 v% water content atmosphere.

Future Direction

- Quantify phases present in as-received and hydrothermally treated Cu-zeolite catalyst and quantify the impact of hydrothermal aging temperature and time on the spatial distribution of copper species in the Cu-zeolite and on platinum crystallite size and distribution.
- Correlate the fundamental degradation mechanisms identified by Oak Ridge National Laboratory with activity and selectivity in ammonia oxidation (evaluated at Cummins, Inc.) on select hydrothermally treated ammonia oxidation catalysts.

Introduction

Commercial off-the-shelf aftertreatment technologies are now available to meet the 2010 U.S. Environmental Protection Agency emission requirements for diesel exhaust (40 CFR 86). However, the performance of these technologies and their integration with engine control systems needs optimization. In particular, the catalytic materials can change or age with exposure to high temperatures and engine exhaust conditions. Consequently, Cummins, Inc. is working to understand the basic science necessary to effectively utilize these catalyst systems. Oak Ridge National Laboratory is assisting with the materials characterization effort. This report will focus on the study of materials used in ammonia oxidation.

Urea is added to diesel exhaust to reduce NO_x to N_2, as in selective catalytic reduction (SCR). The ammonia reduces NO_x to H_2O and N_2.[2] Excess ammonia is often needed, resulting in NH_3 escaping or "slip." This slip is a concern for sociability and environmental reasons. Although not regulated, proactive steps are taken to mitigate even small amounts of ammonia slip by employing a selective oxidation catalyst.

Oxidation catalysts are usually present in after treatment systems to oxidize ammonia that is not being oxidized upstream by the SCR catalysts. These oxidation catalysts ensure that ammonia slip to ambient is minimal and are referred to by several names: ammonia oxidation (AMOX) catalysts, selective catalytic oxidation catalysts, or ammonia slip catalysts. Candidate catalysts are typically zeolite-based, alumina-supported metal or alumina-supported metal oxide catalysts. Hydrothermal conditions, temperature, and water content strongly influence the functioning of these catalysts by changing or "aging" the catalytic materials. These changes and their impact on performance are not well understood.

Goals, Barriers, Relevance, and Integration

In the study area of the Vehicle Technology's Materials Technology subprogram, the Propulsion Materials Technology activity provides materials research and development expertise to enable advanced materials and supports the goals of several Vehicle Technologies subprograms (EERE 2010). Within the Advanced Combustion Engine research and development activity, one primary research and development direction is to develop aftertreatment technologies integrated with combustion strategies for emissions compliance and minimization of an efficiency penalty (EERE 2010). Correspondingly, one goal is to, by 2015, improve the fuel economy of light-duty gasoline vehicles by 25% and of light-duty diesel vehicles by 40%, compared to the baseline 2009 gasoline vehicle. In support of these, this project addresses four barriers related to emission control (EERE 2010): lack of cost-effective emission control, durability, cost (e.g., precious metal content), and improving market perception. This project is relevant to this goal because as the understanding of the material aging underlying AMOX catalyst performance degradation increases, efficient and durable AMOX with higher NO_x conversion efficiencies can be attained. This minimizes constraints on engine-out NO_x emissions and allowing engines to be tuned for optimal fuel efficiency, cost, and durability. This project supports clean diesel, which increases acceptance by the public. Larger acceptance, in turn, results in larger percentages of conversion to diesel, with the resulting reduction in petroleum usage/dependency on foreign oil (Hansen 2013, Ulrich 2013). Similarly, this project also addresses three barriers related to the Propulsion Materials Technology activity itself (EERE 2010): changing internal combustion engine combustion regimes, long lead times for materials commercialization, and costly precious metal content. This project is integrated within the Vehicle Technologies Office because it uses characterization tools acquired and formerly maintained by the High-Temperature Materials Laboratory Program.

Approach

The main focus of the cooperative research and development agreement in fiscal year 2013 was to continue characterization of a practically relevant zeolite AMOX catalyst, which was subjected to hydrothermal aging for lifetime

prediction model input. The technical approach will be as before, experimentally characterize materials supplied by Cummins, Inc. from all stages of the catalyst's lifecycle (i.e., fresh, de-greened, aged, regenerated, on-engine, and off-engine). The crystal structure, morphology, phase distribution, particle size, and surface species of catalytically active materials supplied by Cummins were characterized using transmission electron microscopy, x-ray diffraction (XRD), x-ray photoelectron spectroscopy, and Fourier transform-infrared spectroscopy. Ultimately, an understanding of the thermal and hydrothermal aging processes and other degradation mechanisms is sought throughout the lifecycle of the catalytic material.

Results

NH_3 Desorption and Oxidation of C-Zeolites (Kamasamadrum et al. 2013)

When targeting nearly complete conversion of NOx, the control of NH_3 slip from the SCR catalyst is challenging during transient operation. NH_3 slip from an SCR is minimized by oxidizing it over an AMOX catalyst. However, the selectivity of the AMOX catalyst to N_2 is imperfect.

In order to demonstrate the benefits in transient NH_3 slip control, a particular set of NH_3 storage and oxidation properties of a small-pore Cu-zeolite SCR catalyst were investigated. Temperature program desorption studies using a bench top reactor coupled with a Fourier transform-infrared spectroscopy spectrometer were conducted at Cummins, Inc. to understand the NH_3 desorption and oxidation characteristics of the Cu-zeolite SCR catalyst. Here, cylindrical core samples of Cu-CHA zeolite catalysts (1-in. diameter x 3-in. long) underwent NH_3-temperature program desorption under inert (N_2+8% H_2O+ 8% CO_2) and oxidizing (air: 10 vol% O_2+N_2+8% H_2O, 8% CO_2) environments while steady-state NO_x conversion was ongoing (SV =40kh^{-1}). A single Cu-zeolite core was progressively treated between 2 to 50 h at 600°C.

The black curves in Figure 1 show the desorption of NH_3 and oxidation of same to N_2 and H_2O in an inert N_2 atmosphere and later after hydrothermal aging in an oxidizing atmosphere. The NH_3 oxidation is under steady-state conditions. As a substantial amount of NH_3 desorbed above 375°C is oxidized, maximizing the overlap of the NH_3 desorption and oxidation curves is desired. Under practically relevant conditions, full saturation with NH_3 is virtually never realized. Coverage reflects the balance between rates of adsorption, desorption, and reaction, affected by NO_2/NO_x ratio, reaction temperature, etc. In Figure 1, the two discrete desorption profiles at about 275 and 400°C reflect weak and strong sites for absorption of NH_3, respectively. Hydrothermal aging decreased the extent of the desirable NH_3 desorption and oxidation curve overlap (black versus red curves). Thus, the population of weak NH_3 storage sites increased and the strong site population decreased (red curve without symbols). The NH_3 oxidation is shifting to higher temperatures due to copper agglomeration (see Figure 2). Overall, this represents a decrease in the NH_3 oxidation activity and sets forth further characterization efforts to examine the structural changes (adsorption/desorption) and Cu migration (oxidation) with XRD and spectroscopy techniques and advanced microscopy analysis, respectively.

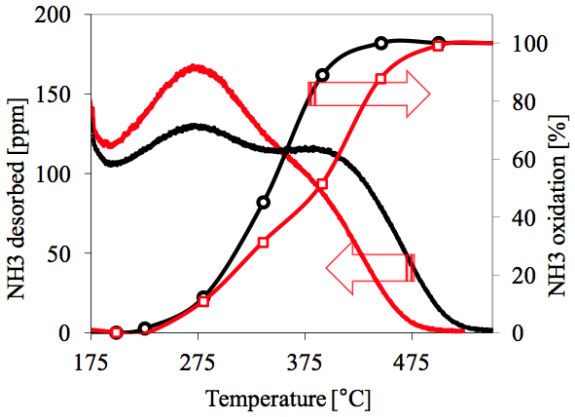

Figure 1. The NH_3 desorption and oxidation curves for the Cu-zeolite SCR catalyst in an inert atmosphere (black) and after hydrothermal gaining in an oxidizing atmosphere (red).

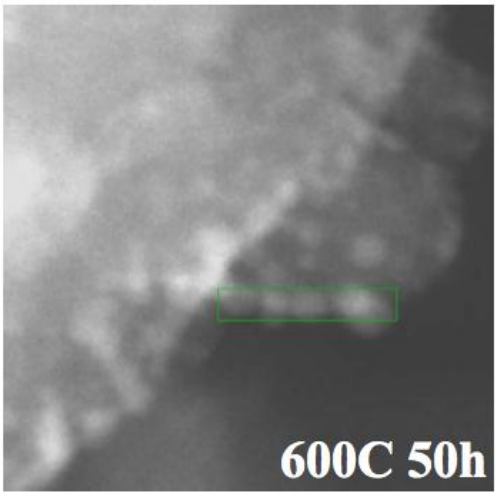

Figure 2. Cu-zeolite SCR catalyst after hydrothermal aging showing Cu particles agglomerating (see green rectangular outline) on the surface of a chabazite particle.

Microstructure and Chemistry of Cu-Zeolites

Initial studies of the structure of a zeolite SCR catalyst material identified it as a Cu-doped "chabazite" structure, with the primary interest being characterization of the behavior of Cu in the catalyst particles as a function of hydrothermal aging. The present report details the general structure of the catalyst and the methods for preparation of thin samples for high-spatial-resolution microchemical characterization using the JEOL 2200FS aberration-corrected electron microscope.

Figure 3 shows secondary electron images the Cu-zeolite SCR catalyst powder dispersed on carbon tape and imaged in the Hitachi S-4800 scanning electron microscope. The powder comprises single particles and small aggregates (Figure 3a) and at higher magnification (Figure 3b). Particles have a general cube-shaped morphology, characteristic of the chabazite phase. The single particle shown in Figure 3c is oriented to view directly down a cube edge, and appears to show a thin coating (such as seen at the arrow in 3c). Particles generally ranged from 2 to 5 μm in size. This thickness is too great for good imaging in the transmission electron microscopy, even at the 200-kV accelerating potential used in the JEOL 2200FS instrument, and with scanning transmission mode for both dark-field and bright-field imaging. Figure 4 shows an example of the latter method, on a small particle with an orientation similar to that of the SEM image of Figure 3c. The material coating the surface is easily visible in the bright-field image of Figure 4b (e.g., the thicker region at the arrow). Because of the size of the zeolite particles, it was impractical to obtain energy-dispersive x-ray spectra from the bulk material; therefore, thin sections were prepared (e.g., less than 0.2μm) of the particles by site-selective focused-ion-beam milling techniques.

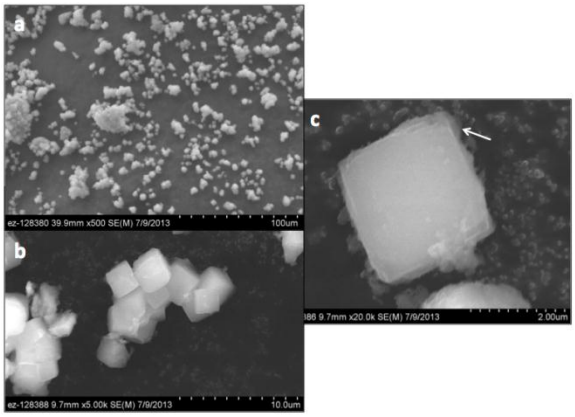

Figure 3. (a) Overall dispersion of Cu-zeolite SCR catalyst, mounted on a carbon tape and imaged in the scanning electron microscope (secondary electron image); (b) higher magnification showing a small aggregate of particles, each having a distinct cubic shape characteristic of the chabizite phase; and (c) an individual cube of chabazite, with the thin coating made visible at the arrow.

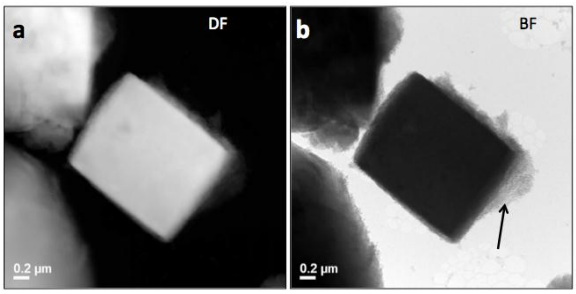

Figure 4. (a) Dark-field image of a chabazite cube on the order of the particle size in Figure 3, and (b) corresponding BF image. The outer coating determined to be AlO_x is seen at arrow.

Note that neither image in Figure 4 shows incontrovertibly the presence of voids in this particle.

Figure 5 shows a region of chabazite aggregates imaged with the electron beam in the Hitachi NB-5000 FIB mill. Particles were chosen that were oriented so that a focused ion beam (FIB) slice could be milled to produce a thin cross section, viewed essentially normal to an original face of the particle(s). The inset of Figure 5 shows a group of particles with layers of first carbon and then tungsten deposited over the aggregate to define the position of the FIB-milled slice, and to protect the underlying particles from damage by the incident Ga beam during the milling process. The initial carbon layer, nominally 200-nm thick, was deposited using the electron beam rather than the Ga beam; therefore, no Ga would embed in the particle surface. The final milling of the slice for the microscope was conducted at a FIB energy of 5 kV (versus 40 kV for initial cutting); again, this was done to minimize damage and Ga embedding in the surface layers of the slice.

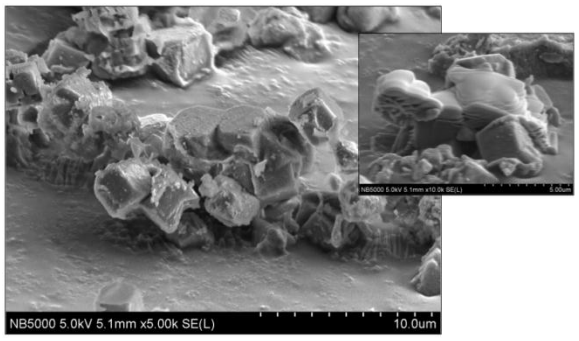

Figure 5. Powder particles dispersed onto C tape. Typical cluster of particles with reasonable orientation for FIB cross section. Inset shows particle group (different view direction) with layers of carbon and tungsten deposited, ready for Ga-beam milling.

Figure 6 is a composite of images from the energy dispersive spectroscopy (EDS) data acquisition of an as-received Cu-zeolite SCR catalyst material. The dark-field image shows contrast related to average atomic number; the brighter areas are higher atomic number than the darker areas. Holes in the FIB slice are labeled H and the outer edge (original surface) of the slice is the W layer, with the vacuum area labeled "vac." An interesting observation from the thin slice from the original bulk particle is that there are voids in the interior region of the chabazite crystal. The voids are obscured by the thickness of bulk particles, but easily revealed when a thin slice from the cross section of the particle is prepared. Outlined in green in the DF image is the area delineated for the EDS "hypermap," shown in the large color display of the overlapped individual "maps."

The hypermap is simply a multiply scanned data acquisition process in which every pixel in the scanned area (in this case, 350 × 350) builds up counts that contribute to a spectrum and thus permits post-acquisition data reduction to obtain the total spectrum for any area selected. It should be noted that the color display of the map of an individual element may contain artifacts, in particular, due to any overlap of peaks from elements present in significant concentrations in other areas of the map. To clarify, as an example, the individual maps in Figure 6 show not only W in the outer layer of the FIB specimen (in chartreuse color), but also Ga, Si, and Cu. However, if an area encompassing a major part of this outer layer is selected to display the total EDS spectrum from the area (Figure 7), it is clear that only W and Ga are present in any concentration. The Si map shows high counts in the W area simply because of the strong overlap of the SiKα peak (1.74 keV with the WMα peak 1.78 keV), whereas Cu counts in the W layer are due to contribution from the background counts in the region of the CuKα (8.04 keV) due to the strong WLα peak at 8.15 keV.

Finally, Ga is present in quantity in the W layer due to the use of the Ga beam to deposit the W layer originally, which causes Ga implantation. It is this effect that is eliminated from the actual sample particles by the e-beam-deposited C film, as described earlier. We see from Figure 7 the important result that there is virtually no Cu present in the spectrum due to artifacts from the electron optical column (such as x-rays being generated by any Cu-based components in the vicinity of the sample). The FIB slice was, in fact, affixed to a Be mount, because Be x-rays are not detected by the EDS

system. The standard mount for FIB samples is typically Cu, but use of that mount would compromise any analysis for distribution of Cu in the sample material. We conclude that hypermap data with these precautions to show Cu distribution is likely to be reliable.

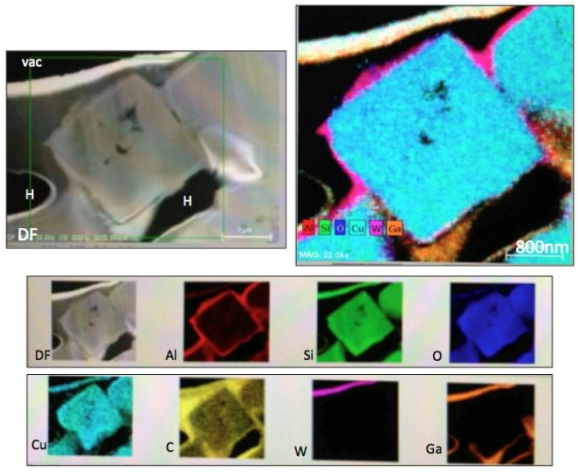

Figure 6. Dark-field (i.e., DF) image of chabazite FIB cross section, with color display hypermap overlap of Al, Si, O, Cu, W, and Ga elemental distributions and (lower) individual elemental maps from the same 350 × 350-px region.

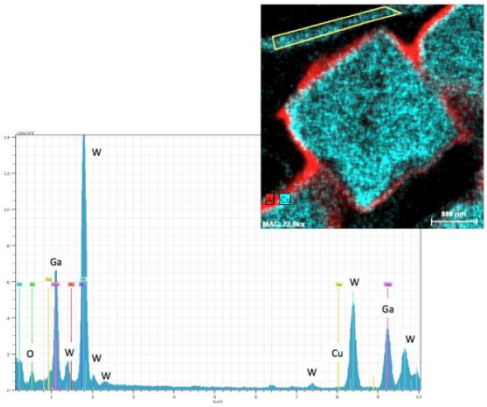

Figure 7. Elements in W layer (yellow outline), deposited during FIB prep. Primarily, W and implanted Ga are seen in the spectrum from the outlined area. Note that even with the high electron scattering from the heavy-element layer, essentially zero Cu is seen in the spectrum, indicating that the microscope systems peak for Cu is nil.

Given the above analysis, we made initial observations from the display of just the Al and Cu distributions in the FIB sample (Figure 8). The surface layer on the chabazite particle is AlO_x, as suggested by the strong Al intensity in the layer. The intensity display of Cu counts seems to indicate that the center region has a lower Cu concentration in general than the area near the surface. This observation is confirmed by comparing the EDS spectra from the center (a) and near the edge (b) areas shown respectively in Figure 8. With both spectra normalized to the SiKα peak, full scale, the Cu counts in the edge spectrum are seen to be higher than the Cu counts in the center region. Aluminum also has a stronger peak intensity in the near edge spectrum possibly due to the beam spread and impingement in the AlO_x layer coating the particle surface (thereby also increasing the counts in the O peak relative to the spectrum from the center region). Because the spectrum shown in Figure 7 from the W/Ga outer layer also shows essentially no Al, we conclude that the presence of an Al peak from the center region of the particle suggests that there is a small concentration of Al in the primarily silicate chabazite particle. These observations comprise the baseline for our further studies on the effects of hydrothermal aging (currently underway) at a series of elevated temperatures on the distribution of Cu in the chabazite zeolite material. These results will be reported in the quarterlies.

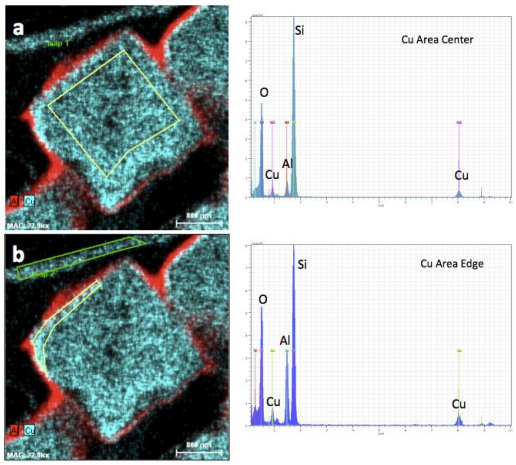

Figure 8. (a) Overlap of Al and Cu elemental maps, showing Al primarily in the outer coating. (b) Apparent higher Cu counts in the edge region are confirmed by the higher intensity Cu peak in the spectrum from the edge.

Thermogravimetric Analyzer, Raman, and XRD

A TA Instruments Q5000 thermogravimetric analyzer was used to measure the weight change in the Cu-zeolite SCR catalyst sample in order to understand water adsorption. Samples were first held in N_2 for 30 minutes in order to purge the room air from the furnace. The sample was then heated at 5°C/min up to 700°C in N_2. In addition to the Cu-zeolite sample, a ground cordierite (Corning Duratrap) and an empty Pt pan also were run in order to establish a baseline for the thermogravimetric analyzer equipment and to see how other materials outgas up to 700°C.

Figure 9A shows the absolute weight loss for the Cu-zeolite sample. The empty pan exhibited about 20 µg of weight change due to changes in buoyancy and the effect of heating on the balance; far smaller than the weight change of the Cu-zeolite sample. This establishes that the weight change measured on the catalyst sample does not come from equipment error. The cordierite powder had less than 1% weight loss in N_2 prior to the start of heating at 30 minutes. This low amount of weight loss likely comes from adsorbed water from these low surface area powders. Conversely, the fresh Cu-zeolite sample lost 8.5% of its weight prior to heating. This shows that the Cu-zeolite sample is retaining a large amount of water, which is readily evaporated at room temperature by immersing the sample in dry N_2. The large weight loss reflects the high specific surface area and cage of structure of the zeolite.

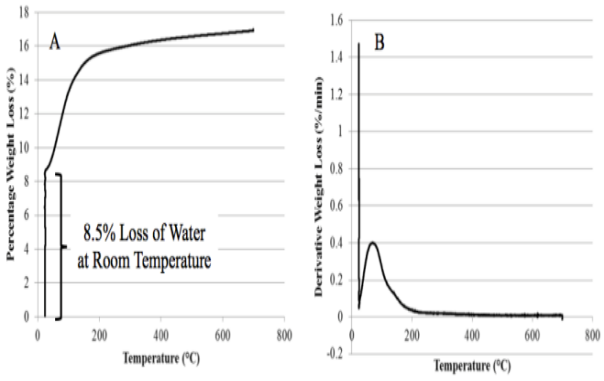

Figure 9. Weight loss of sample Cu-zeolite SCR catalyst sample in N_2 (A) and the derivative weight loss (B).

Figure 9B shows the derivative weight loss as a function of temperature. Once heating starts, the Cu-zeolite SCR catalyst powder loses about 7 wt% more water up to 200°C. These data show that the nascent catalyst powder is approximately 15 wt% water. In addition, Raman spectra were acquired on the sample before and after heating to 700°C in N_2 (see Figure 10). Peaks from adsorbed water were detected on both samples, but the intensity ratio of the water to SiO_2 peaks was about half after heating than before showing that Raman spectroscopy can detect changes in water concentration *in situ*. Future work will focus on using Raman to track structural/chemical changes during hydrothermal aging of catalyst samples.

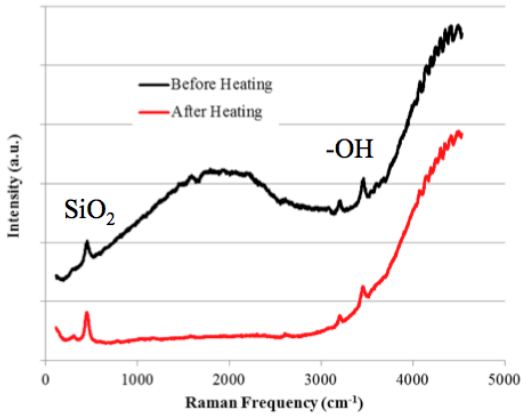

Figure 10. Raman spectra from the Cu-zeolite SCR catalyst sample before and after heating to 700°C in N_2. –OH peaks were present above 3,000 cm^{-1} and two SiO_2 peaks were present below 500 cm^{-1}.

The as-received Cu-zeolite SCR catalyst powder was hydrothermally aged in situ on a stage within an x-ray diffractometer in an atmosphere of 80% N_2, 10% O_2, 8% CO_2, 2 and 4 v%H_2O (each for 4 hours). Figure 11 shows the as-received x-ray diffraction pattern containing a "Chabazite" zeolite at ambient temperature and 550°C and some cordierite (from the support). After 4 hours at either 2 or 4 v% H2O, no appreciable change in peak positions and width, indicating that the zeolite structure is stable and any water desorption is minimal, respectively. This may be investigated

further. Figure 11 clearly shows negative thermal expansion as observed previously (Woodcock et al. 1999, Martinez-Inesta and Lobo 2005). Easily seen in Figure 11, the (101) intensity increase at elevated temperatures. This intensity increase and an interplanar spacing increase upon returning to room temperature immediately after exposure to high temperature is perhaps related to a de and rehydration process (Zema et al. 2008).

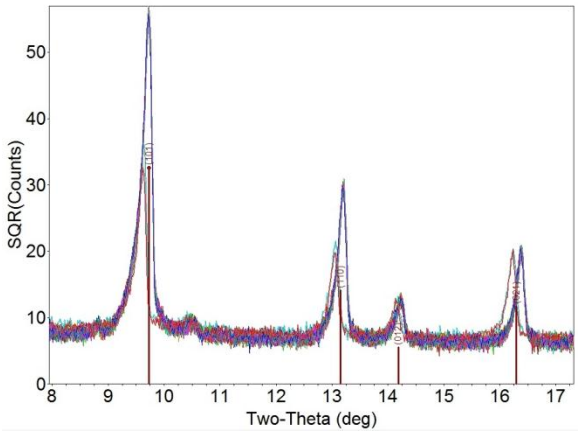

Figure 11. The x-ray diffraction patterns of Cu-zeolite SCR catalyst at ambient (2 scans) and at 550°C (48 scans).

Conclusions

The overlapping NH_3 storage and oxidation functions, observed in one of the Cu-CHA formulations, can potentially reduce NH_3 slip from the SCR catalyst. At least two distinct NH_3 storage sites are present in this Cu-CHA formulation; the feature was not universal to all Cu-CHA formulations. Progressive hydrothermal treatment at 600°C leads to a re-distribution of the NH_3 storage sites, wherein the weak storage site increases at the expense of the strong storage sites.

The above changes in Cu-zeolite catalyst functions reduces the extent of the desirable overlap between the NH_3 desorption and oxidation activity and a decrease in NH_3 oxidation activity. With careful sample preparations, elemental Cu can be mapped in a chabazite particle. Future work will be focused on analysis of the impact of hydrothermal aging on the changes in copper and zeolite structure using advanced microscopy and in situ XRD whose potential is demonstrated in this report.

Presentations

Watkins, T. R., L. F. Allard, M. J. Lance, H. M. Meyer, K. Kamasamudram, and A. Yezerets, 2013, "Catalyst Characterization," presented at the *DOE 2013 Vehicle Technologies Annual Merit Review and Peer Evaluation Meeting*, Washington, D.C., May 14, 2013.

Kamasamudram, K., N. W. Currier, A. Yezerets, T. Watkins, and L. F. Allard, 2013, "New Insights Into the Unique Operation of Small Pore Cu-Zeolite SCR Catalyst: Overlapping NH_3 Desorption and Oxidation Characteristics for Minimizing Undesired Products," presented by K. Kamasamudram at the *23rd North American Catalysis Society Meeting* held in Louisville, KY, June 6, 2013.

References

Chorkendorff, I. and J. W. Niemantsverdriet, 2003, *Concepts of Modern Catalysis and Kinetics*, Wiley-VCH Verlag GmbH & Co. KGaA, Weinheim, 395–400.

Code of Federal Regulations, 40 CFR 86 (7–1–10 Edition), 144–722.

EERE, 2010, *Multi-Year Program Plan 2011-2015*, Vehicle Technologies Office, DOE, 2.3-1, -2, -4, -5; 2.5-8 (http://www1.eere.energy.gov/vehiclesandfuels/resources/fcvt_plans_roadmaps.html).

Hansen, S., 2013, "U.S. Clean Diesel Auto Sales Increase 41% in August 2013, Hybrid Sales Jump 38%," *Diesel Technology Forum*, http://www.dieselforum.org/index.cfm?objectid=4FD0F215-1A56-11E3-95AC000C296BA163, September 11, 2013.

Kamasamudram, K., N. W. Currier, A. Yezerets, T. Watkins, and L. F. Allard, 2013, "New Insights Into the Unique Operation of Small Pore Cu-Zeolite SCR Catalyst: Overlapping NH3 Desorption and Oxidation Characteristics for Minimizing Undesired Products," presented by K. Kamasamudram at the *23rd North American Catalysis*

Society Meeting held in Louisville, KY, June 6, 2013.

Martínez-Iñesta M. M. and R. F. Lobo, 2005, "Investigation of the Negative Thermal Expansion Mechanism of Zeolite Chabazite Using the Pair Distribution Function Method," *J. Phys. Chem. B*, 109, 9389.

Ulrich, L., 2013, "Fossil-Fuel Mileage Champ," *New York Times*, http://www.nytimes.com/2013/07/21/automobiles/autoreviews/fossil-fuel-mileage-champ.html?_r=0&pagewanted=all, July 9, 2013.

Woodcock D. A. et al., 1999, "Negative Thermal Expansion in the Siliceous Zeolites Chabazite and ITQ-4: A Neutron Powder Diffraction Study," *Chem. Mater.*, 11, 2508.

Zema, M. et al., 2008, "Hydration/Dehydration and Cation Migration Processes at High Temperature in Zeolite Chabazite," *Chem. Mater.*, 20, 5876.

Project 18519 – Materials for Exhaust and Energy Recovery

Agreement 10461 – Durability of Diesel Particulate Filters (CRADA with Cummins, Inc.)

Thomas R. Watkins, Amit Shyam, Amit Pandey, and Hua-Tay Lin
Oak Ridge National Laboratory
P.O. Box 2008, MS 6064
Oak Ridge, TN 37831-6068
Phone (865) 387-6472; fax: (865) 574-3940; e-mail: watkinstr@ornl.gov

Randall J. Stafford
Cummins, Inc.
1900 McKinley Av., MC 50183
Columbus, IN 47201
Phone (812) 377-3279; fax: (812) 377-7050; e-mail: randy.j.stafford@cummins.com

DOE Technology Manager: Jerry L. Gibbs
Phone (202) 586-1182; fax: (202) 586-1600; e-mail: jerry.gibbs@ee.doe.gov
ORNL Technical Advisor: J. Allen Haynes
Phone (865) 576-2894; fax: (865) 574-4913; e-mail: haynesa@ornl.gov

Contractor: Oak Ridge National Laboratory, Oak Ridge, Tennessee
Prime Contract No.: DE-AC05-00OR22725

Objectives

- To identify and implement test techniques to characterize the physical and mechanical properties of ceramic substrates used as diesel particulate filters (DPFs), to identify the mechanisms responsible for the progressive thermo-mechanical degradation and resultant fracture of DPFs, and to develop analyses and provide data for simulation tools for predicting the long-term reliability and durability for the DPFs under engine operating conditions.

Approach

- Application of advanced characterization techniques to DPF ceramic substrates.
- Refinement of DPF service lifetime prediction models based on characterization of field-returned filters.

Accomplishments

- Determined the origins of the load-dependent Young's moduli and quantify the impact of the microstructure on the moduli.
- Completed characterization of the dynamic and static fatigue response of silicon carbide (SiC) DPFs.

Future Direction

- Investigate the loading and unloading response of select DPF materials in tension.
- Initiate characterization of the dynamic and static fatigue response under the temperature ranges relevant to the engine operating conditions of a fourth alternate substrate material.
- Initiate the determination of strength, fracture toughness, density/porosity/microstructure, and thermal expansion of a fourth alternate substrate material.

Introduction

The Environmental Protection Agency regulates emissions of nitrogen oxides and particulate matter (PM) from diesels engines. Stringent regulation on PM went into effect in 2007. There are many technologies designed to reduce emissions from diesel engines; prominent among the technologies for PM control are DPFs. A DPF is often a ceramic device that collects particulate matter in the exhaust stream. The high-temperature nature of the ceramic withstands the heat of the exhaust and allows heating to break down (or oxidize) the particles inside. DPFs reduce emissions of PM, hydrocarbons, and CO by 60 to 90%.

Most DPFs consist of a ceramic honeycomb with hundreds of cell passages partitioned by walls (Figure 1). Each cell passage has a square cell opening at one end and a plug at the other end so that the cell passages are alternately closed at each end. The so-called checkerboard plugging structure forces the exhaust gases through the porous, thin ceramic honeycomb walls. When the gases carrying the PM flow through the fine pores of the walls, the PM is filtered out. High porosity values, in the range of 40 to 70%, heighten filtration efficiency to more than 90% and reduce gas-flow resistance (back pressure) for better engine performance.

The process of diesel PM collection is continuous while the engine is operating. The particles are collected on the ceramic walls and, as a result, the backpressure of the system increases. The back pressure is reduced by oxidizing the trapped PM, aided by a catalytic reaction using exhaust gas heat at 400°C or more, into CO_2 and water vapor. This process is called regeneration and results in a cleaner filter. The regeneration process is dependent on exhaust temperature, oxygen, nitrogen oxide content, time, and PM levels.

The key to successful application of DPFs is to reliably regenerate the filter (e.g., to clean up the PM that the filter continues to trap or collect). Traditionally, combustion of soot is done in an oxygen atmosphere (air). In air, the soot will oxidize at about 500°C and up. However, this is not a typical operating temperature for diesel engine exhaust. Therefore, to oxidize soot in air, an active system (i.e., one that increases the temperature of the exhaust using some external heat source) is required. But if an active system is not carefully controlled, or if too much PM collects on the filter walls, the filters can experience an "uncontrolled regeneration," wherein the temperature increases to 600°C or more, resulting in damage to the filter element.

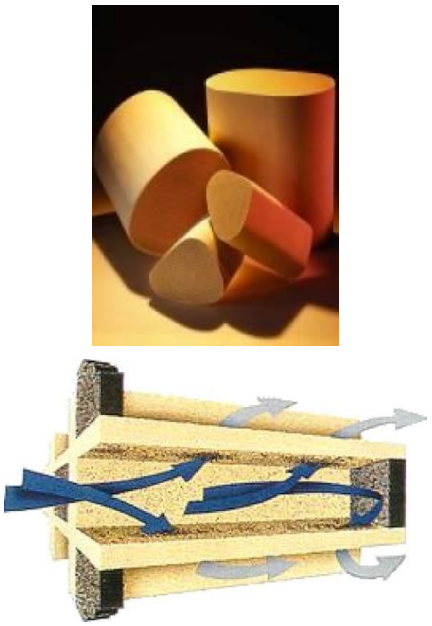

Figure 1. Top is an image of cordierite-based DPFs and bottom is a schematic of exhaust flow through a DPF.

The objective of this project is to identify and implement test techniques to characterize the physical and mechanical properties of ceramic substrates used as DPFs, to identify the mechanisms responsible for the progressive thermo-mechanical degradation and resultant fracture of DPFs, and to develop analyses and provide data for simulation tools for predicting the long-term reliability and durability for DPFs under engine operating conditions, particularly through the regeneration cycle.

Goals, Barriers, Relevance, and Integration

This work is in the study area of the Vehicle Technology's Materials Technology-Propulsion Materials Technology (EERE 2010) and

addresses the goal of, by 2015, developing materials that reduce the fuel economy penalty of particle filter regeneration by at least 25% relative to the 2008 baseline. This project addresses the following three barriers within Materials Technology, Propulsion Materials: changing internal combustion engine combustion regimes, long lead times for materials commercialization, and cost. It also addresses the following four barriers within Advanced Combustion Engine, Research and Development Combustion, and Emission Control Research and Development: lack of cost-effective emission control, lack of modeling capability for combustion and emission control, durability, and cost. This project is relevant to the goal and barriers because the thrust is to characterize the material properties and improve the durability and lifetime prediction, resulting in the lowest overall cost, while preventing emission release in service. This is achieved by understanding the relationships of the material properties for the filter substrates by characterizing the porosity, strength, elastic modulus, thermal conductivity, and thermal expansion, leading to improved regeneration strategies and fuel efficiency. This project supports clean diesel, which increases acceptance by the public by reducing unsightly diesel exhaust plumes. Larger acceptance, in turn, results in larger percentages of conversion to diesel, with the resulting reduction in petroleum usage/dependency upon foreign oil (Hansen 2013, Ulrich 2013). This project is integrated within the Vehicle Technologies Office because DPF substrate material is used in both DPF and catalyst systems and because it uses characterization tools that were acquired and formerly maintained by the High-Temperature Materials Laboratory Program.

Approach

The design process for making DPFs that are durable and reliable includes a complex materials property optimization and selection process (Adler 2005). For example, the porosity of DPFs, which allows the removal of PM from the exhaust gas stream, has a deleterious effect on their mechanical and fracture strength. However, a higher porosity decreases the engine backpressure and increases the efficiency of the diesel engine. Designing mechanically reliable DPFs is important because these components will experience demanding thermo-mechanical conditions during service. These include, for example, thermal shock resulting from rapid heating/cooling and thermal stresses that arise from temperature gradients.

Techniques for assessing the elastic and fracture properties of virgin or unexposed DPF substrates have been identified, implemented, and reported earlier (EERE 2012). The test techniques were applied to rank the suitability of common candidate substrates for application in DPFs. The developed test techniques were applied to characterize DPFs returned from field service. The material properties responsible for thermal shock resistance and mechanical property degradation in the various stages of the bathtub curve were determined. These properties include thermal expansion, thermal conductivity, heat capacity, density, porosity, elastic properties, strength, fracture toughness, and environmentally assisted crack growth at ambient and elevated temperatures in air and in relevant environments.

In turn, the information generated has been input into predictive models. These service life predictions are based on a combination of experimentally determined strength data, stress analyses of the component using a finite-element analysis, and selection of appropriate failure criteria. The durability (service life) of the component also can be predicted using this framework by considering the elastic behavior as a function of load.

Results-Young's Modulus

Wereszczak et al. (2012) were one of the first researchers to begin to address the discrepancies in the reported Young's moduli values for DPF materials, typically varying as a function of technique. The origin of these discrepancies is the non-linear nature of the stress strain curve in these materials (see Figure 2). In response to this, a combination of microtesting and non-contact digital image correlation (DIC) techniques (see Figure 3) were used to obtain the tensile stress-strain response in three porous, microcracked, DPF materials: siliconized SiC, cordierite (CO), and an

aluminum-titanate (AT)-based material. The open porosity values and microcrack densities were found to be 58.3, 50.4, and 51.9 vol.% and zero, medium, and high, respectively (see Figure 4). Three specimens were tested for each material (see Figure 3) and the Young's moduli are shown in Figure 5. The Young's moduli are determined from the initial linear portion of the stress-strain curve. Each data point in the stress-strain curves corresponds to the average of strains over the entire gauge area (i.e., over all of the virtual markers), which is approximately 4 x 2.4 mm (see Figure 6). The uniaxial tensile response of AT is found to be non-linear with a failure stress and strain of 0.9±0.15 MPa and 0.2%, respectively. In contrast, the mechanical response of CO and SiC "appear" to be linear with failure stresses of 2.9±0.1 and 6.2±0.5 MPa and failure strains of 0.03% and 0.04%, respectively. It is worth noting here that the failure strains may be underestimated in the present experiments because some specimens failed at the glued region due to the presence of stress concentrations.

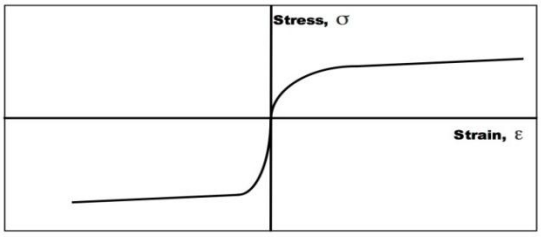

Figure 2. Schematic of a non-linear stress strain curve for a DPF material at low and high strain.

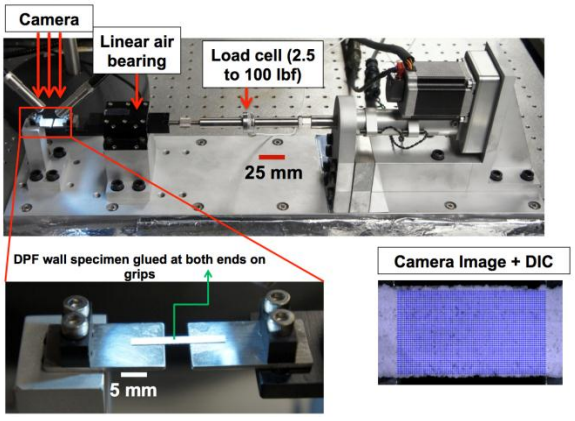

Figure 3. New microtesting rig determines the tensile response of a DPF plate pulled in simple tension and measured the strain using DIC.

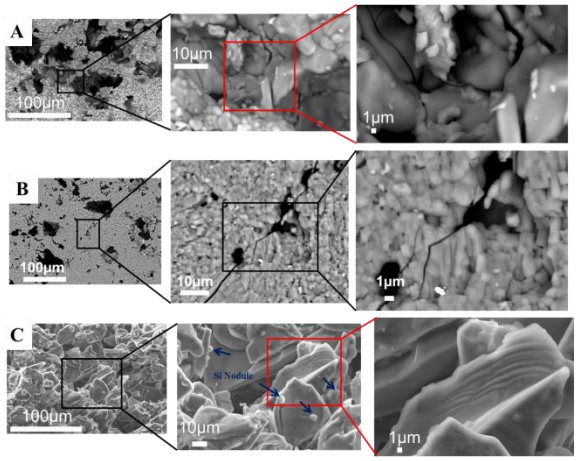

Figure 4. A series scanning electron microscopy micrographs showing how the microcrack density varies with material: (A) AT-based material has a high microcrack ρ and is 52% porous; (B) CO (Duratrap CO) has a medium microcrack ρ and is 50% porous; and (C) SiC-based material has no microcracks and is 58% porous.

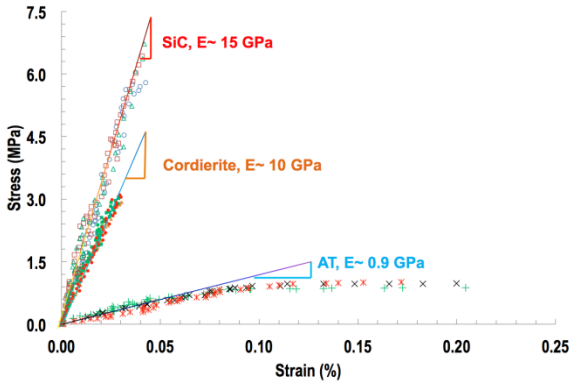

Figure 5. The stress as a function of strain for the three DPF materials investigated.

Given the non-linear nature of the stress-strain behavior of these materials, the linear elastic Young's modulus is not the best choice to describe the material response after low strain. Various definitions of modulus exist for materials with a stress-strain relationship that is non-linear. Figure 7 provides definitions of alternate terms. In Figure 8, the secant Modulus (E_s) decreases with increasing strain, ε, and indicates that as the load increases the microcracks and voids are increasingly operative. As such, microcracks could open more or slide. Permanent deformation or

non-recoverable damage also could occur near the cracks and voids. Note that the non-linearity increases with microcrack density. The compliant nature of these materials obviously contributes to their ability to withstand repeated thermal cycling without catastrophic failure.

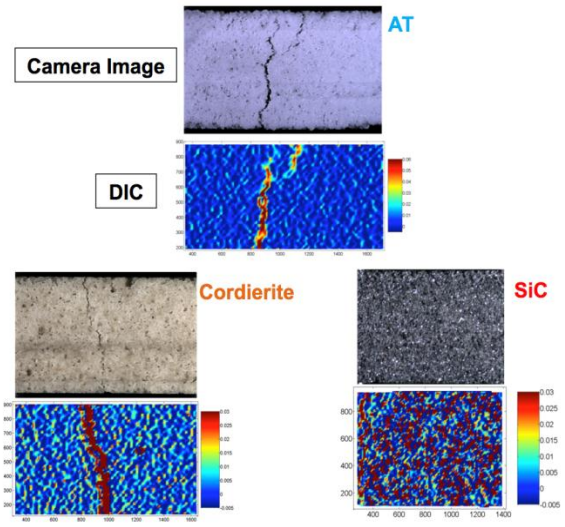

Figure 6. Optical images and two-dimensional DIC strain maps taken in situ during loading on the new microtesting rig. Here, the DIC displays localized strains near failure.

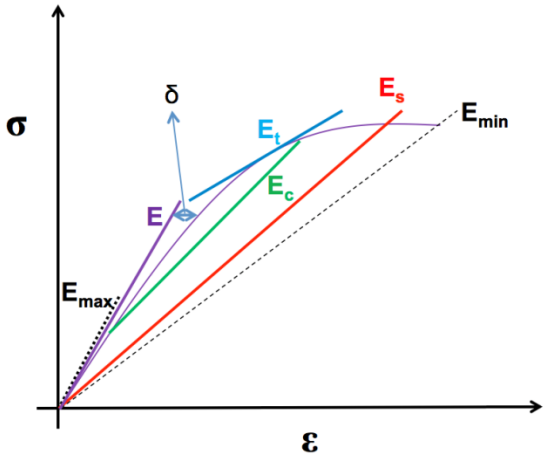

Figure 7. Modulus of elasticity/Young's modulus, E, is the linear portion of the engineering stress-strain curve below the proportional limit. Here, the proportional limit is defined as the stress corresponding to a 50-με deviation from linearity (δ) in the stress-strain curve. Es, Et, and Ec are the secant modulus, 6 tangent modulus, and chord modulus, respectively.

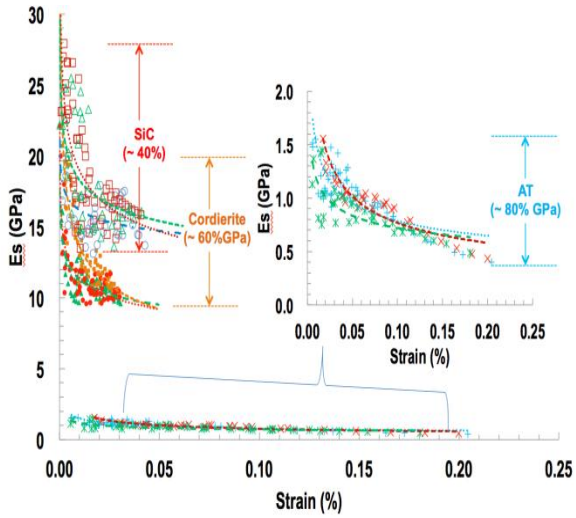

Figure 8. The secant modulus (Es) as a function of strain for the three DPF materials investigated. Inset shows an expanded view of the response of the AT-based material.

Results

SiC

During this fiscal year, additional SiC DPF bend bars with 4 x 3 cell and 6 x 3 cell size were tested under the stressing rates, ranging from 3 to 3 x 10^{-6} MPa/s and at test temperature of 600, 800, and 900°C. These additional tests were critical in order to obtain a useful statistical result for probabilistic DPF component optimization and lifetime prediction carried out by Cummins, Inc. The dynamic fatigue responses of SiC DPF bend bars with 4 x 3 and 6 x 3 cell size are presented in Figure 9. Note that the room temperature fracture strength of 4 x 3 and 6 x 3 cell size samples are 13.9±3.3 MPa and 13.5±2.6 MPa, respectively. The dynamic fatigue results obtained with additional test bend bars showed that there is no size scaling effect (4 x 3 versus 6 x 3 cell size) on the measured fracture strength under the test conditions employed in the present study. Mechanical results for both cell sizes of SiC DPF bend bars showed that there was no stressing-rate dependence of flexural strength (from 3 to 3 x 10^{-6} MPa/s) at 600°C in air. However, results obtained at temperatures of 800 and 900°C showed that there was a minor increase in flexural strength with decreasing stressing rate (from 3 to 3 x 10^{-4} MPa/s), while

there was no apparent change in measured fracture strength from 3 x 10^{-4} to 3 x 10^{-6} MPa/s. As stated before (EERE 2012), the detailed scanning electron microscopy study showed that there was an apparent increase in thickness and extent in oxide (SiO_2) scale formation due to oxidation of SiC at a higher temperature (e.g., 600 vs. 900°C, see Figures 10 and 11, respectively) in an oxidizing environment. The increased oxidation reaction could possibly promote the sealing of defects (such as pores and cracks) present in the as-received SiC DPF components, thus resulting in an increase in fracture strength measured in this study.

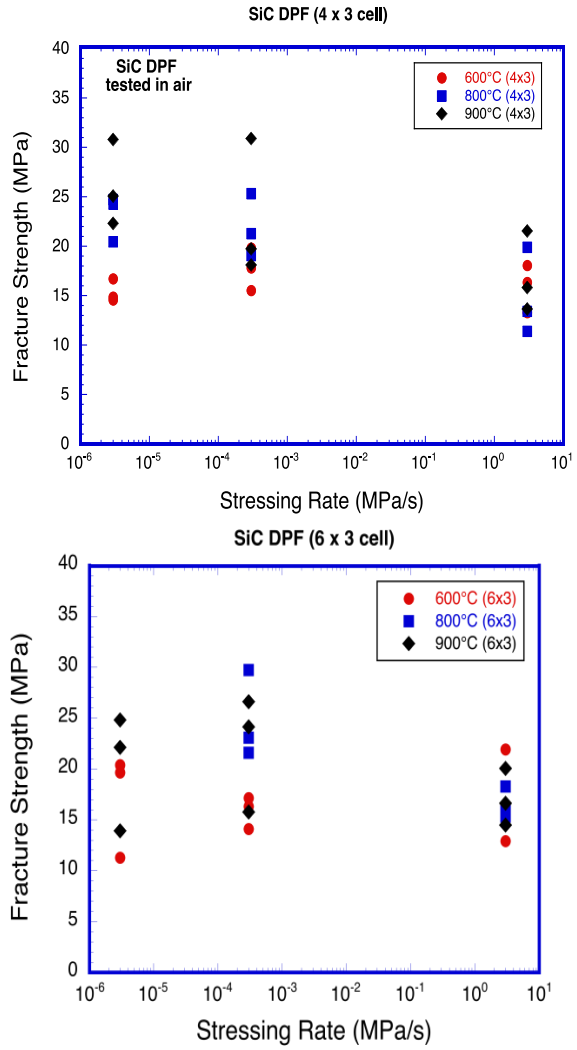

Figure 9. Fracture strength versus stressing rate curves of SiC DPF samples tested as a function of test temperature.

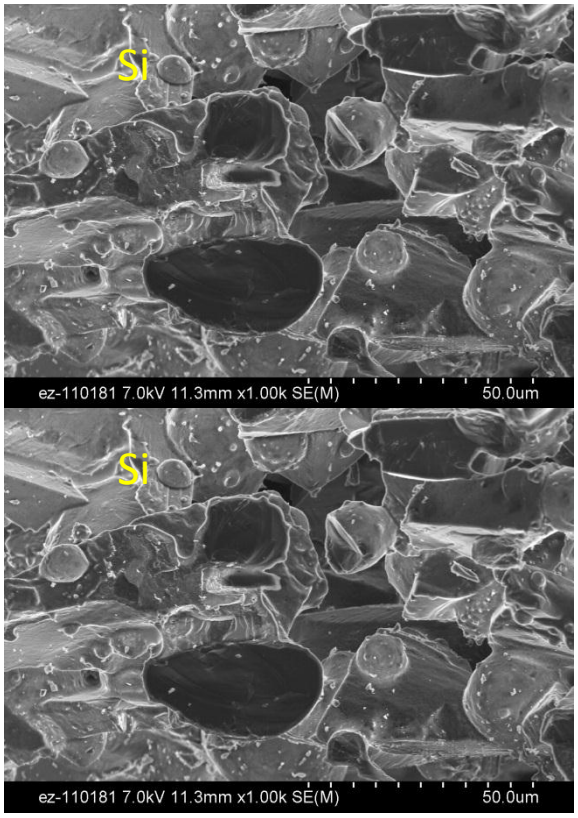

Figure 10. Fracture surfaces of SiC DPF tested at 600°C at a 3 x 10^{-6} MPa/s loading rate. Nodules of free silicon are evident.

Conclusions

The stress strain response of three DPF materials was examined in simple tension using a new microtesting rig, wherein a DPF plate is pulled in simple tension and the strain is measured using DIC. The non-linear stress strain behavior of these materials is a function of both the porosity and microcrack density. As the microcrack density increases, the secant modulus decreases as more defects become "activated" in the load sustaining state (i.e., as the load increases, the DPF materials become more compliant). The characterization of the dynamic and static fatigue response of SiC DPFs also was completed, wherein it was observed that the fracture strength increases with temperatures above 600°C and with a decreasing loading rate. The mechanism thought to be active here is the formation of a glassy phase, which fills in and heals the pre-existing cracks.

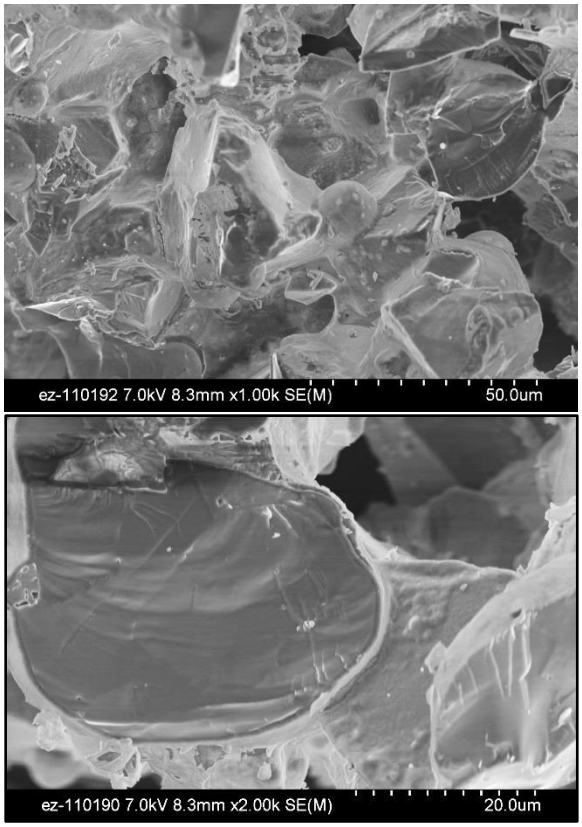

Figure 11. Fracture surfaces of SiC DPF tested at 900°C at a 3 x 10^{-6} MPa/s loading rate.

Presentations

Invited Presentation: Pandey, A., A. Shyam, T. R. Watkins, E. Lara-Curzio, and R. J. Stafford, 2013, "Uniaxial Tensile Response of Microcracked Porous Ceramics," presented at the *37th International Conference on Advanced Ceramics and Composites Meeting* held in Daytona Beach, FL, January 29, 2013.

Watkins, T. R., A. Shyam, H. T. Lin, E. Lara-Curzio, A. Pandey, and R. Stafford, 2013, "Durability of Diesel Engine Particulate Filters," presented at the *DOE 2013 Vehicle Technologies Annual Merit Review and Peer Evaluation Meeting*, Washington, D.C., May 14, 2013.

Publications

The following manuscript is accepted for publication in the *Journal of the American Ceramic Society*: Pandey, A., A. Shyam, T. R. Watkins, E. Lara-Curzio, R. J. Stafford, and K. J. Hemker, "The Uniaxial Tensile Response of Porous and Microcracked Ceramic Materials."

References

Adler, J., 2005, "Ceramic Diesel Particulate Filters," *International Journal of Applied Ceramic Technology*, 2, [6], 429–39.

EERE, 2010, *Multi-Year Program Plan 2011-2015*, Vehicle Technologies Office, DOE, December 2010, 2.3-4; 2.5-7, 8. (http://www1.eere.energy.gov/vehiclesandfuels/resources/fcvt_plans_roadmaps.html).

EERE, 2012, *Propulsion Materials Annual Progress Reports*, Vehicle Technologies Office, US DOE, Energy Efficiency and Renewable Energy, Office of Vehicle Technologies, www.ornl.gov/sci/propulsionmaterials/Reports.html.

Hansen, S., 2013, "U.S. Clean Diesel Auto Sales Increase 41% in August 2013, Hybrid Sales Jump 38%," *Diesel Technology Forum*, http://www.dieselforum.org/index.cfm?objectid=4FD0F215-1A56-11E3-95AC000C296BA163 (September 11, 2013).

Ulrich, L., 2013, "Fossil-Fuel Mileage Champ," *New York Times*, http://www.nytimes.com/2013/07/21/automobiles/autoreviews/fossil-fuel-mileage-champ.html?_r=0&pagewanted=all, (July 19, 2013).

Wereszczak, A., E. Fox, M. Lance, and M. Ferber, 2012, "Failure Stress and Apparent Elastic Modulus of Diesel Particulate Filter Ceramics," *SAE Int. J. Mater. Manuf.*, 5, (2), 517–27.

Project 18519 – Materials for Exhaust and Energy Recovery

Agreement 10635 – Catalysis by First Principles

C. K. Narula and M. Moses-DeBusk
Oak Ridge National Laboratory
P.O. Box 2008, MS 6133
Oak Ridge, TN 37831-6068
Phone (865)574-8445, email: narulack@ornl.govl

DOE Technology Manager: Jerry L. Gibbs
Phone (202) 586-1182; fax: (202) 586-1600; e-mail: jerry.gibbs@ee.doe.gov
Field Technical Manager: J. Allen Haynes
Phone (865) 574-2894; fax: (865) 574-4913; e-mail: haynesa@ornl.gov

Contractor: Oak Ridge National Laboratory, Oak Ridge, Tennessee
Prime Contract No.: DE-AC05-00OR22725

Objectives

- The objective of this work is to search for durable emission treatment catalysts, including lean NOx traps, three-way catalysts, oxidation catalysts, and selective catalytic reduction (SCR) catalysts from a protocol based on the following:
  - An integrated approach between computational modeling and experimental development
  - Design and testing of new catalyst materials to rapidly identify the key physiochemical parameters necessary for improving the catalytic efficiency of these materials.

Approach

- Theoretical and experimental studies of Pt clusters supported on alumina and metal-exchanged zeolites. Interaction of CO, NOx, and HC with Pt clusters supported on alumina and NOx reduction on zeolites.
- Understand non-structural changes in a catalyst under operating conditions and correlating the changes to performance.

Accomplishments

- We completed theoretical and experimental studies to show that single atoms of Pt on θ-alumina are catalytically active for CO oxidation.
- We have shown that Ni (like Pd) prefers surface over core, even for a 4-atom Pt_3Ni supported cluster, and it stabilizes Pt. The experimental studies to validate the results are in progress.
- Our first principles studies offer a rationale for explaining decreased NO oxidation with a decrease in Pt particle size and also predict that single supported Pd will be a better catalyst than single supported Pt. Experimental studies are in progress to validate the prediction.
- We have shown that heterobimetallic zeolites, which are excellent low-temperature catalysts, can be synthesized by the incipient wetness method. The resulting zeolites formed by incipient wetness and ion-exchange methods are identical and exhibit identical low temperature NOx reduction activity under fast SCR conditions.

Future Direction

- Guided by our results, conduct synthesis and evaluation of new durable supported catalysts for lean NOx catalysts and other systems (e.g., three-way catalysts and oxidation catalysts for diesel).
- Focus on the low-temperature NOx catalyst that is effective, even under the standard NOx reduction catalyst.
- Scale up and preparation for engine testing of the CuFe-SSZ-13 catalyst as a low-temperature NOx reduction catalyst for diesel engines.

Introduction

This research focuses on an integrated approach between computational modeling and experimental development, design, and testing of new catalyst materials, which we believe will rapidly identify the key physiochemical parameters necessary for improving the catalytic efficiency of these materials.

The typical solid catalyst consists of nanoparticles on porous supports. The development of new catalytic materials is still dominated by trial and error methods, even though the experimental and theoretical bases for their characterization have improved dramatically in recent years. Although it has been successful, the empirical development of catalytic materials is time consuming and expensive and brings no guarantees of success. Part of the difficulty is that most catalytic materials are highly non-uniform and complex and most characterization methods provide only average structural data (Figure 1). Now, with improved capabilities for synthesis of nearly uniform catalysts, which offer the prospects of high selectivity, combined with state-of-the science characterization methods, we have a compelling opportunity to markedly accelerate the advancement of the science and technology of catalysis.

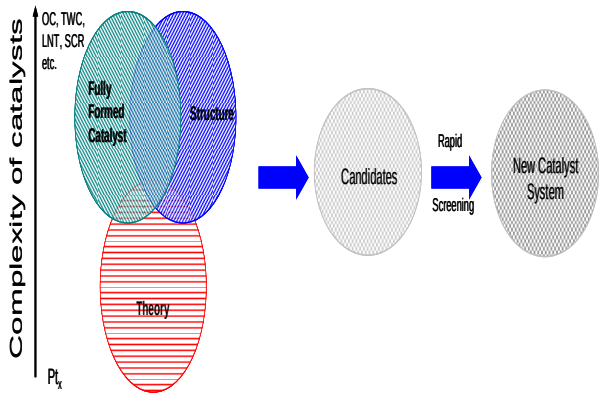

Figure 1. Complexity of catalysis.

Computational approaches, on the other hand, have been limited to examining processes and phenomena using models that had been greatly simplified in comparison to real materials. This limitation was mainly a consequence of limitations in computer hardware and in the development of sophisticated algorithms that are computationally efficient. In particular, experimental catalysis has not benefited from the recent advances in high-performance computing that enables more realistic simulations (empirical and first-principles) of a large ensemble of atoms, including the local environment of a catalyst site in heterogeneous catalysis. These types of simulations, when combined with microscopic and spectroscopic characterization of catalysts, can lead to a much deeper understanding of the reaction chemistry that is difficult to decipher from experimental work alone.

Thus, a protocol to systematically find the optimum catalyst can be developed that combines the power of theory and experiments for the atomistic design of catalytically active sites and can translate the fundamental insights gained from modeling directly to a complete catalyst system that can be technically deployed.

Although it is computationally challenging, the study of surface, nanometer-sized, metal clusters may be accomplished by merging state-of-the-art, density-functional-based, electronic structure techniques and molecular dynamic techniques. These techniques provide accurate energetics, force, and electronic information. Theoretical work must be based on electronic-structure methods, opposed to more empirical-based techniques; this provides realistic energetics and direct electronic information.

It is conceivable that "computationally complex but experimentally simple" system can be examined by both theoretical models and experimental work to forecast improvements to obtain optimum catalyst systems.

Approach

Theoretical modeling is based on DFT studies of Pt group metals (i.e., Ni, Pd, and Pt) supported on θ-alumina. The rationale for choosing θ-alumina for the model is that the distribution of platinum on γ-alumina and θ-alumina and their CO oxidation activity is identical. This led us to propose that Pt

supported on θ-alumina is a better model for Pt supported on γ-alumina than Pt supported on α-alumina or simplified models of γ-alumina. We have completed the structural study of Pt group atoms supported on θ-alumina and modeled CO and NO oxidation on supported single Pt and Pd atoms.

Experimentally, we have synthesized and characterized single atoms of Pt supported on alumina and shown them to be catalytically active toward CO oxidation. We will complete NO oxidation studies on single-supported Pt and Pd atoms in the coming quarters.

We previously reported on a theoretical and experimental study of palladium stabilization of platinum in Pt-Pd nanoparticles. Now, our theoretical work suggests that Ni, which is significantly less expensive than Pd can also stabilize Pt. Experiments to validate this finding are in progress.

In addition, we have found a new, simple, economical route to heterobimetallic zeolites, which we have shown to be excellent low-temperature NO_x reduction catalysts under fast NH_3-SCR conditions.

Finally, guided by the theoretical models of Pt-Pd, we are initiating a new set of catalyst materials with higher durability under operating conditions in FY 2014.

Results

Until recently, our theoretical studies have focused on supported noble metals. We have shown that single platinum atoms supported on θ-alumina slab are in the zero oxidation state. This result is very different from that reported in literature on single platinum atoms supported on α-alumina or simplified models of γ-alumina, where a platinum atom generally has an unpaired electron. This also means that the mechanism of CO, NO_x or HC oxidation on Pt(0) will be different from that on Pt(I) or Pt(II). We also plan to carry out first principle studies of CO oxidation on Pt atoms supported on θ-alumina slab.

Because our experimental work has already shown that the distribution of platinum on γ-alumina and θ-alumina is almost identical, and the surface properties and CO oxidation of both catalysts are identical, we proposed that Pt supported on θ-alumina is a better model for Pt supported on γ-alumina than Pt supported on α-alumina or simplified models of γ-alumina. Unlike α-Al_2O_3, θ-Al_2O_3 is structurally similar to γ-Al_2O_3 because both phases have a combination of tetra and octahedrally coordinated Al atoms and an fcc arrangement of the O ions.

We have completed our work on CO oxidation on single supported Pt atoms and the results have been published (DeBusk et al. 2013). In this report, we summarize our theoretical study of NO oxidation on single supported Pt and Pd atoms. Our work suggests that single-supported Pt atoms require several endothermic steps for NO oxidation, while the energetics of the NO oxidation pathway on single-supported Pd are identical to that of CO oxidation on single-supported Pt. The experiments to validate the results will be completed in the coming year.

Our theoretical study shows that palladium prefers to occupy the shell location in a core-shell Pt-Pd particle imparting thermal durability to Pt-Pd particle as compared with Pt particles. We have found that Ni also can improve the thermal durability of Pt particles and the experiments to validate the results will be carried out in FY 2014. Finally, we have developed a simple impregnation approach to synthesize heterobimetallic zeolites. Characterization by various techniques shows them to be identical with those prepared by ion-exchange methods. Furthermore, the NO_x reduction activity under NH_3-SCR is identical for both ion-exchange or impregnation synthesized heterobimetallic zeolites.

We also have carried out the characterization of CuFe-SSZ-13, a new heterobimetallic zeolite that exhibits high NO_x conversion at 150°C under fast SCR conditions.

Theoretical Studies

CO Oxidation on Pt Single Atoms Supported on θ-Al_2O_3

We employed the Vienna *Ab Initio* simulation package to carry out the first principle total energy calculation within the

supercell density functional theoretical (DFT) framework (Kresse and Hefner 1993a, 1993b, 1994). The generalized gradient approximation in the Perdew-Wang-91 form was employed for electron exchange and correlations (Perdue et al. 1992, 1993). The Kohn-Sham equations were solved using the projector-augmented wave approach for describing electronic core states (Bloch 1994, Kruse and Jobber 1999). The plane-wave basis set was truncated at a kinetic energy cut-off of 500 eV.

We have previously shown a complicated pathway for possible routes to CO oxidation on single-supported Pt atoms. First principle quantum mechanical calculations using the FHI-aims code, which enables all electron DFT calculations combined with the first principles thermodynamic approach, has allowed us to simplify the pathway and rule out alternates that are not energetically favorable.

The dissociative adsorption of O_2 is an endothermic step (i.e., 5.68 eV for the loss of O from I) and is an energetically unfavorable pathway for oxygen adsorption on Pt/θ-Al_2O_3. In addition, our all-electron DFT calculations, combined with the first-principles thermodynamic approach, show that configuration II is only accessible at a very low oxygen pressure (P) (P $<10^{-16}$ bar) and high temperatures (see Figure 3a). The chemical potential differences between oxygen in configuration I and II are still over 2.5eV at 2000K under our experimental condition (P = 1bar) (Figure 2b).

Although DFT calculations suggest that oxygen replacement by CO is energetically feasible, our results from all-electron DFT calculations combined with the first-principles thermodynamic approach show that once oxygen is adsorbed on Pt, it can be replaced by CO only at low oxygen pressure and very high temperatures (Figure 4).

This result is quite different from the conventional LH mechanism, where CO first covers Pt sites and oxygen dissociatively covers residual sites. Because CO oxidation conditions are usually at atmospheric pressure and about 500K, it is unlikely that CO replaces oxygen from I. In view of these results, the likely pathway for CO oxidation will involve CO adsorption on an oxidized surface, resulting in the intermediate V.

After eliminating alternate pathways, the most likely CO oxidation pathway is shown in Figure 4. The energetics of reactions can be summarized as follows:

*Pt + O2	→ *Pt(O2) (**I**)	-1.8736 eV
*Pt(O2) (**I**) - O	→ *Pt(O) (**II**)	5.6875 eV
*Pt(O2) (**I**) + CO	→ *Pt(O2)(CO) (**V**)	-1.9798 eV
*Pt(O2)(CO) (**V**)	→ *Pt(CO3) (**VI**)	-2.6396 eV
*Pt(CO3) (**VI**) - CO2	→ *Pt(O) (**II**)	2.2204 eV
*Pt(O) (**II**) + CO	→ *Pt(O)(CO) (**VII**)	-1.8102 eV
*Pt(O)(CO) (**VII**) - CO2	→ *Pt	-1.4884 eV

All of the reactions are energetically favorable, except the loss of CO_2 from VI, which is an endothermic step.

Regardless of whether the first species formed is Pt with O_2 absorbed on it or CO, the next intermediate forms with the bonding of both CO and O_2 on the same Pt atom. This intermediate formation involves breaking of one Pt-O bond with the surface. The intermediate is still a d^{10} system with magnetization at oxygen atoms of O_2 species. The absorption energy for oxygen is -45.79Kcal/mole. This intermediate undergoes rearrangement to form a carbonate species. The carbonate species is a d^8 species with no magnetization. Density of states analysis shows no electrons in Pt $5d_{xy}$ and $C2p_z$. This species is analogous to an organometallic platinum(0) sixteen electron complex, $(Ph_3P)_2Pt(CO_3)$, which has been shown to exhibit CO_3 bonding via two oxygen atoms by single crystal X-ray structure determination.

The elimination of CO_2 from the carbonate species forms a monoxide high spin d^8 species. Density of states shows Pt d_{xy}, Pt d_{yz}, O $1p_z$, and O $1p_x$ partially occupied. The density of states of p-orbitals of the alumina surface oxygen atoms bonded with platinum are shifted to lower energy and have features similar to the parent compound.

The monoxide complex reacts with CO to form a new intermediate, which eliminates CO_2 to regenerate the catalyst to enable a new catalytic cycle for CO oxidation.

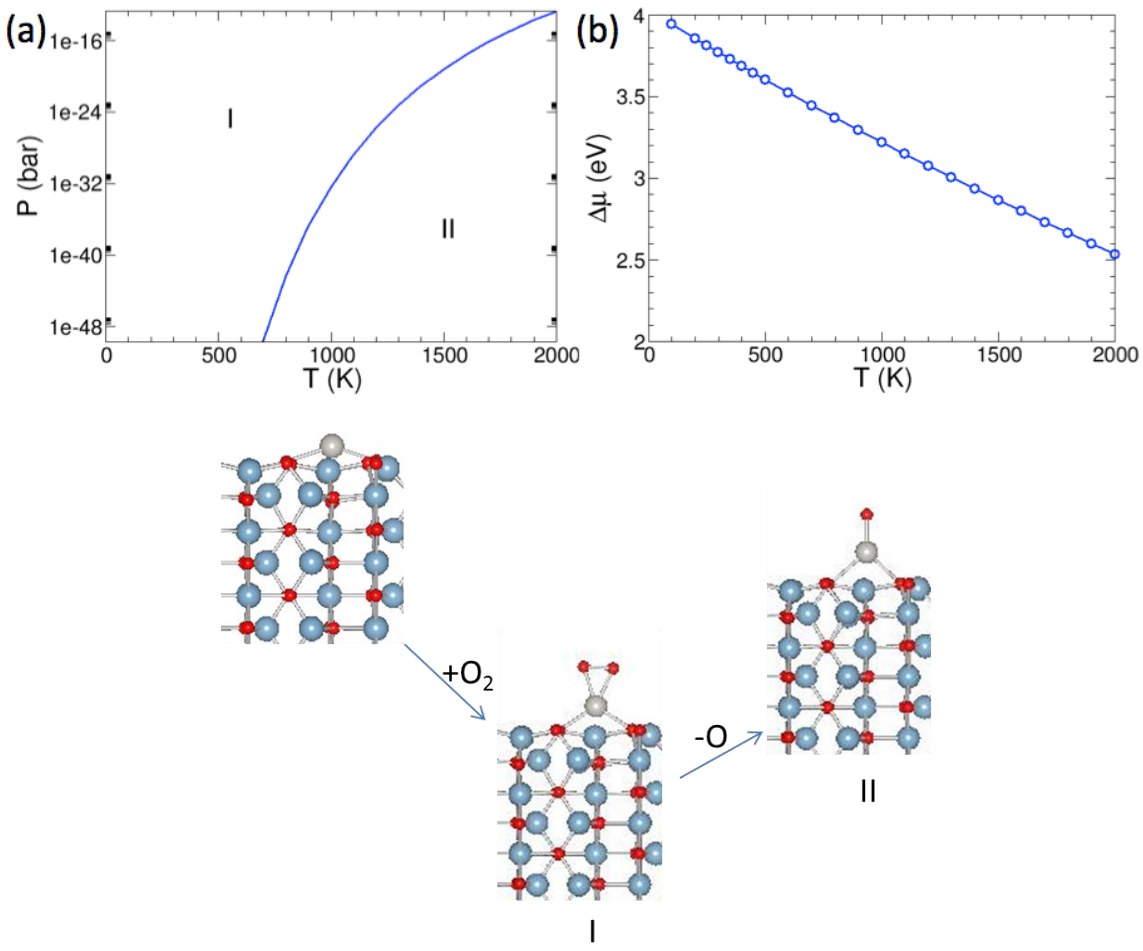

Figure 2. (a) Using a first-principles thermodynamics approach, the relative structural stabilities of configuration I and II (shown in the graphs) were calculated and the phase diagram as a function of oxygen pressure (P) and temperature (T) were constructed. (b) Difference between the oxygen chemical potentials of configuration I and II at P=1bar.

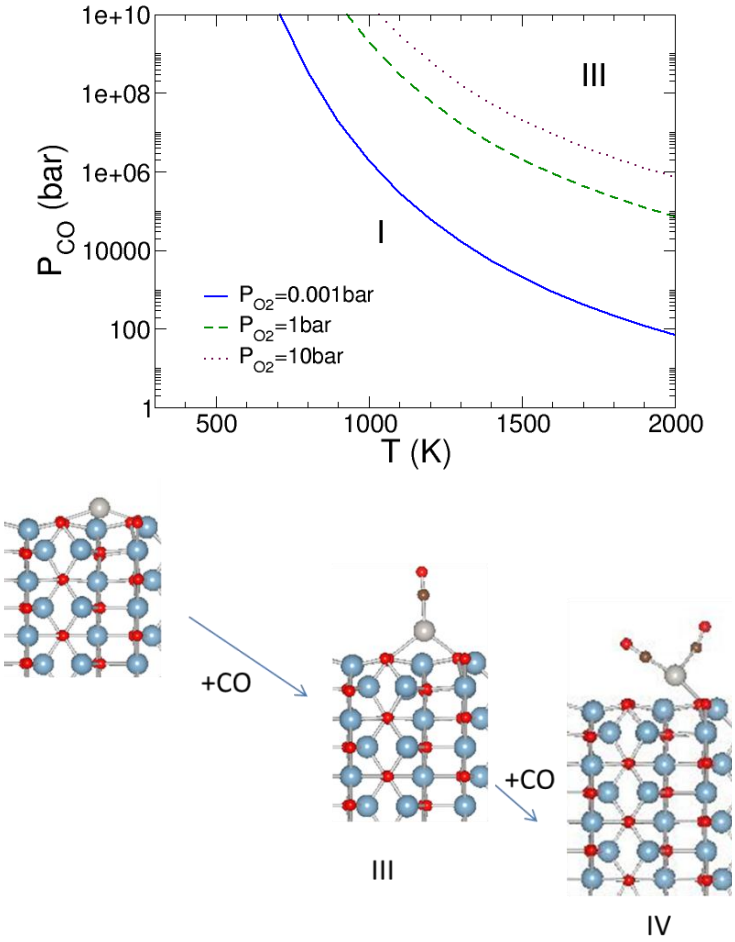

Figure 3. A phase diagram of configurations I and III (shown in the graph) as a function of temperature (T) and CO gas pressure (PCO) was obtained using first-principles thermodynamics approach. Each line defines the phase boundary between I and III. Above the phase boundary, III is relatively more stable than I at given oxygen pressure (PO_2).

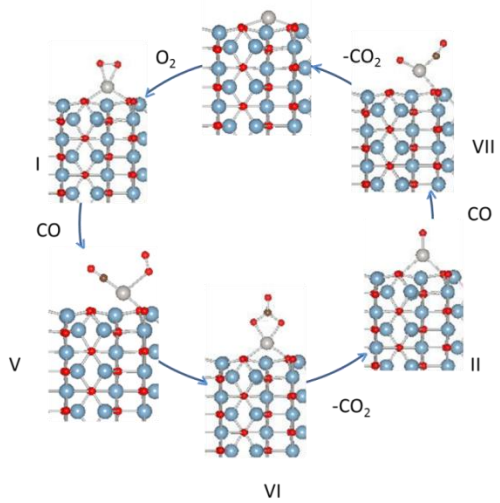

Figure 4. A pathway for CO oxidation on single Pt atoms supported on (010) surface of θ-Al_2O_3.

Bimetallic Systems – Pt-Ni

We previously have reported on the theoretical modeling studies of a Pt-Pd system employing a four atom cluster supported on θ-Al_2O_3 (010) substrate. In order to find a less expensive substitute for Pd, we have initiated a study of various possible candidates, starting with Ni, which is another member of Group IV besides Pd and Pt. The preliminary data suggest that Ni can also stabilize Pt, but not to the extent of Pd.

NO Oxidation on Single-Supported Pt and Pd on θ-Al2O3 (010) Surface

In general, the catalytic activity increases with decreases in particle size; however, NO oxidation is known to have an inverse relationship, where NO oxidation activity decreases with decreases in particle size (Bhatia et al. 2009). There are no conclusive explanations for this phenomenon.

Our ab initio theoretical modeling work suggests that NO oxidation catalyzed by supported single atoms proceeds by a mechanistic pathway that differs from the conventional Langmuir-Hinshelwood scheme that requires metal active sites that contain more than one atom. This pathway is analogous to our proposed pathway (Figure 4) for CO oxidation on supported single atoms on inert substrate (e.g., alumina). The energetics of individual steps are as follows:

*Pt	+ O_2	⟶	*Pt(O_2) (**I**)	-1.8736 eV
*Pt	+ NO	⟶	*Pt(NO)	-1.5833 eV
*Pt(O2) (**I**)	- O	⟶	*Pt(O) (**IV**)	5.6875 eV
*Pt(O_2) (**I**)	+ NO	⟶	*Pt(O_2)(NO) (**II**)	- 2.6238 eV
*Pt(O_2)(NO) (**II**)		⟶	*Pt(NO_3) (**III**)	1.0912 eV
*Pt(NO_3) (**III**)	- NO_2	⟶	*Pt(O) (**IV**)	1.2400 eV
*Pt(O) (**IV**)	+ NO	⟶	*Pt(O)(NO) (**V**)	- 2.5496 eV
*Pt(O)(NO) (**V**)	- NO_2	⟶	*Pt	1.3574 eV

As can be seen, there are several endothermic steps involved in the NO oxidation process. While the bonding of NO to oxidized Pt is exothermic, its transformation to a nitrate is an endothermic step. Furthermore, the decomposition of nitrate is also an endothermic process. The final step, which is loss of second NO_2, is an endothermic step. Our proposed pathway is applicable to 10 to 20 atom rafts, which essentially are single atoms bonded through oxygen.

These results suggest that NO oxidation on Pt single atoms or samples dominated by 10 to 20 atom rafts of Pt is not favorable and occurs by a different pathway than the conventional Langmuir Hinshelwood process. Because nitrate formation and nitrate decomposition steps in NO oxidation are endothermic processes, the NO oxidation is not as efficient as the conventional pathway on Pt particles.

Literature reports (Weiss et al. 2010) show that NO oxidation turnover rates decrease as PdO clusters. It is believed that this decrease is due to stronger oxygen binding and lower vacancy concentrations in small clusters. The catalytic consequences of size are similar on PdO and Pt clusters, despite their different oxidation state, consistent with a common requirement for surface vacancies in O_2 activation steps on both catalysts. However, our first principles studies show that NO oxidation on a single-supported Pd atom can be analogous to CO oxidation. The energetics of steps involved in the process are as follows:

*Pd	+ O_2	⟶	*Pd(O_2) (I)	-1.5071 eV
*Pd	+ NO	⟶	*Pd(NO)	- 1.0547eV
*Pd(O2) (**I**)	- O	⟶	*Pd(O) (**IV**)	6.5826 eV
*Pd(O_2) (**I**)	+ NO	⟶	*Pd(O_2)(NO) (**II**)	- 1.4957 eV
*Pd(O_2)(NO) (**II**)		⟶	*Pd(NO_3) (**III**)	-0.4877 eV
*Pd(NO_3) (**III**)	- NO_2	⟶	*Pd(O) (**IV**)	2.0102 eV
*Pd(O) (**IV**)	+ NO	⟶	*Pd(O)(NO) (**V**)	- 1.8799 eV
*Pd(O)(NO) (**V**)	- NO_2	⟶	*Pd	-0.0017 eV

The dissociation of oxygen bonded to Pd is highly endothermic and is not a feasible step in the mechanistic pathway. Thus, there is only one endothermic step in the pathway, which is decomposition of nitrate to release NO_2. This suggests that Pd of single-supported Pd catalysts will get covered with NO_3 unless external energy is applied to decompose the nitrate.

We have submitted a Center for Nanophase Materials proposal to carry out experimental work to validate the results of this theoretical study.

Experimental Studies

Alternate Methods for the Synthesis of CuFe-SSZ-13

We are employing commercially available ZSM-5 to carry out method development experiments because SSZ-13 is not commercially available in research quantities. We plan to eventually test the successful method with SSZ-13. While several attempts to prepare bimetallic zeolites under moderate conditions failed, the incipient wetness method appears to have been successful and is described here. The diffuse reflectance ultraviolet visible spectrum of CuFe-ZSM-5 prepared by the incipient wetness method matches very well with the one previously reported by us for ion-exchanged CuFe-ZSM-5.

For the synthesis of Cu-ZSM-5, a 2.6 g sample of $Cu(OAc)_2 \cdot H_2O$ was dissolved in 600 mL of de-ionized water (0.022 M), followed by addition of H-ZSM-5 (10.0 g). The slurry was stirred for 2 hours at 50°C. The blue-colored solid was collected by filtration after cooling, washed with de-ionized water, and calcined in air at 500°C (10°C/min) for 4 hours to obtain Cu-ZSM-5. Elemental analysis is Cu 2.76%, Al 3.31%.

For the synthesis of CuFe-ZSM-5, a 1.0-g sample of Cu-ZSM-5 and 0.03-g sample of $Fe(NO_3)_3.9H_2O$ were ground together and transferred to a petri dish. Drops of deionized water were added carefully to wet the sample. The blue color of Cu-ZSM-5 started to disappear quickly and the whole sample became light pink. The sample was allowed to dry in air and calcined in air at 500°C (10°C/minute) for 4 hours.

The diffuse reflectance ultraviolet visible spectrum of CuFe-ZSM-5 (IW) prepared by the incipient wetness method matches very well with the one previously reported by us for ion-exchanged CuFe-ZSM-5 (IE) (Figure 5). The IW in the bracket refers to incipient wetness to differentiate it from ion exchange (IE) CuFe-ZSM-5 reported by us previously. The Cu and Fe EXAFS of both CuFe-ZSM-5 (IW) and CuFe-ZSM-5 (IE) are identical, further supporting the success of the incipient wetness method to yield heterobimetallic CuFe-ZSM-5 (Figure 6).

For the synthesis of CuCo-ZSM-5 (IW), a 1.0-g sample of Cu-ZSM-5 and a 0.022-g sample of $Co(NO_3)_2.6H_2O$ were ground together and transferred to a petri dish. Drops of deionized water were added to wet the sample. The blue color of Cu-ZSM-5 did not change significantly. The sample was allowed to dry in air and calcined in air at 500°C (10°C/minute) for 4 hours to obtain a grey powder of CuCo-ZSM-5 (IW).

For the synthesis of CuMn-ZSM-5 (IW), a 1.0-g sample of Cu-ZSM-5 and a 0.013-g sample of $Mn(NO_3)_2.H_2O$ were ground together and transferred to a petry dish. Drops of deionized water were added carefully to wet the sample. The sample was allowed to dry in air and calcined in air at 500°C (10°C/minute) for 4 hours to obtain a grey powder of CuMn-ZSM-5 (IW).

NO_x Conversion Efficiency of CuFe-ZSM-5 (IW)

The test protocol has been described in previous reports. Briefly, the CuFe-ZSM-5 (IW) powder was mixed with an equal amount of cordierite and transferred to our bench-top reactor. The de-greening was done in a flow of 8.5% O_2, 8.0% CO_2, and 7.25% water with balance N_2 at 600°C at a space velocity of 50,000 h^{-1} for 2 hours. The NO_x conversion efficiency experiments employed simulated diesel exhaust containing 8.5% O_2, 8.0% CO_2, 7.25% H_2O, 250 ppm NO, 250 ppm NO_2, 500 ppm NH_3, and N_2 as balance at a space velocity of 50,000 h^{-1} and tests were done in a 150 to 650°C range.

The results of the NO_x conversion efficiency of CuFe-ZSM-5 (IW) as a function of temperature are shown in Figure 7 and are comparable to the NO_x conversion efficiency of CuFe-ZSM-5 (IE).

Turnover Frequency Study of Pt on Alumina

H_2 chemisorption on a Quantachrome Autosorb-1 was used to determine the number of platinum exposed on the catalyst surface (Pt_s) for the 1% Pt sample and both 2% Pt samples.

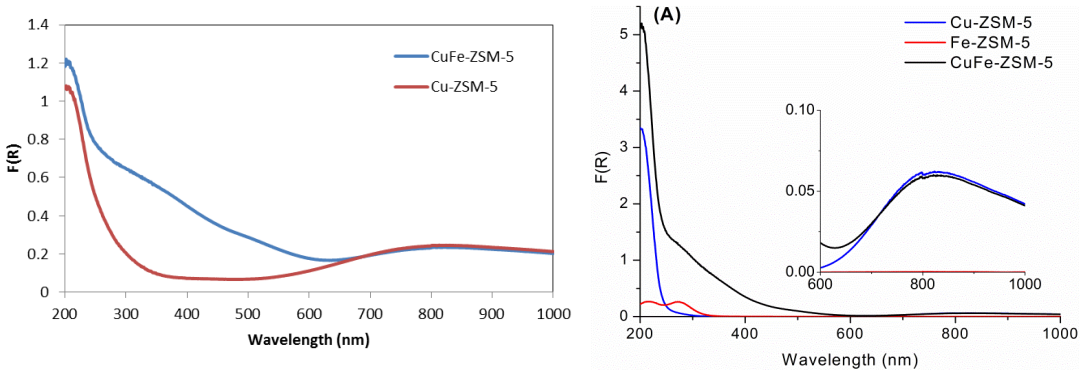

Figure 5. Diffuse-reflectance UV-Vis of CuFe-ZSM-5 by incipient wetness method (left) and impregnation method (right).

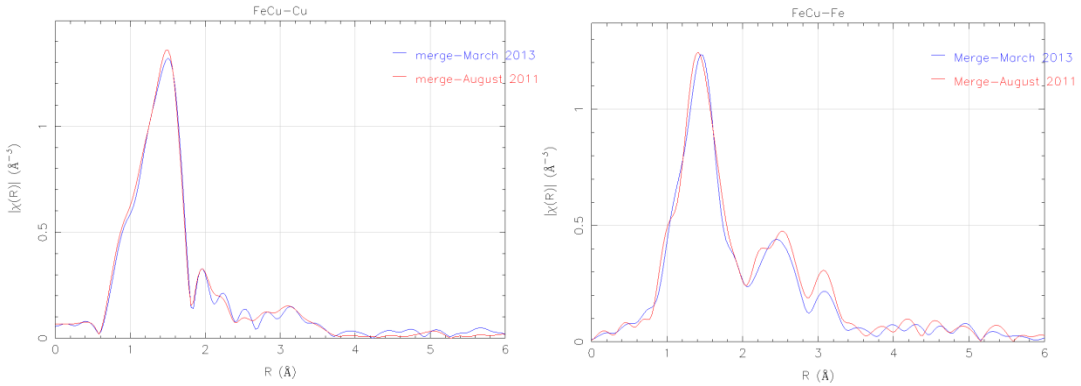

Figure 6. Cu (left) and Fe (right) EXAFS of CuFe-ZSM-5 (IW) and CuFe-ZSM-5 (IE), showing that they are identical.

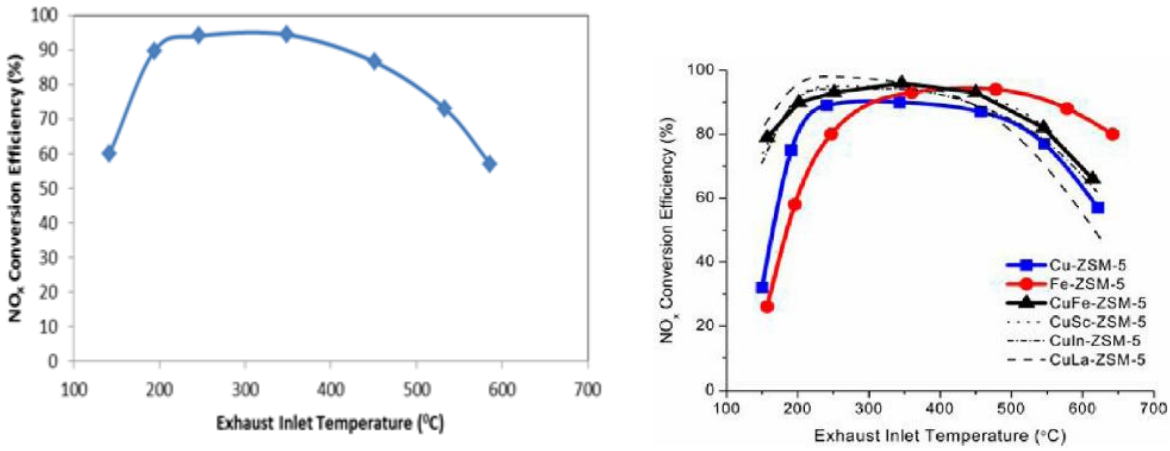

Figure 7. NOx conversion efficiency of CuFe-ZSM-5 (IW) (left) and a variety of heterobimetallic zeolites (right).

Catalyst samples containing approximately 10 mg of platinum (1.0 g for 1%Pt; 0.5 g for 2%Pt) were dried under helium at 120°C for 30 minutes, followed by a hydrogen reduction at 250°C for 120 minutes, and then evacuated at 250°C for 120 minutes. Subsequently, the combined H_2 adsorption isotherm was recorded at 40°C after the samples had cooled under vacuum. The sample was then evacuated and a second adsorption isotherm was obtained to ascertain the weak adsorption isotherm.

The dispersion of surface Pt on each sample was determined by extrapolation of the difference isotherm (i.e., irreversible chemisorption), assuming $H/Pt_s=1$. The dispersion Pt on 0.18%Pt/θ-Al_2O_3 was estimated according to $D = 1/d_{Pt}$.

Extrapolation of the combined H_2 adsorption isotherm for 2.0%Pt/θ-Al_2O_3 indicated approximately 140% dispersion, suggesting hydrogen spillover onto the Al_2O_3 support. Hydrogen spillover from Pt onto alumina support is known to occur at temperatures below 400°C (DeBusk et al. 2013, Kresse and Hefner 1993a). Assuming that all hydrogen adsorption on the alumina was weakly adsorbed, the irreversible chemisorptions, which gave roughly 100% dispersion, was used to estimate the dispersion of Pt. Examination of the sample after chemisorption analysis revealed that the color of the sample had gone from cream to black, indicating a change in the catalyst during analysis. This is not surprising considering the sample change noted by the white line shift of the 1.0%Pt/θ-Al_2O_3 by XANES after the sample had been reduced in hydrogen at only 150°C/60minutes.

H_2 chemisorption analysis of 1.0%Pt/θ-Al_2O_3 failed to reach saturation. In light of the sample change noted by XANES after reduction and that observed for the 2.0%Pt/θ-Al_2O_3 sample during chemisorption, it was reasoned that increasing the reduction temperature in order to obtain dispersion estimates would change the sample properties, potentially making the results irrelevant to the current study, which did not expose the catalyst to reducing environments. Therefore, it is assumed that because chemisorption of 2.0%Pt/θ-Al_2O_3 estimated 100% dispersion, it is reasonable to assume that the 1.0%Pt/θ-Al_2O_3 catalyst would have a similar dispersion.

Platinum dispersion estimated from the combined H_2 adsorption isotherm for 2.0%Pt/θ-Al_2O_3-650 sample is 72%. It is presumed that because the sample was reduced at the same temperature as the 2.0%Pt/θ-Al_2O_3 sample, the weakly adsorbed hydrogen may also be related to hydrogen spillover in the sample. Therefore, the platinum dispersion used for turnover frequency (TOF) calculations was estimated from the irreversible adsorption isotherm, which indicates a Pt dispersion of 50% for 2.0%Pt/θ-Al_2O_3-650.

Because the 0.18, 1.0, and 2.0% Pt/θ-Al_2O_3 catalysts are estimated to have the same dispersion, they differ only in the total number of available active sites indicated by the change in metal loading and should have the same activation energy. Therefore, the decrease in activation temperature with increase in the Pt loading is likely related to the fast and exothermic nature of CO oxidation, which can cause temperature gradients to corrupt the CO oxidation temperature measurements. Furthermore, if CO oxidation on the 2.0%Pt/θ-Al_2O_3-650 catalyst was preceded by the same mechanism as the other samples, its activation temperature would be closer to the 200°C activation temperature of 1.0%Pt/θ-Al_2O_3, which is estimated to have the same TOF. A dispersion of only about 9% would be needed to explain its activation temperature being almost the same as 0.18%Pt/θ-Al_2O_3, and this is not supported by the particle sizes seen by aberration corrected electron microscopy. A closer look at the reaction rates and kinetics of the CO oxidation on these catalysts following the modified mechanism presented in this paper will be the subject of a future study.

Turn over frequencies based on dispersion estimates were calculated at two conditions, 20% CO oxidation and at 200°C, for the purpose of performance comparison (Table 1).

Table 1. Comparison of TOFs.

	Pt Loading (wt%)	COox @ 200°C	TOF x 10^2 (s^{-1})†	Temp @ 20%COox	TOF x 10^2 (s^{-1})†
0.18%Pt/θ-Al_2O_3	0.18	1.40%	1.3	251°C	18.7
1.0%Pt/θ-Al_2O_3	1.0	8.1%	1.4	212°C	3.4
2.0%Pt/θ-Al_2O_3	2.0	59.9%	5.1	182°C	1.7
2.0%Pt/θ-Al_2O_3-650C	2.0	0.9%	0.2	248°C	3.4

†TOF was calculated based on Pt dispersion (mol COox/ mol surface Pt). Pt dispersion was extrapolated from H_2 chemisorption strong/difference isotherms for both 2.0%Pt samples. The dispersion of 0.18%Pt was estimated by the Pt particle size according to $D = 1/d_{Pt}$.

The comparison of TOFs at 20% CO conversion for our samples of 0.18%, 1.0% and 2.0%Pt/θ-Al_2O_3 shows that 0.18%Pt/θ-Al_2O_3 is the most active platinum, but the 20% CO conversion occurs at different temperatures.

Conclusions

We have shown that CO oxidation can occur on single-supported atoms without the involvement of support. Theoretical studies suggest that a single-supported Pd atom will be a better NO oxidation catalyst than single supported Pt.

Theoretical studies also suggest that Ni can impart thermal durability to supported Pt nanoparticles. Experiments to validate theoretical results are in progress.

We also summarized our new impregnation synthesis of the heterobimetallic zeolites and the low-temperature NOx reduction activity under fast NH_3-SCR conditions.

Future studies will focus on scale-up and preparation for engine testing of the new CuFe-SSZ-13 catalyst material, which was designed as a low temperature (150°C) NO_x reduction catalyst for diesel exhaust treatment.

References

Bhatia, D., R. W. McCabe, M. P. Harold, V. Balakotaiah, and J. Catal, 2009, "Experimental and kinetic study of NO oxidation on model Pt catalysts," 266, 106.

Bloch, P. E., 1994, "Projector augmented-wave method," *Phys. Rev. B*, 50, 17953.

DeBusk, M. M., M. M. Yoon, L. F. Allard, D. R. Mullins, Z. Wu, X. Yang, G. Veith, G. M. Stocks, and C. K. Narula, 2013, "CO oxidation on supported single Pt atoms – experimental and ab initio density functional studies of CO interaction with Pt atom on θ-Al2O3(010)," *J. Am. Chem. Soc.*, 135, 12634.

Kresse, G. and J. Hefner, 1993a, "*Ab Initio* molecular dynamics for liquid metals," *Phys. Rev.*, 47, 558.

Kresse, G. and J. Hefner, 1993b, "*Ab Initio* molecular dynamics for open-shell transition metals," *Phys. Rev. B*, 48, 13115.

Kresse, G. and J. Hefner, 1994, "*Ab initio* molecular-dynamics simulation of the liquid-metal–amorphous-semiconductor transition in germanium," *Phys. Rev. B*, 49, 14251

Kruse, G. and D. Jobber, 1999, "From ultrasoft pseudopotentials to the projector augmented-wave method," *Phys. Rev B*, 59, 1758.

Perdue, J. P., J. A. Chivalry, S. H. Vodka, K. A. Jackson, M. R. Pederson, and D. J. Singh, 1992, "Atoms, molecules, solids, and surfaces: Applications of the generalized gradient approximation for exchange and correlation," *Phys. Rev. B.*, 46, 6671

Perdue, J. P., J. A. Chivalry, S. H. Vodka, K. A. Jackson, M. R. Pederson, and D. J. Singh, 1993, "Erratum: Atoms, molecules, solids, and surfaces: Applications of the generalized gradient approximation for exchange and correlation," *Phys. Rev. B*., 48, 4978.

Weiss, B. M., E. Iglesia, and J. Catal, 2010, "Mechanism and site requirements for NO oxidation on Pd catalysts," 272, 74.

Presentations and Publications

DeBusk, M. M., M. Yoon, L. F. Allard, D. R. Mullins, G. M. Stocks, X. Yang, Z. Wu, and C. K. Narula, 2013, "CO oxidation on supported single Pt atoms – experimental and ab initio density functional studies of CO interaction with Pt atom on θ-Al2O3(010)," *J. Am. Chem. Soc.*, 135, 12634-12645. This paper was discussed in *Research Highlights of Nature Chemistry*, 2013, 5, 809.

Narula, C. K. and M. M. DeBusk, 2013, "Catalysis by Design," *Encyclopedia of Nanoscience and Nanotechnology*, Taylor Francis, New York (invited chapter, accepted for publication).

Narula, C. K., L. F. Allard, M. M. DeBusk, D. R. Mullins, G. M. Stocks, X. Yang, M. Yoon, and Z. Wu, 2013, "Single atom catalysis: CO oxidation on single Pt atoms supported on θ-Al2O3(010) Surface," *American Chemical Society Meeting*, New Orleans, PA, April 7-11, 2013.

Narula, C. K., L. F. Allard, M. M. DeBusk, D. R. Mullins, G. M. Stocks, X. Yang, M. Yoon, and Z. Wu, 2013, "Single atom catalysis: CO oxidation on single Pt atoms supported on θ-Al2O3(010) Surface," *North American Catalysis Society Meeting*, Louisville, KY, June 2-7, 2013.

Yang, X., Z. Wu, M. M. DeBusk, D. R. Mullins, S. M. Mahurin, R. A. Geiger, M. Kidder, and C. K. Narula, 2012, "Heterometal Incorporation of M-Exchanged Zeolties enables low temperature catalytic activity of NOx reduction," *J. Phys. Chem. C*, 116, 23322.

Project 18519 – Materials for Exhaust and Energy Recovery

Agreement 19214 – Biofuels Impact on Diesel Particulate Filters Durability

M. J. Lance, T. J. Toops, E. J. Nafziger*, M. K. Ferber, and C. Xie**
Ceramic Science and Technology Group
Oak Ridge National Laboratory
P.O. Box 2008, MS 6068, Bldg. 4515
Oak Ridge, TN 37831-6068
Phone (865) 241-4536; fax: (865) 574-6098; e-mail: lancem@ornl.gov
**Fuels, Engines, and Emissions Research Center*

DOE Technology Manager: Jerry L. Gibbs
Phone (202) 586-1182; fax: (202) 586-1600; e-mail: jerry.gibbs@ee.doe.gov
ORNL Technical Advisor: J. Allen Haynes
Phone (865) 576-2894; fax: (865) 574-4913; e-mail: haynesa@ornl.gov

Contractor: Oak Ridge National Laboratory, Oak Ridge, Tennessee
Prime Contract No.: DE-AC05-00OR22725

Objectives

- To characterize changes in the microstructure and material properties of diesel particulate filters (DPFs) in exhaust gas produced by biodiesel blends.

Approach

- Use a stationary generator to produce diesel exhaust for long-term 24/7 aging of DPFs in diesel and biodiesel exhaust.
- Attempt measurement of DPF sample under pure tension using an hourglass specimen design.
- Characterize emission control devices aged in biodiesel exhaust provided by the National Renewable Energy (NREL)/Ford/Manufacturers of Emission Controls Association (MECA) collaboration.

Accomplishments

- Characterized the degradation mechanisms occurring in selective catalytic reduction (SCR) and diesel oxidation catalyst (DOC) devices run with high levels on potassium doped in biodiesel fuel by NREL.
- Completed 100-hour test of the Gen set at 800°C using a closed loop temperature control.

Future Direction

- This project is ending, but will continue with an expanded focus (beyond DPFs) in Agreement 26463 – Biofuel Impact on Aftertreatment Devices.

Introduction

After collecting soot (from a 1.7-L Mercedes-Benz engine fueled with biodiesel blends) on uncatalyzed cordierite DPFs, significant degradation of the DPFs was observed following a 3-month period where the DPFs resided in a can in a cabinet. No degradation of the DPF run with ultra-low sulfur diesel (ULSD) was found. In addition, after burning the collected soot, the biodiesel soot had cordierite and padding residue in amounts roughly proportional to the biodiesel volume percent in the fuel. This result suggested that biodiesel may cause degradation of DPF materials under some conditions. This project has the objective of investigating this possibility and the potential degradation mechanisms resulting from biodiesel operation. More recently, the scope of the project has broadened to cover the potential deleterious effects of biodiesel on the SCR device and DOC.

Biodiesel can be made from various renewable sources (such as vegetable oil, animal fat, or waste cooking oil) and is produced through transesterification of the oil or fat with methanol; this is a process that occurs in the presence of a catalyst, typically sodium hydroxide or potassium hydroxide. Following production, residual amounts of sodium (Na) or potassium (K) from the catalyst can be left behind and are converted to oxides, sulfates, hydroxides, or carbonates in the combustion process and form an inorganic ash that can be deposited onto the exhaust emission control devices found in modern diesel engines. Alkali metals are well known poisons for catalysts and have been shown to negatively impact the mechanical properties of ceramic substrates (Williams et al. 2011). Furthermore, alkali metal hydroxides (such as Na and K) are volatilized in the presence of steam; therefore, they can penetrate the catalyst washcoat or substrate.

To investigate the effect of biodiesel fuel on DPF material degradation, a stationary generator was purchased and set up to operate 24/7 using different fuels. The exhaust is directed through a DOC, and supplementary fuel is used to produce an exotherm, heating the DPF to temperatures typically experienced during regeneration. Following exposure, the mechanical properties of the DPF can be measured through bending with ring-on-ring biaxial flexure of disks (Wereszczak et al. 2012, Williams et al. 2013). A new method, whereby a tensile load is applied unaxially, was explored during the previous fiscal year with mixed results.

The second approach to better understand potential degradation mechanisms of emission control devices in biodiesel exhaust is to obtain aged samples from a collaboration with NREL, the National Biodiesel Board, MECA, and Ford Motor Company and is funded through the Vehicle Technologies Office's Fuels Program. DPFs aged in biodiesel doped with 7, 14, and 28 ppm K were obtained and analyzed along with the DOC and SCR devices. Our results show that 28 ppm K is too aggressive a dopant level to simulate long-term effects of biodiesel. Future accelerated tests will use the 14 ppm dopant level.

Results

Mechanical Properties of DPFs Tested Under Pure Tension

During fiscal year 2012, a methodology of measuring mechanical properties of DPFs by gripping the ends of a 1 × 3-in. sample at the ends with epoxy was established. This method has numerous advantages over our previously used method of ring-on-ring biaxial flexure (Wereszczak et al. 2012). Coupled with the measurement of tensile elongation using contact extensometers, the sought-after tensile testing enables measurement of a continuous tensile stress (tensile strain curve). Also, the load is applied across a much larger volume of material compared to the bending tests, which improves the statistics of the measurements. Finally, the fracture strength is less likely to be controlled by the surface flaws generated during sample machining because the load is applied uniformly through the thickness of the specimen and not with the maximum load just on the surface as with flexural testing. Stress-strain curves supported the biaxial flexure results; however, failure always occurred near the epoxy (seen in Figure 1), which suggests the epoxy may be creating damage in the DPF during the curing process. Figure 2 shows one of the DPF samples

from Figure 1 after the epoxy had been burned out at 600°C. The sample has been significantly impacted by the epoxy as is evidenced by the large amount of cordierite debris around and in the steel collet that held the epoxy and the DPF. These results demonstrated the need to machine hourglass specimens in order to induce failure away from the epoxy and in the gauge section of the sample.

Figure 1. Tested DPF cylinders still mounted in epoxy.

Figure 2. Epoxy-mounted DPF after the epoxy has been burned off.

Figure 3 shows an hourglass specimen that was used to concentrate stresses away from the epoxy grip. Four attempts to measure the stress-strain curve and fracture load were made with this geometry; however, all specimens failed during specimen alignment due to a combination of the very low strength (less than 10 MPa) and the damage induced during the machining of the hourglass geometry. Additionally, the hourglass geometry may interact with the cellular DPF structure, creating stress concentrators. For these reasons, the previous methodology, which relied on biaxial flexure disks to measure elastic modulus and fracture strength, will be used in the future (Wereszczak et al. 2012, Williams et al. 2013).

Figure 3. Straight 1 × 3-in. cordierite cylinder (left) and an hourglass specimen (right).

Accelerated Aging of Emissions Control Devices

In collaboration with NREL, Ford, MECA and the National Biodiesel Board, full exhaust systems from a 2011 Ford F250 pickup were placed onto an accelerated aging platform, which was described in an earlier study (Williams et al. 2011). B20 test fuels were made from petroleum-based ULSD diesel mixed with a 20-vol%, soy-based biodiesel, neither of which contained any measureable quantity of K at a detection limit of 1 ppm. The B20 was doped with potassium dodecylbenzene to achieve precisely controlled levels of K at 7-ppm, 14-ppm, and 28-ppm levels. The fuel dopant levels were selected to achieve 150,000-miles worth of metal exposure at three different aging rates: 200 hours, 100 hours, and 50 hours, respectively. Post-mortem analysis of the aged catalysts was performed to locate the K and to look for signs of localized catalyst deactivation.

Table 1 summarizes the test conditions and the emission results. All three systems spent the same amount of time above 600°C, which was 45 hours. The ash load in the DPF increased with the test time, which is expected because the ash coming from the lube oil will increase with longer run times despite the ash coming from K additions remaining constant.

Table 1. Testing conditions and emission results. Red text* indicates the system failed the 0.20 g/mile NO_x standard.

	B20 + 28ppm K (50 hrs)	B20 + 14ppm K (100 hrs)	B20 + 7ppm K (200 hrs)
Temp > 600˚C	45.0hrs	45.1hrs	45.0hrs
Ash load on DPF	41 grams	59 grams	104 grams
NOx (pre aging)	0.17 g/mile	0.19	0.10
NOx (mid aging)	0.33*	0.25*	0.17
NOx (post aging)	0.30*	0.12	0.20

Ash was ejected from the silicon carbide DPF by blowing compressed air through the outlet side of the filter and then burning the collected soot and ash at 600°C for 1 hour in order to oxidize the remaining soot. Energy dispersive x-ray spectra were collected on these samples using a scanning electron microscope (SEM); the results are shown in Figure 4. The results show a higher Ca and Zn content for the 7-ppm ash relative to the 28-ppm ash due to the longer run time for this sample (200 hours versus 50 hours). Also, the 28-ppm ash had the highest K content, as would be expected given the higher level of K dosing. It is speculated that the K is gettering the sulfur in the exhaust gas, forming K_2SO_4, which collects as ash in the DPF. The higher K:S ratio in the 28 ppm K sample shows that there is excess K present in the exhaust in species more damaging to the catalyst (i.e., KOH, K_2O), leading to deactivation of the SCR catalyst and the higher NO_x levels shown in Table 1.

In addition to DPF, the DOC and SCR emissions control devices were also characterized. Figure 5a and 5b shows a top-down view of the DOC brick at the front face of the brick from the 7 and 28-ppm K runs, respectively. The 28-ppm K brick exhibited significant fouling within the first centimeter of the front face. Some of this fouling was K_2SO_4 (as measured by Raman spectroscopy).

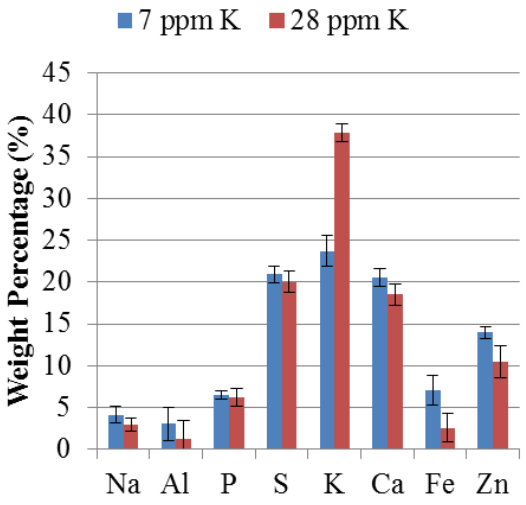

Figure 4. Elemental weight percent of ash for the 7-ppm K and 28-ppm K conditions.

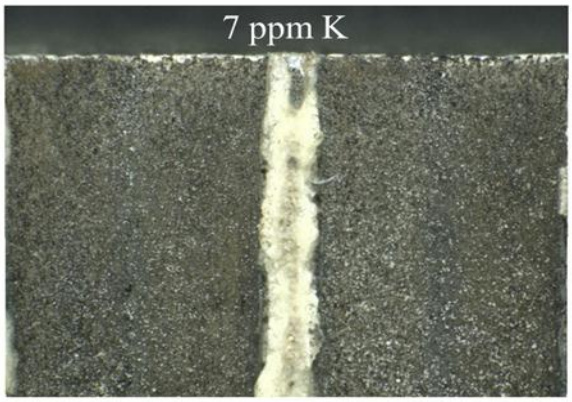

(a)

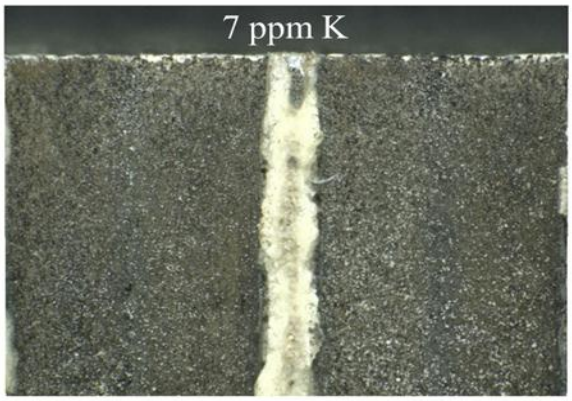

(b)

Figure 5. The surface of the two channels of the DOC from the 7-ppm K (a) and 28-ppm K (b) samples. The inlet is at the top of both images and the flow direction is top to bottom. Each channel is 3.5-mm wide.

Of the DOCs where K was introduced, the 28-ppm K exposure at the inlet had the largest impact on the hydrocarbon and CO light-off temperatures, increasing the temperature of 50% oxidation by 100°C compared to ULSD. All other K-aged samples, including the outlet of the 28-ppm K, increased the light-off temperature by less than 37°C. This shows that the face fouling in Figure 5b is responsible for significant degradation of the catalytic properties of the DOC for the 28-ppm K condition. More importantly, it proves that 28-ppm K is too aggressive a dopant level, causing phenomena not expected to occur in the real world without any dopant. These leads us to conclude that the 14-ppm K dopant for 100 hours in order to simulate 150,000 miles is the highest dopant level (lowest simulation time) that can be used for future testing.

Cores from the SCR catalysts were also extracted and analyzed. Figure 6 compares the fresh and ULSD SCR cores to the one aged with 14-ppm K. Discoloration seen in the inlet of the front SCR bricks exposed to K was initially assumed to be soot; however, using Raman spectroscopy, it was determined to come from Cu_2O and CuO. Figure 7 shows an SEM image of these particles. The origin of these copper oxide particles is from K atoms exchanging for Cu atoms in the zeolite structure, thereby deactivating the catalyst. It explains the cause of the failure of the NO_x emission test in Table 1. To the authors' knowledge, this is the first time such dramatic evidence of zeolite deactivation (due to the presence of alkali metals) has been shown.

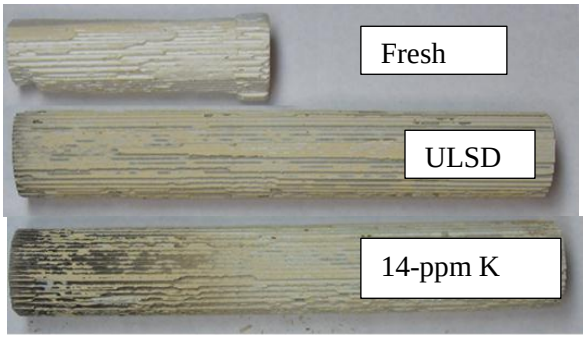

Figure 6. SCR catalyst cores from the fresh, ULSD, and 14-ppm K bricks.

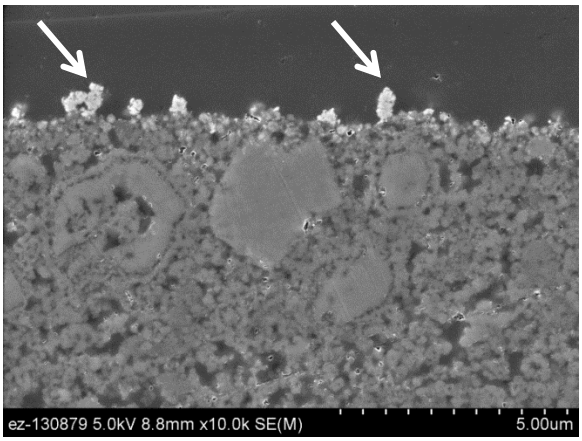

Figure 7. SEM image of the wash coat surface from the 14-ppm K SCR sample. The white arrows point to Cu_xO particles.

Stationary Generator

Because emission control devices are required to operate on-road for 435,000 miles without failure and in order to test devices for this duration, an accelerated aging method needs to be employed or else the test will be too costly and time-consuming to be practical. In addition to our collaboration with NREL and Ford, a second approach we are using is to employ a single-cylinder stationary generator to produce diesel exhaust, which is used to produce the temperature excursion expected during DPF regeneration. This approach allows us to generate diesel exhaust using different fuels that have been doped with chemicals to increase the Na and K content to match long-term operation with biodiesel fuel. At the same time, the stationary generator can be operated unattended for 24/7 with just daily refueling. During fiscal year 2012, the stationary generator shown in Figure 8 was installed and tested.

During fiscal year 2013, additional problems were encountered, whereby failed thermocouples led to large temperature excursions. In order to control this problem, an overtemp control, which will initiate a shutdown in the event the system exceeds a set temperature, was added to the Labview program. Also, a closed loop control was programmed into Labview, which controls the temperature at the DPF inlet by changing the fuel injection pump speed. Figure 9 shows the DPF inlet temperature of one complete cycle using the

closed loop control. The high temperature set point is now maintained within about 10°C. Unfortunately, this stationary generator has since failed due to being operated well outside its intended purpose. During the next fiscal year, a more robust system will be purchased and used to simulate long-term aging with biodiesel fuel.

Figure 8. Picture of the stationary generator.

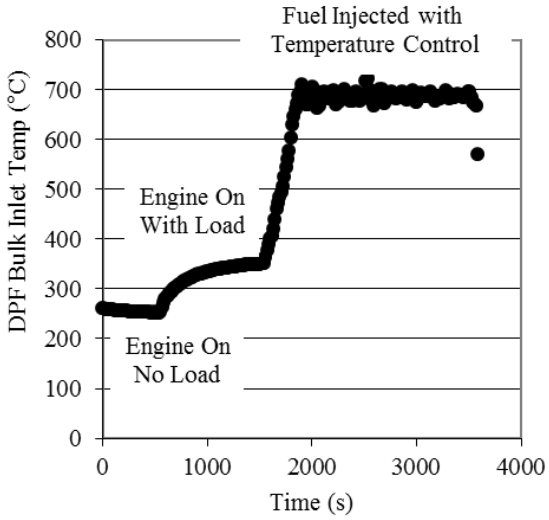

Figure 9. One temperature cycle on the stationary generator using the closed loop temperature control.

Conclusions

- Tensile testing of DPF coupons using epoxy to grip the sample was found to induce damage in the sample, making the test results unreliable. Future DPF measurement will employ the previously established biaxial flexure methodology for measuring mechanical properties.
- Accelerated tests were conducted using three K dopant levels: 7, 14, and 28 ppm. The 28-ppm K level induced degradation of both the DOC and the SCR that would not be expected during undoped normal conditions. The next round of testing will use 14-ppm K as the dopant level for accelerated testing.
- A closed loop temperature control was established on the stationary generator, which stabilized the DPF inlet temperature to within 10°C.

References

Wereszczak, A. et al., 2012, "Failure Stress and Apparent Elastic Modulus of Diesel Particulate Filter Ceramics," *SAE Int. J. Mater. Manf.*, 5, 2, 517–527.

Williams, A. et al., 2011, "Impact of Biodiesel Impurities on the Performance and Durability of DOC DPF and SCR Technologies," *SAE Int. J. Fuels Lubr.*, 4, 1, 110–124.

Williams, A. et al., 2013, "Impact of Fuel Metal Impurities on the Durability of a Light-Duty Diesel Aftertreatment System," *SAE International*.

Publications and Presentations

Toops, Todd J., Michael Lance, Andrew A. Wereszczak, D. William Brookshear, and Ke Nguyen, 2012, "Materials Characterization to Investigate Location of Fuel-borne Metals," *Biodiesel Technical Workshop*, October 30, 2012.

Williams, Aaron, Jonathan Burton, Robert L. McCormick, Todd Toops, Andrew A. Wereszczak, Ethan E. Fox, Michael J. Lance, Giovanni Cavataio, Douglas Dobson, Jim Warner, Rasto Brezny, K. Nguyen, and D. William Brookshear, 2013, "Impact of Fuel Metal Impurities on the Durability of a Light-Duty Diesel Aftertreatment System," SAE Technical Paper 2013-01-0513.

Awards

The Oak Ridge National Laboratory, NREL, and Ford team were recognized as "Researcher(s) of the Year" at the 2012 Biodiesel Technical Workshop.

Todd J. Toops and Michael J. Lance (Oak Ridge National Laboratory), Aaron Williams (NREL), and Giovanni Cavataio (Ford) were recognized for their collaborative effort to investigate the impact of trace metal impurities (Na, K, and Ca) on the end-of-life functionality and mechanical properties of emissions control devices. This effort focused on the light-duty application and employed the Ford aftertreatment system that includes a DOC/SCR/DPF arrangement.

The long-term introduction of the metal impurities and the evaluation of the entire aftertreatment system on an FTP drive cycle was performed at NREL, the evaluation of the performance of the individual devices and sections were performed at Ford, and the characterization of the metals location and chemical nature were performed at Oak Ridge National Laboratory and the University of Tennessee-Knoxville. The team was able to show that the aftertreatment system was durable and able to meet the 2010 emissions standards at 150,000 miles (based on equivalent metal exposure and thermal cycling), but that some deactivation did occur of both the DOC and the front of the SCR relative to the base case, such that stricter emissions regulations or further exposure may result in failed emissions standards.

Project 18519 – Materials for Exhaust and Energy Recovery

Agreement 26462 – International Characterization Methods

H. Wang
Materials Science and Technology Division
Oak Ridge National Laboratory
P.O. Box 2008, MS 6064, Bldg. 4515
Oak Ridge, TN 37831-6068
Phone (865) 576-5074; fax: (865) 574-3940; e-mail: wangh2@ornl.gov

DOE Technology Manager: Jerry L. Gibbs
Phone (202) 586-1182; fax: (202) 586-1600; e-mail: jerry.gibbs@ee.doe.gov
ORNL Technical Advisor: J. Allen Haynes
Phone (865) 576-2894; fax: (865) 574-4913; e-mail: haynesa@ornl.gov

Contractor: Oak Ridge National Laboratory, Oak Ridge, Tennessee
Prime Contract No.: DE-AC05-00OR22725

Objectives

- Conduct international round-robin studies on materials characterization methods and develop standard testing procedures.
- Conduct international round-robin studies on energy conversion devices for vehicles and develop standard testing methods and procedures.

Approach

- ***International Round-Robin Study of High-Temperature Bulk Thermoelectric (2013 through 2014):*** Lead the International Energy Agency (IEA)-AMT annex to conduct and complete an international round-robin study on high-temperature bulk thermoelectrics. The identified n-type half-heusler material will be circulated among the participating laboratories in five countries. All properties (i.e. thermal conductivity, electrical conductivity, and Seebeck coefficient) needed for ZT calculation will be tested form 300 to 800K. The results will be summarized and published to promote standardization of transport property measurements.
- ***Reliability of Low-Dimensional Thermoelectric Materials Measurements (2014):*** Following the bulk materials study, the IEA annex will organize an international study to evaluate the reliability of transport properties of low-dimensional materials. Past studies on thin film and nano-wire thermoelectrics will be reviewed and evaluated on measurement technique and data analysis. The potential of low-dimensional materials in applications and materials development will be accessed.
- ***Survey Efficiency Testing of Energy Conversion Devices (2013 through 2014):*** The IEA annex will conduct a study of the current state-of-the-art methods for determining energy conversion efficiency of thermoelectric devices for vehicle applications. An intentional collaboration will be coordinated by Oak Ridge National Laboratory to assess the efficiency testing system in each participating laboratory and the published results in the literature. This is a preliminary study for the follow-on IEA efforts to evaluate and standardize efficiency testing methods for advanced vehicle energy conversion materials.

Accomplishments

- This new project started late in the fourth quarter of fiscal year 2013, with limited accomplishments thus far:
  - High-temperature, round-robin studies on the half-heusler completed in NPL (UK). The tests will complete in the first quarter of fiscal year 2014 and will be analyzed in the second and third quarters.
  - A survey of thermoelectric conversion efficiency testing was completed in collaboration with Marlow Industries, GM R&D, Fraunhofer IPM (Germany), and AIST (Japan)

Future Direction

- After conclusion of the IEA study on thermoelectric materials, the annex will focus on evaluating the efficiency of energy conversion devices (such as thermoelectric and other propulsion materials) beyond fiscal year 2014. Efforts will include international round-robin studies of devices and development of testing standards.

Presentation

- Wang, H. "Thermoelectric Module Efficiency Tests –A Survey," at the *30th International Thermoelectric Conference (ICT2013)*, Kobe, Japan, June 30 – July 4, 2013.

Publication

- Wang, H., R. McCarty, J. R. Salvador, J. Konig, and A. Yamamoto, 2013, "Thermoelectric Module Efficiency Tests –A Survey," submitted to *Journal of Electronic Materials*, July 2013.

Project 18519 – Materials for Exhaust and Energy Recovery

Agreement 26463 – Biofuel Impact on Aftertreatment Devices

M. J. Lance, T. J. Toops, E. J. Nafziger*, and C. Xie**
Ceramic Science and Technology Group
Oak Ridge National Laboratory
P.O. Box 2008, MS 6068, Bldg. 4515
Oak Ridge, TN 37831-6068
Phone (865) 241-4536; fax: (865) 574-6098; e-mail: lancem@ornl.gov
** Fuels, Engines, and Emissions Research Center, ORNL*

DOE Technology Manager: Jerry L. Gibbs
Phone (202) 586-1182; fax: (202) 586-1600; e-mail: jerry.gibbs@ee.doe.gov
ORNL Technical Advisor: J. Allen Haynes
Phone (865) 576-2894; fax: (865) 574-4913; e-mail: haynesa@ornl.gov

Contractor: Oak Ridge National Laboratory, Oak Ridge, Tennessee
Prime Contract No.: DE-AC05-00OR22725

Objectives

- Characterize selective catalytic reduction, diesel oxidation catalyst, and diesel particulate filter devices following exposure to elevated levels of metal contaminants present in biodiesel; this is done to identify the deactivation and degradation mechanisms that may occur in emissions control devices operated with biodiesel fuel.

Approach

- Use state-of-the-art characterization tools within the High-Temperature Materials Laboratory to analyze the degradation mechanisms occurring in emissions control devices that had underwent accelerated aging in biodiesel received from our collaboration with Ford, the National Renewable Energy Laboratory (NREL), the Manufacturers of Emission Controls Association, and the National Biodiesel Board.
- Establish an accelerated aging methodology using an ORNL stationary diesel generator.

Accomplishments

- This new project started late in the fourth quarter of fiscal year 2013 and builds on a previous project focused solely on biofuel impact on diesel particulate filters.
- Obtained and installed a micro-X-ray fluorescence system, which will be used to characterize the chemical composition of the catalyst systems.

Future Direction

- Phase three testing, which will employ a heavy-duty engine and have cordierite diesel particulate filters, will commence soon at NREL; aged emission control devices will be studied to better understand degradation mechanisms.
- A new stationary generator will be purchased and installed at the National Transportation Research Center and will be used to conduct targeted aging studies of emission control devices.

Expected Benefits/Background

To enable renewable fuels to displace petroleum, it is critical to evaluate their compatibility with emissions control devices. Biodiesel fuel is known to contain elevated alkaline (Na and K) and alkaline earth (Ca) metal levels left over from the processing methods of these fuels. These metallic fuel contaminants are converted to oxides, sulfates, hydroxides, or carbonates in the combustion process to form an inorganic ash that can be deposited onto the exhaust emission control devices found in modern diesel engines. Alkali metals are well known poisons for catalysts and have been shown to negatively impact the mechanical properties of ceramic substrates. Furthermore, alkali metal hydroxides (such as Na and K) are volatilized in the presence of steam; therefore, they can penetrate the catalyst washcoat or substrate.

We are collaborating with Ford, NREL, the Manufacturers of Emission Controls Association, and the National Biodiesel Board to characterize accelerated biodiesel-aged specimens. Using a testing protocol developed at Ford, full-production exhaust systems will be aged at NREL with biodiesel fuel doped with metal species in order to determine if there will be increased degradation of the emission control devices when operated with 20 vol% biodiesel compared to ultra-low sulfur diesel. Samples will be characterized using tools and techniques at the High-Temperature Materials Laboratory at ORNL, such as scanning electron microscopy, energy dispersive x-ray spectroscopy, x-ray fluorescence, x-ray diffraction, Raman spectroscopy, and thermogravimetry.

Long-term, low-cost testing of materials in real diesel engine exhaust was established through a previous annual operating plan at the National Transportation Research Center) using a stationary diesel generator (gen-set). A second genset will be added this fiscal year which will be better suited for testing conditions necessary for these samples. This genset can be run unattended overnight with different fuels, enabling low-cost testing without the use of an entire test-cell and full-scale diesel engine. Accelerated aging with alkaline (Na or K) doping of biodiesel fuel will be conducted with the genset for targeted testing of some samples to further specify the effect of metal impurities on emission control device performance.

The expected benefit of this project is to identify the poisoning mechanisms of alkali metals by tracking local chemical changes in the washcoat or substrate using high-resolution probes (both electron and photon). With this information, we will be able to make recommendations to industry regarding the fuel composition and operating conditions necessary to ensure the same lifetime of emission control devices operated with B20 that they currently have with ultra-low sulfur diesel.

Project 18865 – Application-Specific Materials Simulation, Characterization, and Synthesis

Agreement 9105 – Ultra-High Resolution Electron Microscopy for Characterization of Catalyst Microstructures and Reaction Mechanisms

L. F. Allard, W. C. Bigelow, M. B. Katz*, S. Zhang*, X-Q. Pan*, G. Graham***, A. Drews**, D. P. Nackashi***, and J. Damiano****
Oak Ridge National Laboratory
P.O. Box 2008, MS 6064
Oak Ridge, TN 37831-6068
** Materials Science and Technology, University of Michigan, Ann Arbor, Michigan*
*** Ford Research Laboratory, Dearborn, Michigan*
**** Protochips, Inc., Raleigh, North Carolina*

DOE Technology Manager: Jerry L. Gibbs
Phone (202) 586-1182; fax: (202) 586-1600; e-mail: jerry.gibbs@ee.doe.gov
ORNL Technical Advisor: J. Allen Haynes
Phone (865) 576-2894; fax: (865) 574-4913; e-mail: haynesa@ornl.gov

Contractor: Oak Ridge National Laboratory, Oak Ridge, Tennessee
Prime Contract No.: DE-AC05-00OR22725

Objectives

- Develop and utilize new in situ techniques for ultra-high resolution imaging of catalytic materials in gaseous environments to study the reduction of NOx emissions in diesel and automotive exhaust systems.

Approach

- Partner with Protochips, Inc. to expand capabilities for in situ reaction studies with a unique gas-cell reactor system for the aberration-corrected electron microscope. Develop a Gen 4 gas cell holder design and beta-test commercial version of the computer-controlled gas manifold system.
- Continue current studies of experimental "self-regenerating catalysts" (based on precious metal/perovskite structure materials) for NOx reduction applications, with the goal of understanding the mechanisms of metal dissolution into the lattice, and then re-extrusion to form surface catalytic species in redox cycling experiments.

Accomplishments

- Methods for direct characterization of the temperature behavior of the Protochips Aduro™ heater for the Gen 3 gas cell holder as a function of gas pressure and flow conditions were developed and utilized to allow more accurate gas-reaction studies.
- Completion of in situ reaction studies of Pt and Rh-doped perovskite self-regenerating catalysts contributed to this year's defense of the PhD thesis for Michael Katz, with whom we worked closely for the past 3 years.

- Contributed ultra high-resolution microscopy results for further publications in the area of "single-atom catalysis" studies (e.g., with Dr. C. Narula and colleagues, publishing in *J. of the American Chemical Soc*).

Future Direction

- Initiate new studies of self-regenerating catalyst materials with Prof. X. Pan and graduate student Shuyi Zhang, concentrating on the Ba-Ce-Pt perovskite with a much finer support particle size.
- Complete introduction of new Gen 4 gas-cell reactor specimen holder and the commercial version of the computer-controlled gas manifold system. Utilize the Gen 4 system for self-regenerating catalyst studies.
- Resume "single-atom-catalysis" studies, adding a new thrust toward understanding "low-temperature reactivity" for automotive emission catalysts, in collaboration with colleagues from the University of New Mexico.

Introduction

During our research this year, we continued utilization of the in situ gas cell holder for the JEOL 2200FS aberration-corrected electron microscope for concentrated studies of perovskite-based "self-regenerating" catalysts aimed at reduction of NOx emissions in automotive engine systems. We also completed characterization of the temperature behavior of the gas-cell heater devices as a function of gas composition, pressure, and flow rate conditions. These studies allowed completion of the PhD thesis research on Pt and Rh-based perovskite "CTO" (e.g., $CaPt_{0.05}Ti_{0.95}O_3$) materials by Dr. Michael Katz, who defended in April 2013.

Results

In Situ Microscopy Development

Temperature Calibrations

A major accomplishment this year was the effort to understand the behavior of Protochips AduroTM heater devices when operated in the gas-cell reactor holder (Allard et al. 2013a, 2013b). Aduro heater devices for elevated temperature experiments in a specimen holder exposed only to the vacuum of the microscope (e.g., a single-tilt holder) are calibrated over the temperature range of RT to 1200°C using two precision infra-red camera systems. However, a similarly calibrated heater device used in a gas-cell configuration does not give a reliable measure of the temperature, because the device is exposed to the vacuum on the outside and to gas at a given pressure, composition, and flow condition on the inside. Calibrations of the devices exposed fully to gas in the calibration system showed a strong effect of gas pressure on the temperature behavior of the device (Allard et al. 2013a), with a current 85% higher at 100 Torr required to heat the device to 600°C than the current at 0 Torr. We adapted the gas-cell holder to the calibration chamber and measured the temperature of the heater devices (originally calibrated in vacuum) under both static and flowing gas conditions. As an example result, a device that required 4.5 mA to heat to 700°C in vacuum required 7.0 mA instead to heat to 700°C when fully exposed to N_2 at 300 Torr. However, the same device, when assembled into the gas cell configuration, required only 5 mA to heat to 700°C with 300 Torr N_2 in the cell. When the gas was allowed to flow through a 175-µm ID capillary (the cell pressure was initially set to about 424 Torr to achieve 300 Torr when flowing), we found that the curve of temperature versus current for the gas flowing at 300 Torr in the cell precisely overlapped the curve for static gas at 300 Torr. Figure 1 is a second example of the effects of pressure on the temperature of the heater device in the gas-cell reactor, measured for N_2 gas. For the vacuum calibration (upper curve), a heater temperature of 880°C required about 4.3 mA, but at this current and with 300 Torr N_2 gas inside the cell, the temperature dropped to 750°C. To return to the original 880°C level, a heater current of 5.15 mA was required. Many additional calibration runs were conducted, using several gas compositions over a significant molecular weight range (e.g., helium to argon) and have resulted in a better understanding of the relationships that govern the temperature behavior of gas-cell heater devices in general.

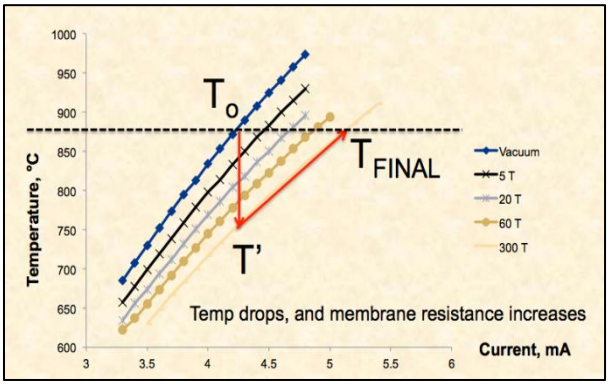

Figure 1. Example calibration of the Aduro heater device in the Gen 4 gas cell configuration for N_2 gas.

Development of Gen 4 Reactor Holder and Gas Manifold

Experience over the past 3 years with the Gen 3 reactor holder and gradual development and modification of the Oak Ridge National

Laboratory (ORNL) gas manifold system to allow precise control of gas pressure and flow conditions for in situ experiments has led to production of the next-generation holder and gas manifold fabricated by Protochips, Inc.

A comparison of the Gen 3 and Gen 4 gas cell interiors is shown in Figure 2a. The Gen 4 holder offers four electrical leads rather than two and these leads are specially fabricated with a proprietary "flexicable" design (arrowed) for proper electrical insulation and contact pads to assure easy loading of the heater and lower window devices when the cell is built for in situ experiments.

The Gen 4 gas cell will be interfaced with a Protochips-fabricated gas manifold that is run via computer control, with all valves, pumps, gas supply, gauges, and heater power able to be programmed or run remotely. The entire system will be delivered and tested at ORNL in the first quarter of fiscal year 2014, with results reported in the quarterly report for the first quarter. Figure 2b shows a view of the prototype gas manifold system.

In Situ Reaction Studies of Self-Regenerating Catalysts

Collaboration with our University of Michigan and Ford Scientific Laboratory colleagues on studies of perovskite-based self-regenerating catalyst materials culminated in the PhD thesis defense earlier this year by Dr. Michael Katz. The self-regenerative automotive catalysts are materials aimed at retaining precious metal dispersion more robustly than current automotive catalyst formulations. Further effort to understand the mechanistics of these systems has led to two complementary sets of studies: electron microscopy (both in situ and ex situ) studies are being supported by density functional theory to further understand the systems at a fundamental thermodynamic level (Pan et al. 2013). For example, for the $Pt/CaTiO_3$ system, phase diagrams were calculated under various oxygen pressures in order to fully understand the stabilities of the various phases in the system. Computed phase diagrams have provided information on the thermodynamic origin of the cyclability of the self-regenerative catalyst.

Figure 2. Comparison of the interior geometry of the Gen 3 and Gen 4 gas cell holders. The Gen 4 holder provides a new four-contact "flexicable" technology and modified cell dimensions to facilitate loading the Aduro heater and lower window devices during building of the cell for an experiment. Two additional contacts allow for future incorporation of additional electrical devices.

The in situ microscopy (i.e., gas-reaction experiments conducted at ORNL) on catalyst powder materials were used to study the redox reaction dynamics at conditions that mimicked the ex situ studies conducted at the University of Michigan on model single-crystal perovskites with deposited precious metals. For example, the reaction in the Pt-based CTO system proved to be asymmetric, with metal extruding from the oxide within several seconds upon reduction, but dissolving back into the support only with hours of aggressive oxidation. The finer particles

dissolved more readily than the larger particles. Many of the particles that formed during the reduction cycle were located in the interior of the crystal support and were not available for the catalytic process. Figure 3 is an example of an in situ reaction sequence from the Pt-CTO work where the increase in discrete particles from the as-prepared (oxidized condition) sample (Figure 3a) to the first reduction condition (800°C, 10 min, Figure 3b) is evident. Some Pt particles seen in profile on the surface of the CTO are arrowed. After a number of oxidation cycles from 450 to 800°C for more than 2 hours of total time, many of the larger particles still remain, but the original surface particles are apparently re-dissolved (Figure 3c).

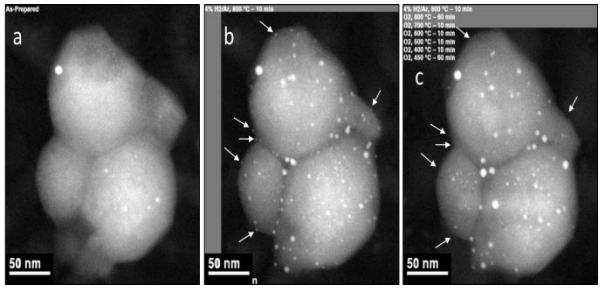

Figure 3. Example of an in situ reaction sequence from the Pt-CTO work.

Studies of the Pt-based barium cerate system (BCPO) showed a better behavior of the Pt particles during redox cycling. Figure 4 shows the near complete reversibility of Pt in the thin-film BCPO ex situ sample under redox conditions. The thrust of the new work recently started with graduate student Shuyi Zhang will focus on this system. Both powder-based and single crystal-based samples will be characterized using the JEOL 2200FS ACEM at ORNL. The first effort in the new work has concentrated on production of BCPO powders that have a significantly smaller particle size than the materials used in the CTO studies and that are more homogenous (i.e., little evidence of phase separation into the BaO and CeO_2 phases). The finer particle size will result in a greater surface area and more precious metal particles present on the surface after the reduction cycle rather than in the interior, where they are not available to participate in the catalytic reaction. The new BCPO samples will be amongst the first that are characterized in situ using the Gen 4 gas reactor system from Protochips.

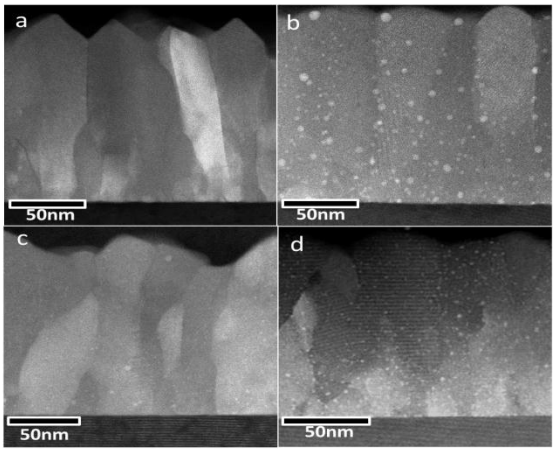

Figure 4. Comparison of $BaCe_{0.95}Pt_{0.05}O_3$ thin film after different thermal treatments: (a) as-made film is shown, where Pt ions are atomically dispersed through the BCO matrix; (b) Pt particles segregated out of the lattice after 1 hour of reduction at 800°C with 10% H_2/N_2; (c) most of them were re-absorbed into the lattice after 1 hour of re-oxidation at 800°C in air and particles with finer size distribution show up again; and (d) after 1 hour of reduction at the same condition.

Update on "Single-Atom-Catalysis" Studies

Since our publication of the first definitive paper (Qiao et al. 2011) showing unequivocally that single atom dispersions (e.g., Pt_1/FeOx) can yield stable catalysts with remarkably improved performance (e.g., for CO oxidation), many groups worldwide have undertaken further studies of this phenomenon. At this writing, our *Nature Chemistry* paper has been cited 96 times since the original July 2011 publication. Single-atom imaging work with Dr. Chaitanya Narula and Dr. Melanie Moses-Debusk at ORNL led to publication of a new single-atom contribution based on Pt/theta-alumina for CO oxidation (Moses-DeBusk et al. 2013). A long effort by colleagues at the University of New Mexico (Professor A. K. Datye and group) from which our atomic imaging of Pd single atoms on alumina has led to the submission of a *Science* paper (Peterson et al. 2013) and a plan to resume studies in fiscal year 2014 at ORNL, with the

thrust to understand whether the low-temperature reactivity of Pt and Pd on supports such as TiO_2, CeO_2, and □-Fe_2O_3 can be related to atomically dispersed species.

Conclusions

We have continued to make significant progress in our capabilities for studies of catalyst reaction mechanisms at elevated temperatures under selected gaseous environments, utilizing the unique MEMS-based heating technology offered by our collaborator Protochips, Inc. Our collaboration has led to many publications and presentations on studies of materials of both EERE-VT-PM interest and of catalyst and nanoparticulate materials in support of work with other external and ORNL (e.g., ShaRE User Program) colleagues. The opportunity to see this unique technology come to commercial fruition during our fiscal year 2014 effort is exciting. We hope that in the future this technology will in significantly enhance the research capabilities in many laboratories internationally.

References and Publications

Allard, Lawrence F., James E. Wittig, Miaofang Chi, Karren L. More, Wilbur C. Bigelow, John Damiano, and David P. Nackashi, 2013a, "Novel Closed-Cell Gas-Reaction Holder Allows Characterization of Behavior of Bimetallic Nanoparticles Under Elevated Temperatures and Gas Pressures," *Micros Microanal*, Suppl 2.

Allard, Lawrence F., Wilbur C. Bigelow, John Damiano, and David P. Nackashi, 2013b, "Operational Parameters of a MEMS-based Closed Cell Gas-Reaction Holder for In Situ Atomic-Level STEM Imaging at Elevated Temperatures and Pressures," Abstract for Program of Microscopy Society of America, *Pre-Meeting Congress on Electron Microscopy in Liquids and Gases*, Indianapolis, IN.

Howe, J. Y., L. F. Allard, H. Demers, W. C. Bigelow, and S. H. Overbury, 2013, "Synergy of Combined Secondary Electron and Transmitted Electron Imaging Techniques for the Characterization of Catalyst Behavior During In Situ Heating," submitted to *Applied Physics Letters*, August 2013.

M&M, 2013a, "Novel Closed-Cell Gas-Reaction Holder Allows Characterization of Behavior of Bimetallic Nanoparticles Under Elevated Temperatures and Gas Pressures," *M&M, Aug 4 through 8, 2013*, invited talk.

M&M, 2013b, "Operational Parameters of a MEMS-based Closed Cell Gas-Reaction Holder for In Situ Atomic-Level STEM Imaging at Elevated Temperatures and Pressures," *M&M, Pre-Meeting Congress on Electron Microscopy in Liquids and Gases, Aug. 4, 2013*, invited talk.

Moses-DeBusk, Melanie, Mina Yoon, Lawrence F. Allard, David R. Mullins, Zili Wu, Xiaofan Yang, Gabriel Veith, G. Malcolm Stocks, and Chaitanya K. Narula, 2013, "CO Oxidation on Supported Single Pt Atoms: Experimental and Ab Initio Density Functional Studies of CO Interaction with Pt Atom on θ-Al_2O_3(010) Surface," *J. Am. Chem. Soc.*, 135, 34, 12634–12645.

Pan, X. Q., M. B. Katz, B. H. Li, X. F. Du, K. Zhang, Y. W. Duan, L. F. Allard, L. Chen, A. Van der Ven, and G. W. Graham, 2013, "Understanding Behavior of Self-Regenerative Catalysts by Transmission Electron Microscopy and Density Functional Theory," *Micros Microanal,* Suppl 2.

Peterson, E. J., A. T. DeLaRiva, R. Johnson, H. Guo, J. T. Miller, J. H. Kwak, C. H. F. Peden, B. Kiefer, L. F. Allard, F. H. Ribeiro, and A. K. Datye, 2013, "Low-Temperature CO oxidation catalyzed by atomically dispersed palladium on alumina," submitted to *Science*, September 2013.

Qiao, B., A. Wang, X. Yang, L. F. Allard, Z. Jiang, Y. Cui, J. Liu, J. Li, and T. Zhang, 2011, "Single-atom catalysis of CO oxidation using Pt_1/FeOx," *Nature Chemistry*, 3, 634–641.

O'Keefe, Michael A., Lawrence F. Allard, and Douglas A. Blom, 2013, "Resolution of the Electron Microscope at the Atomic Scale," *Micros Microanal,* Suppl 2.

Suntivich, J., Z. Wu, C. E. Carlton, J. Kim, B. Han, S. W. Lee, N. Bonnet, N. Marzani, L. F. Allard, H. A. Gasteiger, K. Hamad-Schifferli, and Y. Shao-horn, 2013, "Surface Composition Tuning of Au–Pt Bimetallic Nanoparticles for Enhanced Carbon Monoxide and Methanol Electro-oxidation," *J. Am. Chem. Soc.*, 135, 21, 7985–7991.

Communications/Visits/Travel

Larry Allard presented an invited talk, "In-Situ Atomic-level Electron Microscopy of Catalysts at Elevated Temperatures and Pressures, via Innovative Closed-Cell Reactor Specimen Holder Technology," at a bi-annual corporate retreat sponsored by ExxonMobil Co. The workshop comprised three extended invited talks (Prof. Fabio Ribeiro, Purdue University, and Dr. Gabriel Vieth, ORNL) on topics involving catalytic science, with significant discussion amongst the 70 company scientists from both domestic and international ExxonMobil corporate research laboratories. ExxonMobil and ORNL currently are processing a work for others project that is expected to start in January 2014, based on this visit.

Status of Milestones

On schedule.

Project 18865 – Application-Specific Materials Simulation, Characterization, and Synthesis

Agreement 14957 – Modeling of Thermoelectrics

A. A. Wereszczak, H. Wang, and M. K. Ferber
Materials Science and Technology Division
Oak Ridge National Laboratory
P.O. Box 2008, MS 6068, Bldg. 4515
Oak Ridge, TN 37831-6068
Phone (865) 576-1169; fax: (865) 574-6098; e-mail: wereszczakaa@ornl.gov

J. Sharp, R. McCarty, A. Thompson, and M. Gilley
Marlow Industries, Inc.
10451 Vista Park Road
Dallas, TX 75238-1645
Phone (214) 342-4287; e-mail: rmccarty@marlow.com

DOE Technology Manager: Jerry L. Gibbs
Phone (202) 586-1182; fax: (202) 586-1600; e-mail: jerry.gibbs@ee.doe.gov
ORNL Technical Advisor: J. Allen Haynes
Phone (865) 576-2894; fax: (865) 574-4913; e-mail: haynesa@ornl.gov

---

Contractor: Oak Ridge National Laboratory, Oak Ridge, Tennessee
Prime Contract No.: DE-AC05-00OR22725

Objectives

- Non-Cooperative Research and Development Agreement (CRADA) subproject: Measure thermomechanical and thermophysical properties of candidate thermoelectric (TE) materials (TEMats) for waste heat recovery to advance TEMats and devices (TEDs).
- CRADA subproject: Support Marlow with their development and testing of high-temperature TEMats and TEDs.

Approach

- Non-CRADA subproject: Develop characterization test methods that will benefit the TEs and TEDs manufacturing and end-user communities.
- CRADA subproject: Measure properties of proprietary Marlow materials and provide development support.

Accomplishments

- Non-CRADA subproject: Seebeck coefficients and electrical resistivities were measured by numerous laboratories as part of a round-robin study and interlaboratory variability was assessed. The laboratories measured equivalent Seebeck coefficients; however, there was variability in the measured electrical resistivities.
- CRADA subproject: Performed testing of Marlow TEMats and supportive evaluation and mechanical test modeling of their TEDs and the constituents used in them.

Future Direction

- Non-CRADA subproject: Measure properties of additional high-temperature capable TEMats and provide supportive characterization research and development to support the improvement of TEMats and TED modeling.
- CRADA subproject: Perform thermomechanical and thermophysical property measurements of proprietary Marlow TEMats and assist in development of Marlow TEDs.
- The non-CRADA and CRADA projects are scheduled to complete in the first quarter of fiscal year (FY) 2014.

Introduction

Potential next generation TEDs comprised of p and n-type materials enjoy strong interest for implementation in high-temperature and oxidizing environments in which waste heat could be used to generate electricity. However, the intended TE function of these devices will only be enabled if the TED is designed to overcome the thermomechanical limitations (e.g., brittleness) that are usually inherent to these materials. A TEMat with a combination of poor strength and low thermal conductivity can readily fail in the presence of a thermal gradient, thereby preventing exploitation of the desired TE function.

This challenging problem can be overcome with the combined use of established probabilistic design methods developed for brittle structural components, good thermoelastic and thermomechanical databases of the candidate TEMat comprising the TED, and iteratively applied design sensitivity analysis. This project executes this process to involve TEDs.

This project has two parts. The first subproject focuses on the thermomechanical and thermophysical evaluation of candidate TEMats that are of interest to the entire TE community for high-temperature (e.g., 550°C) waste heat recovery. Development of appropriate strength test fixturing and methods are required, because there are no widely accepted strength test practices (e.g., American Society for Testing and Materials) for TE materials. The second subproject involves a CRADA with Marlow Industries and the thermomechanical and thermophysical characterization of their proprietary TEMats and supportive evaluations of their TEDs and the constituents used in them.

There will be several outcomes from this work. This work will benefit TEMat and TED developers and end-users of these potentially high-temperature TEDs. Mechanical reliability of prototypical TEDs will be evaluated from a structural brittle-material perspective and suggested redesigns will be identified. Thermomechanical reliability of developmental TEMats will be assessed and minimum required thermomechanical properties of hypothetical TEMats would be identified that produce desired reliability in a TED.

Results

The results from FY 2013 work are broken up into two sections: the non-CRADA and CRADA subprojects.

Non-CRADA Subproject (Non-Sensitive Research and Development)

The non-CRADA section is comprised of three different subsections: mechanical and dilatometry evaluations, transport property and residual stress evaluations, and International Energy Agency activities.

Mechanical Evaluations

The majority of the mechanical evaluations in FY 2013 focused on the attempt to develop a test method that could mimic the deformation and stresses in a TED experiencing a temperature gradient across it and be used as a laboratory accelerated test. An illustration of the deformation field due to an arbitrary temperature gradient is shown in Figure 1. The imposed stresses in the TED's legs were always monitored (see examples in Figures 2 and 3), and their resulting stress fields and directions of tensile stress were used to guide the considerations of many different loading scenarios for the accelerated test.

Numerous loading scenarios were considered and undesirable limitations were found with most. The most promising test methods involved customized shear testing or tension testing. Their continued refinement is being pursued in another project because this (non-CRADA) project is ending during the first quarter of FY 2014.

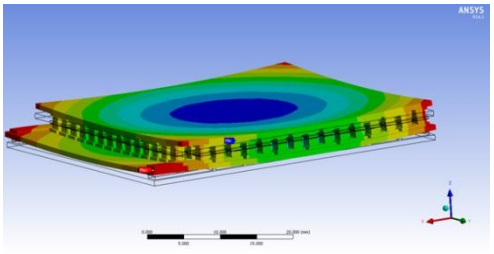

Figure 1. Temperature-gradient-induced deformation field in a TE device.

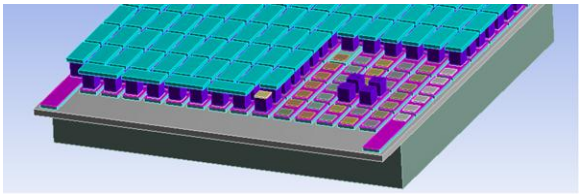

Figure 2. Exposed section showing an example of an interior region of a TED leg layout.

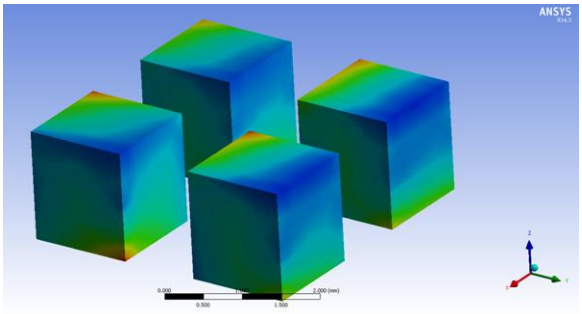

Figure 3. Example of the first principal stress field on the four legs that are shown in Figure 2.

Transport Property and Residual Stress Evaluations

Neutron residual stress measurements were continued at the High-Flux Isotope Reactor at Oak Ridge National Laboratory. In order to get accurate stress-free information, neutron powder diffraction was carried out at the POWGEN beam line at the spallation neutron source. Powers of n-type and p-type skutterudite from Marlow were tested. The POWGEN beam line is shown in Figure 4 and has the following features:

- Covers d-spacing from 0.3 to 3.0Å in a single scan
- Less than 1% resolution in all d-spacings
- Measurement time is 2 to 4 hours.

Data collected at SNS for Marlow skutterudite materials are shown in Figures 5 and 6. The neutron data cover the entire d-spacing and detailed structure refinement was able to be carried out on the materials. The p-type material shows a significantly different spectrum than the n-type material, although the basic $CoSb_3$ crystal structure remained. Secondary phases difficult to resolve from x-ray diffraction data gave more diffraction peaks in neutron results.

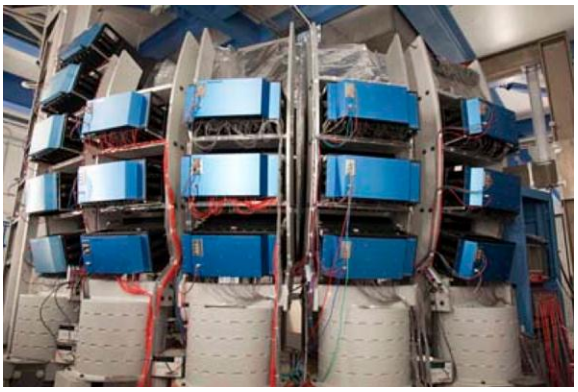

Figure 4. POWGEN beam line at SNS (detectors).

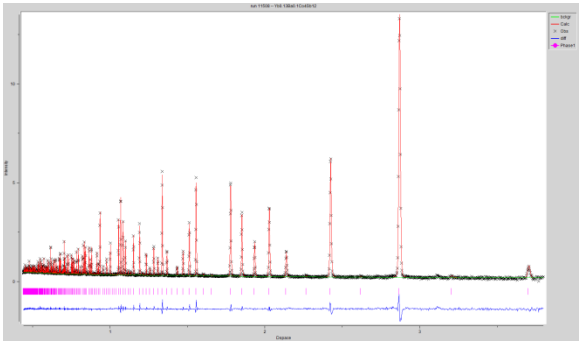

Figure 5. Neutron powder diffraction peaks for n-type skutterudite.

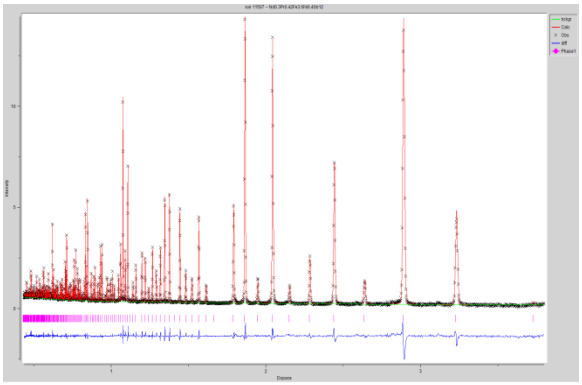

Figure 6. Neutron powder diffraction peaks for p-type skutterudite.

The detailed crystal structures of these phases were resolved. In addition to providing a zero-stress background for the follow-on High-Flux Isotope Reactor testing, the POWGEN data also gave Marlow a better understanding of the crystal structure of

skutterudite materials produced in their research and development laboratory in Dallas, Texas.

The following analyses are summarized from the diffraction data:

- The extra phases occurred in the Yb/Ba sample with a higher amount of Yb and Ba filler atoms and in the Nd/Pr sample with the smaller lattice parameter, resulting in smaller cages.
- The lattice parameters are comparable to those found via x-ray diffraction, with the Fe/Ni sample having a significantly larger lattice parameter than the others and the Yb/Ba-filled samples having the smallest lattice parameters.
- The composition of the skutterudite framework seems to be the predominate factor in determining the lattice parameter; the filler atoms do not have much effect.
- The atomic parameters of the framework atoms (i.e., Co, Fe, Ni, and Sb) are consistent across all four samples and quite stable. The Fe/Co site occupancies for Marlow p-type are refined to approximately 1/3 Fe and 2/3 Co.
- The amount of filling seems to be lower than the nominal compositions. Also, the displacement parameters of the filler atoms are generally higher than those of the framework atoms, which make sense if the filler atoms are rattling around in the cages.

International Energy Agency Progress

Oak Ridge National Laboratory also leads the International Energy Agency Annex VIII on Thermoelectrics under the Implementing Agreement of Advanced Transportation Materials. In FY 2013, the TE annex participants conducted the third international round-robin on half-heusler materials. The materials were sent to 8 laboratories in 5 countries. The preliminary results on the transport properties are shown in Figure 7.

In Figure 8, thermal diffusivity and specific heat results showed very good consistency among the participating laboratories. Unlike the previous round-robin results, the preliminary results on specific heat show much better reproducibility. The round-robin study on high-temperature thermoelectrics is expected to complete by the end of 2013 and the report will be available in 2014. This is in support of the ongoing U.S. Department of Energy waste heat recovery program and covers application temperatures of 300 to 800K.

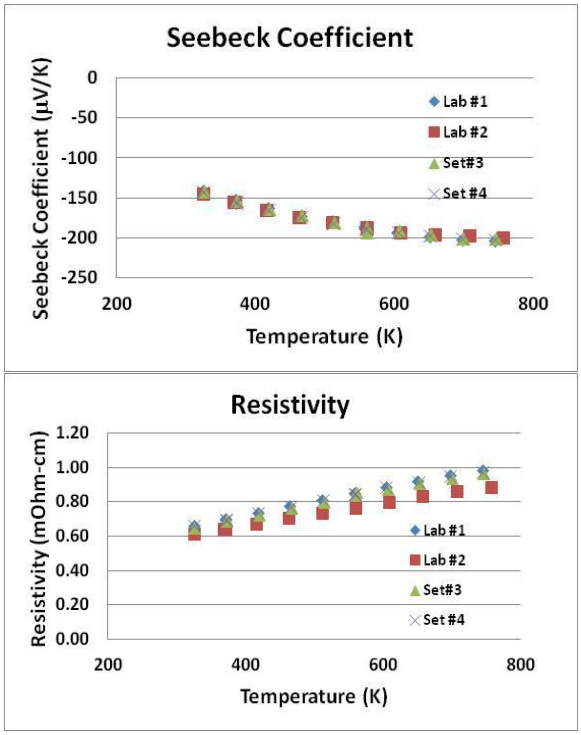

Figure 7. Seebeck coefficient and electrical resistivity of round-robin No. 3 on n-type half-heusler.

CRADA Subproject (Sensitive Research and Development)

A CRADA with Marlow Industries continued in FY 2013. It presently is scheduled to end November 30, 2013 (2 months into FY 2014). The primary intents were to measure the mechanical properties and transport properties, thermomechanically and thermophysically characterize their proprietary TEMats, and provide supportive mechanical evaluation of their TEDs and the constituents used in them. Testing of their materials continued throughout FY 2013. Transport properties of Marlow production and research TE materials were evaluated. Hundreds of specimens were tested but their results are not

divulged here owing to the sensitivity of the CRADA.

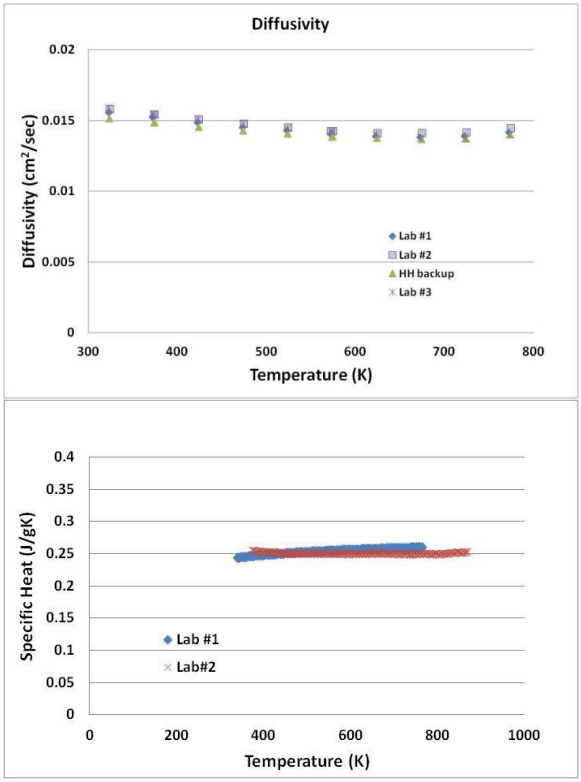

Figure 8. Prelinary thermal diffusivity and specific heat results of round-robin #3.

Oak Ridge National Laboratory continued to provide support to Marlow on high-temperature transport properties' measurements. Transport properties on melt-spun skutterudites and other Marlow materials were performed. The results are being used at Marlow as a basis for materials selection and device design.

Conclusions

For the non-CRADA portion of this project, new test methods to mechanically evaluate TEDs were conceived and transport property measurements were generated in FY 2013, including a second International Energy Agency round-robin measurement effort. For the CRADA portion, numerous tests were completed to assess mechanical and transport properties of Marlow TEMats and Marlow TEDs.

Publications

Salvador, J. R., J. Y. Cho, Z. Ye, J. E. Moczygemba, A. J. Thompson, J. W. Sharp, J. D. Konig, R. Maloney, T. Thompson, J. Sakamoto, H. Wang, A. A. Wereszczak, and G. P. Meisner, 2012, "Thermal to Electric Energy Conversion of Skutterudite-Based Thermoelectric Modules," *Journal of Electronic Materials*, DOI: 10.1007/s1 1664-012-2261-9.

Salvador, J. R., R. A. Waldo, C. A. Wong, M. Tessema, D. N. Brown, D. J. Miller, H. Wang, A. A. Wereszczak, and W. Cai, 2013, "Thermoelectric and Mechanical Properties of Melt Spun and Spark Plasma Sintered n-Type Yb- and Ba-Filled Skutterudites," *Materials Science and Engineering B*, 17, 178, 1087–1096.

Wang, H., W. D. Porter, H. Böttner, J. König, L. Chen, S. Bai, T. Tritt, A. Mayolett, J. Senawiratne, C. Smith, F. Harris, P. Gilbert, J. Sharp, J. Lo, H. Kleinke, and L. Kiss, 2013, "Transport Properties of Bulk Thermoelectrics – An International Round-Robin Study, Part I: Seebeck Coefficient and Electrical Resistivity," *Journal of Electronic Materials*, 42, 654–664.

Wang, H., W. D. Porter, H. Böttner, J. König, L. Chen, S. Bai, T. Tritt, A. Mayolett, J. Senawiratne, C. Smith, F. Harris, P. Gilbert, J. Sharp, J. Lo, H. Kleinke, and L. Kiss, 2013, "Transport Properties of Bulk Thermoelectrics – An International Round-Robin Study, Part II: Specific heat, Thermal Diffusivity and Thermal Conductivity," *Journal of Electronic Materials*, 42, 1073-1084.

Project 18865 – Application-Specific Materials Simulation, Characterization, and Synthesis

Agreement 15529 – Erosion of Materials by Nanofluids

Dileep Singh
Argonne National Laboratory
9700 S. Cass Avenue
Argonne, IL 60439
Phone (630) 252-5009; fax: (630) 252-2785; e-mail: dsingh@anl.gov

DOE Technology Manager: Jerry L. Gibbs
Phone (202) 586-1182; fax: (202) 586-1600; e-mail: jerry.gibbs@ee.doe.gov

Contractor: UChicago Argonne LLC
Prime Contract No.: DE AC03 06CH11357

Objectives

- Determine if the use of fluids containing a variety of nanoparticles results in erosive damage to radiator materials and coolant pumps
- Determine figures of merit for use of nanofluids for cooling power electronics
- Measure pumping power of nanofluids in a real system and compare results to theoretical calculations
- Determine if nanofluids will clog a pumping system.

Approach

- Characterize the thermal conductivity, viscosity, and heat transfer of various nanofluids
- Use surfactants and/or adjustments of pH to lower the viscosity of nanofluids
- Conduct experiments to study erosive damage, clogging of nanofluids, and power for pumping various nanofluids in a real system.

Accomplishments

- Designed, built, and calibrated a new erosion apparatus to measure wear in an automotive water pump and the torque required to pump nanofluids
- No significant erosive damage has been observed in the cast aluminum pump impeller and no erosion has been observed for aluminum target material
- The measured pumping power agrees with the power calculated using single-phase parameters based on measured values of the nanofluids
- Developed stable graphene-based nanofluids for power electronics with enhanced thermal performance
- Clogging test equipment was built and tested over the long term, using the graphitic nanofluids
- 12 papers were published in peer-review publications and 2 patent applications were filed.

Future Direction

- The project on erosion of nanofluids ended in fiscal year 2011. However, efforts were redirected to develop nanofluids for cooling of power electronics for hybrid electric vehicles and to evaluate fouling of channels with the developed nanofluids.

Introduction

Many industrial technologies face the challenge of thermal management. With ever-increasing thermal loads due to trends toward greater power output for engines and exhaust gas recirculation for diesel engines, cooling is a crucial issue in transportation. The conventional approach for increasing cooling rates is use of extended surfaces such as fins and microchannels. Reducing radiator size will reduce the frontal area, which will reduce the aerodynamic drag. However, current radiator designs have already stretched these approaches to their limits. Therefore, an urgent need exists for new and innovative concepts to achieve ultra-high-performance cooling. Nanofluids seem to show enormous potential as coolant for radiators. The literature provides many examples of increased fluid thermal conductivity by adding nanoparticles (see review by Yu et al. 2008). Enhanced thermal conductivity could lead to enhanced heat transfer. A computational fluid dynamics calculation of a Cummins, 500-hp, diesel engine using an ideal nanofluid as coolant has shown that the radiator size could be reduced by 5% (Saripella et al. 2007), which would reduce weight and size and aerodynamic drag.

In order for the enhanced thermal conductivity to be utilized, it must be shown that liquid erosion of typical radiator materials will be tolerable and that the increased pumping power resulting from higher viscosity will not exceed the gain in parasitic energy losses from enhanced cooling. Furthermore nanofluids cannot clog the pumping system. If nanofluids result in excessive erosive wear, clog the pumping system, or require very high increased pumping power, they cannot be used. Therefore, the Vehicle Technologies Office funds an investigation of liquid erosion of radiator materials, clogging, and pumping power using nanofluids.

During the past year, graphene-based nanofluids were developed and characterized for their thermophysical properties and fouling behavior in small channels. It has been shown that nanofluids' (Timofeeva 2011)high level of enhancement in thermal conductivity can be achieved with either addition of metallic or high aspect ratio graphitic nanoparticles. Metallic nanoparticles do not perform well because of their propensity to oxidize and agglomerate. However, carbon nanomaterials show 200 to 300% increases in thermal conductivity with carbon nanotubes (Sastry et al. 2008, Choi et al. 2001) and graphene oxides (Yu et al. 2010, 2011). These dramatic increases in thermal conductivity of nanofluids are most likely due to the unique nature of anisotropic carbon nanomaterials, which allows engagement of multiple heat transfer mechanisms in suspensions (i.e., effective medium theory, percolation, and plasmon resonances).

The drawback of carbonaceous nanofluids with high aspect ratio particles is very high viscosity (up to 3 orders of magnitude higher than viscosity of the base fluid). These viscosity increases result in pumping power penalties that are higher than the benefits in thermal conductivity of suspensions.

The focus has been on developing grapheme-based nanofluids with enhanced thermal conductivities and a minimal increase in viscosities. Subsequently, focus also has been on conducting fouling experiments with optimized nanofluid formulations.

Experimental Details and Results

Three commercial grades of graphene nanoparticles (A, B, and C) were obtained and dispersed in ethylene glycol/water. Surface functionalization of graphene particles was done prior to dispersion. Surface functionalization leads to electrostatic stabilization of the particles and, at the same time, provides thermal conductivity of the fluid by a percolation mechanism. Figure 1 shows the scanning electron microscopy images of the three functionalized graphite nanoparticles.

The effect of GnP surface functionalization of the thermo-physical properties of nanofluids were compared for unmodified GnP and f-GnP at 5 wt% loadings (Figures 2 and 3). One can see that the highest increases in thermal conductivity were achieved in C grade, followed by B grade and A grade, provided the smallest thermal conductivity increases. The observed enhancements are well beyond the effective

medium theory prediction. Surface functionalization of graphitic nanoparticles reduces the thermal conductivity enhancements across all grades by 30 to 50% of analogous GnP suspensions. However, the increases in thermal conductivity are still way beyond the effective medium prediction, reaching 75 to 85% above the base fluid at about 2.25 vol. %.

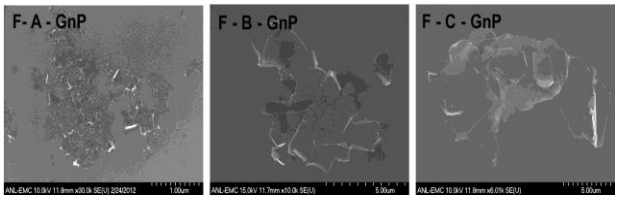

Figure 1. Scanning electron microscopy images of corresponding surface functionalized (f-GnP) graphitic materials.

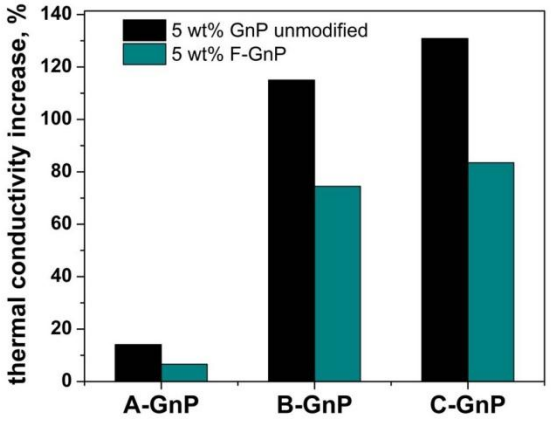

Figure 2. Thermal conductivity of graphitic nanofluids with unmodified GnP and f-GnP nanoparticles measured at room temperature.

Figure 3 shows the effect of surface modification on the viscosity of nanofluids with unmodified GnP and f-GnP dispersed in EG/H_2O at the same concentration. The viscosity of f-GnP is nearly two orders of magnitude less than viscosity of the same grade unmodified GnP. The viscosity of nanofluid is about 30% higher than the viscosity of base fluid, which is very promising for heat transfer, considering a still significant increase in thermal conductivity. It should be mentioned here that B grade had is the most dramatic drop in viscosity amongst all three grades.

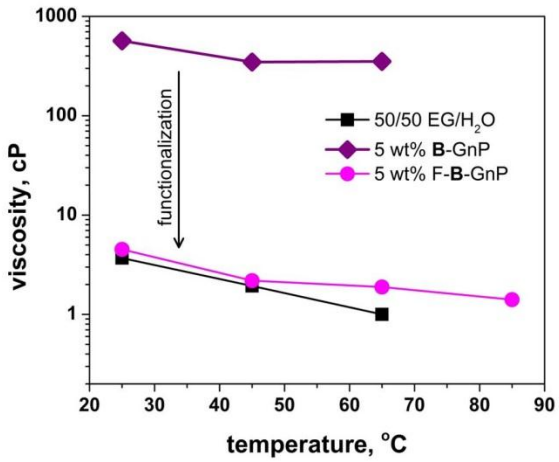

Figure 3. Viscosity of 5 wt/% B-grade dispersions with unmodified GnP (purple diamonds) and f-GnP (magenta circles).

Because cooling efficiency of the heat transfer fluids is the main consideration in current nanofluid development, the ratio of heat transfer coefficients for the suspensions and the base fluid was estimated for fully developed (hydrodynamically and thermally), laminar, and turbulent flow regimes using the fluid dynamic equations (Yu et al. 2010, Etherington 1958). The ratio of heat transfer coefficients is a convenient measure for comparison of two fluids flowing in the same geometry and at the same flow rates. In a laminar flow regime, the heat transfer coefficients are proportional to the thermal conductivity (within the acceptable range of inlet/outlet temperature difference). However, in a turbulent flow regime, the heat transfer coefficients depend on a set of thermo-physical properties. Introduction of nanoparticles to the fluids changes density (ρ), thermal conductivity (k), viscosity (μ), and specific heat (c_p) of the coolant.

The overall efficiencies of the nanofluids developed were estimated based on the measure properties; they are presented in Figure 4 for grade B functionalized nanofluids. The ratio of heat transfer coefficients (hnf/h0) for the nanofluid and the base fluid, calculated for different temperatures, shows that the inclusion

of graphitic nanoparticles in EG/H_2O coolant can provide significant (i.e., 75 to 90%) improvement in heat transfer rates when used in the laminar flow regime, improving with an increase in temperature. Heat transfer coefficients in the turbulent flow regime show 30 to 40% improvement in heat transfer compared to the base fluid. These results are very encouraging, because the enhancements levels not only meet the power electronics cooling criteria, but also will be beneficial in several other applications.

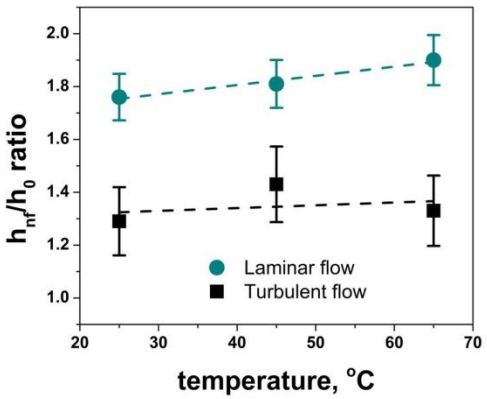

Figure 4. Calculated ratio of heat transfer coefficients for 5 wt.% B- f-GnP in EG/H_2O in laminar and turbulent flow regimes.

A photograph of the clogging apparatus used in fouling experiments is shown in Figure 5. The fouling/clogging test apparatus is a closed loop where nanofluid is circulated at a controlled temperature. A pressure drop between the two channels indicates clogging/fouling of channels and separation of nanoparticles from nanofluid. It consists of a "U"-shaped tube, 1.6 mm inside diameter, that can be heated to about 100°C. A peristaltic pump is used to move the fluid at about 120 ml/min.

Tests were conducted using a graphitic-based nanofluid (5 wt% F-B-GnP in ethylene glycol and water) for 80 to 200 h. The pump was stopped and restarted several times at ambient temperatures. Clogging is measured by a differential pressure gauge. No recorded pressure change that was interpreted as no clogging was observed with the graphite nanofluids. To–date, the results (Figure 6) indicate a stable reading of pressure drop over a week of testing, which indicates stable performance of the developed graphitic nanofluid.

Figure 5. View of clogging apparatus.

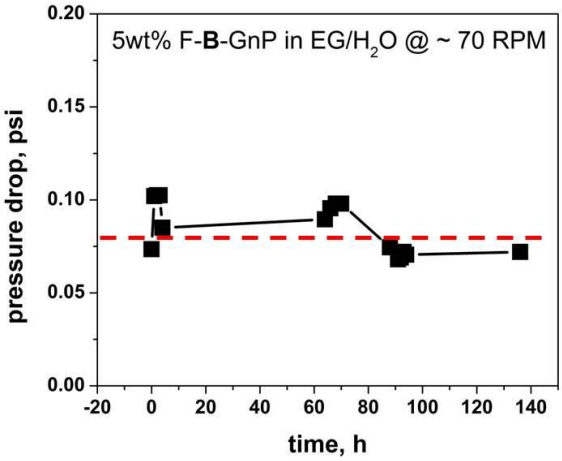

Figure 6. Experimental data on clogging/fouling test of 5 wt% f-GnP nanofluid. Insignificant fluctuation in pressure drop indicates no clogging of the channels.

Conclusions

Nanofluids with enhanced performance have been developed using functionalized graphene nanoparticles. Property measurements have shown that the overall efficiencies of these fluids are significant in both laminar and turbulent regimes. Further, preliminary fouling experiments do not indicate any clogging of channels from the developed nanofluids. Implementation of this technology in hybrid electric vehicles and electric vehicles will result in reducing the size, weight**,** and number of heat exchangers, further improving vehicle efficiency.

References

Choi, S. U. S. et al., 2001, "Anomalous thermal conductivity enhancement in nanotube suspensions," *Applied Physics Letters*, 79(14), 2252–2254.

Etherington, H., ed. *Nuclear Engineering Handbook*. 1958, McGraw-Hill Book Company, Inc.: New York, USA.

Saripella, S. K., W. Yu, J. L. Routbort, D. M. France, and Rizwan-uddin, 2007, "Effects of Nanofluid Coolant in a Class 8 Truck Engine," SAE Technical Paper 2007-01-21413.

Sastry, N. N. V. et al., 2008, "Predicting the effective thermal conductivity of carbon nanotube based nanofluids," *Nanotechnology*, 19, 055704.

Timofeeva, E. V., 2011, *Nanofluids for Heat Transfer: Potential and Engineering Strategies*, in *Two Phase Flow, Phase Change and Numerical Modeling*, A. Ahsan, Editor, InTech., 435–450.

Yu, W., H. Q. Xie, and D. Bao, 2010, "Enhanced thermal conductivities of nanofluids containing graphene oxide nanosheets," *Nanotechnology*, 21(5), 055705.

Yu, W., D. M. France, J. Routbort, and S. U. S. Choi, 2008, "Review and Comparison of Nanofluid thermal Conductivity and Heat Transfer Enhancements," *Heat Transfer Engineering*, 29, 432–460.

Yu, W. et al., 2010, "Thermophysical property-related comparison criteria for nanofluid heat transfer enhancement in turbulent flow," *Applied Physics Letters*, 96, 213109-3.

Yu, W. et al., 2011, "Significant thermal conductivity enhancement for nanofluids containing graphene nanosheets," *Physics Letters A*, 375(10), 1323–1328.

Project 18865 – Application-Specific Materials Simulation, Characterization, and Synthesis

Agreement 16308 – Thermoelectrics Theory and Structure

D.J. Singh
Materials Science and Technology Division
Oak Ridge National Laboratory
P.O. Box 2008, MS 6056
Oak Ridge, TN 37831-6068
Phone (865) 241-1944; fax: (865) 574-7659; e-mail: singhdj@ornl.gov

DOE Technology Manager: Jerry L. Gibbs
Phone (202) 586-1182; fax: (202) 586-1600; e-mail: jerry.gibbs@ee.doe.gov
ORNL Technical Advisor: J. Allen Haynes
Phone (865) 576-2894; fax: (865) 574-4913; e-mail: haynesa@ornl.gov

Contractor: Oak Ridge National Laboratory, Oak Ridge, Tennessee
Prime Contract No.: DE-AC05-00OR22725

Objectives

- Find ways to optimize existing thermoelectric materials and discover new families of high-performance thermoelectrics for waste heat recovery applications using modern, science-based materials design strategies.
- Find low-cost materials that have high thermoelectric figures of merit and are suitable for vehicular applications.

Approach

- First principles calculations, based on quantum mechanics, are used to calculate the electronic structure and thermoelectric properties of materials.
- Boltzmann transport equations are solved to obtain electrical transport properties.
- Vibrational properties are investigated and mechanisms for thermal conductivity reduction are assessed.

Accomplishments

- Found that an entire family of alkaline earth plumbide semiconductors (Ca_2Pb, Sr_2Pb, and Ba_2Pb) may exhibit good thermoelectric performance, for both p-type and n-type, at a range of temperatures from room temperature (suitable for heating and cooling applications) to 900K (suitable for exhaust waste heat recovery).
- Found that a corresponding family of environmentally friendly stannide semiconductors (Ca_2Sn, Sr_2Sn, and Ba_2Sn) may also show good thermoelectric performance at elevated temperatures.
- Found that the chalcogenide semiconductor PbS may show ZT values as high as 1.7 to 2.0 for both p-type and n-type at elevated temperatures.
- Identified acoustic impedance mismatch scattering as the agent of thermal conductivity reduction in nanostructured thermoelectrics and proposed a nanostructuring "figure-of-merit" for the likely efficacy of such scattering.
- Identified low-dimensional electronic structures, which can exist even in electrically isotropic materials, as a potential paradigm for high thermoelectric performance.

Future Direction

- Identify new, high-performance, low-cost thermoelectric compositions suitable for vehicular applications such as exhaust waste heat recovery and cabin heating/cooling.
- Calculate doping level dependence of thermoelectric properties to guide optimization of existing materials.

Introduction

The use of thermoelectric devices to convert waste heat in vehicle exhaust to electricity offers potentially significant energy savings. Among the requirements for effective use of such devices is the availability of high-performance thermoelectric materials, with low cost and other properties needed for application in vehicles. The dual requirement for both high performance and low cost has constrained thermoelectric applications in the automotive industry, although thermoelectrics have been effectively inserted in the context of seat cooling. In this regard, there is interest in improved thermoelectric materials, not only for waste heat recovery, but for zonal heating and cooling in automobiles as well. High-performance thermoelectric materials have the potential for improving fuel efficiency and, at the same time, improving occupant comfort by directing cooling where needed in the cabin.

We are developing improved materials using a science-based approach, with a primary focus on materials for waste heat recovery. In particular, we are using materials design strategies based on first principles calculations of electronic, vibrational, and transport properties to identify potentially low-cost, high-performance thermoelectric materials suitable for application in vehicles. We also are calculating the properties of existing materials as a function of doping and other parameters to obtain information needed for optimization of these materials. The emphasis is on the thermoelectric figure of merit (ZT) at temperatures relevant to waste heat recovery, as well as materials properties of importance in engineering thermoelectric modules (e.g., anisotropy and mechanical properties). High $ZT=\sigma S^2T/\kappa$ requires a combination of high thermopower (S), good electrical conductivity (σ), and low thermal conductivity (κ). Finding materials with the needed combination of properties is challenging because high thermopower and high conductivity most commonly occur in different doping regimes (Singh and Terasaki 2008). We use state-of-the-art computational tools such as the linearized augmented planewave method (Singh 2006) and the BoltzTraP code (Madsen and Singh 2006).

Results

Alkaline Earth Plumbides Ca_2Pb, Sr_2Pb, and Ba_2Pb

Vehicular waste heat recovery and heating/cooling applications require both high performance and low cost. In this regard, we have identified, in a recently published technical report (Parker and Singh 2013), three alkaline earth plumbides as potential low-cost, high-performance thermoelectrics for use in vehicular applications, both at room temperature (heating/cooling) and elevated temperature (waste heat recovery) and for both p-type and n-type.

Figures 1 through 3 present calculated thermopowers for the three materials. As shown in the figures, large thermopowers have a range of temperatures from 300 to 800 K and as high as 1000 K, depending on the material. This is important given that the only experimental study (Russell and Klein 1961) of these materials found a significant room temperature ZT of 0.2 at a likely non-optimal carrier concentration.

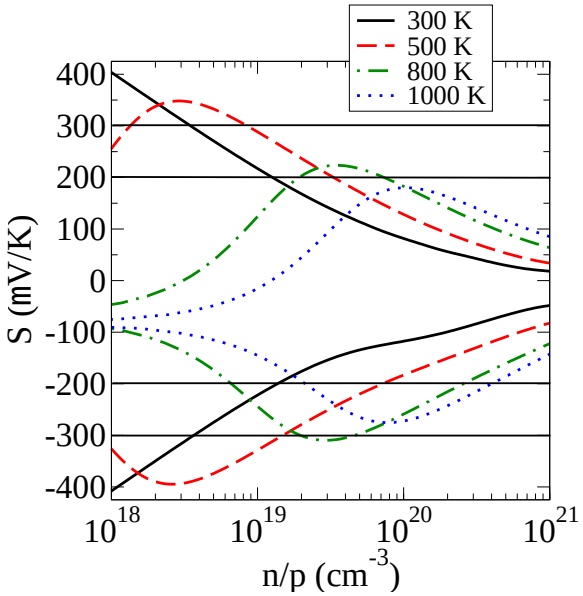

Figure 10. Calculated thermopower of Ca_2Pb at various temperatures and doping levels.

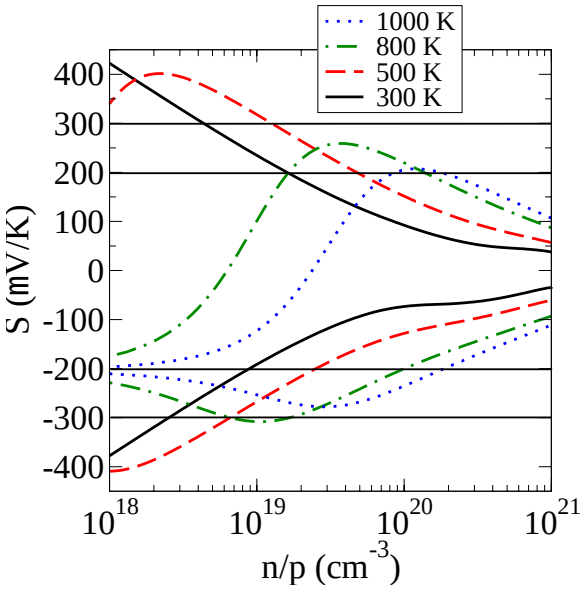

Figure 2. Calculated thermopower of Sr_2Pb.

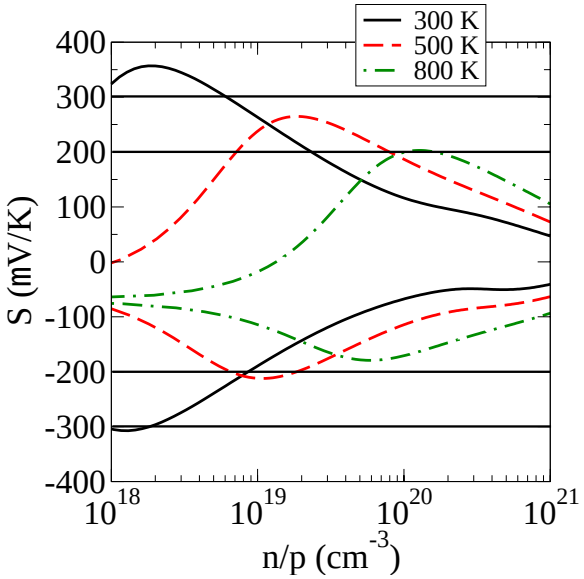

Figure 3. Calculated thermopower of Ba_2Pb.

Thermopower is an indispensable ingredient of a useful thermoelectric; all three materials have viable thermopower values for both p-type and n-type across a broad range of temperatures. Additionally, we calculated the bulk moduli of these materials (Figure 4) and compared them with the better known chalcogenide materials (PbTe, PbSe, and PbS), finding values roughly half of those for these better-known materials. This is important because low bulk moduli are indicative of low sound speeds, which, in turn, implies low lattice thermal conductivity (this is a key characteristic of a usable thermoelectric).

Compound	B (GPa)	Density (g cm^{-3})
Ca_2Pb	29.7	4.8
Sr_2Pb	23.4	5.5
Ba_2Pb	18.9	6.1
PbS	55.7	7.6
PbSe	49.2	8.1
PbTe	40.4	8.2

Figure 4. Bulk moduli calculated for the alkaline earth compounds (our calculations) and the lead chalcogenides (from Zhang et al. 2009).

These findings suggest experimental investigation of these materials. We are in touch with experimentalists in the community regarding such investigations.

Environmentally Friendly Alkaline Earth Stannides Ca_2Sn, Sr_2Sn, and Ba_2Sn

We also studied the related tin compounds. These share a common orthorhombic structure and, in fact, are isoelectronic to the lead compounds. However, they replace the lead (which may pose regulatory concerns for implementation into vehicular applications) with the environmentally benign tin. The physical structure similarities suggest that the electronic structure of these materials (like the corresponding lead compounds) is likely to be favorable for thermoelectric performance. With this in mind, we performed some initial calculations on these materials and found that, indeed, the electronic structure is favorable and nearly identical to that of the lead compounds (Figure 5).

The main difference is the somewhat larger calculated band gaps in the tin compounds. The implication is that at the highest temperatures, the performance of these materials could outstrip that of the lead compounds due to the smaller negative effects of bipolar conduction.

One final point is that because all six materials are isoelectronic and isostructural, it should be possible to alloy on both the alkaline earth and tin/lead site, which may be useful in reducing the lattice thermal conductivity.

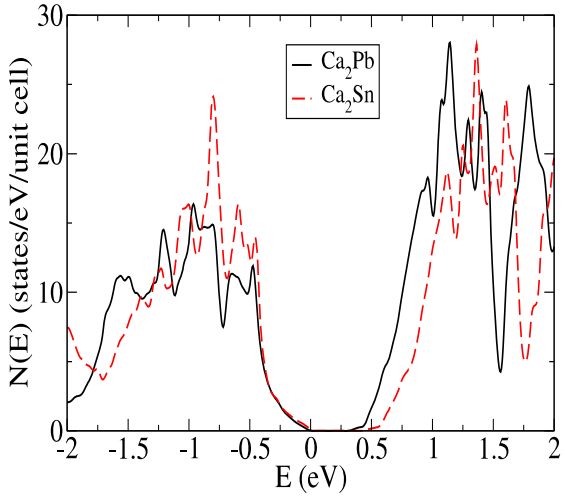

Figure 5. The calculated densities-of-state for Ca_2Pb and Ca_2Sn. Note the great similarity in electronic structure, particularly in the first half of an eV from the band edge, which is the relevant region for thermoelectric transport.

Earth-Abundant Potential High-Performance Thermoelectric PbS

The high-thermoelectric performance (i.e., ZT) of PbTe and PbSe is well known, with current ZT values in the former material (Xie et al. 2012) now exceeding 2 and the latter at 1.7 (Zhang et al. 2012). By contrast, the sister lead chalcogenide PbS has undergone much less study and optimization and partly as a result of this, the currently achieved ZT values for this material do not exceed 1.3 (Zhao et al. 2012).

We performed a theoretical study of this material and found (see Figures 6 and 7) that at elevated temperatures of 1000 to 1200K (i.e., the upper end of the waste heat recovery temperatures), this material may show ZT values as high as 1.6 to 2. In addition, these ZT values appear to be attainable for both p-type and n-type materials, a substantial advantage when compared to the other lead chalcogenides PbSe and PbTe, for which p-type performance significantly exceeds n-type performance. This is particularly true when considering issues of thermal expansion in the legs of a thermoelectric generator for which it is a distinct benefit to have both legs made of the same base material.

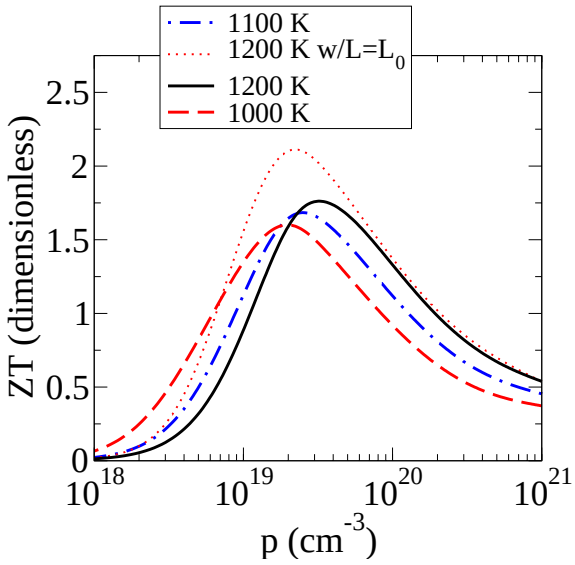

Figure 6. The predicted p-type ZT values for PbS at 1000, 1100, and 1200K. The dotted line refers to a scenario in which the negative effects of bipolar conduction are minimized, potentially by alloying with tin to increase the band gap.

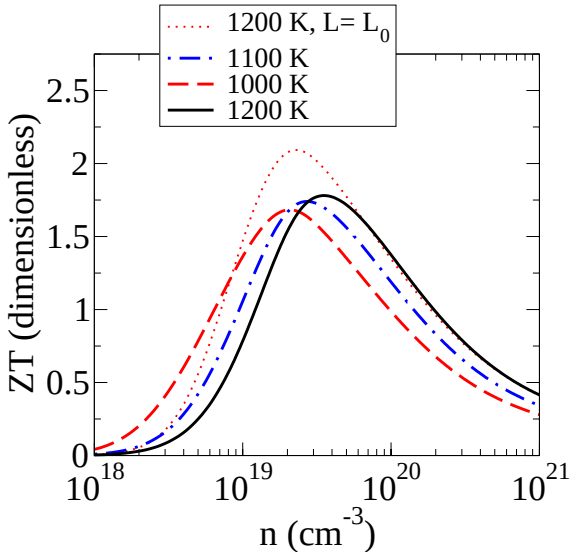

Figure 7. The predicted n-type ZT values for PbS at the indicated temperatures.

Acoustic Impedance Mismatch Scattering in Nanostructured Thermoelectrics

Although it has been recognized (Zhang and Tritt 2009, Poudel et al. 2008) that "bulk" nanostructuring (such as melt-spinning and hot pressing) can be an effective method of reducing

thermal conductivity and thereby enhancing performance (i.e., ZT), the precise reason for this has remained unclear. In a recent published work (Chen et al. 2013), we identified the acoustic impedance mismatch, or the effective resistance to the transmission of a sound wave, at the nanograin boundaries as the agent for this thermal conductivity. In particular, we identified the anisotropy (see Figure 8) of this sound speed as the key determining factor and developed a quantitative measure of this anisotropy that is easily obtainable from the measured elastic constants of the material. This quantitative measure of anisotropy is of considerable value to experimentalists considering whether to apply bulk nanostructuring to a given material. We also pointed out that it is possible to have significant sound speed anisotropy even in a cubic material; this is a fact of importance given the prominence of the cubic lead chalcogenides in the thermoelectrics field.

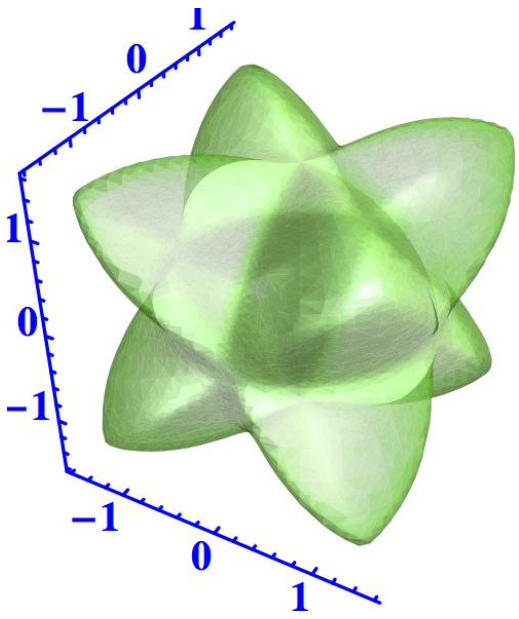

Figure 8. The calculated sound speed, in km/sec, of a transverse mode in PbTe. Distances from the origin represent the sound speed in that direction.

We also performed calculations of the phonon dispersions of Bi_2Te_3 (Figure 9), finding a substantial sound speed anisotropy that is consistent with experimental results on bulk nanostructuring (Zhang and Tritt 2009, Poudel et al. 2008).

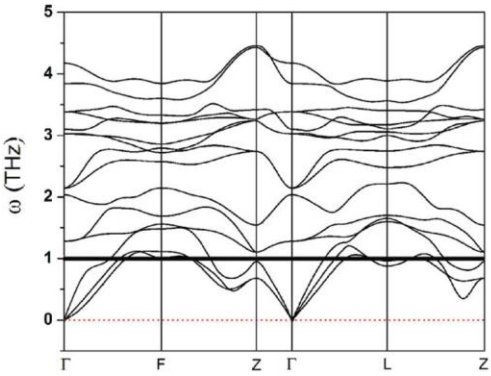

Figure 9. The calculated phonon dispersion of Bi_2Te_3 in the rhombohedral Brillouin zone. The heavy black line indicates the upper frequency limit of the heat-carrying acoustic modes.

We studied the impact of low-dimensional electronic structures (as found in high-performance thermoelectrics PbTe, PbSe and Bi_2Te_3) (Parker et al. 2013a) on thermoelectric performance. We found (see Figure 10) that the presence of such structures can significantly enhance thermoelectric performance, even in cubic materials such as PbTe and PbSe. This provides a useful paradigm for the selection of future thermoelectric materials for study and optimization.

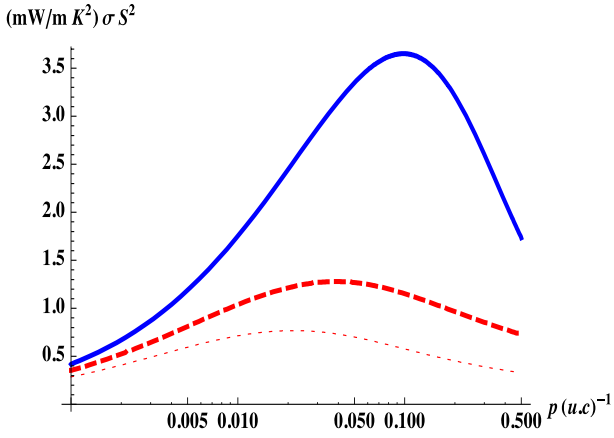

Figure 10. The calculated power factor, in holes per unit cell, for a two-dimensional "pipe"-like feature (blue) as is present in the valence bands of PbTe and PbSe) compared with that of a three-dimensional feature (red).

Combined Experimental and Theoretical Study of Thermoelectric Performance of CoSbS

In a recently published technical report (Parker et al. 2013b) in collaboration with Michael McGuire, we found that the semiconductor CoSbS exhibited ZT values of 0.35 at 773K and is expected to exhibit ZT values of unity or higher when fully optimized.

Conclusions

We are obtaining new insights into thermoelectric materials performance using the Boltzmann transport theory based on first principles electronic structures. We have identified two families – the alkaline earth plumbides and stannides – of materials likely to show good thermoelectric performance at a range of temperatures from room temperature to waste heat recovery temperatures.

We also found that if suitably optimized, the earth-abundant chalcogenide PbS may show ZT values from 1.6 to 2 at waste heat recovery temperatures. We have identified sound speed anisotropy as the determining factor in the effectiveness of nanostructuring in reducing thermal conductivity and the potential benefits to thermoelectric performance of low-dimensional electronic features.

Finally, our previously published predictions (Parker and Singh 2010, Singh 2010) concerning the potential thermoelectric performance of optimized PbTe and PbSe have been confirmed (Zhao et al. 2012, Zhang and Tritt 2009, Pei et al. 2011, Wang et al. 2011) by the groups of G. J. Snyder, M. G Kanatzidis, and Z. F. Ren. The highest reported ZT values in these materials are 2.2 (PbTe) (Zao et al. 2012) and 1.7 (PbSe) (Zhang and Tritt 2009).

References

Chen, X., D. Parker, and D. J. Singh, 2013, "Acoustic impedance and interface phonon scattering in Bi2Te3 and other semiconducting materials," *Phys. Rev. B*, 87, 045317.

Madsen, G. K. H. and D. J. Singh, 2006, "BoltzTraP: A code for calculating band-structure dependent quantities," *Computer Physics Communications*, 175, 67.

Parker, D. and D. J. Singh, 2010, "High-temperature thermoelectric performance of heavily doped PbSe," *Phys. Rev. B*, 81, 035204.

Parker, D. and D. J. Singh, 2013, "Alkaline earth lead and tin compounds Ae2Pb, Ae2Sn, Ae = Ca, Sr, Ba, as thermoelectric materials," *Science and Technology of Advanced Materials*, 14, 055003.

Parker, D., X. Chen, and D. J. Singh, 2013a, "High three dimensional thermoelectric performance from low dimensional bands," *Phys. Rev. Lett.*, 110, 146601.

Parker, D. A. F. May, H. Wang, M. A. McGuire, B. C. Sales, and D. J. Singh, 2013b, "Electronic and thermoelectric properties of CoSbS," *Phys. Rev. B*, 87, 045205.

Pei, Y., X. Shi, A. LaLonde, H. Wang, L. Chen, and G. J. Snyder, 2011, "Convergence of electronic bands for high performance bulk thermoelectrics," *Nature*, 473, 66.

Poudel, B. et al., 2008, "High-Thermoelectric Performance of Nanostructured Bismuth Antimony Telluride Bulk Alloys," *Science*, 320, 634.

Russell, V. A. and P. H. Klein, 1961, "The Synthesis, Structure and Thermoelectric Properties of Some II-IV Compounds," *Adv. Ener. Conv.*, 1, 147.

Singh, D. J., 2006, *Planewaves, Pseudopotentials and the LAPW Method*, 2nd Edition, Springer, Berlin.

Singh, D. J., 2010, "Doping-dependent thermopower of PbTe from Boltzmann transport calculations," *Phys. Rev. B*, 81, 195217.

Singh, D. J. and I. Terasaki, 2008, "Nanostructuring and more," *Nature Materials*, 7, 616.

Wang, H., Y. Pei, A. D. LaLonde, and G. J. Snyder, 2011, "Heavily doped p-Type PbSe with high thermoelectric performance: an alternative for PbTe," *Adv. Mat.*, 23, 1366.

Xie, W., X. Tang, Y. Yan, K. Biswas, J. He, I. D. Blum, C-I Wu, T. P. Hogan, D. N Seidman, V. P. Dravid, and M. G. Kanatzidis, 2012, "High-performance bulk thermoelectrics with all-scale hierarchical architectures," *Nature*, 489, 414.

Zhang, Q. and T. M. Tritt, 2009, "Unique nanostructures and enhanced thermoelectric performance of melt-spun BiSbTe alloys," *Appl. Phys. Lett.*, 94, 102111.

Zhang, Y., X. Ke, C. Chen, J. Yang, and P. R. C. Kent, 2009, "Thermodynamic properties of PbTe, PbSe, and PbS: First-principles study," *Phys. Rev. B*, 80, 024304.

Zhang, Q., F. Cao, W. Liu, K. Lukas, B. Yu, S. Chen, C. Opeil, D. Broido, G. Chen, and Z. Ren, 2012, "Heavy Doping and Band Engineering by Potassium to Improve the Thermoelectric Figure of Merit in p-Type PbTe, PbSe, and PbTe1−ySey," *J. Am. Chem. Soc.*, 134, 10031.

Zhao, L. D., J. He, C.-I. Wu, T. P. Hogan, X. Zhou, C. Uher, V. P. Dravid, and M. G. Kanatzidis, 2012, "Thermoelectrics with Earth Abundant Elements: High Performance p-type PbS Nanostructured with SrS and CaS," *J. Am. Chem. Soc*., 134, 7902.

Project 18865 – Application-Specific Materials Simulation, Characterization, and Synthesis

Agreement 26391 – Applied ICME for New Propulsion Materials

D. J. Singh
Materials Science and Technology Division
Oak Ridge National Laboratory
P.O. Box 2008, MS 6064, Bldg. 4515
Oak Ridge, TN 37831-6068
Phone (865) 241-1944; fax: (865) 574-7659; e-mail: singhdj@ornl.gov

DOE Technology Manager: Jerry L. Gibbs
Phone (202) 586-1182; fax: (202) 586-1600; e-mail: jerry.gibbs@ee.doe.gov
ORNL Technical Advisor: J. Allen Haynes
Phone (865) 576-2894; fax: (865) 574-4913; e-mail: haynesa@ornl.gov

Contractor: Oak Ridge National Laboratory, Oak Ridge, Tennessee
Prime Contract No.: DE-AC05-00OR22725

Objectives

- Develop and demonstrate integrated computational materials engineering (ICME) approaches applicable to propulsion materials needed for improving the energy efficiency of vehicles.
- Find new, rare earth–free, permanent, magnetic materials for use in electric motors.
- Identify and develop durable, supported catalysts to treat exhaust at lower temperatures than currently possible.
- Find low-cost, high-performance thermoelectric materials for waste heat recovery and cabin climate control.
- Identify high-performance piezoelectric materials for precisely controlled high-pressure fuel injection.

Approach

- Perform first principles calculations of the structure and properties of perovskite oxides related to $Pb(Zr,Ti)O_3$ (PZT), along with synthesis and characterization of perovskite oxides with feedback between theory and experiment to optimize properties.
- Perform synthesis and magnetic measurements for potential high-performance ferromagnets, including Fe_3P-based, $Co_{23}Hf_6$-based, and related materials and first principles calculations of magnetization and anisotropy as a function of composition to guide magnet optimization.
- Use an integrated approach with computational modeling and experimental development, design, and testing of new catalyst materials.
- Perform Boltzmann transport calculations of thermoelectric properties.

Accomplishments

- Completed initial down select of modified pseudoternary perovskite compositions based on $Pb(Zr,Ti)O_3$.
- Initiated experimental study of Fe_3P-based and $Co_{23}Hf_6$-based materials as potential high-performance magnets.

Future Direction

- Development and use of ICME approaches for propulsion materials.
- Identification of practical high-performance, rare earth–free, permanent magnet materials; durable, low-temperature catalysts; high-performance thermoelectrics; and advanced piezoelectric materials.

Introduction

The goal of meeting vehicle efficiency targets will benefit from and, in some cases, critically depends on development of advanced materials. However, traditional approaches to materials discovery and development are time consuming, with pathways from recognition of a need to deployment of a new material often taking many years. The need for better approaches for materials development has been recognized in recent initiatives, including the Materials Genome Initiative and Materials by Design activities. One approach that has been proposed in the context of applied materials is Integrated Computational Materials Engineering (ICME). This involves integration and feedback between computation, theory, and experiment. This project has the overarching goal of developing and demonstrating ICME tools applied to propulsion materials and specific materials challenges that are addressed.

This project addresses barriers in four areas using modern materials discovery approaches, including integrated computational materials engineering. (1) Practical piezoelectrics with higher performance are needed for fuel injectors to enable high-efficiency, emissions-compliant, advanced combustion engines. (2) Rare earth-free, high-energy product, permanent magnets are needed to have a sufficient supply of material for electric propulsion in vehicles. (3) High-figure–of-merit thermoelectric materials will enable combustion engine waste heat recovery and efficient electric vehicle climate control. (4) Low-temperature-supported catalysts are needed for emission treatment in advanced engines. The goal is to identify practical materials that reduce petroleum dependence by enabling higher efficiency vehicle propulsion. Specifically, in the context of electric vehicles, identify rare earth-free permanent magnets that can replace $Nd_2Fe_{17}B$-type material in electric drive motors and thermoelectrics that enable vehicle climate control with reduced electric load. Likewise, in the context of efficient combustion engine vehicles, identify supported catalysts for exhaust treatment, high-performance piezoelectrics for advanced fuel injection and thermoelectric materials for waste heat recovery.

The overall approach is collaborative, using a combination of theory and experiment to identify new useful materials.

Permanent Magnets

We will investigate under-studied, known materials and examine new compounds in rare earth-free chemical systems that have the potential to produce strong permanent magnets with operating temperatures above room temperature.

Major breakthroughs in the field of permanent magnet materials require the discovery and development of new classes of advanced magnetic materials. We will focus on complex materials with anisotropic crystal structures and use heavy transition metals (e.g., Hf, Ta, W, and Mo) to provide the spin orbit coupling that is provided by rare earths in conventional permanent magnets. We will make use of theory to get trends that will help identify synthesis targets. We will apply Oak Ridge National Laboratories world-class capabilities in materials synthesis, characterization, processing, and modeling to promising chemical systems and compounds with high concentrations of magnetic three-dimensional transition metals in combination with heavy transition metals and/or other light elements.

Catalysts

We will use an integrated approach with computational modeling and experimental development, design, and testing of new catalyst materials. This will enable rapid identification of the key physiochemical parameters necessary for improving the catalytic efficiency at low temperatures. Improvements in engines and combustion strategies are resulting in lowering exhaust temperatures, thus necessitating the need for catalysts that can treat exhaust at lower temperatures than currently possible. The results will have direct impact on the optimal design, low-temperature performance, and durability of supported catalysts employed in emission treatment, including lean NO_x catalysts, three-way catalysts, oxidation catalysts, and lean NO_x traps.

Thermoelectrics

We will use density functional-based first principles methods to obtain thermoelectric properties of materials. We will calculate the electronic and vibrational properties of existing and notional thermoelectric compounds. These will provide input for transport calculations using a computer code developed by Oak Ridge National Laboratory in collaboration with Aarhus University. These will provide quantitative predictions of thermoelectric properties and their variation with chemical composition.

Trends will be identified and used to suggest other compositions to be tested by detailed calculations. A specific emphasis will be on materials that are potentially low cost. We will especially emphasize alternatives to tellurium-containing compounds (such as PbTe and Bi_2Te_3) because tellurium is a very rare element and, as such, its low availability is a barrier to widespread application in vehicles.

Piezoelectrics

The currently used material is a perovskite lead that contains ceramic of composition $PbZr_xTi_{1-x}O_3$ with x near 0.5 and is known as PZT. There are three technical issues that need to be addressed: (a) maximum strain – this is the relative length change under practical electric fields and determines the length of the piezo-stack needed; (2) actuation force; and (3) temperature stability and operating temperature range.

We will use first principles calculations to identify new, higher performance piezoelectric materials. High-performance piezoelectrics are ferroelectric materials near morphotropic phase boundaries. The focus of our work will be on identification of morphotropic phase boundary perovskites with performance better than PZT.

Prior work shows that certain types of disorder can be useful in this context; we will use this strategy to find new materials. The materials parameters that address the barriers above are (a) lattice distortion at the morphotropic phase boundary (maximum actuation); (b) ferroelectric polarization and (c) ferroelectric Curie temperature at the morphotropic phase boundary. The initial focus will be on perovskite structure oxides with low cost that may have larger lattice distortion at a morphotropic phase boundary and adequate Curie temperature for application. We will calculate the properties of the phases in relation to PZT.

Results

This is a new project that started in the fourth quarter of fiscal year 2013. The following summarizes the results obtained during this period.

We selected materials based on Fe_3P and $Co_{23}Hf_6$ as starting points for potential high-performance permanent magnets. We also selected materials for study as potential thermoelectrics, focusing on the need for both low cost and high performance.

We did preliminary screens to identify what perovskite alloys, based on PZT, might be most promising for investigation. We selected an initial strategy based on increasing the ferroelectric polarization by incorporating Bismuth perovskites, specifically alloys related to $(Na,Bi)TiO_3$ and $Bi(Zn,Ti)O_3$. We also designed computational cells that will be used for the first principles investigation of the alloys of these with PZT.

We have shown that CuFe-SSZ-13 is an excellent catalyst capable of converting 80% NOx at 150°C under fast selective catalytic reduction conditions of simulated lean emission. Our focus is two-fold: (1) prepare for engine testing of CuFe-SSZ-13 and (2) explore new catalysts that can function effectively at low temperatures under standard selective catalytic reduction conditions.

For supported catalysts, we have previously shown that single supported Pt atoms are catalytically active, and we have proposed a new mechanism to explain the catalytic activity for CO oxidation. We are focusing on exploring NO oxidation on single supported catalysts. First principles modeling results suggest that single supported Pt will not be a good NO oxidation catalyst, while single-supported Pd will be an effective NO oxidation catalyst. Experimental work is in progress to validate the results. This

will enable us to selectively prepare a low-temperature catalyst that can effectively treat stoichiometric emissions.

Conclusions

We are developing and demonstrating ICME strategies for propulsion materials development as applied to four key materials challenges. These are rare earth-free permanent magnetic materials for electric motors, high-performance piezoelectrics for fuel injectors, thermoelectrics for waste heat recovery, and cabin climate control and low-temperature catalysts for emissions treatment.

Project 18865 – Application-Specific Materials Simulation, Characterization, and Synthesis

Agreement 26464 – Materials Characterization and Evaluation

J.A. Haynes
Materials Science and Technology Division
Oak Ridge National Laboratory
P.O. Box 2008, MS 6056
Oak Ridge, TN 37831-6056
Phone (865) 576-2894; fax: (865) 574-4913; e-mail: haynesa@ornl.gov

DOE Technology Manager: Jerry L. Gibbs
Phone (202) 586-1182; fax: (202) 586-1600; e-mail: jerry.gibbs@ee.doe.gov
ORNL Technical Advisor: J. Allen Haynes
Phone (865) 576-2894; fax: (865) 574-4913; e-mail: haynesa@ornl.gov

Contractor: Oak Ridge National Laboratory, Oak Ridge, Tennessee
Prime Contract No.: DE-AC05-00OR22725

Objectives

- Facilitate support and coverage for the critical characterization facilities at Oak Ridge National Laboratory (ORNL) that support VT research goals. This effort is necessary due to the absence of direct support for the suite of equipment formerly supported by the High-Temperature Materials Laboratory program.
- Evaluate materials needs and support strategies related to emerging, high-efficiency propulsion trends, including needs related to higher-temperature engine materials and natural gas-fired and dual fuel engines.
- Provide field management support for the propulsion materials activities at ORNL.

Approach

- Identify and monitor all critical materials characterization and testing facilities at ORNL necessary to accomplish VT materials research objectives for fiscal year 2014 and beyond; fill gaps where necessary and possible within budget limits to ensure all instruments have adequate funding and maintenance.
- Explore natural gas-related materials issues within advanced powertrains.
- Evaluate needs and opportunities for higher-temperature materials and low-cost coating systems.

Accomplishments

- Identification of critical materials characterization and testing facilities within the High-Temperature Materials Laboratory and the existing support and maintenance plans for each.
- Facilitation of instrument support contracts, user costs, and maintenance plans for fiscal year 2014 with the Materials Analysis and Characterization group.
- Acquired an x-ray fluorescence unit for characterization of after-treatment devices.
- Initiated high-temperature, instrumented oxidation testing (gen-set) of high-temperature alloys in diesel exhaust.

Future Direction

- Facilitation of a more durable gen-set unit for testing high-temperature alloys and coatings in diesel exhaust at controlled temperatures.
- Continued support of characterization and testing facilities at ORNL.

Introduction

This project, which began late in the fourth quarter of fiscal year 2013, will provide field management support for propulsion materials activities at ORNL, as well as evaluation of materials needs and strategies related to selected emerging propulsion trends. Much of the propulsion materials and other vehicle technologies efforts at ORNL rely heavily on state-of-the-art characterization facilities in the Materials Science and Technology Division.

These project-critical characterization instruments, such as the aberration-corrected transmission electron microscopes, focused ion beam mill, electron probe microanalyzer, scanning electron microscopes, and the x-ray photoelectron spectroscopy system, require extensive maintenance and support. This project will support gaps in instrument maintenance needs and will ensure that adequate support remains available to keep key instruments in operating condition and projects on schedule.

The project also will begin to evaluate strategies for long-term support of high-cost, state-of-the-art characterization tools at ORNL that are necessary to enable VT to continue to support world-class transportation materials research. This effort is necessary due to the absence of direct support for the suite of equipment formerly supported by the High-Temperature Materials Laboratory Program.

The project also will seek to identify and engage emerging needs and opportunities related to advanced powertrain materials. One emerging trend that has potential to impact propulsion materials is the rapidly increasing use of natural gas–fired heavy-duty engines for applications other than buses and local waste hauling. This project will survey industry and others to evaluate whether there are materials needs and trends related to the emerging increase in natural gas-fired heavy-duty truck engines. Retrofitting or replacing diesel engines with natural gas-fired engines or dual fuel engines is an increasing trend due to the low cost and wide availability of natural gas in the United States, which is resulting from the natural gas shale drilling boom.

Natural gas is cheaper and burns cleaner than diesel (although with lower energy density) and is abundantly available domestically. Therefore, fleets are able to reduce fuel costs, improve emissions, and ensure better fuel cost stability by switching to natural gas, even though the initial capital investment is higher for natural gas-fired vehicles and the fuel distribution infrastructure is currently very limited. However, because of the driving force of lower fuel costs, there has been a significant recent increase in heavy truck fleets partially converting to natural gas use. For example, United Postal Service reports that it is increasing its fleet of liquefied natural gas vehicles from 112 to over 800 in 2013, hoping to make liquefied natural gas vehicles the majority of its new acquisitions within 2 years. Shell Energy, Pilot Travel Centers, Clean Energy Fuels, and ENN have built or are building hundreds of new natural gas fueling stations along major routes in the United States. Cummins executives have been quoted in the press as stating that their projections show that natural gas could capture as much as 10% of the heavy-duty truck market in the United States in the next 5 years. On the other hand, original equipment manufacturers have indicated that potential materials-related concerns and opportunities exist related to natural gas use for reciprocating engines, which include, but are not limited to, catalyst systems, spark ignition, sulfur effects, acids, higher combustion and peak temperatures than diesel, and tribological issues with rings, liners, and valves.

Another emerging trend that will significantly impact powertrain materials over the next decade is increasing engine temperatures. One of the primary goals for the transportation industry, and for Energy Efficiency and Renewable Energy, is to achieve unprecedented increases in engine efficiency over the next decade. For example, the VT Multi-Year Program Plan set a goal of increasing the thermal efficiency of heavy truck engines by 30%, whereas in 2012, new Corporate Average Fuel Economy standards of 54.5 mpg by 2025 (a 99% increase over the 2011 standard of 27.3 mpg) were announced.

As escalating efficiency demands continue to drive vehicle technologies, some advanced gasoline, diesel, and natural gas reciprocating engine designs will require increasing pressures and elevated engine and exhaust temperatures. Eventual maximum temperatures between 900 and 1000°C are anticipated, requiring new classes of automotive materials with significantly improved high-temperature mechanical properties and advanced oxidation and corrosion resistance. The projected temperatures above 900°C move into the realm of structural materials used for gas turbine engines. However, the automotive industry faces much more severe cost restrictions than the power generation or aircraft industries.

Direct adoption of high-temperature turbine materials for automotive applications will be difficult; therefore, lower-cost versions of these materials will have to be developed, likely resulting in further reduction of their inherent oxidation/corrosion resistance in order to retain adequate strength. The aircraft industry addressed the design balance of needing both high-temperature structural integrity and corrosion resistance by aggressively developing a diverse suite of protective high-temperature coatings for hot section alloys. Such an approach allowed the use of stronger materials with lower oxidation/corrosion resistance, or in some cases, lower cost structural materials at higher temperatures. However, similar coatings systems presently do not exist for reciprocating engines, because previous design temperatures have not required their presence.

In this project, we will begin to evaluate the potential for low-cost, high-temperature, protective coating materials to enable affordable, higher-temperature structural materials for next generation reciprocating engines and exhaust systems operating above 760°C and up to 950°C.

The proposed new effort would leverage ORNL's expertise in both coatings and high-temperature structural materials to identify the potential protective coating or coating/alloy systems capable of increasing the allowable operating temperature and/or improving the life time of current and future high-temperature engine and exhaust materials. Preliminary experiments to evaluate oxidation behavior of candidate higher-temperature alloys at 800°C in actual diesel exhaust were initiated using a diesel generator set.

Results

A characterization support plan has been created to support the critical instruments in the materials science division at ORNL. An x-ray fluorescence unit has been acquired from another division. The unit is being repaired and installed to provide improved evaluation of after-treatment materials. Visits were made to two heavy-duty diesel engine manufacturers, with discussions including their natural gas-related materials needs. Preliminary experiments to evaluate oxidation behavior of candidate higher-temperature alloys at 800°C in actual diesel exhaust were initiated using an instrumented diesel generator set. These results are intended to provide a method of more accurately linking accelerated laboratory oxidation tests in air and water vapor to actual engine exhaust results for both alloys and coatings.

Conclusions

This new project started late in the fourth quarter of fiscal year 2013 and provides field management support, facilitation of characterization instrumentation and support, and technical evaluation of higher-temperature materials.

DOE/EE-1103 January 2014
Printed with a renewable-source ink on paper containing
at least 50% wastepaper, including 10% post consumer waste.

U.S. DEPARTMENT OF ENERGY | Energy Efficiency & Renewable Energy

For more information
eere.energy.gov